Université de Lille

Ecole doctorale : ENGSYS

Thèse

Pour obtenir le grade de docteur

Spécialité : Electronique, Microélectronique, Nanoélectronique et Micro-ondes

Conception et Développement d'Etalons de Paramètres S pour la Caractérisation des Nanodispositifs Haute Fréquence

Daouda SECK

Soutenue le 01 décembre 2025 devant la commission d'examen

Membres du Jury

Président du jury et Rapporteur : Pr. Aziz BENLARBI-DELAÏ – Université Sorbonne

Rapporteur : Dr. Katia GRENIER – Directrice de recherche (DR), LAAS-CNRS

Examinateur : Dr. Sébastien FREGONESE – Chargé de recherche, Université de Bordeaux

Examinateur : Dr. Nicolas DEFRANCE – Maître de conférences (MCF), Université de Lille

Encadrant : Dr. Djamel ALLAL – Ingénieur de recherche (IR), LNE, Paris

Directeur de thèse : Pr. Kamel HADDADI – Université de Lille

University of Lille

Doctoral School (ENGSYS)

PhD THESIS

Submitted to obtain the degree of doctor.

Specialty: Electronics, Microelectronics, Nanoelectronics, and Microwave

Design and Development of S-Parameter Standards for High-Frequency Nanodevices Characterization

Daouda SECK

Defended on December 01, 2025, before the Examination Committee

Jury Members

President and Reviewer: Prof. Aziz BENLARBI-DELAÏ – Sorbonne University

Reviewer: Dr. Katia GRENIER – Research Director (DR), LAAS-CNRS

Examiner: Dr. Sébastien FRÉGONÈSE – Research Fellow, University of Bordeaux

Examiner: Dr. Nicolas DEFRANCE – Associate Professor (MCF), University of Lille

Supervisor: Dr. Djamel ALLAL – Research Engineer (IR), LNE, Paris

Doctoral Advisor: Prof. Kamel HADDADI – University of Lille

Résumé

La présente thèse s'inscrit dans le prolongement de travaux visant à établir des méthodes fiables et traçables pour la mesure des paramètres S de circuits planaires. Portée par le Laboratoire National de Métrologie et d'Essai (LNE) en partenariat avec l'Institut d'Électronique, de Microélectronique et de Nanotechnologie (IEMN), cette recherche répond aux besoins croissants de l'industrie des radiofréquences (RF) et des micro-ondes, tout en accordant une attention particulière à la miniaturisation des dispositifs électroniques.

La réduction de la taille des composants représente un levier essentiel du progrès technologique, mais elle impacte fortement les performances électriques des dispositifs. Ces performances sont évaluées à l'aide d'instruments de référence tels que les analyseurs de réseaux vectoriels (VNAs), optimisés pour une impédance nominale de 50 Ω et sensibles aux variations induites par le composant testé.

La miniaturisation des dispositifs peut engendrer des plages d'impédance extrêmes. La mesure d'un nanocomposant avec un VNA pose alors des défis majeurs, tant en termes d'adaptation d'impédance que de sensibilité de mesure. Par exemple, un dispositif à haute impédance risque d'être interprété comme un court-circuit, un circuit ouvert ou une condition similaire par l'instrument, ce qui complexifie la détection et génère du bruit dans les mesures.

Face à ces difficultés, le LNE développe de nouvelles méthodologies de mesure par VNA. L'objectif est d'élargir la bande de fréquences couverte, de cibler des domaines d'impédance spécifiques et de travailler à l'échelle nanométrique. Ce travail consiste à concevoir et à développer des nanostructures coplanaires traçables pour l'étalonnage vectoriel, capables de couvrir une large gamme d'impédances, y compris les valeurs extrêmes. Des méthodes d'étalonnage spécifiques sont également mises en place afin d'assurer la vérification métrologique du système de mesure.

La thèse est consacrée à la conception de nanocomposants coplanaires en configuration Ground–Signal–Ground (GSG) destinés à l'étalonnage des VNAs, avec un focus particulier sur les mesures de paramètres S réalisées sur wafer. Elle aborde les principaux défis et avancées dans le domaine de la mesure RF et micro-ondes sur wafer, avec un accent sur la caractérisation précise des nanodispositifs jusqu'à des fréquences de 110 GHz.

Le document présente le contexte scientifique, les motivations et objectifs de la recherche, un état de l'art en métrologie RF couvrant les lignes de transmission et les systèmes de mesure de paramètres S, les méthodes d'étalonnage et de de-embedding, ainsi que l'évaluation des incertitudes selon le GUM. Une attention particulière est accordée aux techniques de mesure sur wafer, à l'influence de la miniaturisation et aux problématiques liées aux mesures à haute impédance.

La thèse détaille la conception et la fabrication de kits d'étalonnage dédiés, en abordant le choix des technologies, des matériaux et des dimensions, les simulations électromagnétiques et la validation des algorithmes d'étalonnage. Elle expose également le dispositif expérimental utilisé pour caractériser les dispositifs de DC à 110 GHz, les protocoles de mesure, les procédures de correction des données, les études de reproductibilité et l'analyse des incertitudes via la méthode TRL, sur la base de standards mesurés et modélisés.

Le travail introduit de nouvelles approches pour les mesures à haute impédance, validées expérimentalement avec divers kits d'étalonnage basés sur la méthode multiline-TRL. Ces approches incluent la méthode Short-Open-Load-Thru (SOLT) et des variantes intégrant des offsets, telles que Short-Short-Short-Thru (SSST), Open-Open-Open-Thru (OOOT) et $\mathrm{High}_{\mathrm{impedance}}$-$\mathrm{High}_{\mathrm{impedance}}$-$\mathrm{High}_{\mathrm{impedance}}$-Thru (HHHT).

Enfin, la thèse propose des perspectives d'extension de ces méthodes à de nouvelles applications. Globalement, cette recherche apporte des contributions théoriques et expérimentales pour améliorer la précision, la répétabilité et l'applicabilité des mesures RF et micro-ondes sur wafer, notamment pour des dispositifs de plus en plus miniaturisés et à forte impédance.

Mots clés : Etalons de paramètres S, Analyseur de réseau vectoriel (VNA), Haute fréquence, Méthodes d'étalonnage, Incertitudes, Traçabilité, guide d'onde coplanaire, Nanodispositifs, Métrologie, Impédance.

Abstract

This thesis arises from work undertaking to establish reliable and traceable methods for S-parameter measurements of planar circuits. The LNE, in partnership with IEMN, is committed to continually meeting the growing needs of the RF and microwave industry, with a particular focus on the miniaturization of electronic devices.

While reducing component size is essential for technological advancement, it also impacts electrical performance. These performance characteristics are assessed using measurement instruments such as vector network analyzers (VNAs), which typically operate with a nominal impedance of 50 Ω. These instruments are optimized for this impedance and are especially sensitive to variations introduced by the device under test.

Miniaturization can significantly alter the impedance range, sometimes resulting in extreme values. Measuring a nanocomponent with a VNA therefore introduces challenges related to impedance matching and measurement sensitivity. For example, a high impedance nanodevice might be interpreted by the instrument as either a short or open circuit, or something close to these conditions, making accurate detection difficult and leading to highly noisy measurements.

In response to these challenges, LNE is expanding its research on VNA measurement methodologies. The work aims to cover a wider frequency range, target specific impedance domains, and operate at the nanoscale. The objective is to design and develop traceable coplanar nanostructures for vector calibration, supporting an extended impedance range including extreme, low, and high values and to establish associated calibration methods that ensure the metrological verification of the measurement system.

This thesis is devoted entirely to the design of new coplanar nanocomponents in a Ground–Signal–Ground (GSG) configuration for VNA calibration, specifically for on-wafer S-parameter measurements.

The work addresses the key challenges and advances in RF and microwave on-wafer measurements, with special emphasis on the precise characterization of nanodevices up to 110 GHz. It covers the overall scientific context, motivations, and objectives, the state of the art in RF metrology including the fundamentals of transmission lines and S-parameters RF measurement systems, calibration and de-embedding methods, and uncertainty assessment according to the GUM. A particular focus is placed on on-wafer measurement techniques, the influence of device miniaturization, and issues related to high-impedance measurements.

The thesis details the steps involved in designing and fabricating dedicated calibration kits, including the choice of technology, materials, and dimensions, electromagnetic simulations, and validation of calibration algorithms. It also presents the experimental setup for characterizing devices from DC to 110 GHz, measurement protocols, data correction procedures, reproducibility studies, and uncertainty analysis using the TRL method based on both measured and modeled standards.

Furthermore, the work focuses on developing new approaches for high-impedance measurements. These approaches are experimentally validated using different calibration kits based on the multiline-TRL

method. The new approaches include the well-known Short-Open-Load-Thru (SOLT) method, as well as derivative methods that integrate offsets into the standards, including Short-Short-Short-Thru (SSST), Open-Open-Open-Thru (OOOT), and $High_{impedance}$-$High_{impedance}$-$High_{impedance}$-Thru (HHHT).

The thesis concludes by outlining prospects for extending these methods to new applications. Overall, this research makes both theoretical and experimental contributions aimed at improving the accuracy, repeatability, and applicability of RF and microwave on-wafer measurements, particularly for increasingly miniaturized and high-impedance devices.

Keywords: S-parameter standards, Vector Network Analyzer (VNA), High Frequency, Calibration Methods, Uncertainties, Traceability, Coplanar Waveguide (CPW), Nanodevice, Metrology, Impedance.

Acknowledgments

The research described in this dissertation was conducted at the Laboratoire National de Métrologie et d'Essai (LNE), in close collaboration with the Institut d'Électronique, de Microélectronique et de Nanotechnologie (IEMN), under the framework of CIFRE funding. I am deeply thankful to the leadership and research staff at both institutions for their invaluable support and for providing an environment conducive to scientific research and progress.

First and foremost, I would like to express my heartfelt appreciation to the members of the thesis jury for the honor they have bestowed upon me by evaluating this work. I extend my sincere gratitude to the president of the jury for kindly accepting to preside over the defense. I am deeply thankful to the reviewers, Dr. Katia GRENIER, CNRS Research Director at LAAS-CNRS, and Full Professor Aziz BENLARBI-DELAÏ from Sorbonne University, for their careful reading and insightful feedback, which have greatly contributed to improving the quality of this manuscript. I also wish to express my gratitude to Associate Professor Nicolas DEFRANCE from the University of Lille for serving as an examiner, and to Dr. Sébastien FREGONESE, CNRS Research Fellow at the University of Bordeaux, for his participation and valuable comments.

I wish to express my sincere gratitude to Mr. Jean-Marie LERAT, Head of the High-Frequency Electrical Metrology Department at LNE, and Mr. Hubert BERRY, Head of the Electrical Metrology Division, for granting me the opportunity to pursue this thesis and for their warm welcome. Their support was instrumental in ensuring excellent working conditions throughout the research. I am also grateful to Mr. Thierry MELLIN, Director of IEMN, for welcoming me into the institute, as well as to Mr. Henry HAPPY and Mr. Vincent THOMY, Professors at the University of Lille, for their guidance and encouragement.

I am especially thankful to Full Professor Kamel HADDADI from the University of Lille for his trust and oversight as my thesis supervisor. His availability, insightful advice, meticulous proofreading, and consistently relevant suggestions were crucial to the successful completion of this work. His scientific and moral support played a decisive role in bringing the thesis to fruition.

Special thanks are also due to Mr. Djamel ALLAL, Research Engineer at LNE, for his unwavering support, enriching scientific discussions, and thoughtful guidance. Working alongside him has been a pleasure, and I am grateful for the opportunity to benefit from his expertise and generosity.

I warmly acknowledge my colleagues and friends for their technical assistance, stimulating discussions, and ongoing support: Doudou BA, Thi Dao PHAM, Alexis LITWIN, Houssemeddine KRRAOUI, Seif BEN HASSINE, José MORAN, as well as all members of the laboratory Pierre-Jean JANIN, Daniela ISTRATE, Ousmane NDIR, Mohamed AGAZAR, Mohamed OUAMEUR, Fabrice FISTON, Remy PICOU, Emmanuel PATOIS, Alexandre DERNIAUX, Kamel DOUGDAG, Omer MOREAU, Christel COSTANTINO, Mathilde GONTIER, Hanane SAADEDDINE. Their friendship and the pleasant moments we have shared have greatly enriched my experience.

I also thank my colleagues at IEMN Florent MARLEC, Sylvie LEPILIET, Mohamed SEBBACHE, Clément LENOIR, Cerine MOKHTARI, Nora BENBAHLOULI, Alexandre RENAU for their involvement and support throughout the course of this research.

Finally, I wish to express my deepest gratitude to my family, especially my parents, brothers, and sisters, for their love, patience, and steadfast support during these years. Their encouragement has been a continuous source of strength and motivation.

List of Figures

List of Tables

Contents

General Introduction

1. Context

Technological advancements over the past several decades have been largely propelled by the ongoing exploration and manipulation of ever-smaller structures, reaching dimensions at the nanometer scale. This continual drive toward miniaturization has had a profound impact on a wide range of scientific and engineering fields.

When working at the micrometer scale, the area of study is known as microtechnology. However, as dimensions decrease further specifically to the range of 1 to 100 nanometers, which constitutes one billionth of a meter the field transitions into what is recognized as nanotechnology.

The term "nano" is broadly used to describe both extremely small particles, known as nanoparticles, and highly miniaturized electronic systems, commonly referred to as nanoelectronics. In the realm of electronics, such progress has enabled a significant reduction in the size of transistors, achieving technological nodes as small as 2 nanometers.

Looking ahead, forecasts suggest that this trend of increasing transistor density will continue through 2030, with characteristic device dimensions expected to approach the angstrom scale [1].

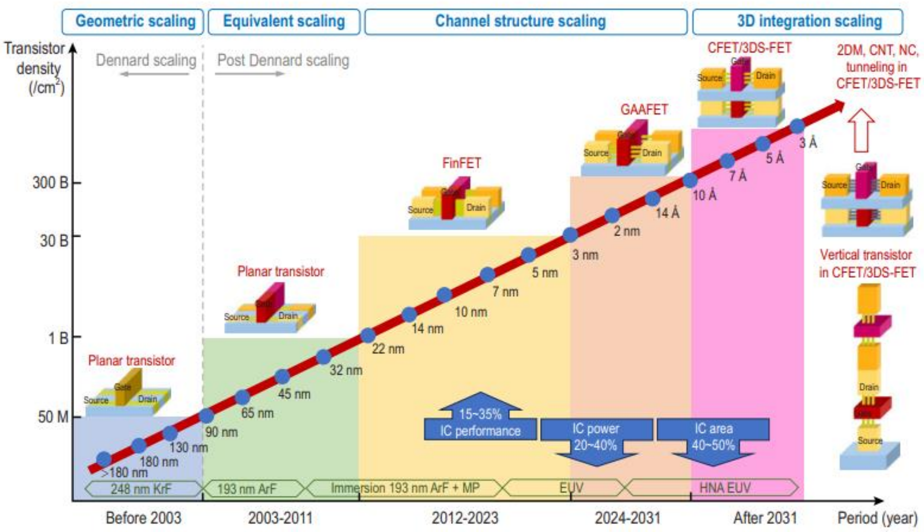

Fig. 0.1: Trend in MOSFET Transistor Density [1].

Transmission lines are essential elements in radiofrequency, microwave, and electronic systems, serving as the primary means of interconnecting components and facilitating efficient signal propagation. Their effectiveness in these applications hinges on careful design and selection, with impedance matching being a crucial factor for optimizing transmission and minimizing signal losses.

The magnitude of these losses is determined by the intrinsic physical properties of the materials used to construct the lines, including both conductive and dielectric substances. Key material characteristics, such as electrical conductivity, thermal conductivity, and dielectric loss tangent, play significant roles in the overall performance. In integrated circuits operating at millimeter-wave or submillimeter-wave frequencies, transmission lines are typically fabricated from semiconductors like silicon, germanium, or carbon, as well as metals such as gold, copper, or aluminum.

The electrical performance of a transmission line is directly related to its conductivity and the geometrical parameters of the structure, specifically its width and thickness. As the dimensions of these lines are reduced to the nanometric scale, their characteristics become increasingly sensitive to factors such as surface roughness, which can no longer be ignored. This sensitivity is particularly pronounced in semiconductor nanowires incorporated into field-effect transistors (FETs), where even minor deviations in geometry can have a substantial impact on functionality and efficiency [2].

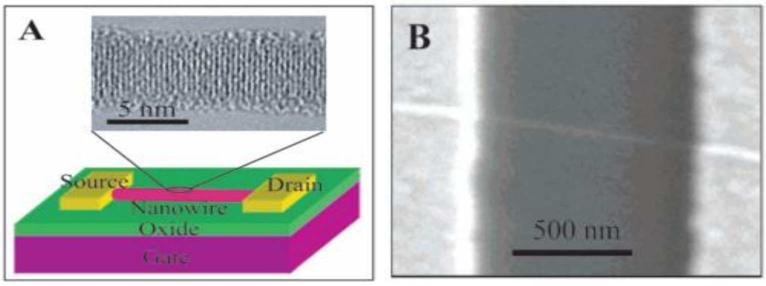

Fig. 0.2: A) Silicon nanowires connecting the drain and source of a FET transistor | B) Scanning electron microscopy image [3].

Nanowires have found applications beyond electronics, playing a significant role in chemical and biological sensing. For example, they can be employed as pH probes, where changes in the pH of a solution trigger the protonation or deprotonation of surface functional groups, such as $–NH_2$ or Si–OH [3]. This property allows nanowires to be integrated into diagnostic platforms capable of detecting a variety of biological targets, including proteins, DNA, and viruses. Beyond sensing, nanowires also show potential for use in energy storage and photovoltaic systems due to their unique properties and nanoscale dimensions.

The fabrication of silicon nanowires can be achieved through several distinct methods. These include the physical evaporation of silicon powder, the Vapor–Liquid–Solid (VLS) growth process, growth assisted by transmission electron microscopy, laser ablation, and the Solid–Liquid–Solid (SLS) technique, among others. Each method offers unique advantages and is selected based on the intended application and desired properties of the resulting nanowires.

Another significant class of nanodevices within nanotechnology is carbon nanotubes (CNTs). Carbon nanotubes are created by rolling sheets of graphene into cylindrical shapes. The simplest form, known as a single-walled carbon nanotube (SWCNT), may exist at various diameters. When multiple graphene cylinders are arranged concentrically, they form multi-walled carbon nanotubes (MWCNTs). Both SWCNTs and MWCNTs have become key components in a wide range of nanoscale applications, benefiting from their unique structural and electronic properties [4].

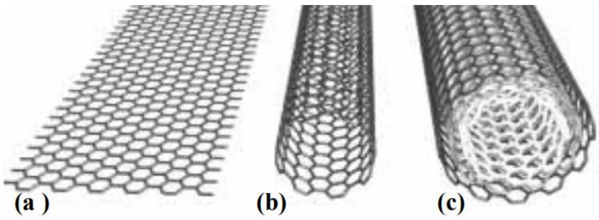

Fig. 0.3: (a) Section of a carbon nanotube wall (b) Single-walled carbon nanotube (c) multi-walled carbon nanotube [4].

Single-walled carbon nanotubes (SWCNTs) are defined by their extremely small diameters, typically ranging from 0.2 to 2 nanometers. In contrast, multi-walled carbon nanotubes (MWCNTs) possess larger diameters, usually between 5 and 20 nanometers, although in some instances, their diameters can extend up to 100 nanometers. These structural differences are important in determining the specific properties and potential uses of each type of carbon nanotube.

Like nanowires, carbon nanotubes have found widespread application within the field of electronics. One notable example is the integration of a thin layer of carbon nanotubes onto field-effect transistors (FETs). This approach has demonstrated significant performance enhancements in organic light-emitting diodes (OLEDs). The primary reason for this improvement is the superior charge carrier mobility exhibited by carbon nanotubes when compared to conventional amorphous silicon. This enhanced mobility leads to more efficient charge transport, which is crucial for the performance and efficiency of electronic devices such as OLEDs.

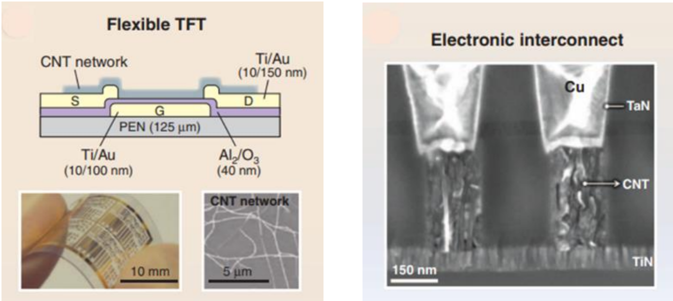

Fig. 0.4 : Nanotube de carbone sur du transistor FET (left); Nanotube de carbone pour interconnexion (right).

One notable advantage of incorporating carbon nanotubes (CNTs) into field-effect transistor (FET) structures is the relative ease of their deposition. The fabrication of CNT-based interconnects is particularly efficient, as these interconnects can achieve diameters down to just a few nanometers. Such fine-scale fabrication is highly compatible with existing CMOS (complementary metal-oxide-semiconductor) technologies, facilitating the integration of CNTs into modern electronic devices.

Beyond their role in electronics, carbon nanotubes are extensively utilized in various energy storage systems. Their unique properties make them valuable in the development of batteries, supercapacitors, and solar cells, where they contribute to improved performance and efficiency.

As nanotechnology continues to advance, the array of nanodevices is rapidly expanding. This includes not only nanometric transmission lines, such as nanowires and carbon nanotubes, but also a broad spectrum of other devices. Among these are nanotransistors, nanorobots [6], nanosensors [7], and nanoantennas [8], each offering unique capabilities and applications in various technological fields.

2. Motivations

Electronic components form the foundational structure of devices across a range of sectors, including telecommunications, transportation, security, and technology. The recent shift toward monolithic microwave integrated circuit (MMIC) technology has been driven by its versatility and adaptability, making it increasingly central to the design of modern electronic devices. For design engineers, accurately assessing the electrical performance of these components is essential, requiring both a solid conceptual understanding and appropriate measurement tools.

To evaluate the electrical properties of components, instruments such as Vector Network Analyzers are commonly used. VNAs measure the frequency-dependent behavior of a device by determining its scattering parameters (S-parameters), which reflect both reflection and transmission coefficients. This process involves applying voltage and current waves to the device and monitoring the resulting signals. The use of S-parameters becomes particularly useful when the physical size of the component under test is comparable to the wavelength of the signal. At the instrumentation level, questions related to the reliability of measuring instruments and standards validating measurement results can arise. These questions lead to the broader field of metrology.

Metrology is fundamental in any domain where precise measurement of fundamental or derived quantities is required, as it provides the principles and methodologies necessary for trustworthy results and reliable instruments. Over time, metrology has evolved into distinct branches: fundamental (or scientific) metrology focuses on creating and maintaining reference standards; legal metrology addresses regulatory and certification issues; and industrial metrology pertains to measurements within manufacturing processes. Success in metrology relies on a specialized vocabulary and adherence to international standards, often involving accredited laboratories.

The “Laboratory National de Métrologie et d’Essais” (LNE) exemplifies this role, with a broad scope of activities in industry, defense, energy, construction, transportation, healthcare, consumer goods, and instrumentation. LNE is responsible for ensuring the traceability and quality of measurement results, issuing certifications, and acting as a reference institution. Its responsibilities include balancing considerations of safety, health, environment, reliability, performance, and cost. Through collaborations with other laboratories, LNE also supports joint research projects and inter-laboratory comparisons, thereby reinforcing global metrological standards and trust.

Building on previous work at LNE in S-parameter metrology, current efforts are expanding to address the demands of rapidly evolving technologies. The ongoing miniaturization of electronic components and the trend toward higher operating frequencies are persistent challenges for engineers and researchers. Nanodevices, distinguished by their nanometric dimensions and complex geometries, are typically fabricated on dielectric or semiconductor substrates, resulting in wafer-based components.

Reducing the size of components has notable implications. It alters the impedance characteristics of the devices, which can deviate significantly from the standard 50 Ω reference impedance of VNAs. At such extremes, whether very low or very high, the sensitivity and accuracy of VNAs in measuring S-parameters are diminished, requiring adjustments to the measurement systems. Commercially available calibration standards often fail to match the geometry and dimensions of nanocomponents, which reduces calibration accuracy. In addition, the diverse materials used in nanodevices exhibit frequency-dependent behavior, further complicating electrical measurements.

In effect, the reduction in component dimensions raises fundamental questions about the validity of VNA-based measurements, which typically rely on standard impedances. Under these conditions, analyzers may misinterpret device responses, producing impedance readings that resemble open- or short-circuit conditions and introducing significant measurement noise. Therefore, it is essential to develop measurement systems and calibration standards specifically tailored to these unique conditions. For wafer-based nanocomponents, S-parameter measurements using VNAs are facilitated by probes designed to match the planar topology of the devices under test.

RF measurements are indispensable for characterizing electronic devices, especially in integrated circuits and communication systems. As component sizes continue to shrink and operating frequencies increase, the challenge of ensuring measurement accuracy becomes more pronounced. Among available methodologies, on-wafer measurements are particularly effective as they allow direct characterization of components on their substrate, minimizing the parasitic effects associated with external interconnections.

In this context, the calibration of measurement systems is vital for achieving reliable and reproducible results. However, traditional calibration kits designed for 50 Ω transmission lines become inadequate when applied to devices with higher or unconventional impedances. This necessitates the development of adapted calibration strategies that can precisely compensate for measurement errors and ensure the reliability of results in advanced RF characterization.

3. Objectives

This thesis represents a joint endeavor between the Laboratoire National de Métrologie et d'Essais (LNE) and the Institute of Electronics, Microelectronics, and Nanotechnology of Lille (IEMN). The collaboration leverages the extensive expertise of both institutions, encompassing areas of metrology and various technological domains, and utilizes sophisticated technical platforms to support the research objectives. The central theme of this work is the traceability of S-parameter measurements for coplanar components. This focus has become increasingly critical due to the continuous trend of reducing component sizes, which in turn, leads to significant variations in circuit impedance. As electronic devices become more miniaturized, maintaining accurate and traceable measurements is essential for reliable characterization and advancement in technology.

The principal aim of this thesis is to develop traceable coplanar S-parameter standards specifically designed for nanometric-scale applications. These standards utilize a Ground-Signal-Ground (GSG) configuration to ensure compatibility with the unique requirements of high-frequency nanodevices. By defining the standards at such a small scale, the work addresses the challenges associated with the calibration of vector network analyzers, which are essential for precise S-parameter measurements in modern electronic components. The proposed standards serve as a critical foundation for accurate and reliable characterization of nanodevices fabricated on high-frequency substrates. This approach enables the calibration process to account for the distinctive properties inherent to nanometric devices, thereby enhancing measurement traceability and supporting advancements in the field of radio frequency metrology.

The coplanar S-parameter standards proposed in this thesis are categorized as passive components. Achieving accurate modeling and characterization of these standards requires careful consideration of multiple factors, including their geometric dimensions, electrical properties, and the characteristics of the materials used in their fabrication. These standards comprise several fundamental component types, such as transmission lines, short circuits, open circuits, and matched loads. Each type of component calls for the application of specific calibration methodologies. These methodologies are meticulously tailored to ensure that measurement reliability and precision are maintained at the highest possible levels throughout the characterization process.

Given that the proposed S-parameter standards are defined at the nanometric scale, it is essential that the associated measurement systems are precisely tailored to function effectively at this level of miniaturization. This meticulous adaptation is necessary to ensure that these standards consistently deliver reliable performance and remain in compliance with regulatory requirements during the calibration for nanodevices measurement. By employing measurement systems specifically designed for nanometric dimensions, the integrity and accuracy of calibration processes are preserved. Consequently, this approach directly supports ongoing advancements in the design and characterization of high-frequency electronic components, enabling industry to keep pace with the stringent demands of cutting-edge technological innovation.

4. Organization of manuscript

Calibration of measurement systems plays a critical role in achieving reliable and reproducible results, especially in the context of advanced RF characterization. Traditional calibration kits, which are typically designed for standard 50 Ω transmission lines, encounter significant limitations when they are used with devices that possess higher or unconventional impedances. These limitations introduce new challenges and highlight the need to develop adapted methodologies that provide precise compensation for measurement errors.

This manuscript is organized into four comprehensive chapters, each addressing a key aspect of RF metrology in the context of emerging technological challenges:

- Chapter 1: State of the art in on-wafer measurements
  This chapter offers an in-depth review of current RF measurement techniques. It covers fundamental concepts of high-frequency characterization and emphasizes the challenges that arise from miniaturization, precision requirements, and the measurement of high-impedance devices.
- Chapter 2: Design and Fabrication of Calibration Kits
  The second chapter focuses on the design and fabrication of calibration kits. These kits form the basis for advancing calibration methodologies, addressing the need for more accurate standards that can accommodate the unique properties of modern electronic components.
- Chapter 3: Experimental On-Wafer RF Characterization
  This chapter discusses experimental methods for on-wafer RF characterization. It details the approaches and instruments used to evaluate the performance of devices, ensuring that the measurement techniques are properly adapted to the characteristics of the components under test.
- Chapter 4: Development of Calibration Techniques for High-Impedance Structures
  The fourth chapter addresses the development of calibration techniques specifically tailored for high-impedance structures. It proposes and examines solutions aimed at enhancing measurement reliability in this challenging domain.

Through the work presented in this manuscript, the aim is to advance the field of RF metrology by developing methodologies that effectively address the challenges posed by component miniaturization and high-impedance devices. The findings are intended to contribute to significant improvements in both measurement precision and reliability.

References 0

[1] ZHANG, Qingzhu, ZHANG, Yongkui, LUO, Yanna, et al. *New structure transistors for advanced technology node CMOS ICs.* National Science Review, 2024, vol. 11, no 3, p. nwae008.
[2] LU, Wei et LIEBER, Charles M. Semiconductor nanowires. *Journal of Physics D: Applied Physics*, 2006, vol. 39, no 21, p. R387.
[3] SALHI, Billel, HOSSAIN, M. K., MUKHAIMER, A. W., *et al.* Nanowires: a new pathway to nanotechnology-based applications. *Journal of electroceramics*, 2016, vol. 37, p. 34-49.
[4] KREUPL, Franz, GRAHAM, Andrew P., DUESBERG, G. S., *et al.* Carbon nanotubes in interconnect applications. *Microelectronic Engineering*, 2002, vol. 64, no 1-4, p. 399-408.
[5] DE VOLDER, Michael FL, TAWFICK, Sameh H., BAUGHMAN, Ray H., *et al.* Carbon nanotubes: present and future commercial applications. *science*, 2013, vol. 339, no 6119, p. 535-539.
[6] BUI, Minh Phu, PARK, Myeongjin, LE, Tuan-Anh, *et al.* A Development of 3D navigation system for micro-nano robot based on a Magnetic Particle Imaging system. *International Journal on Magnetic Particle Imaging IJMPI*, 2023, vol. 9, no 1 Suppl 1.
[7] BAO, Rongrong, TAO, Juan, PAN, Caofeng, *et al.* Piezophototronic effect in nanosensors. *Small Science*, 2021, vol. 1, no 6, p. 2000060.
[8] MUBARAK, Mohamed H., SIDEK, Othman, ABDEL-RAHMAN, Mohamed R., *et al.* Nano-antenna coupled infrared detector design. *Sensors*, 2018, vol. 18, no 11, p. 3714.
[9] PUCEL, Robert A. Design considerations for monolithic microwave circuits. *IEEE Transactions on microwave theory and techniques*, 1981, vol. 29, no 6, p. 513-534.
[10] CASPERS, Fritz. RF engineering basic concepts: S-parameters. *arXiv preprint arXiv:1201.2346*, 2012.
[11] VIM, I. S. O. International vocabulary of basic and general terms in metrology (VIM). *International Organization*, 2004, vol. 2004, p. 09-14.
[12] ROMANO, Raffaele, MUBARAK, Faisal, SPIRITO, Marco, *et al.* The HΓ-VNA, an interferometric approach for the accurate measurement of extreme impedances. In : *2019 93rd ARFTG Microwave Measurement Conference (ARFTG)*. IEEE, 2019. p. 1-6.
[13] R. N. Simons, “Coplanar waveguide circuits, components, and systems,” *John Wiley & Sons*, 2004.

Chapter 1: State of the art in on-wafer measurements …………………………………… 8

Introduction

RF and microwave electronic devices have become integral to a wide array of modern technologies, including telecommunications, sensors, and microwave integrated circuits. The proper functioning of these devices, as well as their adherence to industrial and scientific standards, relies heavily on accurate performance measurements. These measurements are crucial for evaluating fundamental circuit parameters such as impedance, power, gain, and losses.

Among the various measurement techniques, S-parameters (Scattering Parameters) are especially important. S-parameters provide a quantitative description of how RF signals are transmitted and reflected within a device or network. Their use is central to the characterization of RF components, enabling engineers to understand and optimize device behavior in high-frequency environments.

Obtaining precise and reliable RF measurements depends significantly on the use of specialized instruments, such as the VNA. The accuracy of the results is also influenced by the calibration components and the techniques employed. Calibration is a critical step that compensates for imperfections in the measurement setup, ensuring that the data collected accurately reflects the true performance of the device under test.

This chapter introduces the key concepts underpinning RF measurement. It emphasizes the physical quantities involved, the characterization parameters used, and the principal measurement methods. Additionally, it underscores the importance of proper calibration and adherence to best experimental practices. The chapter also provides an overview of high-frequency on-wafer measurement techniques, which are essential in evaluating the latest generation of microwave devices.

1. Fundamentals of RF and Microwave measurements

1.1. Transmission Lines

Transmission lines occupy a fundamental position in the design and implementation of electronic components. Their main function is to facilitate the propagation of electrical signals from one location to another within a circuit. The ability of transmission lines to transport signals efficiently is essential for maintaining the integrity and performance of electronic systems.

There are several common configurations for transmission lines, each suited to specific applications and layout requirements. These configurations include coplanar, coaxial, rectangular, and circular forms. Fig. 1.1 provides visual representations of these various transmission line types, highlighting the diversity in their physical structures.

Despite differences in topology, all transmission lines share a basic construction: they are composed of a conductive metal, which carries the electrical signal, and a dielectric material, which insulates and separates the conductors. Both the conductive and dielectric materials play significant roles in determining the propagation characteristics of the signal, such as speed, attenuation, and impedance.

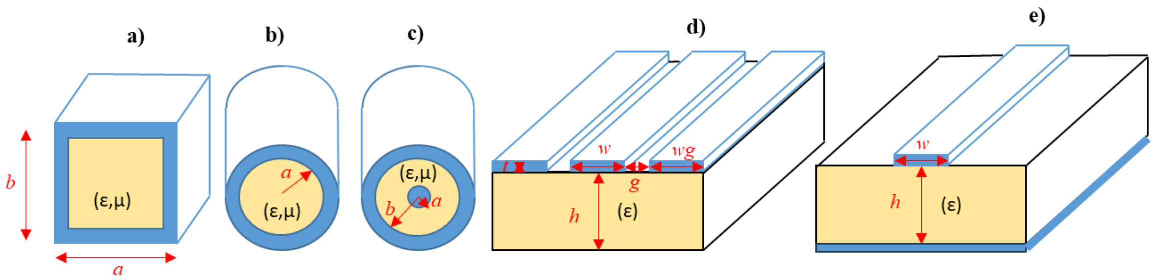

Fig. 1.1: Transmission line topology - a) rectangular, b) circular, c) coaxial, d) and e) coplanar.

In transmission line theory, the relationship between the physical dimensions of the line and the signal wavelength plays a crucial role in determining signal behavior. When the dimensions of the transmission line are much smaller than the signal's wavelength, the concept of "propagation" becomes irrelevant. In this regime, the voltage and current magnitudes do not vary along the length of the line; instead, they remain essentially uniform at every point.

However, as the signal wavelength approaches or becomes smaller than the physical length of the transmission line, the situation changes significantly. In this case, voltage and current magnitudes begin to vary spatially along the line. The term "propagation" gains full importance, as the electromagnetic wave travels and interacts with the distributed properties of the transmission line.

The transmission line can be modeled electrically as a system composed of distributed elements. Specifically, it consists of a linear resistance (*R*), a linear inductance (*L*), a linear capacitance (*C*), and a linear conductance (*G*). These elements are distributed continuously along the length of the line, as depicted in Fig. 1.2.

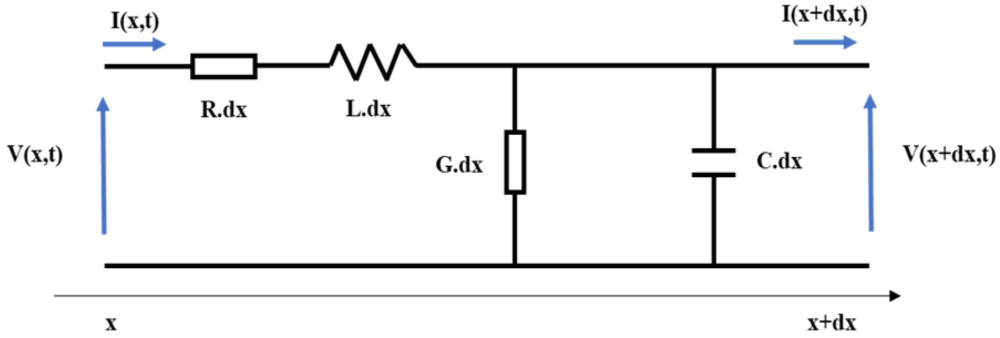

Fig. 1.2: Equivalent electrical circuit model of a transmission line.

Each of these elements plays a distinct role in the performance and characteristics of the transmission line.

The series resistance arises from the finite conductivity of the conductor material. As electrical current flows through the conductor, there is an inherent resistance to the movement of electrons, which leads to energy dissipation in the form of heat.

Inductance is a result of the current passing through the conductor and producing a magnetic field around it. This magnetic field stores energy and affects the way the current changes over time within the transmission line.

Capacitance originates from the separation between the two conductors in the transmission line. The spatial gap allows the conductors to store electrical energy in the electric field formed between them.

Conductance is related to the dielectric losses of the medium that separates the conductors. It represents the ability of the insulating material to allow a small leakage current to pass through, contributing to the total energy loss in the transmission line.

As a result of these distributed elements, the transmission line behaves like an electrical network. By applying Kirchhoff's laws for voltage and current, one can derive the fundamental equations that describe the voltage and current relationships along the transmission line, specifically equations (E.1.1) and (E.1.2).

$$V(x,t) - R.dx.I(x,t) - L.dx.\frac{\partial I(x,t)}{\partial t} - V(x+dx,t) = 0 \qquad \text{(E.1.1)}$$

$$I(x,t) - G.dx.V(x+dx,t) - C.dx.\frac{\partial V(x+dx,t)}{\partial t} - I(x+dx,t) = 0 \qquad \text{(E.1.2)}$$

By dividing these equations by the quantity dx and taking the limit as dx approaches zero, we obtain the following two differential equations. These equations express the incremental changes in voltage and current along the transmission line and are fundamental to understanding the behavior of distributed parameter systems such as transmission lines. The process involves applying Kirchhoff's voltage and current laws to an infinitesimal segment of the line, then normalizing the resulting expressions by dx and considering the behavior as the segment length becomes vanishingly small. This leads to the establishment of partial differential equations that govern the voltage and current as functions of both position and time along the transmission line.

$$\frac{\partial V(x,t)}{\partial x} = -R.I(x,t) - L\frac{\partial I(x,t)}{\partial t} \tag{E.1.3}$$

$$\frac{\partial I(x,t)}{\partial x} = -G.V(x,t) - C\frac{\partial V(x,t)}{\partial t} \tag{E.1.4}$$

When analyzing the behavior of transmission lines, it is common to represent the time-dependent quantities such as voltage and current as sinusoidal functions. By assuming a sinusoidal variation with time, differentiation with respect to time in the telegrapher's equations introduces a multiplicative factor of jω, where ω is the angular frequency of the sinusoidal signal and j is the imaginary unit. This mathematical operation allows for the separation of variables, simplifying the original partial differential equations into forms that depend only on spatial variation.

As a result, equations (E.1.3) and (E.1.4), which describe the incremental changes in voltage and current along the transmission line, are transformed into equations (E.1.5) and (E.1.6). These new equations express the relationships between voltage and current along the line when the time dependence is sinusoidal, making them more suitable for frequency-domain analysis.

$$\frac{dV(x)}{dx} = -(R + j\omega L).I(x) \tag{E.1.5}$$

$$\frac{dI(x)}{dx} = -(G + j\omega C).V(x) \tag{E.1.6}$$

The differential equations derived from applying Kirchhoff's laws to the transmission line, specifically equations (E.1.3) and (E.1.4), serve as the foundation for understanding how voltage and current propagate along the line. These equations relate the incremental changes in voltage and current with respect to position and time, reflecting the distributed nature of the line's electrical properties.

Through the process of assuming sinusoidal time dependence, the partial differential equations can be simplified for frequency-domain analysis. This approach transforms the equations into a form where voltage and current variations along the line are more readily analyzed. The resulting relations explicitly describe how voltage and current behave as they travel through the transmission line, incorporating the effects of line parameters such as resistance, inductance, conductance, and capacitance.

Consequently, these equations provide the means to establish the propagation relations (E.1.7) and (E.1.8) for both voltage and current, forming the basis for further analysis and understanding of transmission line behavior in various electrical engineering applications.

$$\frac{d^2V(x)}{d^2x} - \gamma^2 V(x) = 0 \tag{E.1.7}$$

$$\frac{d^2I(x)}{d^2x} - \gamma^2 I(x) = 0 \tag{E.1.8}$$

The propagation constant of the transmission line, denoted by $\gamma = \alpha + j\beta = \sqrt{(R + j\omega L)(G + j\omega C)}$, plays a fundamental role in understanding how electrical signals travel along the line. This complex parameter combines both the attenuation constant α, which describes the loss of signal strength as it propagates, and the phase constant β, which accounts for the phase shift experienced by the signal.

The general solutions to the governing differential equations for voltage and current along the transmission line are composed of two components: progressive waves, which move forward along the direction of propagation, and regressive waves, which move in the opposite direction. This superposition of forward and backward traveling waves reflects the distributed nature of the line's parameters and is essential for analyzing signal behavior, including phenomena such as reflections and standing waves.

$$V(x) = V_0^+ e^{-\gamma x} + V_0^- e^{+\gamma x} \quad \text{(E.1.9)}$$

$$I(x) = I_0^+ e^{-\gamma x} - I_0^- e^{+\gamma x} \quad \text{(E.1.10)}$$

An important parameter of the line can thus be defined: the characteristic impedance *Zc*. It is a fundamental property of the transmission line that quantifies the relationship between voltage and current for waves propagating along the line. It is determined by the distributed resistance, inductance, conductance, and capacitance per unit length of the transmission line. The value of *Zc* plays a critical role in understanding how signals travel and interact within the transmission line, influencing factors such as signal reflection and power transfer. By establishing *Zc*, one can better predict and control the behavior of electrical signals, ensuring efficient transmission and minimal signal loss. It is given by:

$$Z_c = \frac{R+j\omega L}{\gamma} = \sqrt{\frac{R+j\omega L}{G+j\omega C}} = \frac{V_0^+}{I_0^+} = \frac{V_0^-}{I_0^-} \quad \text{(E.1.11)}$$

In a transmission line, the phase velocity, denoted as V_p, refers to the speed at which a point of constant phase travels along the line. The phase velocity is a fundamental parameter that describes how quickly the phase of a sinusoidal wave moves down the transmission line. It is particularly relevant in the context of wave propagation, as it indicates the rate at which the phase of the voltage or current wavefront advances along the direction of propagation. The phase velocity is given by the expression:

$$V_p = \frac{dx}{dt} = \frac{d(\omega t - constante)}{dt.\beta} = \frac{\omega}{\beta} = \frac{\omega}{\omega\sqrt{\mu\varepsilon}} = \frac{c}{\sqrt{\mu_r \varepsilon_r}} \quad \text{(E.1.12)}$$

Similarly, the distance between two points exhibiting the same pattern at a given time is called the wavelength. This physical quantity, commonly denoted by the symbol λ, represents the spatial period of the wave, the length over which the wave's shape repeats. In other words, the wavelength is the distance between consecutive points, such as crests or troughs, that are in phase with each other at a specific moment in time. Understanding the concept of wavelength is essential for analyzing wave propagation along transmission lines, as it directly relates to the phase constant and frequency of the signal.

$$\lambda = \frac{2\pi}{\beta} = \frac{2\pi c}{\omega\sqrt{\mu_r \varepsilon_r}} \quad \text{(E.1.13)}$$

In the case of an ideal lossless transmission line, the resistance (R) and conductance (G) are both zero. This simplification means that there are no energy losses due to resistive heating or dielectric leakage along the line. As a result, the propagation constant γ and the characteristic impedance Zc are determined solely by the distributed inductance (L) and capacitance (C) per unit length of the transmission line.

Under these ideal conditions, the behavior of signals on the transmission line is governed entirely by the energy stored in the magnetic and electric fields, as characterized by L and C. This leads to undistorted signal propagation with no attenuation, making the analysis of the line more straightforward and allowing for clearer predictions of voltage and current behavior along the length of the line.

1.1.1. Rectangular waveguide

The development of radio frequency (RF) and microwave technologies has been significantly influenced by the introduction of rectangular waveguides. These waveguides are renowned for their ability to transmit signals with high quality and minimal loss, making them a preferred choice in many applications where signal integrity is paramount.

Despite their advantages in signal transmission, rectangular waveguides exhibit a fundamental limitation: they do not support broadband frequency transmission. This restriction arises from the presence of a cutoff frequency, below which electromagnetic waves cannot propagate through the waveguide. As illustrated in Fig. 1.3, the cutoff frequency is a defining characteristic that determines the operational bandwidth of the waveguide, and only frequencies above this threshold are efficiently transmitted.

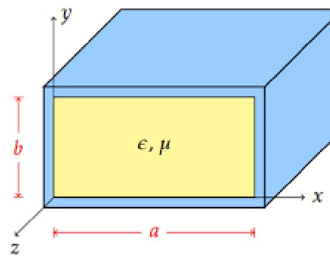

Fig. 1.3: Cross-section of rectangular waveguide.

Only Transverse Electric (TE) and Transverse Magnetic (TM) modes can propagate within rectangular or hollow circular waveguides. These modes, which are denoted as $TE_{n,m}$ and $TM_{n,m}$, are defined by two integers, n and m. These integers represent the number of standing wave maxima that appear in the electromagnetic field patterns along the transverse dimensions of the waveguide.

Each specific mode is associated with a unique cutoff frequency, denoted as $f_{n,m}$. This cutoff frequency establishes a lower limit: electromagnetic waves with frequencies below this threshold will not propagate through the waveguide in that mode, while those with frequencies above the cutoff are supported and can travel along the guide. The value of the cutoff frequency is determined by the physical dimensions of the waveguide's cross-section, specifically the parameters *a* and *b*.

In this manuscript, we present two examples of transverse TE and TM modes for a rectangular waveguide. However, a more detailed discussion of these modes and their properties is not included here.

- Transverse Electric (TE) modes, also known as H-waves, are a fundamental class of electromagnetic wave propagation in rectangular waveguides. In these modes, the electric field component in the direction of propagation, denoted as Ez, is zero. This means that the electric field E is entirely transverse to the direction in which the wave travels inside the waveguide.
  The magnetic field H, on the other hand, does have a component along the direction of propagation. Its distribution within the waveguide is governed by the wave equation, which describes how the magnetic field varies spatially and temporally as it propagates. This unique configuration, where the electric field is purely transverse while the magnetic field propagates according to the wave equation, defines the TE modes and distinguishes them from other propagation modes in waveguides.

  $$\nabla^2 H_z + k^2 H_z = 0$$

  $$\frac{\partial^2}{\partial x^2}.H_z + \frac{\partial^2}{\partial y^2}.H_z + k_c H_z = 0 \qquad \text{(E.1.14)}$$

  Where ∇^2 is the Laplacian operator and *k* is the wave number.
  The previous equation can be solved straightforwardly by decomposing the field *Hz* into two functions, *f(x)* and *g(y)* like *Hz = f(x).g(y)*. The general solutions for *f* and *g* are given by:

  $$f(x) = A.\cos\left(\frac{n\pi}{a}.x\right) + B.\sin\left(\frac{n\pi}{a}.x\right) \qquad .$$

$$g(y) = C.cos\left(\frac{m\pi}{b}.y\right) + D.sin\,(\frac{m\pi}{b}.y) \qquad \text{(E.1.15)}$$

The constants A, B, C, and D, as well as the integers n and m that define the mode indices, are determined by analyzing the boundary conditions imposed on the magnetic field component Hz. In the case of a perfect conducting waveguide, the normal component of Hz must vanish at the boundaries of the waveguide. This requirement ensures that the magnetic field behaves appropriately at the surface of the conductor.

Mathematically, this condition is equivalent to stating that the divergence of the magnetic field Hz is zero at the boundaries. To satisfy this, the following equations must be considered, which describe how Hz must behave at the edges of the waveguide. By applying these boundary conditions to the general solutions for the functions f(x) and g(y), the appropriate values for the constants and the mode indices can be found, ensuring the physical validity of the electromagnetic fields within the waveguide.

$$\frac{\partial H_z}{\partial x} = 0\,;\text{à}\; x = 0\; et\; x = a$$

$$\frac{\partial H_z}{\partial y} = 0\,;\text{à}\; y = 0\; et\; y = b \qquad \text{(E.1.16)}$$

By applying these boundary conditions to both variables *x* and *y*, the constants can be identified as follows:

$$B = 0\,;\; D = 0\,;\; A\,.\,C = A_{n,m} \qquad \text{(E.1.17)}$$

The resulting magnetic field *Hz* is thus given by:

$$H_z = A_{nm}.\,cos\left(\frac{n\pi}{a}.x\right).\,cos\,(\frac{m\pi}{b}.y) \qquad \text{(E.1.18)}$$

The cutoff frequency $f_{c\,n,m}$ can thus be defined by the following expression:

$$f_{c\,n,m} = \frac{c}{2\pi}\left[\left(\frac{n^2\pi^2}{a^2}\right) + \left(\frac{m^2\pi^2}{b^2}\right)\right]^{1/2} \qquad \text{(E.1.19)}$$

Similarly, the cutoff wavenumber $k_{c\,n,m}$ and the cutoff wavelength $\lambda_{c\,n,m}$ can be expressed respectively as:

$$k_{c\,n,m} = \left[\left(\frac{n^2\pi^2}{a^2}\right) + \left(\frac{m^2\pi^2}{b^2}\right)\right]^{1/2},\, \lambda_{c\,n,m} = 2.\left[\left(\frac{n^2}{a^2}\right) + \left(\frac{m^2}{b^2}\right)\right]^{-1/2} \qquad \text{(E.1.20)}$$

- Unlike the previous scenario, TM modes (also known as E-waves) are characterized by the presence of the electric field component Ez along the direction of propagation. In these modes, the magnetic field is strictly perpendicular to the direction of propagation and does not have any component along this axis. Therefore, we have Hz = 0.

  To describe the behavior of TM modes within a waveguide, the Helmholtz propagation equation is employed. This equation provides a mathematical framework for analyzing the distribution and dynamics of the electric field Ez in the system.

$$\nabla^2 E_z + k^2 E_z = 0 \qquad \text{(E.1.21)}$$

Thus, a similar situation arises for the TM modes, which requires the use of boundary conditions, with the electric field *Ez* vanishing at the walls of the waveguide. By applying these conditions, the general solution can be written in the following form:

$$E_z = B_{nm}.\,sin\left(\frac{n\pi}{a}.x\right).\,sin\,(\frac{m\pi}{b}.y) \qquad \text{(E.1.22)}$$

Cutoff parameters such as frequency, wavelength and wavenumber are simply retrieved in the same way as previously.

Fig. 1.4 shows an example of rectangular waveguide.

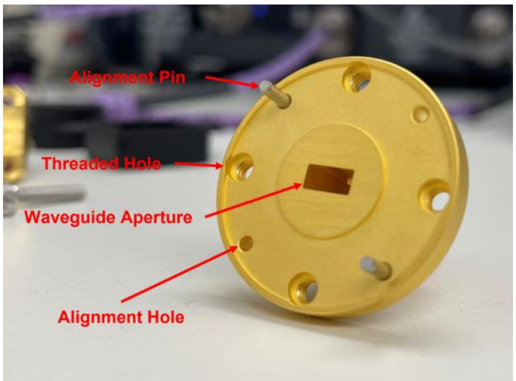

Fig. 1.4: Rectangular waveguide [51].

1.1.2. Coaxial Line

A coaxial transmission line is a type of cylindrical waveguide characterized by the presence of a central conductor that is precisely aligned along the axis of symmetry. This structure is mainly composed of two conductors: a central conductor and an outer conductor that forms the periphery. These conductors are separated by a dielectric material, as illustrated in Fig. 1.5.

One of the main advantages of a coaxial waveguide is its capability to provide a significantly wider frequency bandwidth compared to a rectangular waveguide. This attribute allows it to support the propagation of a dominant mode without the existence of a cutoff frequency. Furthermore, the coaxial design supports the pure Transverse Electromagnetic (TEM) mode.

Despite these benefits, there are some considerations to keep in mind. The fabrication process for coaxial waveguides can be costly due to their precise construction requirements. Additionally, integrating coaxial lines with other components in a system may present certain complexities.

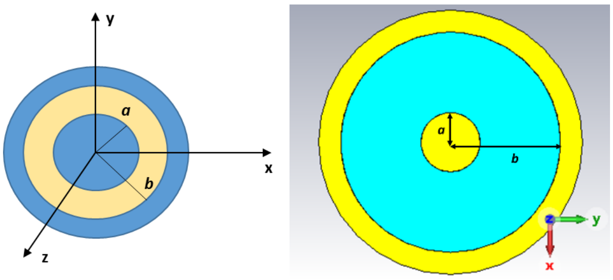

Fig. 1.5: Cross-section of coaxial line.

An important advantage of the coaxial line is its suitability for miniaturization, especially when compared to rectangular waveguides. This attribute has enabled the development of coaxial lines with various diameters tailored for specific applications, making them highly versatile in modern RF and microwave systems.

The electrical properties of coaxial lines, such as characteristic impedance (Zc) and propagation velocity (v), are determined by both the physical geometry of the guide and the properties of the dielectric material separating the conductors. Adjusting these parameters allows engineers to optimize coaxial lines for a wide range of frequencies and system requirements.

$$Z_c = \sqrt{\frac{L}{C}} \; ; \; v = \frac{1}{\sqrt{LC}} \tag{E.1.23}$$

$$C = \frac{2\pi\varepsilon}{ln\,(b/a)} \; ; L = \frac{\mu.ln\,(b/a)}{2\pi} \tag{E.1.24}$$

The parameters *L* and *C* in coaxial lines denote the linear inductance (measured in Henrys per meter, H/m) and the linear capacitance (measured in Farads per meter, F/m), respectively. These values are critical in determining the electrical behavior of the transmission line.

The constant ε0, which equals 8.85×10^{-12} F/m, represents the free-space permittivity, while μ_0, equal to $4\pi \times 10^{-7}$ H/m, is the free-space permeability. These universal constants are fundamental in the calculation of electromagnetic wave propagation and the properties of coaxial cables.

The characteristic impedance (Zc) of a coaxial transmission line expresses the ratio of voltage to current at any point along the line. This parameter is one of the most essential quantities in measurement setups, as it ensures proper signal transmission and system compatibility.

In practice, a common system reference impedance is 50 Ω. This standard value emerges from theoretical considerations: the impedance that gives minimum attenuation is 77.5 Ω, while the impedance for maximum power transfer is 30 Ω, as shown in Fig. 1.6. By averaging these two theoretical values, one obtains 53.75 Ω, which has been rounded and standardized to 50 Ω for simplicity and widespread adoption in RF and microwave engineering.

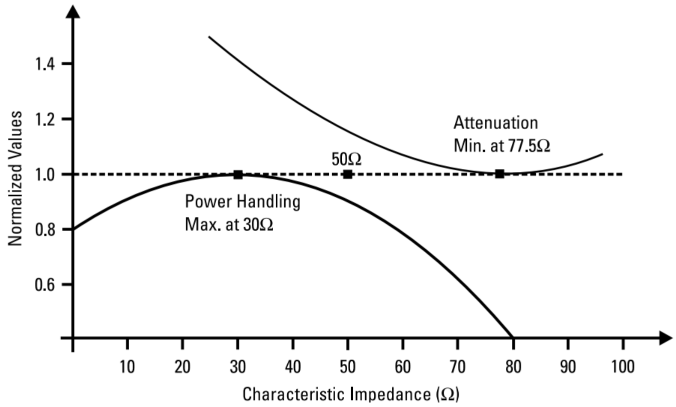

Fig. 1.6: Attenuation and power handling trade-off [24].

The coaxial cable configuration inherently supports the Transverse Electromagnetic (TEM) mode at all frequencies. This mode is essential for reliable signal transmission in RF and microwave applications. However, when the operating frequency surpasses a specific threshold, known as the cutoff frequency (fc), the TE_{11} mode can also begin to propagate within the coaxial line.

The emergence of the TE_{11} mode is undesirable, as it interferes with the intended TEM mode. This interference disrupts the voltage standing wave ratio (VSWR), leading to increased signal losses and compromised system performance. The exact value of the cutoff frequency at which the TE_{11} mode can propagate is determined by the geometric and material properties of the coaxial cable. By carefully selecting these parameters, engineers can ensure that the TE_{11} mode remains suppressed within the operating frequency range, thereby maintaining signal integrity and minimizing losses.

$$f_c = \frac{2c}{\pi(a+b)\sqrt{\mu_r \varepsilon_r}} \tag{E.1.25}$$

They are widely utilized in RF and microwave instruments, serving as both channels and connectors. Their primary function is to interconnect various components within these systems, ensuring that impedance matching is achieved for optimal signal transmission. By maintaining proper impedance, these structures help minimize signal loss and maintain system performance. Coaxial connectors are available in male and female types, which are distinguished by their physical size and the maximum frequency they can support. The selection of connector type depends on the specific requirements of the application, including frequency range and mechanical compatibility. Fig. 1.7 illustrates the different types of RF connectors commonly used in these systems.

Connector Size (mm)	Maximum Frequency (GHz)
7	18
3.5	30
2.92	40
2.4	50
1.85	67
1	110

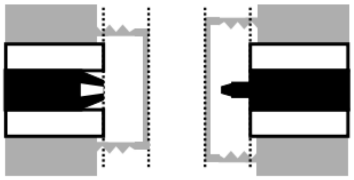

Fig. 1.7: RF Connector Types [24].

Female and male connectors are essential components that enable the connection and disconnection of various coaxial cables and system elements. These connectors are designed to interface with instrumentation ports, providing a reliable mechanical connection by securely tightening one connector to the other.

Achieving an optimal connection between the two connectors requires that there is no air gap present at the interface. Additionally, the electrical reference planes of both connectors must be precisely aligned. When these conditions are met, the connection is considered perfect, ensuring minimal signal loss and maximum system performance [24].

1.1.3. Microstrip line

The microstrip line is one of the most widely used types of planar transmission lines in RF and microwave engineering. Its popularity stems from its versatility and ease of integration into printed circuit boards and other planar structures.

Microstrip lines are characterized by several key electrical properties, including impedance, attenuation, wavelength, and propagation constant. These properties are not fixed but instead depend on a variety of dimensional and material parameters [47]. Specifically, the choice of conductor and dielectric materials plays a significant role in determining the performance of the microstrip line. In addition to material selection, the geometric dimensions of the line such as the trace width (W), conductor thickness (t), and substrate height (h) are also crucial factors. The combination of these parameters influences how signals propagate along the microstrip line and determines the overall effectiveness of the transmission path.

Fig. 1.8 provides a visual representation of the microstrip line, highlighting the key dimensions and structural components that affect its electrical behavior.

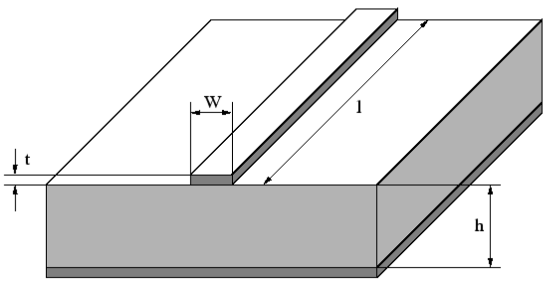

Fig. 1.8: Microstrip line.

The microstrip line exhibits an inhomogeneous structure because its insulating region consists of both air and dielectric material. As a result, not all electric and magnetic field lines are confined strictly between the metal conductor and the substrate. This unique arrangement causes the fields to spread partially into the air above the substrate and partially within the dielectric material below the conductor.

Due to this field distribution, the signal propagation mode in a microstrip line is known as quasi-TEM (Transverse Electromagnetic). Although it closely resembles the ideal TEM mode, the presence of different insulating materials (air and dielectric) means that the fields are not completely transverse nor uniformly distributed across the cross-section. Fig. 1.9 illustrates the typical configuration of the electric and magnetic fields in a microstrip line, highlighting the partial confinement and the resulting quasi-TEM propagation mode.

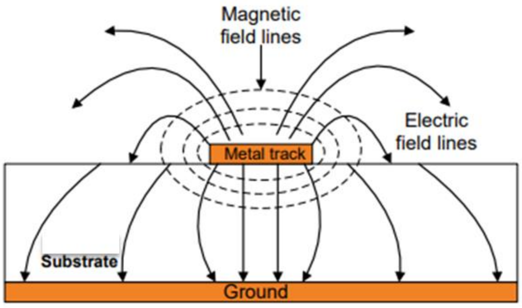

Fig. 1.9: Electrical and magnetic fields of microstrip line.

The effective permittivity, denoted as ε_{reff}, is a critical parameter in the analysis and design of microstrip line structures. This parameter represents the resultant permittivity experienced by electromagnetic waves as they propagate along the microstrip line, considering the combined effects of the dielectric substrate and the surrounding air.

An approximate function for calculating the effective permittivity of a microstrip line has been formulated by M.V. Schneider. This formula provides reliable accuracy, with a margin of error of ± 2% for ε_{reff} and ±1% for $\sqrt{\varepsilon_{reff}}$ itself. Such precision makes it a valuable tool for engineers and designers working with planar transmission lines, allowing for accurate prediction of electrical characteristics and performance in practical applications [48].

$$\varepsilon_{reff} = \frac{\varepsilon_r+1}{2} + \frac{\varepsilon_r-1}{2}.\frac{1}{\sqrt{1+10.\frac{h}{W}}} \quad \text{(E.1.26)}$$

The quasi-static characteristic impedance, Zc, of a microstrip line is determined by three main parameters: the trace width (W), the substrate height (h), and the relative permittivity (εr). Various approximations are used to calculate Zc based on the aspect ratio (W/h) of the structure.

One notable approach was introduced by Harold A. Wheeler [49], who proposed analyzing two distinct cases depending on the value of the aspect ratio (W/h). These cases allow for more accurate estimations of the characteristic impedance across a range of microstrip geometries. The use of such approximations enables designers to efficiently compute Zc for different microstrip configurations without resorting to complex numerical methods.

- Wide strip (W/h > 3.3)

$$Z_c = \frac{Z_{FO}}{2\sqrt{\varepsilon_r}}.\frac{1}{\frac{W}{2h}+\frac{1}{\pi}.ln(4)+\frac{\varepsilon_r+1}{2\pi\varepsilon_r}.ln\left(\frac{\pi e}{2}.\left(\frac{W}{2h}+0.94\right)\right)+\frac{\varepsilon_r-1}{2\pi{\varepsilon_r}^2}.ln\left(\frac{e\pi^2}{16}\right)} \quad \text{(E.1.27)}$$

- Narrow strip (W/h < 3.3)

$$Z_c = \frac{Z_{FO}}{2\sqrt{2(\varepsilon_r+1)}}.\left(\ln\left(\frac{4h}{W}+\sqrt{\frac{16h^2}{W^2}+2}\right)-\frac{1}{2}.\frac{\varepsilon_r-1}{\varepsilon_r+1}.\left(\ln\left(\frac{\pi}{2}\right)+\frac{1}{\varepsilon_r}ln\left(\frac{4}{\pi}\right)\right)\right) \quad \text{(E.1.28)}$$

Schneider thought about the range of importance for most engineering applications and found the following approximation of Zc:

$$Z_c = \frac{Z_{FO}}{2\sqrt{\varepsilon_{reff}}} \cdot \begin{cases} \frac{1}{2\pi} \ln \left(\frac{8.h}{W} + \frac{W}{4h}\right), & \frac{W}{h} \leq 1 \\ \frac{1}{\frac{W}{h} + 2.44 - 0.44\frac{h}{W} + (1+\frac{h}{W})^6}, & \frac{W}{h} > 1 \end{cases} \qquad \text{(E.1.29)}$$

Hammerstad and Ø. Jensen contributed their part in the same logic of approximation by incorporating some additional function [50].

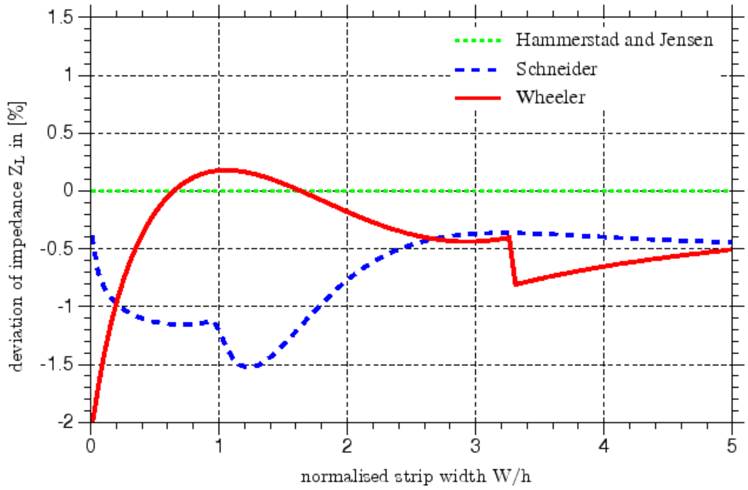

Fig. 1.10: Characteristic impedance in comparison for ε_r=9.8 [47].

Fig. 1.10 presents a comparison of the quasi-static characteristic impedance, as calculated using the closed-form expressions provided by various authors. This comparison highlights the effectiveness of these closed-form formulas, which facilitate quick and reliable estimation of the characteristic impedance for microstrip lines across different geometries.

An important observation from the comparison is the behavior of Wheeler's formula at the aspect ratio (W/h = 3.3). At this specific ratio, there is a noticeable impedance step of approximately 0.1 Ω, as reported in the literature [47]. This step illustrates the transition between the different cases considered in Wheeler's approach and underlines the practical utility of selecting the appropriate expression based on the aspect ratio.

1.1.4. Coplanar Line

Coplanar lines are waveguides used to propagate electromagnetic signals. Introduced in 1969 by C.P. Wen [1], they consist of three metal strips: a central strip carrying the signal and two lateral strips serving as ground planes. These metal strips are deposited on a dielectric substrate.

The properties of a transmission line, such as its characteristic impedance and phase constant, depend on the materials from which it is made, the frequency, and the dimensions of its cross-sectional area. Among these dimensions, there are the width of the central strip *W*, the spacing between the ground planes and the central strip (gap) *G*, the thickness of the strips *t*, the height of the substrate *h*, the width of the ground planes *WG*, the inter-ground distance *d*, the length of the line *L*, and the permittivity of the substrate ε_r (Fig. 1.11).

Coplanar lines offer several advantages, including ease of integration with a surface ground plane, low manufacturing cost, reduced dispersive effects at small geometric scales, limited radiative losses, easily accessible electrical characteristics, and the ability to design directional couplers. Furthermore, they enable a simplified photolithography process for structures that are minimally dependent on the substrate thickness.

Coplanar lines are a type of waveguide designed for the propagation of electromagnetic signals. First introduced in 1969 by C.P. Wen [1], a coplanar line is constructed using three metal strips deposited on a dielectric substrate. The central metal strip is responsible for carrying the signal, while the two lateral strips function as ground planes, providing a reference potential for signal transmission.

The electrical properties of a coplanar transmission line, including its characteristic impedance and phase constant, are determined by several factors. These factors encompass the materials used in fabrication, the operational frequency, and the specific dimensions of the line's cross-sectional area. Important geometric parameters include:

- Width of the central strip (W): Defines the signal-carrying region.
- Gap (G): The spacing between the central strip and each ground plane.
- Thickness of the strips (t): Influences the properties of conductor.
- Substrate height (h): Determines the separation between the strips and the underlying material.
- Width of the ground planes (WG): Affects the grounding characteristics.
- Inter-ground distance (d): The separation between the two ground planes.
- Length of the line (L): Specifies the total transmission path.
- Permittivity of the substrate (εr): Governs the dielectric response.

These parameters are illustrated in Fig. 1.11.

Coplanar lines offer several notable benefits in electronic design and fabrication:

- Ease of integration with a surface ground plane simplifies circuit layout and assembly.
- Low manufacturing cost, making them suitable for mass production.
- Reduced dispersive effects at small geometric scales, which enhances signal integrity.
- Limited radiative losses, minimizing unwanted energy emission.
- Easily accessible electrical characteristics facilitate straightforward measurement and adjustment.
- Support for directional coupler design, enabling advanced signal routing and processing.
- Simplified photolithography process, particularly for structures that are minimally affected by substrate thickness.

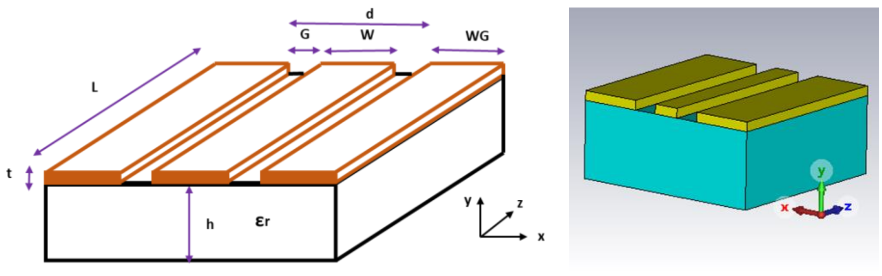

Fig. 1.11: Coplanar line.

Unlike waveguides that utilize uniform substrates such as coaxial lines, which support the Transverse Electromagnetic (TEM) mode, or rectangular waveguides, which support Transverse Electric (TE) and Transverse Magnetic (TM) modes coplanar lines exhibit different propagation characteristics. This distinction arises from their inhomogeneous dielectric medium, which consists of both air and substrate materials. As a result, coplanar lines can support two distinct modes:

- **Coplanar mode (odd mode):** In the coplanar mode, also known as the odd mode, both ground planes maintain the same electrical potential. The electric field generated in this configuration is primarily confined within the slots located between the ground planes and the central conductor. As depicted in Fig. 1.12, this coplanar mode exhibits transverse electric characteristics, meaning the electric field is oriented perpendicular to the direction of propagation and predominantly remains within the slot regions.

- **Even mode (slot mode):** The even mode, also referred to as the slot mode, is a propagation mode that is characterized by a transverse magnetic field orientation. In this configuration, the longitudinal components of the electromagnetic field are considered with respect to the y-axis, enabling a clear definition of parity within the system.

  Specifically, the nature of the field distribution allows for a distinction between even and odd modes. The even mode exhibits symmetry in its field components relative to the y-axis, differentiating it from the odd (coplanar) mode, which displays an anti-symmetric field profile. As a result, the classification of even and odd modes is based on this parity in the longitudinal electromagnetic field components.

$$E_z(-x,y) = E_z(-x,y) \tag{E.1.30}$$

$$E_z(-x,y) = -E_z(x,y) \tag{E.1.31}$$

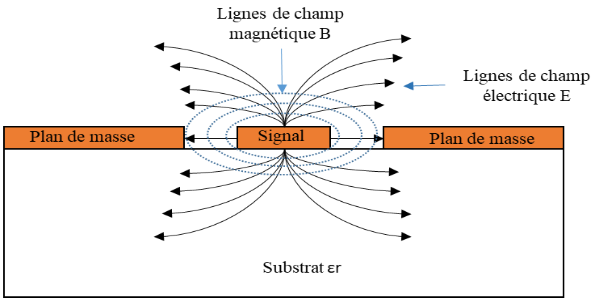

Fig. 1.12: Propagation modes of a coplanar line.

The odd mode, also known as the coplanar mode, is defined by the propagation of radio frequency (RF) or microwave signals along the central conductor strip of the transmission line. In this mode, both ground planes are maintained at the same electrical potential, which helps establish the characteristic electric field distribution within the structure.

Despite the intended symmetry, a potential imbalance may arise between the ground planes. This imbalance is particularly evident when there are discontinuities, such as junctions or defects in the geometry of the coplanar line. In such cases, the central conductor remains at zero potential, while the ground planes may experience slight differences in potential due to these imperfections. These effects can influence the overall performance of the transmission line by altering the intended field distribution and possibly introducing unwanted modes or losses.

Coplanar transmission lines can be modeled in different configurations depending on the dimensions of the ground planes, the substrate height, and the materials used. The two main theoretical considerations are:

- **Ideal case (infinite ground planes and substrate height):** This theoretical model assumes that the substrate is sufficiently large and the ground planes are infinite, simplifying the calculations of propagation modes. It primarily focuses on the effects of the line's dimensions and materials without considering edge effects or discontinuities.

- **Realistic case (finite dimensions):** In practice, dimensions are always limited, leading to edge effects that influence the propagation mode, field distribution, and characteristic impedance. The finite ground planes can also affect transmission quality, especially at higher frequencies.

The propagation modes in coplanar lines are influenced by several parameters [4]:

- **Dimensions:** The width of the central conductor (*W*), the spacing between the central conductor and the ground planes (*G*), the substrate height (*h*), and the width of the ground planes (*WG*).
- **Materials:** The relative permittivity of the substrate (ε_r) plays a crucial role in determining the characteristic impedance and the signal propagation speed.
- **Configuration:** Depending on whether the line has a ground plane beneath the substrate or not, the electromagnetic field distribution changes, affecting the line's performance (impedance, losses, etc.).

The Table 1.1 illustrates the different propagation modes and their characteristics based on various configurations of the coplanar transmission line:

Table 1.1: Different Modes of a Coplanar Line [2].

Structure type	Semi-Infinite Ground Planes		Finite Ground Planes	
	Without Backside Metallization	With Backside Metallization	Without Backside Metallization	With Backside Metallization
	Case (a)	Case (b)	Case (c)	Case (d)
Propagated Modes	Surface waves (TE and TM modes)	Parallel plate guided modes (TEM, TE, TM)	Higher-order coplanar modes without cut-off frequency TE_0 and TM_0	- Slot mode - Microstrip mode - Coplanar mode
Propagation conditions	TM_0: $h > 0.15\ \lambda$ TE_0: $h > 0.125\ \lambda$	TE_1: $h > 0.125\ \lambda$ TM_1: $h > 0.125\ \lambda$	- Inevitable propagation of these modes -Strong interaction for: $h < 0.1\ \lambda$	
Minimization Criteria	$h < 0.12\ \lambda$	$h < 0.12\ \lambda$	$h > 0.1\ \lambda$	$h \gg W + 2 * G$ $W_g \gg W + 2 * G$

In this table, we note that the propagation of volume waves can be limited by applying a condition between the substrate height *h* and the wavelength of the guide λ/2 [2]:

$$h < 0.12 * \lambda \tag{E.1.32}$$

In the same logic, it is possible to adjust the gap *G* and the width of the central strip *W* relative to the wavelength λ, to achieve:

$$W + 2 * G \leq \frac{\lambda}{10} \tag{E.1.33}$$

The propagation of the wave along the line is sensitive to the inter-mass distance, defined by *d=W+2G*. Its optimal choice depends on both the substrate and the frequency. For example, as shown in (Fig. 1.13), the attenuation decreases with this distance *d*.

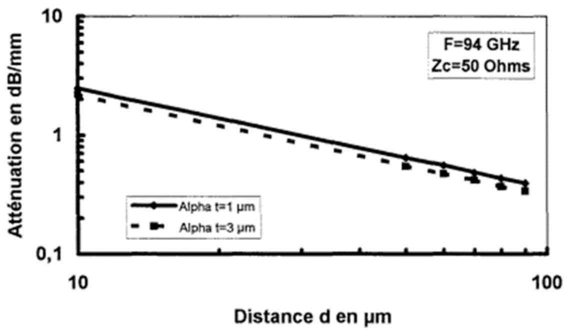

Fig. 1.13: Influence of distance d on the propagation [2].

A much stricter restriction on *d* such that $d \leq \frac{\lambda}{20}$ helps reduce radiation. The term quasi-TEM mode for a coplanar line arises from the fact that there can be a combination of TEM and non-TEM modes, although the latter are sometimes neglected. Two additional conditions can be met to limit these non-TEM modes [2]:

$$h \gg W + 2 * G \quad ; \quad W_g \gg W + 2 * G \qquad \text{(E.1.32)}$$

1.2. S-parameters Concept

High-frequency systems engineering has experienced considerable advancement, driven largely by the evolution of modern device technologies and the increasing requirements of telecommunications services. Additional factors contributing to this growth include the development of new materials and advances in electronics. These collective innovations have significantly shaped the field, enabling more sophisticated and reliable high-frequency systems.

The electromagnetic spectrum relevant to high-frequency systems can be categorized into several distinct bands. The primary divisions are as follows:

- Audio Frequencies: Spanning from 30 Hz to 300 kHz, this range covers the frequencies typically associated with audible sound.
- Radio Frequency (RF) Range: Extends from 300 kHz to 1 GHz. This segment encompasses medium frequency (MF), high frequency (HF), and very high frequency (VHF) bands, all of which are essential for various wireless communication applications.
- Microwave Range: Covers frequencies from 1 GHz to 300 GHz. The microwave region begins at the upper edge of the VHF band and continues up to just below the terahertz (THz) range and optical frequencies.
- THz and Optical Frequencies: The THz range and optical frequencies include those found in the far-infrared region, starting around 0.3 THz and extending beyond. These frequencies are particularly relevant for advanced communication systems and specialized applications.

As illustrated in Fig. 1.14, these frequency bands form the foundation for understanding the propagation characteristics and application domains of high-frequency systems.

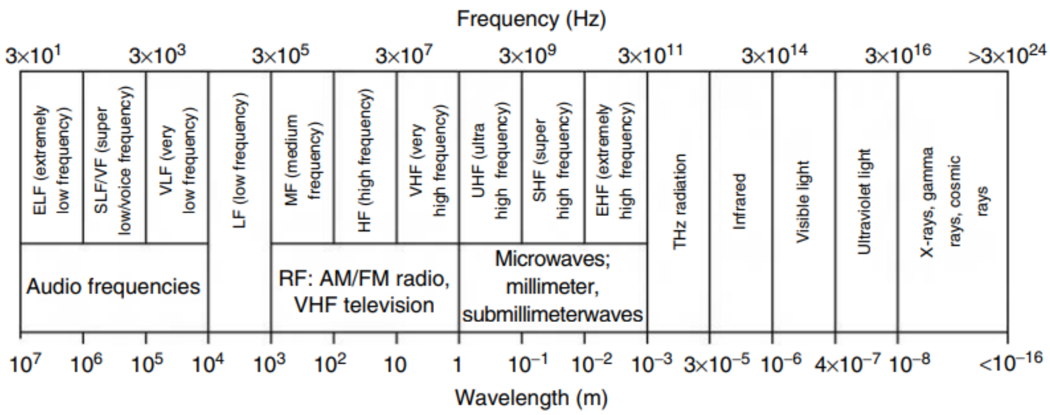

Fig. 1.14: Frequency spectrum and associated wavelengths.

In the radio frequency (RF) and microwave domain, vector network analyzers play a critical role in characterizing the performance of electronic components and systems. VNAs are widely utilized to conduct both linear and non-linear measurements on passive and active devices, providing valuable insights into their behavior at high frequencies.

The primary quantities measured by VNAs are the scattering parameters, commonly referred to as S-parameters. These are dimensionless, complex numbers that describe how RF signals behave as they encounter a network with one or more ports. Specifically, S-parameters represent the reflection and transmission characteristics of the network in terms of power waves.

S-parameters are defined as ratios of power waves: they relate the magnitude and phase of the incident wave to those of the reflected or transmitted wave at each port of the network. This approach allows engineers to systematically evaluate how much of the signal is reflected toward the source and how much is transmitted through the device under test, making S-parameters essential for the analysis and design of high-frequency circuits.

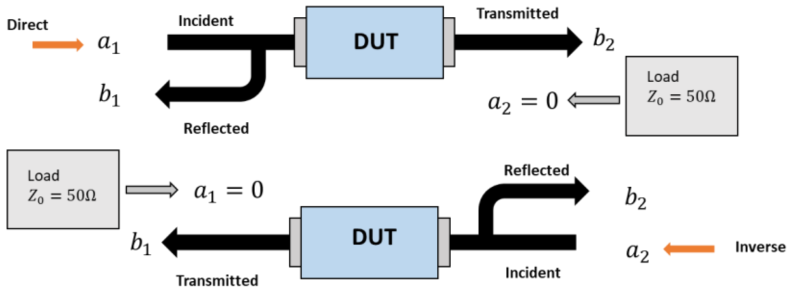

Fig. 1.15: Concept on S-parameters.

The elements of the S-matrix of a two-port network are literally given by the following expressions:

$$S_{11} = \frac{b_1}{a_1} \quad ; \quad S_{21} = \frac{b_2}{a_1} \qquad \text{(E.1.35)}$$

$$S_{22} = \frac{b_2}{a_2} \quad ; \quad S_{12} = \frac{b_1}{a_2} \qquad \text{(E.1.36)}$$

$$[\mathrm{b}] = [\mathbf{S}].[a] \quad \leftrightarrow \quad \begin{bmatrix} b_1 \\ b_2 \end{bmatrix} = \begin{bmatrix} S_{11} & S_{12} \\ S_{21} & S_{22} \end{bmatrix} . \begin{bmatrix} a_1 \\ a_2 \end{bmatrix} \qquad \text{(E.1.37)}$$

Where $a_i = \frac{V_i + Z*I_i}{2\sqrt{\mathrm{Re(Z)}}}$ and $b_i = \frac{V_i - Z*I_i}{2\sqrt{\mathrm{Re(Z)}}}$ represent incident and transmitted power waves.

For a two-port component, the reflection coefficient S_{11} and transmission coefficient S_{21}, in the forward direction, are evaluated by matching the output (second port of the VNA) to Z_0=50Ω, so that a_2 is null (*Fig. 1.15*).

In RF circuit analysis, scattering transfer parameters or the T-matrix are widely used because they allow cascading circuits similarly to the ABCD chain matrix. The *T* transfer matrix is derived from the relationships between power waves, just like the S-parameters.

The advantage of the T-matrix over the ABCD matrix is that it does not require knowledge of the input impedance circuit. This makes it particularly useful for analyzing multi-stage RF networks.

1.3. RF and Microwave measurements system

A Vector Network Analyzer is a sophisticated measurement instrument designed to evaluate the scattering parameters, commonly referred to as S-parameters, of electronic components. These S-parameters encompass both the amplitude and phase characteristics, providing a comprehensive analysis of how signals behave in an RF or microwave network.

VNAs can conduct measurements on either single-port or multi-port devices, depending on the requirements of the test setup. The measurement process typically involves sweeping across a range of frequencies or power levels to assess the device's performance under various operating conditions.

There are several types of VNAs, and they can be categorized based on their receiver configuration, internal structure, and overall performance characteristics. This variety allows users to select a VNA that best suits their specific measurement needs, whether for basic component testing or advanced network analysis.

1.3.1. Structure of VNA

The fundamental operation of a Vector Network Analyzer involves sending radio frequency (RF) signals from its internal signal source to a Device Under Test (DUT). Upon reaching the DUT, a portion of the incident RF signal is reflected at the input port of the DUT. The remaining portion of the signal passes through the device and arrives at the output port, provided that the DUT acts as a transmission component. This process is illustrated in Fig. 1.16.

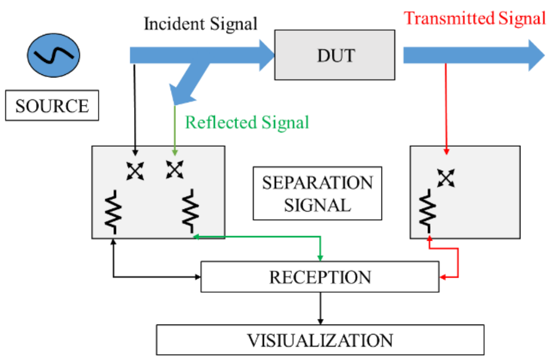

Fig. 1.16: Schematic diagram of VNA operating principle.

The VNA can be divided into three main blocks:

1.3.1.1. Signal generation module

The Vector Network Analyzer generates microwave signals essential for testing and characterizing devices in RF and microwave networks. The performance of a VNA is defined by its bandwidth, which specifies the frequency range over which it can operate, and by its output power, determining the strength of the transmitted signal.

The signals emitted by a VNA can take several distinct forms, each suited to specific measurement and application needs. These include:

- Sinusoidal signals (Continuous Wave): These provide precise frequency-domain analysis and are commonly used when detailed examination of amplitude and phase response is required.
- Pulsed signals: Used for time-domain measurements and radar applications, these signals allow the study of transient responses and the behavior of systems under pulsed excitation.
- Square wave signals: Useful for the characterization of digital circuits, square waves enable the analysis of switching behavior and the performance of logic-based components.
- Modulated signals: Including amplitude modulation (AM), frequency modulation (FM), and phase modulation, these signals are employed for testing communication systems and evaluating the response of devices to real-world modulation formats.

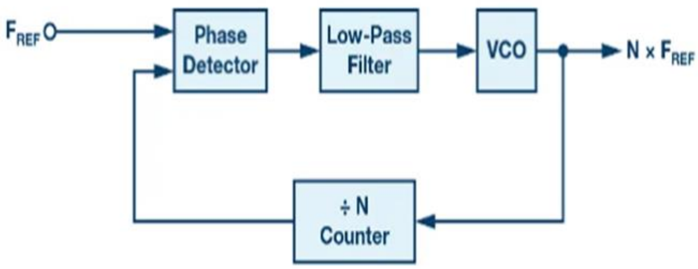

Fig. 1.17: Signal generation module.

Within the signal generation module, a voltage-controlled oscillator (VCO) works in conjunction with a phase-locked loop (PLL) to produce signals across the specified frequency range, as illustrated in Fig. 1.17. This arrangement ensures that the generated signal remains stable and accurately tuned to the desired frequency. In addition, the module is equipped with an automatic control loop, which continually monitors and adjusts the output power to maintain it at the required level for precise measurements and device characterization.

1.3.1.2. Signal separation module

This is a hardware module, which can be either separate or integrated into the VNA, performing two main functions:

- Reference Signal Measurement

A portion of the incident signal is measured to provide a reference for subsequent calculations and analysis. This measurement is accomplished using either a power divider or a directional element. Power dividers, which are typically resistive based, enable wideband operation but may introduce losses. Directional couplers, on the other hand, offer improved isolation and directivity with minimal insertion loss, although they may present limitations at low frequencies or across broad bandwidths (Fig. 1.18).

- Separation of Transmitted and Reflected RF Signals

A directional coupler is used to differentiate between signals that are reflected from and those transmitted through the device under test (DUT). This separation is essential for the accurate measurement of S-parameters, which are critical for the precise characterization of RF components.

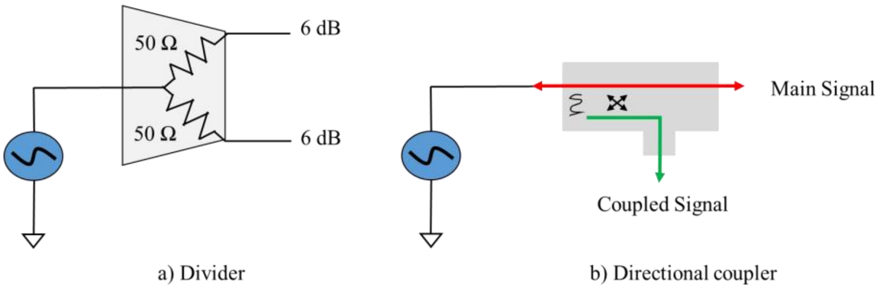

Fig. 1.18: Signal separation module.

To evaluate the S-parameters of the Device Under Test (DUT), the generated and received signals are sampled by the measurement receiver. However, the measured reflection coefficient can be affected by imperfections in the directional element.

To overcome the broadband limitations of directional couplers, a resistive bridge can be used as an alternative. A directional coupler is characterized by three key parameters: Coupling (C), Isolation (I) and Directivity (D).

For example, in a 20 dB coupler, if an incident power of 0 dBm (1 mW) is injected from the source, a portion of this power or coupled power is directed toward the coupling port with an attenuation of -20 dB (0.01 mW) (Fig. 1.19). The coupling factor (C) is defined as:

$$\mathrm{C} = -10.\log\frac{\mathrm{P}_{\text{direct oupling}}}{\mathrm{P}_{\text{incident}}} \tag{E.1.38}$$

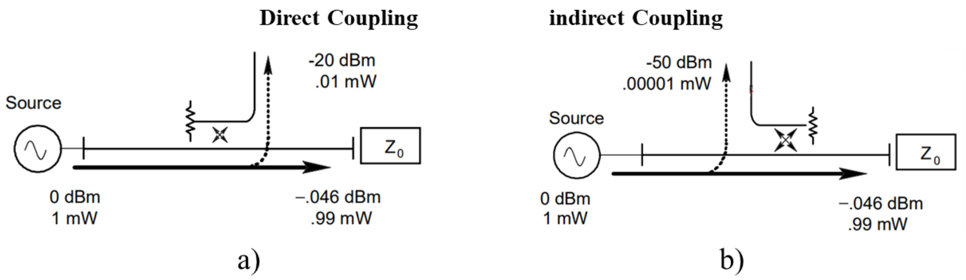

Fig. 1.19: 20 dB coupler - a) direct coupling - b) indirect coupling.

In the reverse direction, an indirect coupling power of -50 dB (0.00001 mW) reaches the coupler port. Analyzing the coupler in this configuration allows us to evaluate its isolation factor (I), defined as:

$$\mathrm{I} = -10.\log\frac{\mathrm{P}_{\text{indirect coupling}}}{\mathrm{P}_{\text{incident}}} \tag{E.1.39}$$

An essential parameter in the characterization of directional couplers is their directivity (D), which quantifies the device ability to distinguish between signals traveling in different directions. Directivity is defined as the difference between the isolation factor (I) and the coupling factor (C), both measured in decibels (dB):

$$D = I(dB) - C(dB) \tag{E.1.40}$$

For example, consider a typical 20 dB coupler with an isolation factor of 50 dB. The directivity of this coupler can be calculated as follows:

$$\mathrm{D} = 50\ \mathrm{dB} - 20\ \mathrm{dB} = 30\ \mathrm{dB}$$

In practical applications, it is important to account for losses (L) within the system, which can influence the coupler to separate transmitted and reflected signals. When losses are considered, the expression for directivity is modified to:

$$D = I(dB) - C(dB) - L(dB) \tag{E.1.40}$$

By incorporating losses into the calculation, a more accurate assessment of the coupler's performance is achieved. Higher directivity values, especially when adjusted for losses, indicate improved separation and discrimination between the signal paths. This is crucial for obtaining reliable and precise S-parameter measurements during network analysis.

Higher directivity ensures better discrimination between the transmitted and reflected signals, improving the accuracy of S-parameter measurements.

1.3.1.3. Reception and analysis module

In the process of analyzing incident and reflected power waves, the detection of these signals can be achieved through two primary approaches. Each method offers distinct advantages and limitations, particularly in terms of the information retained about the signal.

The first approach utilizes receiving diodes to convert the radio frequency (RF) signal into either a direct current (DC) or alternating current (AC) signal. This method is depicted in Fig. 1.20. While this technique is straightforward and effective for certain measurements, it has the significant drawback of losing the phase information present in the original RF signal. Because of this, the approach is classified as a scalar detection method, as it only measures the magnitude of the signal without capturing its phase characteristics.

The second approach employs a tuned detector, which incorporates a local oscillator (LO) to generate an intermediate frequency (IF) from the incoming RF signals. The local oscillator can be synchronized, or "locked," either to the RF signal itself or to the IF signal. This process ensures that the vector network analyzer receivers are accurately tuned to the frequency of the incoming RF signal. Once the IF signal is generated, it undergoes narrowband filtering. This filtering step is crucial, as it reduces the bandwidth of the receiver. The result is an improvement in both the sensitivity and the dynamic range of the network analyzer, enhancing the accuracy and reliability of the measurements.

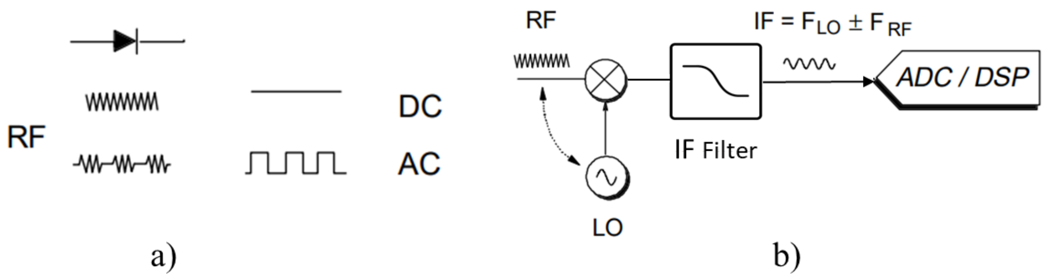

Fig. 1.20: Types of detectors for receiving signals from a VNA a) diode detection | b) tuned detector.

The receivers in Vector Network Analyzers typically operate using heterodyne architecture. This means that two signals of different frequencies are mixed: the incoming signal that is being measured and a signal generated by a local oscillator (LO).

The process begins with the input signal passing through a bandpass filter (BPF). The role of this filter is to eliminate unwanted image frequencies, ensuring that only the desired frequency range reaches the next stage. After filtering, the signal is directed into the RF mixer.

Within the mixer, the filtered input signal is combined with the LO signal. This mixing process produces a new signal at an intermediate frequency (IF), which is typically lower than the original input frequency. The IF signal then passes through a low-pass filter (LPF), which further refines the signal by removing any high-frequency components or noise that may have been introduced during mixing.

Finally, the cleaned IF signal is converted from its analog form into a digital signal using an analog-to-digital converter (ADC). This digitized signal can then be processed for analysis and measurement by the VNA.

These blocks can influence the overall system performance, particularly in terms of frequency range, dynamic range, measurement speed, and stability, among other factors.

1.3.2. Types of measurement with a VNA

The Vector Network Analyzer is a vital instrument for high-frequency characterization, enabling a wide range of essential measurements in RF and microwave engineering. Below are the principal measurement types that can be conducted using a VNA, along with their respective significance and applications:

Gain, Attenuation, and Distortion Measurements: Gain, attenuation, and distortion measurements are fundamental when analyzing RF and microwave devices. For example, in the design of radar systems, accurately measuring gain and attenuation is crucial for evaluating the power delivered to the antenna and assessing the noise factor [4]. VNAs are equipped with calibration capabilities and offer a broad dynamic range, making them highly precise tools for these measurements [5].

Group delay and Phase Measurements: Group delay and phase measurements involve assessing the phase shift introduced by the device under test (DUT) between its input and output. The phase measurement captures this shift, while the delay is determined by taking the derivative of the phase with respect to frequency [5]. These measurements are important for understanding signal integrity and the temporal behavior of RF devices.

Noise Figure Measurement: As measurement systems become increasingly integrated and operate in complex high-frequency environments, measuring the noise figure becomes essential. Accurate noise figure measurements improve the reliability of overall measurement results, ensuring that system performance can be properly evaluated and optimized.

Pulsed RF Measurements: Pulsed RF measurements are necessary for characterizing RF components and systems under conditions that closely resemble real-world operation. These measurements are especially important in high-power and pulsed applications, such as radar, telecommunications, and aerospace, where the behavior of components during pulsed operation must be thoroughly understood.

Antenna Measurements: Antenna measurements are critical for evaluating the performance of RF and microwave transmission and reception systems. By measuring key parameters like gain, directivity, impedance, and radiation pattern, VNAs help ensure that antennas function optimally and efficiently in communication and radar applications.

Materials Measurements: VNAs can be used to analyze material properties through specialized measurement techniques. These include using resonator structures to determine dielectric properties by observing resonant frequency shifts and quality factor variations. Transmission structures involve measuring transmission and reflection coefficients to extract material parameters. Additionally, contact or non-contact probes enable localized measurements of permittivity and permeability, which are valuable for characterizing substrates and coatings. Such techniques are widely applied in RF and microwave contexts to evaluate dielectric constants, loss tangents, and magnetic properties of materials.

Load-pull and Load-pull harmonic Measurements: The load-pull technique involves systematically varying the load impedance (ZL) presented to a DUT and analyzing the resulting changes in its performance. This method is extensively used in RF and microwave engineering to optimize power amplifiers, transistors, and other active components by identifying the optimal load conditions required to achieve desired performance parameters.

1.4. Error sources and measurement model

1.4.1. Error sources

Two types of errors can affect Measurements with a Vector Network Analyzer. They include systematic errors and uncorrectable errors (uncalibratable)

When conducting measurements with a Vector Network Analyzer, two primary types of errors can affect the accuracy and reliability of the results: systematic errors and uncorrectable (uncalibratable) errors. Understanding these errors is crucial for ensuring precise and consistent measurements in RF and microwave applications.

1.4.1.1. Errors uncorrected by calibration

The errors that are not corrected during calibration consist of:

a. Drift errors

Drift errors occur because of environmental influences such as temperature fluctuations, changes in humidity, the aging of components, and other variations in the measurement environment. These factors can cause changes in the performance of critical system components, including couplers, receivers, and signal traces. Some materials used within the measurement setup are particularly sensitive to temperature, meaning that even after performing a calibration, the system can still experience drift. This drift alters the systematic error coefficients determined during calibration, thereby impacting measurement accuracy over time.

The validity of calibration is therefore dependent on the stability of the measurement environment and the rate of system drift. In situations where drift is significant, frequent recalibration is required to maintain accurate and reliable measurements.

b. Random errors

Random errors are unpredictable in nature and arise from sources such as thermal noise, phase noise, and random fluctuations within the measurement system itself. Unlike systematic errors, random errors cannot be corrected through calibration procedures. The best way to minimize their impact is to improve the measurement conditions this can involve using improved shielding, averaging multiple measurements, or reducing external sources of interference.

1.4.1.2. Systematic errors

Systematic errors are inherent to the VNA system and are caused by imperfections in the instrument's internal components. These types of errors are repeatable and, importantly, can be corrected through a proper system calibration. Common systematic errors include:

- Directivity error: Results from the imperfect isolation of the directional coupler within the measurement system.

- Source and load mismatch errors: Caused by impedance mismatches in the test setup, which affect the accuracy of power transfer and reflection measurements.
- Isolation or crosstalk errors: Stem from signal leakage between different signal paths within the VNA or test setup.
- Transmission and Reflection Tracking or Frequency Response errors: Arise due to variations in test cables or connectors, impacting the consistency of measured signals across different frequencies.

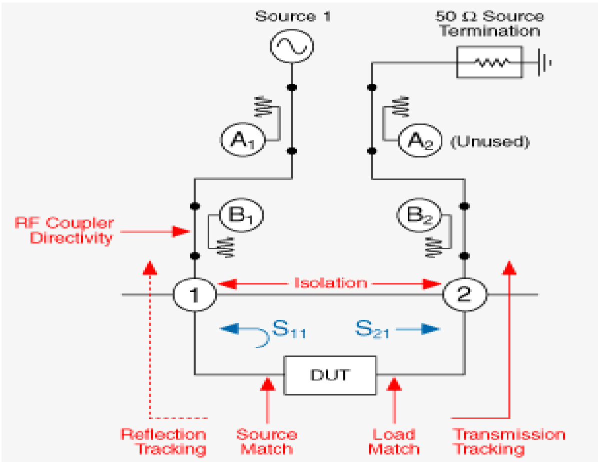

Fig. 1.21: Systematic errors [6].

1.4.2. Measurement model

S-parameter measurements conducted with a Vector Network Analyzer rely on a specific measurement model to ensure the accuracy and reliability of results. This model takes into account the VNA itself, any imperfections present in the measurement system, and the device under test (DUT), which may have one or multiple ports.

The measurement model employs mathematical formalism to describe how the VNA interacts with the DUT and accounts for all potential sources of error. These errors are categorized based on the configuration of the component, whether in reflection or transmission mode. By associating the measurement model with a corresponding error model, it becomes possible to systematically evaluate and, where applicable, correct for the imperfections that affect measurement integrity.

This approach enables precise characterization of components by delineating the contributions of the VNA, the DUT, and the error sources within the measurement system.

1.4.2.1. One-port measurement model

In the one-port measurement model, the Vector Network Analyzer and the Device Under Test (DUT) are separated by an element known as the error box. This error box symbolizes the systematic imperfections or errors present within the measurement system. These imperfections are modeled using a network, often depicted as a quadrupole that includes specific error terms. The three primary error terms are directivity error (E_D), source matching error (E_S), and reflection tracking error (E_R). Each of these represents a distinct source of error within the measurement setup and collectively, they are referred to as calibration coefficients.

Within this framework, the typical measurement performed is the reflection coefficient of DUT. However, the actual reflection response of the DUT ($S11_{DUT}$) differs from the raw response measured by the VNA ($S11_M$), due to the influence of these systematic errors. The calibration process uses the characterization of these error terms to allow for correction, thereby improving the accuracy and reliability of the measurement results.

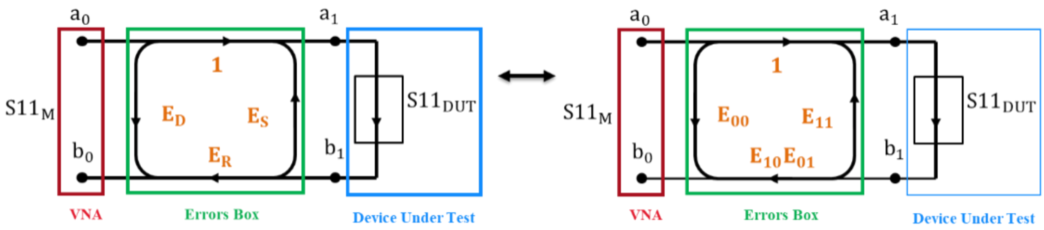

Fig. 1.22: One-port measurement model (3-errors terms).

To accurately determine the actual reflection coefficient of the Device Under Test (DUT) from the raw coefficient measured by the Vector Network Analyzer, a calibration process is employed. This procedure utilizes three well-established standards Short, Open, and Load to systematically identify and correct for measurement errors.

The calibration involves measuring the response of these three known standards and then using their results to solve a system of equations. Each equation corresponds to one of the standards and contains three unknowns, which represent the primary error terms inherent in the measurement system: directivity error, source matching error, and reflection tracking error. By solving this system of equations (E.1.41), the errors are determined and extracted, allowing for correction of the measured data.

This method ensures that the influence of systematic imperfections is minimized, thereby yielding a more accurate and reliable reflection coefficient for the DUT.

$$S11_M = E_D + \frac{S11_{DUT} \, . \, E_R}{1 - E_S \, . \, S11_{DUT}} \tag{E.1.41}$$

$$S11_{DUT} = \frac{S11_M - E_D}{E_S(S11_M - E_D) + E_R} \tag{E.1.42}$$

The well-known one-port calibration method, referred to as Short-Open-Load (SOL), utilizes three distinct calibration standards:

- The short-circuit standard (Short) is modeled by a series resistor R with a reactance X_L typical of an inductance that is a polynomial function of degree 3 of the frequency [5] (Fig. 1.23).

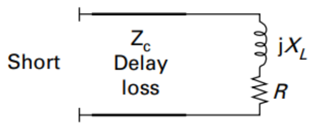

Fig. 1.23: Equivalent model of Short.

$$X_L = 2\pi f(L_0 + L_1 f + L_2 f^2 + L_3 f^3) \tag{E.1.43}$$

- The open-circuit standard is modeled by a resistor R in parallel with a reactance Bc, typical of capacitance that is a polynomial function of degree 3 of the frequency [5] (Fig. 1.24).

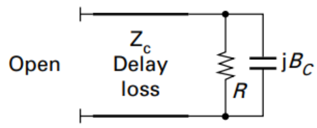

Fig. 1.24: Equivalent model of Open.

$$B_C = 2\pi f. \, (C_0 + C_1 f + C_2 f^2 + C_3 f^3) \tag{E.1.44}$$

- The matched load standard (Load) is modeled by a series resistor R with an inductance L (Fig. 1.25).

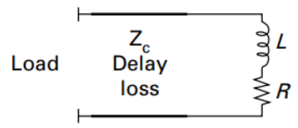

Fig. 1.25: Equivalent model of Open.

1.4.2.2. Two-ports measurement model

The two-port measurement model is essential for accurately characterizing devices using a Vector Network Analyzer. This model considers the measurement reference planes established by the VNA, as well as the error boxes placed on each side of the Device Under Test (DUT). These error boxes represent all systematic imperfections introduced by the measurement system, such as directivity, source and load match, and tracking errors.

In addition to the errors typically considered in the one-port measurement calibration such as directivity, source match, and reflection tracking, the two-port model introduces further error mechanisms that must be accounted for. Specifically, it includes the transmission frequency response error, denoted as E_T, which corresponds to inaccuracies in the measured transmission characteristic between ports. Another important term is the load matching error, E_L, which arises from mismatches at the load side of the DUT.

The architecture of the VNA plays a significant role in determining the complexity and nature of the error model. Depending on whether the VNA employs a three-receiver or four-receiver architecture (see Fig. 1.26), the configuration and influence of these errors may vary. In three-receiver designs, one reference receiver is positioned before the switch, with two additional receivers detecting reflection and transmission after the switch. In contrast, four-receiver architectures place all receivers after the switch, altering how certain errors are modeled and corrected.

Additionally, isolation faults between ports commonly referred to as crosstalk and represented by $E_X$can be significant for transmission measurements. Crosstalk describes unintended signal leakage between the VNA ports, which can impact the accuracy of the transmission parameter measurements.

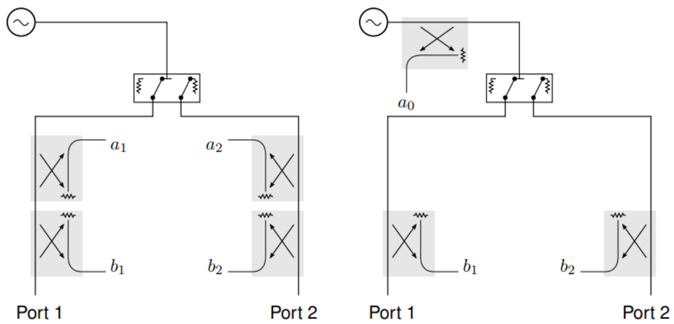

Fig. 1.26: Four-receiver (left) vs. three-receiver (right) VNA architecture [7].

In the three-receiver architecture, a reference receiver is positioned before the switch, while the two remaining directional elements responsible for detecting reflection and transmission are located after the switch. Within this setup, errors introduced by the switch are incorporated into the overall error model. This configuration allows the measurement process to be conducted in both the forward and reverse directions.

Conversely, in the four-receiver architecture, all receivers are situated after the switch. In this arrangement, the terms associated with the switch are not integrated into the error model and, therefore, must be corrected separately.

1.4.2.2.1. Eight-term error model.

The eight-term error model is commonly applied in Vector Network Analyzers that utilize a four-receiver architecture. As depicted in Fig. 1.27, this model incorporates eight distinct error terms to account for systematic imperfections affecting two-port measurements. However, through normalization procedures, it is possible to reduce the number of independent error terms from eight to seven. This simplification streamlines the calibration and error correction process without compromising measurement accuracy.

It is important to note that the error terms identified as, E_{30} and E_{03}, which correspond to crosstalk between the VNA ports, are generally much less significant than the other error contributions in the model. As a result, while these crosstalk errors are included for completeness, their impact on overall measurement accuracy is typically minimal compared to the primary error mechanisms addressed by the model.

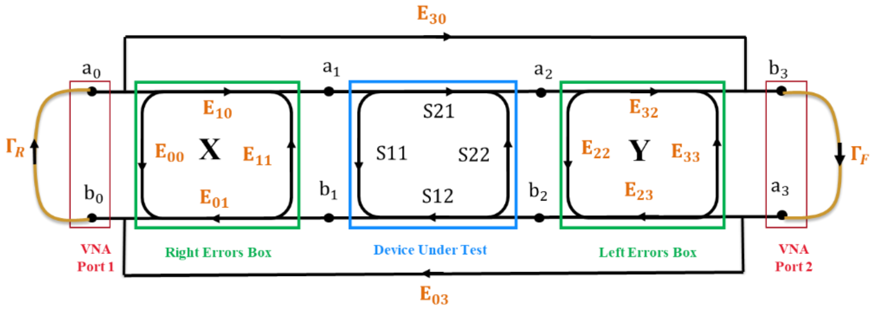

Fig. 1.27: Two-port measurement model (8-errors terms).

The signal flowgraph for a two-port network, as referenced in [8], provides a framework for establishing mathematical relationships connecting the error quadrupoles $\boldsymbol{X}$ and $\boldsymbol{Y}$ to the Device Under Test (DUT). The model for a two-port network measurement employs transfer matrices that are derived from the corresponding S-parameter matrices of each component in the measurement system. Within this framework, the measurement model is described by equation (E.1.45). In this equation, each matrix term represents a distinct transfer matrix: M corresponds to the raw measurement, $\boldsymbol{X}$ denotes the error box on the left side of the DUT, $\boldsymbol{T_{DUT}}$ represents the actual DUT, and $\boldsymbol{Y}$ refers to the error boxes on the right side. By structuring the measurement in this way, the model systematically accounts for the influence of error sources at both the input and output of the DUT, enabling more accurate extraction of the DUT characteristics from the measured data.

$$\boldsymbol{M} = \boldsymbol{X}.\boldsymbol{T_{DUT}}.\boldsymbol{Y} \tag{E.1.45}$$

Where these transfer matrices are obtained from the transformation of their S matrices, which are described as follows:

$$\boldsymbol{M} = \frac{1}{S_{21m}}\begin{bmatrix} -\Delta_{Sm} & S_{11m} \\ -S_{22m} & 1 \end{bmatrix} \; ; \; \Delta_{Sm} = S_{11m}S_{22m} - S_{21m}S_{12m} \tag{E.1.46}$$

$$\boldsymbol{X} = \frac{1}{E_{10}}\begin{bmatrix} -\Delta_{X} & E_{00} \\ -E_{11} & 1 \end{bmatrix} \; ; \Delta_{X} = E_{00}E_{11} - E_{10}E_{01} \tag{E.1.47}$$

$$\boldsymbol{T_{DUT}} = \frac{1}{S_{21}}\begin{bmatrix} -\Delta_{S} & S_{11} \\ -S_{22} & 1 \end{bmatrix} \; ; \; \Delta_{S} = S_{11}S_{22} - S_{21}S_{12} \tag{E.1.48}$$

$$\boldsymbol{Y} = \frac{1}{E_{32}}\begin{bmatrix} -\Delta_{Y} & E_{22} \\ -E_{33} & 1 \end{bmatrix} \; ; \; \Delta_{Y} = E_{22}E_{33} - E_{32}E_{23} \tag{E.1.49}$$

For VNAs with a four-receiver architecture as shown in (Fig. 1.26), the switching terms Γ_F and Γ_R must be corrected via a transmission component by considering the sources at port 1 for forward and port 2 for reverse, respectively.

For Vector Network Analyzers that employ a four-receiver architecture, as illustrated in Fig. 1.26, the correction of switching terms is essential for accurate two-port measurements. Specifically, the switching terms, Γ_F (forward) and Γ_R (reverse) must be addressed to ensure proper calibration and error compensation.

To correct these switching terms, a transmission component is utilized, which considers the sources at the respective ports of the VNA. For the forward direction, the source at port 1 is considered, while for the reverse direction, the source at port 2 is used. This approach allows the measurement system to accurately represent the signal paths and switching behavior within the VNA, thereby improving the reliability of the extracted device parameters.

$$\Gamma_F = \frac{a_3}{b_3}\ ;\ \Gamma_F = \frac{a_0}{b_0} \qquad \text{(E.1.50)}$$

There are multiple calibration methods available for two-port measurements, each designed to identify and extract the error boxes associated with the measurement model. These techniques can be broadly classified based on whether or not they require complete information about the calibration standards being used.

Certain calibration methods, commonly referred to as self-calibration techniques, do not demand full knowledge of the standards employed. Examples of such techniques include Thru-Reflect-Line (TRL) [9], Line-Reflect-Line (LRL) [10], Line-Reflect-Match (LRM), and Line-Reflect-Reflect-Match (LRRM) [11]. These approaches allow for effective calibration by relying on specific combinations and arrangements of standards, minimizing the need for comprehensive characterization of each standard.

Other calibration techniques, in contrast, do require precise and complete knowledge of the standards used. Examples of these methods include Short-Open-Load-Reciprocal (SOLR) and Quick-Short-Open-Load-Thru (QSOLT) [12 - 13]. In these cases, accurate information about the electrical properties of the standards is essential for the successful extraction and correction of error terms during calibration.

1.4.2.2.2. Twelve-term error model.

The 12-term error model is a widely used approach in two-port Vector Network Analyzer calibration for addressing systematic measurement errors. This model is distinguished by its comprehensive treatment of all systematic errors, while not accounting for switching errors specifically.

Within the 12-term error model, a total of twelve error terms is considered: six errors associated with the forward measurement direction and six errors with the reverse direction, as illustrated in Fig. 1.28. These terms collectively capture the systematic effects that may distort both the incident and transmitted signals through the measurement system.

To resolve these twelve unknown error terms, only twelve independent equations are necessary. In some cases, crosstalk can be neglected, reducing the system to ten equations. These equations are obtained by measuring three one-port calibration standards in each direction, along with an additional measurement using a transmission standard. This calibration strategy allows for the accurate identification and characterization of the error boxes required for reliable two-port measurements.

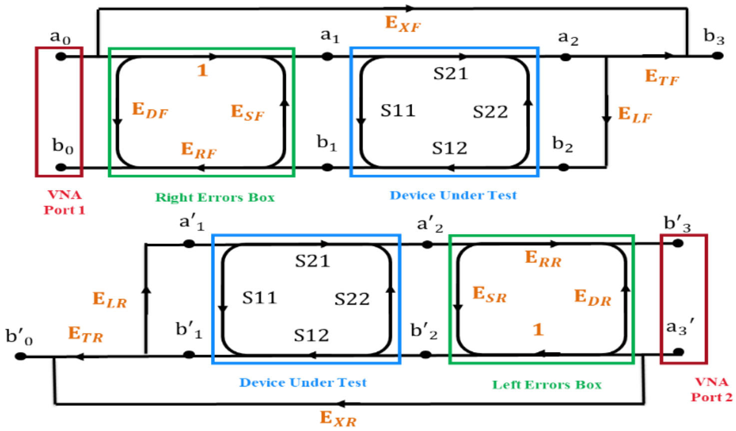

Fig 1.28: Two-port measurement model (12-errors terms).

A widely adopted approach for determining the error terms within the 12-term error model is the Short-Open-Load-Thru (SOLT) calibration technique [15]. This method involves the use of four fundamental calibration standards short, open, load, and thru which are sequentially measured to characterize and correct systematic errors present in two-port Vector Network Analyzer measurements. Through careful application of the SOLT method, the measurement system can accurately extract the necessary error terms, thereby improving the precision of device parameter extraction.

With the continuous advancement of RF and microwave technologies, designers have recognized the need to further refine error models to achieve even higher measurement accuracy. In pursuit of measurements that more closely reflect the true values of the components under test, additional error terms have been introduced. For example, the sixteen-term error model has been developed to account for additional phenomena such as coupling effects, which are not addressed by the standard 12-term model. These expanded models enable more comprehensive error correction and contribute to the ongoing improvement of measurement reliability in increasingly complex systems.

1.5. Calibration methods

According to the International Vocabulary of basic and general terms in Metrology, calibration means "*set of operations that establish, under specified conditions, the relationship between values of quantities indicated by a measuring instrument or measuring system, or values represented by a material measure or a reference material, and the corresponding values realized by standards*" [16]. For VNA, calibration consists of the determination of the systematic errors called errors terms, errors or calibration coefficients. The process is based on a measurement model with an associated error model by using standards and algorithm method.

1.5.1. One-port Calibration

The measurement of one-port devices using a Vector Network Analyzer is illustrated by the signal flow graph shown in Fig. 1.16. This type of measurement focuses on determining the reflection coefficient of the device under test (DUT). In this process, three main quantities are involved:

- The raw measurement value of the device denoted as S_{11_M}.
- The systematic error terms, specifically directivity (E_D), source match (E_S), and reflection tracking (E_R).
- The actual value of the device, represented as S_{11}.

To obtain accurate measurements, the calibration process is employed. Calibration enables the extraction of these error coefficients by solving equation (E.1.41), which requires the use of three known standards.

For the calibration to be valid, each standard must satisfy the equality condition prescribed by the measurement model. This leads to the formation of a system of three equations with three unknowns, as described by equation (E.1.54). These unknowns correspond to the systematic errors inherent in the measurement setup.

$$\begin{bmatrix} 1 & S_{11M1}.S_{11_1} & -S_{11_1} \\ 1 & S_{11M2}.S_{11_2} & -S_{11_2} \\ 1 & S_{11M3}.S_{11_3} & -S_{11_3} \end{bmatrix} . \begin{bmatrix} E_D \\ E_S \\ \Delta \end{bmatrix} = \begin{bmatrix} S_{11_1} \\ S_{11_2} \\ S_{11_3} \end{bmatrix} \; ; \; \Delta = \mathrm{E_D}.\mathrm{E_S} - 1.\mathrm{E_R} \qquad \text{(E.1.51)}$$

Short-Open-Load (SOL) calibration is a widely adopted approach for calibrating measurement systems, especially in the context of vector network analyzer measurements. The SOL method relies on the use of three distinct standards: a short circuit, an open circuit, and a load. Each standard serves a specific role in characterizing the systematic errors within the measurement setup.

While the SOL calibration method is prevalent, it is not the only technique available for this purpose. An alternative approach involves using three shorts with offset lengths, known as the SSS method. The SSS method also enables error characterization by providing three different short standards, each with a unique offset length.

Regardless of the chosen method, one critical requirement remains: all calibration standards must be accurately characterized and must differ from one another. This ensures the validity of the calibration process and the reliability of the resulting measurement corrections.

1.5.2. Two-port Calibration

Two-port calibration is fundamentally influenced by the selected error model and the standards employed during the process. At a minimum, four distinct standards are required to perform this type of calibration effectively. Multiple calibration techniques are available, each with its own approach to standard utilization. Some calibration methods necessitate complete and detailed information about the standards being used. In contrast, self-calibration methods offer an alternative by not requiring comprehensive knowledge of the standards, making them more flexible in certain measurement scenarios.

Within this context, the focus is placed on two specific error models: the eight-term and twelve-term error models. These models, as illustrated in Fig. 1.27 and Fig. 1.28, are discussed in detail in this manuscript, providing a foundation for understanding the systematic errors that can arise in two-port measurements and the calibration strategies used to address them.

a. Thru-Reflect-Line (multiline) Calibration

TRL calibration is recognized as one of the self-calibration techniques for measurement systems. Initially introduced by Engen and Hoer in 1974, this method is distinguished by its minimal requirement for detailed knowledge of the calibration standards. Instead, the process employs three components: a short line, a second line with a different length, and a reflective element, which can be either an open or a short circuit, as illustrated in Fig. 1.29.

Unlike other calibration methods, TRL does not demand comprehensive information about the standards used. However, it is essential that the two lines employed in the calibration possess different lengths to ensure a phase shift between 20° and 160° is established. This phase difference is critical for the method's effectiveness. Additionally, the reflector used in the process must have minimal loss and maintain consistent reflection coefficients at each port, ensuring reliable calibration results.

Through the TRL approach, it becomes possible to determine key electrical characteristics of a transmission line, specifically the propagation constant (γ) and the characteristic impedance (Zc). These properties are fundamental to accurate measurement and calibration in microwave and RF applications.

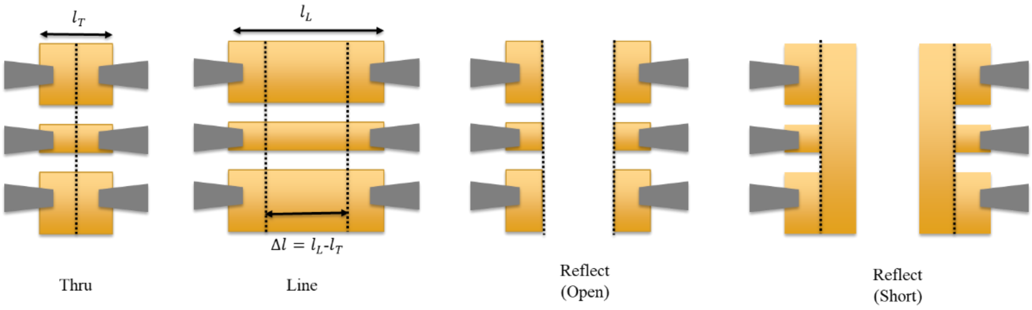

Fig. 1.29: On-wafer calibration standards for TRL method.

The Thru-Reflect-Line (TRL) method is a robust and widely used calibration technique that enables accurate calibration and strong traceability, particularly when primary standards such as airlines are utilized [16]. However, one of the main limitations of the TRL method is its restriction in applicable frequency range. This frequency band limitation arises because the difference in length between the Thru and Line standards must be suitably chosen in relation to the frequency of interest. In other words, for calibration to be effective, these two standards must have an adequate length difference that matches the operating frequency range.

To address this constraint, the multiline TRL approach has been implemented [17]. This variant expands the usable frequency range by incorporating additional lines of varying lengths into the calibration procedure. By doing so, multiline TRL mitigates the frequency limitations of the basic TRL method, allowing for more versatile and accurate calibration across a broader spectrum.

The TRL calibration process is fundamentally concerned with evaluating systematic measurement errors when using a vector network analyzer This is achieved by employing three distinct calibration standards:

- A Thru standard (T)
- A Reflect standard (R), which can be either an open or short circuit
- A Line standard (L) of different length than the Thru

Using these three standards, the TRL method allows for the determination of eight error terms. These include four error terms associated with each side of the device under test (DUT): directivity (E_{00}), source adaptation (E_{11}), frequency responses in transmission ($E_{10}.E_{32}$), and reflection ($E_{10}.E_{01}$) as depicted in Fig. 1.20.

These systematic errors are represented by hypothetical networks often called "error boxes" which embed the DUT. The DUT itself is modeled by a network of S-parameters or T-parameters positioned between the two ports of the VNA. Each error box contains specific calibration terms or coefficients that characterize the error contributions on either side of the DUT.

The final measurement results, as observed at the VNA measurement reference planes, are the outcome of the cascaded networks formed by these error boxes and the DUT. This relationship is mathematically described by equation (E.1.45). Within the TRL procedure, the Thru and Line standards are crucial for resolving a portion of the error terms, while the Reflect standard completes the determination of all error terms.

A key aspect of the TRL process is the use of a transfer matrix T, which encapsulates both the theoretical and measured responses of the Thru and Line standards. This matrix-based approach enables systematic evaluation and correction of measurement errors, ensuring the reliability and accuracy of the calibration.

$$\boldsymbol{T_{thru}} = \begin{bmatrix} 1 & 0 \\ 0 & 1 \end{bmatrix} \quad ; \quad \boldsymbol{M_{thru}} = \begin{bmatrix} M_{11thu} & M_{12thu} \\ M_{21thu} & M_{22thu} \end{bmatrix} \tag{E.1.52}$$

$$\boldsymbol{T_{line}} = \begin{bmatrix} e^{-\gamma l} & 0 \\ 0 & e^{\gamma l} \end{bmatrix} ; \quad \boldsymbol{M_{line}} = \begin{bmatrix} M_{11line} & M_{12line} \\ M_{21line} & M_{22line} \end{bmatrix} \tag{E.1.53}$$

In the TRL process, a transfer matrix T of the theoretical and measured responses of thru and line standards is used (E.1.52 and E.1.53).

The reflect standard is specified by its S-parameter matrix.

$$\boldsymbol{S_{Reflect}} = \begin{pmatrix} \Gamma_r & 0 \\ 0 & \Gamma_r \end{pmatrix} \tag{E.1.54}$$

The relationship in (E.1.45) is the basis of TRL algorithm. With it, one can determine the initial unknowns by redundancy applying proprieties of matrix algebra. The TRL algorithm is more detailed in Appendix 1.

In addition to being able to extract error boxes and determine line propagation characteristics (i.e. propagation constant and characteristic impedance), TRL allows the reference plane to be shifted. Just after calibration, the reference plane is located in the middle of the Thru standard (Fig. 1.30).

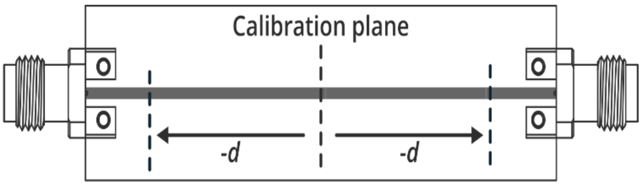

Fig. 1.30: Illustration of negative plane shift of a TRL calibration done with a thru standard as microstrip line [18].

For example, error boxes ***X*** and ***Y*** can be shifted to a distance (*d*) from the center of the Thru standard, resulting in new error boxes denoted as ***Xnew*** and ***Ynew***. This adjustment is accomplished by applying a mathematical transformation, which effectively repositions the reference planes relative to the Thru standard. By doing so, the calibration reference planes are moved away from the original center point, providing flexibility in the calibration setup. This process allows for more accurate alignment of the measurement system with the physical test structure, ensuring that the extracted device characteristics correspond to the desired reference locations within the measurement environment.

$$\boldsymbol{X_{new}} = \boldsymbol{X} \, . \begin{bmatrix} e^{-2\gamma d} & 0 \\ 0 & 1 \end{bmatrix} \quad ; \quad \boldsymbol{Y_{new}} = \boldsymbol{Y} \, . \begin{bmatrix} e^{-2\gamma d} & 0 \\ 0 & 1 \end{bmatrix} \tag{E.1.55}$$

The reference impedance Zc can be transformed into a new impedance Zn via the impedance transformation matrix [18 - 19].

$$\boldsymbol{Q^{cn}} = \frac{1}{\sqrt{1-\Gamma_{cn}{}^2}} \begin{bmatrix} 1 & \Gamma_{cn} \\ \Gamma_{cn} & 1 \end{bmatrix} \quad ; \quad \Gamma_{cn} = \frac{Z_n - Z_c}{Z_n + Z_c} \tag{E.1.56}$$

b. Line-Reflect-Reflect-Match (LRRM) and Line-Reflect-Match (LRM) Calibration

*** LRRM calibration**

The Line-Reflect-Reflect-Match (LRRM) technique is a calibration method that relies on the use of four distinct standards: a Line (L), an Open (R), a Short (R), and a Match (M) (see Fig. 1.31). This approach is characterized by its self-calibration capability, which means that it does not require complete prior knowledge of the individual standards involved in the process.

One of the critical aspects of the LRRM method is the control of the propagation constant associated with the Line standard. Additionally, it is important that both the Open and Short standards provide sufficient reflectivity, specifically with phase shifts of approximately ±90 degrees. The Match standard typically consists of a resistor (Rs) in series with an inductor (Ls), serving as its model in practical implementations.

The fundamental principle underlying the LRRM technique involves the combined use of all four standards. By employing various combinations of the Reflect standards (Open and Short) along with the Match standard, the method introduces redundancy into the calibration process. This redundancy is essential, as it effectively resolves indeterminacies related to certain unknown parameters, thereby enabling their accurate determination.

A detailed description of the LRRM procedure and its implementation can be found in Appendix 2.

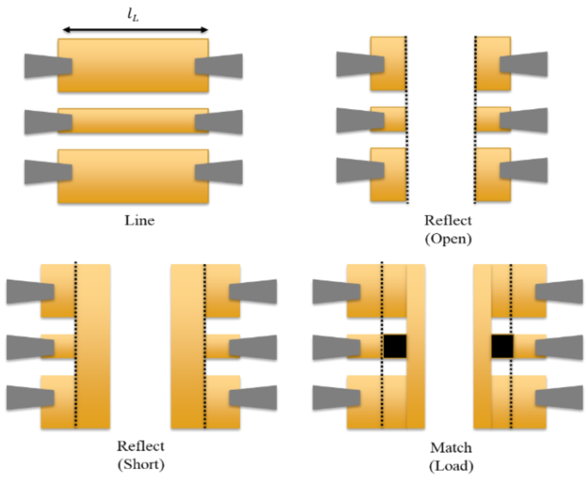

Fig. 1.31: On-wafer calibration standards for LRRM method.

*** LRM calibration**

The Line-Reflect-Match (LRM) method was introduced in the 1980s [21]. Like the Thru-Reflect-Line (TRL) technique, LRM replaces the second line standard with a matched load, also known as the Match standard. This calibration method is classified as a self-calibration technique, which means it generally does not require prior knowledge of all the standards involved, except for the Match standard.

For successful LRM calibration, the Match standard must be well defined and symmetrical at both ports. Typically, its impedance consists of a resistor (Rdc) close to 50 Ω in series with a frequency-dependent reactance (L). This configuration provides the LRM method with a broader bandwidth compared to the traditional TRL approach.

The reflect standard used in LRM calibration can be either an Open or a Short. Over time, the original LRM method has been refined; the improved version is now referred to as LRM+ [22-23]. A step-by-step outline of the LRM routine is provided in Appendix 3.

c. Short- Open-Load-Thru (SOLT) Calibration

The Short-Open-Load-Thru (SOLT) calibration is among the most utilized calibration techniques in radio frequency and microwave measurements. This method relies on four distinct standards: the Short Circuit, Open Circuit, Matched Load, and Thru Connection [16] (see Fig. 1.32). Each standard must be precisely defined and thoroughly characterized using established models and measurement data. By ensuring that these standards are well known, they can be measured or tested using a Vector Network Analyzer, allowing for the determination of the system's error terms.

Employing all four standards enables the identification and correction of various error components, including directivity, matching, reflection tracking, transmission tracking, and isolation errors. The first three standards Short, Open, and Load are utilized as one-port calibration components, as described in the one-port calibration section. The error model associated with SOLT calibration corresponds to the twelve-term model, which is illustrated in the signal flow graph on Fig. 1.28. This model accounts for six error terms in both the forward and reverse measurement directions.

A detailed procedure for the SOLT calibration method is provided in Appendix 4.

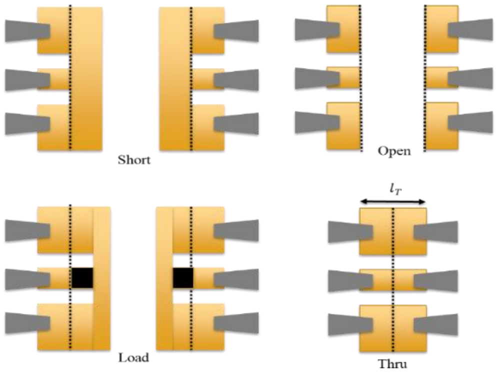

Fig. 1.32 On-wafer calibration standards for SOLT method.

Calibration methods play a significant role in determining the accuracy and reliability of measurement results. The calibration standards are fabricated on standard impedance substrates (ISS), which are specifically designed for this purpose. However, variations in the dimensions and materials between the calibration ISS and the device under test can introduce discrepancies in the measurements obtained.

To evaluate the influence of calibration methods, a study was conducted involving a set of coplanar structures. These structures included a transmission line, a step impedance line, and a passband filter, as illustrated in Fig. 1.33. The study was designed to account for the effects of the calibration method on the measurement process.

For each calibration method, twenty separate measurements were performed, and both the mean value and the standard deviation of the S parameters were calculated. These results provided insight into the consistency and accuracy of the different calibration approaches. Furthermore, the measurement data obtained from these calibrations were systematically compared with corresponding simulation results, enabling an assessment of how closely the experimental outcomes matched theoretical predictions.

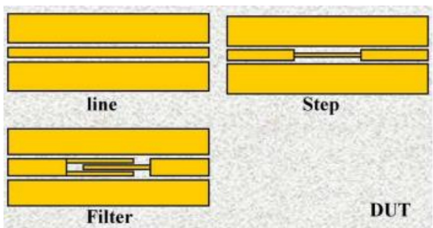

Fig. 1.33: Different DUTs [29].

To further assess the performance and consistency of different calibration methods, twenty measurements were carried out for each device under test (DUT) calibration. The results, presented in Fig. 1.34, reveal a general trend: the standard deviation of the transmission coefficient S21 increases with frequency across all DUTs.

Among the filter measurements, the ML-TRL algorithm yields the lowest standard deviation for S21, indicating superior measurement stability. This is followed by the LRM and SOLT methods, while the LRRM approach exhibits the highest standard deviation, suggesting greater variability in its results.

For step DUT, the ML-TRL method demonstrates the highest standard deviation among the calibration approaches tested. In contrast, the other methods LRM, SOLT, and LRRM produce relatively similar standard deviation values, reflecting comparable levels of measurement consistency.

Examining the line DUT reveals that the SOLT calibration method achieves the smallest standard deviation for S21, signifying the most consistent performance in this case. Conversely, the ML-TRL approach registers the largest standard deviation, indicating a higher degree of measurement fluctuation for this structure.

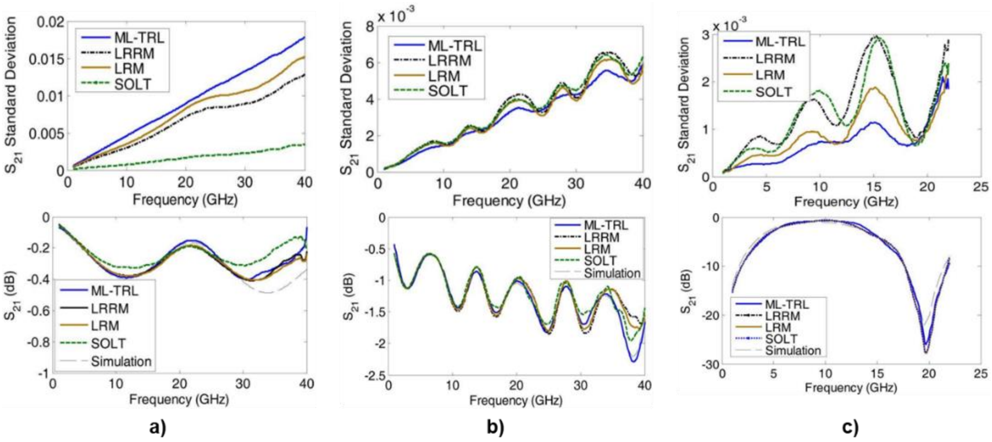

Fig. 1.34: Transmission coefficient S21 with Standard deviation | a) line, b) step, c) filter [29].

A comparative analysis was conducted between the average results obtained from twenty separate measurements following each calibration procedure and the corresponding simulation results for the S21 parameters across the three coplanar structures. As illustrated in Fig. 1.34, the data reveal that at frequencies above 29 GHz, all measured S21 values begin to noticeably diverge from the simulation predictions. In contrast, for frequencies below 29 GHz, the measurements calibrated using the TRL multiline algorithm closely align with the simulated data, demonstrating greater accuracy and agreement within this lower frequency range.

While calibration methods may vary depending on the standards employed, they share a common objective: to correct the systematic errors that are inherent within the measurement system. Each technique offers specific advantages and faces certain limitations with regard to accuracy, sensitivity, and self-determination. These aspects are summarized in Table 1.2, which provides a comparative overview of the different calibration approaches.

Table 1.2: Comparison of calibration methods.

Calibration Methods	**Advantages**	**Limits**
Thru-Reflect-Line: **TRL**	Traceable measurements Self-determination Unknown standards	Frequency band limitation Complex for substrate measurements Sensitive to Reflect asymmetry
Short-Open-Load-Thru: **SOLT**	Low frequency robustness	Sensitive to repeatability Inaccuracy of high frequency standards

Line-Reflect-Reflect-Match: **LRRM**	Self-determination Reflect asymmetry Good repeatability	Sensitive to VNA asymmetry high frequency deficiency
Line-Reflect-Match: **LRM**	Self-determination Good repeatability Wide bandwidth	Sensitive to VNA asymmetry high frequency deficiency
Multiline TRL: **mTRL**	Broadband	-

1.5.3. Residual errors

Calibration standards play a crucial role in determining the error terms during the Vector Network Analyzer calibration process. However, any inaccuracies or uncertainties in the characterization of these standards directly impact the calculation of the error terms. Such inaccuracies introduce what are known as residual errors [7]. Residual errors represent the remaining inaccuracies in the measurement system after calibration and are a key factor in evaluating the overall uncertainty of VNA measurements.

A common approach to calculate the measurement uncertainty of a VNA is to treat the analyzer as a "black box" and assess the residual errors remaining after calibration. For two-port measurements, these residual errors consist primarily of the terms of directivity (δE_D.), tracking (δE_R), and source match (δE_S). The parameters for directivity (D) and match (M) are typically evaluated using the ripple method. This involves making measurements on an airline terminated with a load and a short, respectively. The tracking error (δE_D) is generally taken from the manufacturer's specification for the VNA calibration standards [46].

The methodology assumes that the dominant sources of residual errors directivity (δE_D.), tracking (δE_R), and source match (δE_S) arise primarily from imperfect knowledge of the calibration standards used in estimating the VNA's error terms. The derivation of equations for estimating these error terms typically assumes that the VNA hardware itself is ideal and does not contribute additional errors [46].

Verification of the VNA calibration can be performed using different verification elements, depending on the type of device under test (DUT). For one-port verification, it is possible to measure various calibrated one-port standards, such as Load, Short, or Open. In this scenario, the relationship between the error-corrected reflection coefficient (${S_{11}}^{C}$) and the actual reflection coefficient (S_{11}) of the DUT can be expressed using the residual error coefficients for one-port calibration, namely δE_D (directivity), δE_S (source match), and δE_R (reflection tracking), as given by equation (E.1.57).

$$ {S_{11}}^{C} = \delta E_D + (1 + \delta E_R).S_{11} + \delta E_S\,.{S_{11}}^{2} \tag{E.1.57} $$

The sensitivity of the error-corrected reflection coefficient (${S_{11}}^{C}$) to individual residual error terms is influenced by the reflectivity of the device under test (DUT), represented by S11. In practice, this means that the degree to which each residual error term affects the corrected measurement result will vary depending on how reflective the DUT is. This relationship serves as a valuable guideline for the selection of verification standards, as it enables the identification of potential calibration faults by choosing standards that emphasize the influence of specific residual errors.

In a similar manner, when analyzing a transmission component, it is possible to derive the relationship between the error terms and both the raw and actual S-parameters of the DUT. This derivation leads to the determination of the corresponding residual errors, or sensitivity coefficients, for transmission measurements. These sensitivity coefficients help quantify how much each residual error term impacts the corrected transmission parameter, allowing for the effective assessment and verification of the calibration status.

$$S_{11}{}^{C} = \delta E_{00} + (1 + \delta E_{01}).S_{11} + \delta E_{11}\,.S_{11}{}^{2} + \delta E_{22}\,.S_{21}.\ S_{12} \quad (E.1.58)$$

$$S_{21}{}^{C} = \delta E_{11}.S_{11}.S_{21} + \delta E_{22}.S_{22}.S_{21} + (1 + \delta E_{32}).S_{21} \quad (E.1.59)$$

The equations (E.1.58) and (E.1.59) establish how the error-corrected S-parameters, specifically, $S_{11}{}^{C}$C and $S_{21}{}^{C}$, are connected to the true S-parameters of the device under test (DUT), S_{11} and S_{21} This connection is made through the inclusion of several residual error coefficients. These coefficients include directivity (δE_{00}), source match (δE_{11}), reflection tracking (δE_{01}), load match (δE_{22}), and transmission tracking (δE_{32}). Each coefficient represents a specific type of residual error that can affect the accuracy of the corrected measurement values after calibration. By quantifying these residual errors, the equations provide a means to assess how each error source influences the corrected S-parameters, thus enabling a more reliable evaluation of the DUT's actual performance.

1.6. De-embedding methods

On-wafer RF and microwave characterization presents significant complexity, primarily since the measurement reference plane does not usually coincide with the reference plane of the device under test (DUT). This misalignment leads to discrepancies between the raw measurement values and the true values of the DUT. Such differences are often the result of system imperfections or the presence of contact pads, which introduce unwanted parasitic effects.

To address these challenges, de-embedding techniques are employed. These methods are designed to eliminate the influence of discrepancy by mathematically shifting the measurement reference plane to the DUT itself [24]. De-embedding relies on mathematical approaches, which often involve equivalent circuit models that can incorporate both distributed and lumped elements. By doing so, these techniques enable a more accurate extraction of the DUT's intrinsic electrical characteristics, ensuring that the measurements reflect the actual device performance rather than the combined effects of the DUT and the test environment.

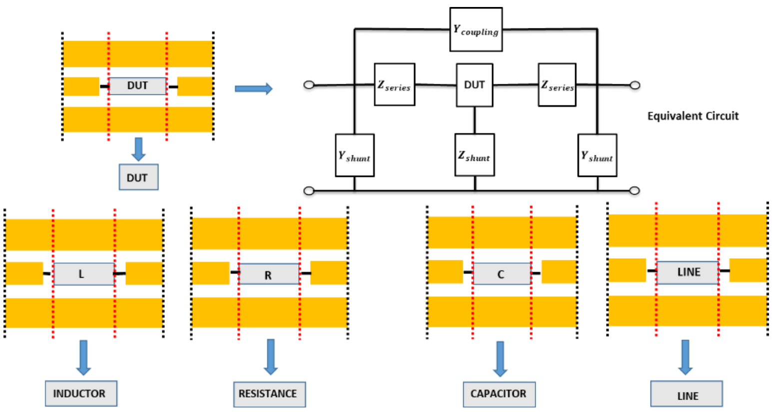

Fig. 1.35: Examples of embedded components.

The use of de-embedding is highly relevant when it comes to characterizing on-chip or packaged components. As the measurement reference plane in on-wafer RF and microwave characterization typically does not coincide with the reference plane of the device under test (DUT), it becomes essential to employ de-embedding techniques. These methods mathematically shift the measurement reference plane to the DUT, enabling the extraction of the device's true electrical properties by removing the influence of parasitic effects and system imperfections.

In this manuscript, several de-embedding methods are presented with consideration for Ground-Signal-Ground (GSG) topology. The GSG configuration is common in high-frequency testing setups and is particularly susceptible to parasitic effects arising from contact pads and interconnections. By applying de-embedding techniques tailored for GSG topology, it is possible to achieve more accurate characterization results, ensuring that the measurements reflect the intrinsic behavior of the on-chip or packaged components rather than artifacts introduced by the measurement environment.

1.6.1. Open-Short (OS) De-embedding

The OS de-embedding supposes the raw and actual values indexed by the letters R_{DUT} and A_{DUT} respectively. It is based on the equivalent circuit model, which considers parasitic effects such as metallic interconnection and coupling, represented by impedances and admittances (Fig. 1.35).

The term z_{series} is the series impedance modeling metallic effect, which can be associated with a specific resistance R and inductance L. The connection between signal and ground leads some parasitic shunt capacitances and shunt resistance, represented by y_{shunt} and z_{shunt}, the coupling capacitance is the partition of port-to-port impact is [25].

The OS method needs only two structures: an Open structure, which is symbolic to the test structure when the DUT is removed and a Short structure for directly connecting signal to ground (Fig. 1.36).

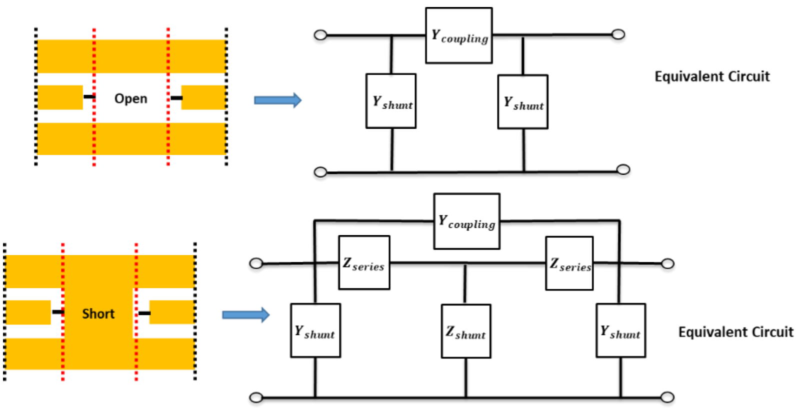

Fig. 1.36: Test structures on left (Open - Short) | Equivalent circuits on right.

The Open device can be electrically modeled as a pi-network. This network comprises two shunt capacitances, which arise from the separation between signal and ground, and a port-to-port capacitance or coupling admittance. Typically, the port-to-port capacitance is considered to have a negligible impact and is sometimes omitted from calculations due to its minimal contribution.

In contrast, the Short artefact builds upon the Open device model by incorporating additional components. Specifically, it includes both series and parallel resistances, which account for the metallic effects of the signal conductor and the resistive (ohmic) contact between the signal and ground.

Two-port networks such as these can be represented using several mathematical matrices, including the S-matrix, T-matrix, ABCD-matrix, Z-matrix, and Y-matrix, among others. Appendix 5 contains a comprehensive table detailing the conversion between these matrix representations, facilitating analysis and interpretation.

The use of these matrices is essential for implementing the Open-Short (OS) de-embedding technique. The process begins by subtracting the admittance of the Open device ($\boldsymbol{Y_{Open}}$) from the measured or raw admittance ($\boldsymbol{Y_R}$) of the device under test (DUT). This initial step is mathematically expressed by relationship (E.1.60).

$$\boldsymbol{Y_{RO}} = \boldsymbol{Y_R} - \boldsymbol{Y_{Open}} \tag{E.1.60}$$

Then the same operation is performed by extracting the Open device admittance $\boldsymbol{Y_{Open}}$ from the Short device admittance $\boldsymbol{Y_{Short}}$ as follows.

$$\boldsymbol{Y_{SO}} = \boldsymbol{Y_{Short}} - \boldsymbol{Y_{Open}} \tag{E.1.61}$$

The two resulting admittance matrices $\boldsymbol{Y_{RO}}$ and $\boldsymbol{Y_{SO}}$ must be converted to impedance matrices $\boldsymbol{Z_{RO}}$ and $\boldsymbol{Z_{SO}}$. These last ones enable finally to get the actual impedance matrix $\boldsymbol{Z_{DUT}}$ of the DUT by subtracting one from another. This is literally given by relationship (E.1.62).

$$\boldsymbol{Z_{DUT}} = \boldsymbol{Z_{RO}} - \boldsymbol{Z_{SO}} \tag{E.1.62}$$

The true S-matrix ($\boldsymbol{S_{DUT}}$) of the DUT is obtained by transforming his corresponding Z-matrix ($\boldsymbol{Z_{DUT}}$).

1.6.2. Open-Short-Thru (OST) De-embedding

The Open-Short-Thru technique [26-27] integrates the principles of the Open-Short method by accounting for both lumped elements and distributed elements. This approach specifically incorporates sections of transmission line, as depicted in Fig. 1.37. By considering lumped components such as series and parallel resistances, as well as distributed transmission line segments, the OST method enables a more comprehensive de-embedding process that accurately reflects both the localized and distributed effects present in high-frequency device measurements.

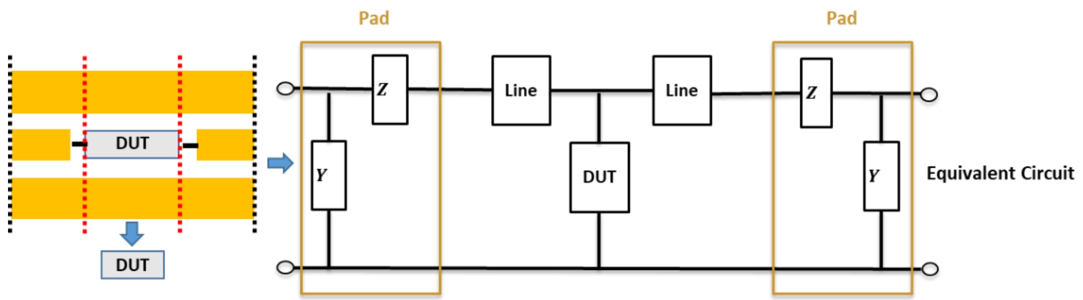

Fig. 1.37: Equivalent circuit model with OST de-embedding.

The located elements, including series impedance and shunt admittance, are used to describe the effects of the pads on the left and right sides of the device under test (DUT). These elements specifically account for the localized electrical characteristics introduced by the pads, which can influence the overall measurement accuracy if not properly considered.

In addition to the pad effects, the characteristic impedance (Zc), propagation constant (γ), and line length (l) are used to represent the electrical properties of the transmission line sections present in the measurement setup. These parameters are critical for capturing the distributed effects of the transmission lines that connect the DUT to the measurement system.

For the Open-Short-Thru (OST) de-embedding method, it is advantageous to utilize the cascade network formalism. This approach involves representing the system using ABCD (or T) matrices, which are well-suited for describing cascaded two-port networks such as those encountered in high-frequency measurements. By employing ABCD matrices, the complex interactions between pads, transmission lines, and the DUT can be systematically accounted for.

Using this formalism, the raw measured response of the DUT, denoted as $\boldsymbol{R_{DUT}}$, can be effectively expressed in terms of the cascade of its constituent network elements through the multiplication of their respective ABCD matrices.

$$\boldsymbol{R_{DUT}} = \boldsymbol{Pad_L} \,.\, \boldsymbol{T_{l1}} \,.\, \boldsymbol{A_{DUT}} \,.\, \boldsymbol{T_{l2}} \,.\, \boldsymbol{Pad_R} \tag{E.1.63}$$

Where $\boldsymbol{Pad_L}$ and $\boldsymbol{Pad_R}$ are ABCD matrices of pads on left and right. $\boldsymbol{T_{l1}}$ and $\boldsymbol{T_{l2}}$ are ABCD matrices of sections of lines. $\boldsymbol{A_{DUT}}$ is actual response of the DUT. The relationship (E.1.64) gives the pads matrices.

$$\boldsymbol{Pad_L} = \begin{bmatrix} 1 & z \\ y & 1 + z.y \end{bmatrix} \; ; \; \boldsymbol{Pad_R} = \begin{bmatrix} 1 + z.y & z \\ y & 1 \end{bmatrix} \tag{E.1.64}$$

The thru structure corresponds to the direct connection of pads via the line section. His measured and actual values are formulated respectively as:

$$\boldsymbol{R_{Thru}} = \boldsymbol{Pad_L} \,.\, \boldsymbol{T_l} \,.\, \boldsymbol{Pad_R} \tag{E.1.65}$$

$$\boldsymbol{T_l} = \begin{bmatrix} \cosh(\gamma l) & Zc.\sinh(\gamma l) \\ \frac{1}{Zc}.\sinh(\gamma l) & \cosh(\gamma l) \end{bmatrix} \tag{E.1.66}$$

The pads effects z and y (impedance – admittance) are extracted using the Open and Short structures. y is the sum of the elements (1,1, :) and (1,2, :) of the measured Open admittance matrix. z is the difference of the elements (1,1, :) and (1,2, :) of the measured Open impedance matrix Z_{SO} obtained by inverting the previous admittance matrix Y_{SO} resulting of difference between the Short and Open

$$y = Y^{11}{}_{Open} + Y^{12}{}_{Open} \; ; \; z = Z^{11}{}_{SO} - Z^{12}{}_{SO} \tag{E.1.67}$$

The short and open data are used to determine the actual ACBD matrix Thru structure via equation (E.1.46), and then to calculate line characteristics such as Zc and γ. Now one has all that is needed to extract the true or actual ABCD matrix of the DUT by inverting relation (E.1.44).

1.6.3. Thru (T) De-embedding

The Thru de-embedding method [28] is recognized as the simplest de-embedding approach, relying on a single, unique test structure. In this method, the contributions of the measurement pads are modeled as lumped elements. Specifically, these lumped elements account for the metal signal's series resistance and the shunt capacitance that exists between the signal and ground. This representation can be visualized in the equivalent circuit diagram (see Fig. 1.38).

The mathematical modeling of this technique is captured by the following relationship, which describes how the measured response incorporates the pad effects:

$$\boldsymbol{R_{DUT}} = \boldsymbol{Pad_L} \,.\, \boldsymbol{T_{DUT}} \,.\, \boldsymbol{Pad_R} \tag{E.1.68}$$

Where $\boldsymbol{R_{DUT}}$ and $\boldsymbol{T_{DUT}}$ are respectively raw measurement and actual response of device under test.

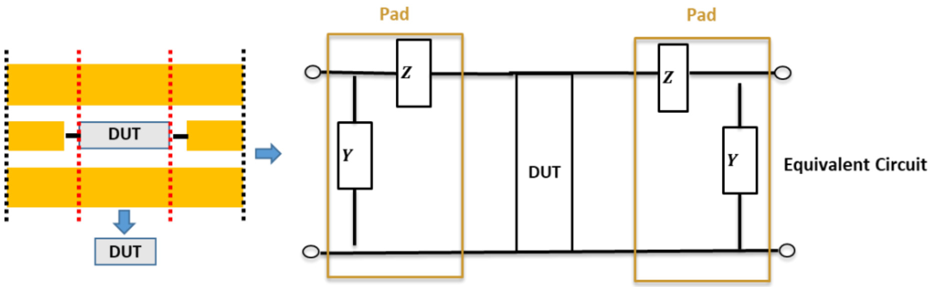

Fig. 1.38: Equivalent circuit model with Thru de-embedding.

The Thru device corresponds to the cascade of two pads (left L / right R). In this case, it is easier to deal with T-matrix concept. The equation (E.1.69) expresses the exact relationship for his measurement.

$$\boldsymbol{R_{Thru}} = \boldsymbol{Pad_L} \, . \, \boldsymbol{Pad_R} \tag{E.1.69}$$

This means that pads effects are included in the Thru measurement. The admittance matrices $\boldsymbol{Y_L}$ and $\boldsymbol{Y_R}$ obtained from elements of Thru Y-matrix (Y_{Thru}) represent these pads impacts.

$$\boldsymbol{Y_L} = \begin{bmatrix} Y^{11}{}_{Thru} - Y^{21}{}_{Thru} & 2.Y^{21}{}_{Thru} \\ 2.Y^{21}{}_{Thru} & -2.Y^{21}{}_{Thru} \end{bmatrix} \; ; \; \boldsymbol{Y_R} = \begin{bmatrix} -2.Y^{12}{}_{Thru} & 2.Y^{12}{}_{Thru} \\ 2.Y^{12}{}_{Thru} & Y^{22}{}_{Thru} - Y^{12}{}_{Thru} \end{bmatrix} \tag{E.1.70}$$

Once these matrices have been converted to the T-matrix defined by Pad_L and Pad_R, all that remains is to invert expression (E.1.68) to achieve the de-embedding result of the DUT.

There are several de-embedding techniques, which one has covered here. Although their approaches differ in terms of test structures and mathematics, their objective is similar, i.e. to get rid of the effects that move the component measurement away from its true response.

2. On-wafer high impedance measurements

S-parameter measurement techniques can be broadly classified based on the type of measurement system employed. The two primary categories are conventional and interferometric techniques.

In the fields of RF and Microwave engineering, these techniques are further distinguished by the reference impedance used during measurement. There are systems designed for 50Ω measurements, which are suitable for components with traditional impedances close to 50 Ω. Alternatively, there are measurement systems that cater to non-50 Ω scenarios, allowing for accurate assessment of components with extreme impedances, that is, those far from the standard 50 Ω reference.

2.1. Measurement with conventional system

Conventional techniques focus on the measurement of S-parameters for nano-devices that are integrated into test structures coplanar with both the measurement system and traditional methods. These techniques are not limited to coplanar configurations and can also be applied to various types of coaxial or waveguide components. The distinguishing feature of these methods is the use of a reference impedance, which is commonly set at 50 Ω.

It has been shown that high-impedance devices can be characterized effectively using a measurement system designed for a 50 Ω reference impedance. For example, the National Institute of Standards and Technology (NIST) conducted a study that involved the broadband characterization of a platinum nanowire (Pt NW), demonstrating the applicability of conventional systems for such measurements [30] (Fig. 1.39).

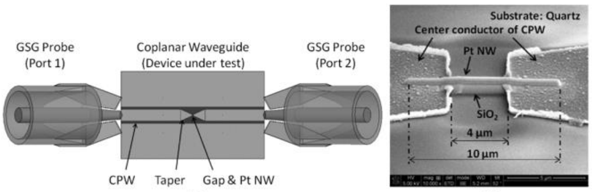

(a) (b)

Fig. 1.39: Drawing of a CPW based measurement setup (a) and SEM of 250 nm [30].

This study demonstrated that the conductivity and contact resistance of nanowires can be determined by examining the diameter of the wire. Measurements and simulations of S-parameters provide a range of values for these electrical properties, as shown in Fig. 1.40. The results highlight how variations in wire diameter influence both conductivity and contact resistance, offering valuable insight into the performance of nanowires in high-frequency on-wafer measurement applications.

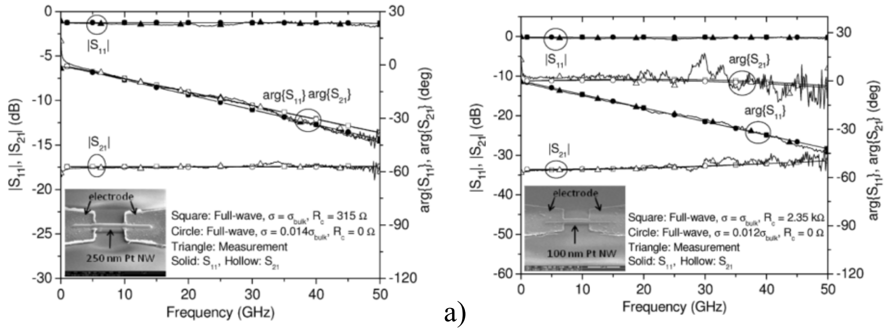

a) b)

Fig. 1.40: Measured and simulated S-parameters. Inset: SEM of measured device with Pt NW a) S11 for the device with the 250 nm – b) S21 for the device with the 100 nm diameter Pt NW [30].

In parallel with other research efforts, the IMEP-LAHC laboratory has conducted significant work on the broadband characterization of aluminum (Al) nanowires intended for metal-level interconnection in CMOS structures. Their methodology utilizes a conventional measurement system comprising the ANRITSU ME7808C Broadband Vector Network Analyzer and a semi-automatic Cascade S300 station. By employing coplanar waveguide (CPW) test structures that incorporate nanowires of varying lengths, the laboratory can assess the electrical properties and performance of these nanowires in detail. As illustrated in Fig. 1.41, this approach enables comprehensive analysis of the behavior of aluminum nanowires under high-frequency conditions, which is essential for advancing interconnect technologies in CMOS applications.

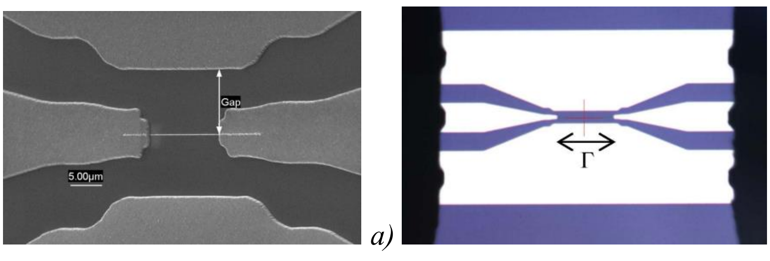

a) *b)*

Fig. 1.41: a) SEM image of an Al NW embedded in a CPW structure. b) Complete CPW structure compatible with GSG probing [31].

Experimental results, such as those presented in Fig. 1.42, demonstrate that nanowires function as high-impedance structures, leading to notable attenuation in the measured signals [31]. This attenuation is a significant factor to consider in the design and evaluation of nanowire-based devices for high-frequency applications.

When selecting the appropriate nanowire length for testing, it is important to strike a balance. The nanowire should be sufficiently long to ensure its contribution to the radiofrequency (RF) response is both clear and distinguishable. However, if the nanowire is excessively long, it may result in distorted transmission characteristics, primarily due to the increased influence of surface defects and imperfections. Therefore, optimizing the nanowire length is crucial in obtaining accurate and reliable measurements of their electrical properties and ensuring the integrity of high-frequency signals in practical applications.

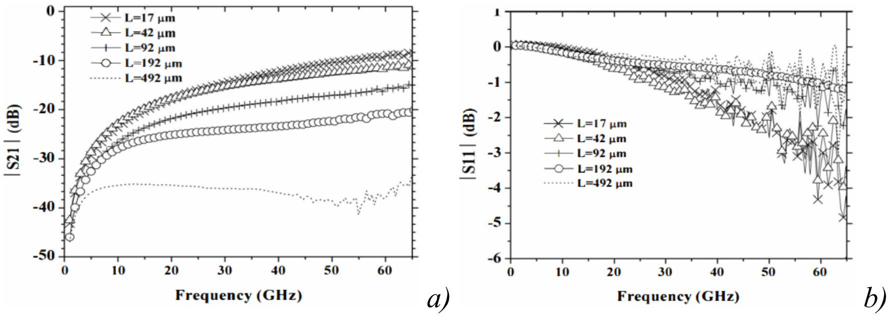

Fig. 1.42: a) Magnitude of measured S21 from CPW devices. b) Magnitude of measured S11 from CPW devices [31].

The observed results can be attributed primarily to the effects of surface roughness and grain boundaries within the nanowires. As previously demonstrated in reference [32], electrical resistivity exhibits an increase as the width of the wire decreases. This phenomenon is especially significant at the nanoscale, where the high surface-to-volume ratio intensifies the impact of imperfections and grain boundaries on the transport properties of electrons. Consequently, shorter nanowires are generally favored for use in interconnect applications, as they help to minimize the detrimental effects associated with elevated resistivity.

The Advanced Technology Institute has undertaken a detailed broadband characterization of carbon nanotubes by incorporating a single-walled carbon nanotube (SWCNT) into a coplanar test structure, as depicted in Fig. 1.43. This experimental setup utilizes the VNA HP 4753E system to evaluate the electrical properties of the SWCNT within the structure, providing valuable insights into the behavior of carbon nanotubes under high-frequency conditions [33].

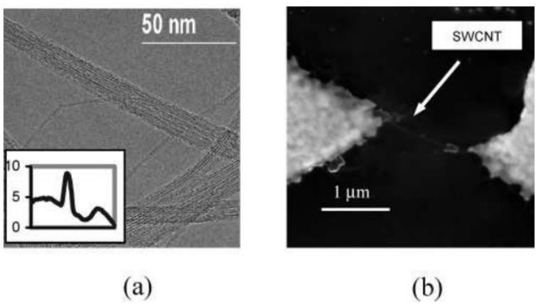

Fig. 1.43: (a) High-resolution electronic microscopy of SWCNT used in this experiment. The inset in (a) shows a cross-sectional AFM scan of the height distribution in nm. (b) SEM micrograph of a single-walled carbon nanotube rope between metal electrodes [33].

The broadband characterization of the single-walled carbon nanotube (SWCNT) test structure reveals notable transmission losses across the frequency range of interest. Specifically, as shown in Fig. 1.44, the measured S-parameters indicate that the sample exhibits a relatively high transmission loss, with values consistently ranging between -28 dB and -24 dB throughout the entire 0–6 GHz spectrum. This significant attenuation underscores the high-impedance nature of the SWCNT and highlights the challenges associated with efficient signal transmission in such nanostructures under high-frequency conditions. The observed losses must be carefully considered when evaluating the suitability of carbon nanotubes for use in advanced nanoscale interconnects and other high-frequency electronic applications.

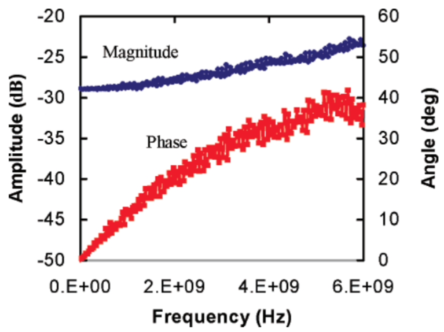

Fig. 1.44: Measured S-parameter of SWCNT; plot in dB of transmitted power vs frequency [33].

Coplanar test structures incorporating integrated nano-resistors have been systematically investigated to evaluate their performance in high-impedance broadband measurement applications (see Fig. 1.45) [34]. In a study conducted at the IEMN Institute, resistive nanowire-based test components were embedded within coplanar waveguide (CPW) structures. The nanowires utilized in these experiments exhibited conductance values ranging from 100 to 500 µS, while the associated capacitance values were on the order of several hundred attofarads (aF). This approach allowed for detailed analysis of the electrical response of nanowire-integrated CPW structures under broadband conditions, providing important insights into the behavior of high-impedance nanoscale devices and their suitability for advanced high-frequency applications.

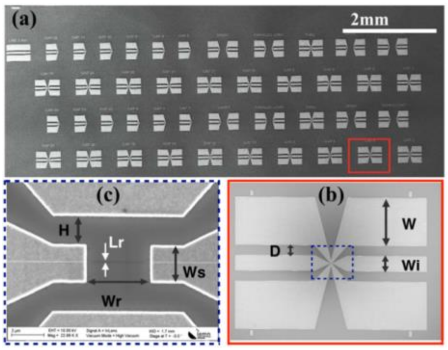

Fig. 1.45: Scanning electron microscopy (SEM) images of (a) the general view of the wafer, (b) the zoomed view of 4µm gap with the CPW accesses and (c) magnified view of the 4µm gap with integrated nano-resistance [34].

The reflection and transmission characteristics of nanowires positioned across the *Wr* gap, which varies from 4 µm to 20 µm, have been systematically examined to assess their impact on device performance. For reflection measurements, it is observed that the amplitude decreases as the gap narrows; specifically, the reflection amplitude drops from -0.1 dB at larger gaps to -0.4 dB at smaller gaps. This reduction in amplitude suggests improved impedance matching as the gap size decreases. Notably, the phase of the reflection coefficient demonstrates minimal sensitivity to changes in gap size, indicating that phase behavior remains relatively stable across the measured range.

In terms of transmission, the amplitude displays a marked increase as the gap decreases, rising from -40 dB to -25 dB. This trend signifies enhanced signal transmission through the nanowire as the gap narrows. Additionally, the phase of the transmission coefficient shows a corresponding decrease, shifting from 30° to 55° over the range of gap sizes analyzed. These results, illustrated in Fig. 1.46, provide important insights into the influence of gap dimensions on both the reflection and transmission properties of nanowire-integrated coplanar waveguide (CPW) structures.

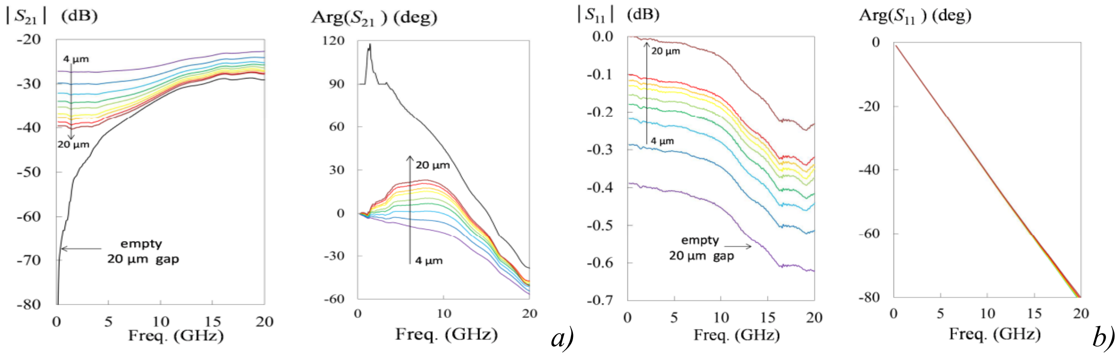

Fig. 1.46: Measured magnitude and phase of S-parameters for CPW structures with integrated nano-resistances in gaps varying from 4µm to 20µm – a) S21, b) S11 [34].

A consistent theme emerging from the studies cited in this section is the inherently high-impedance nature of nanodevices. These devices are characterized by low transmission coefficients, meaning that only a small portion of the input signal is transmitted through them. Conversely, they exhibit high reflection coefficients, indicating that a significant fraction of the signal is reflected rather than transmitted. Such characteristics are typical of nanoscale structures and have important implications for their performance in electronic applications.

Furthermore, measurements involving these high impedance nanodevices are often accompanied by increased noise levels. This observation raises concerns regarding the sensitivity of the measurement systems employed, particularly when using vector network analyzers. The reliability and accuracy of the data obtained are heavily dependent on the capability of the measurement system to distinguish true signal responses from noise.

The study presented in reference [35] specifically examines how the impedance range of the component under test affects the sensitivity of the VNA. It is shown that as the load impedance deviates substantially from the nominal 50 Ω value effectively when the modulus of the reflection coefficient approaches one the measurement is increasingly affected by noise. This relationship is depicted in Fig. 1.47, which demonstrates the heightened noise levels encountered when the impedance is either much higher or much lower than 50 Ω.

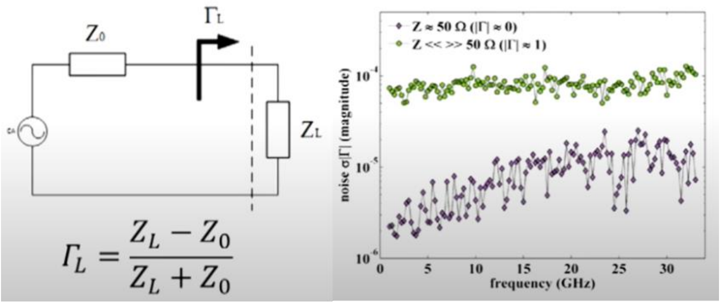

Fig. 1.47: Load connected to VNA port (left), Noise depending on component impedance range (right) [35].

Fig. 1.48 presents a comparison of three distinct impedance ranges low, classic (medium), and high that a component may exhibit when measured using a vector network analyzer. This illustration highlights a critical limitation inherent to VNAs: the sensitivity of the measurement system is significantly diminished when dealing with components whose impedances deviate substantially from the nominal value, specifically in the cases of extremely high or low impedance devices. As the component impedance moves toward these extremes, the VNA ability to accurately resolve the reflection coefficient is reduced, resulting in less precise measurements for such components.

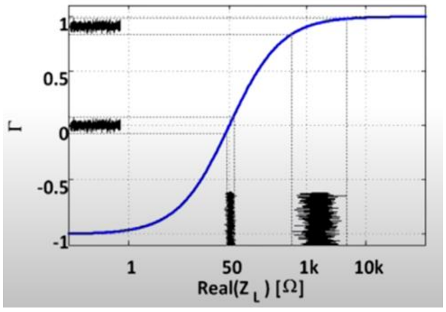

Fig. 1.48: Reflection coefficient according to impedance range [35].

To address the challenge of insufficient sensitivity in measuring components with extreme impedances using a vector network analyzer, an interferometer can be incorporated into the measurement system. This addition serves to improve the accuracy and reliability of measurements for high-impedance or highly reflective devices.

There are two types of interferometric modules that can be utilized for this purpose: passive and active. Both configurations share the common objective of enhancing measurement sensitivity. The passive module typically employs a power divider, while the active module uses a coupler combined with an external power source. By introducing either module to the VNA setup, the reflected power from components with extreme impedance values can be more effectively attenuated or manipulated, resulting in a more sensitive and compliant measurement range.

2.2. Measurement with interferometric system

When measuring various highly reflective components using a classical measurement system, such as a standard vector network analyzer, it is often challenging to obtain sufficient information to distinguish between different components. This is because their responses tend to mimic either open or short circuits, making it difficult to accurately characterize them based solely on conventional reflection measurements.

Given this limitation, enhancing the sensitivity of the measurement system becomes crucial. One effective approach is to incorporate an interferometric module into the setup. As depicted in Fig. 1.49, the integration of an interferometric module either passive or active can significantly improve the system's ability to resolve differences between highly reflective components. By introducing such a module, the measurement system becomes more capable of detecting subtle variations in reflection, thereby providing a more informative and accurate characterization of components with extreme impedance values.

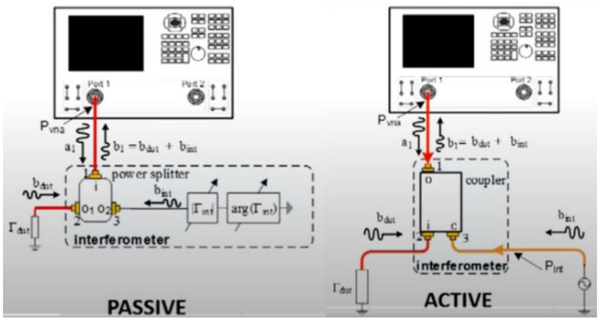

Fig. 1.49: VNA with interferometric module: passive (left) and active (right) [35].

To improve measurement sensitivity when characterizing components with extreme impedance values, interferometric modules can be integrated into the vector network analyzer setup. These modules are available in two forms: passive and active. The passive module employs a power divider, while the active module utilizes a coupler in conjunction with an external power source. The core concept behind both configurations is to generate an internal power wave, referred to as b-int, which serves to attenuate the power wave reflected by the highly reflective or extreme impedance component under test, as illustrated in Fig. 1.49. This approach enables the measurement system to more effectively manage reflected signals from components with impedances that significantly deviate from the nominal value, thereby extending the sensitive and compliant measurement range of the VNA.

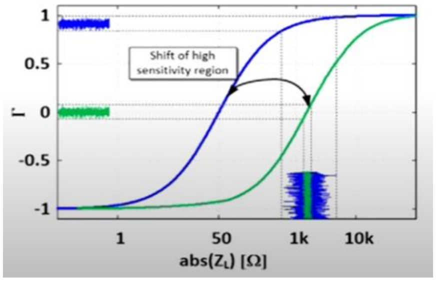

Fig. 1.50: Reflection coefficient before (blue) and after (green) integration of the interferometric module [35].

As illustrated in Fig. 1.50, the integration of an interferometric module into the measurement system has a significant impact when characterizing high-impedance components, such as those around 1 kΩ. The interferometer effectively shifts the conventional sensitivity range, enabling the measurement system to operate within a compliant and more accurate range for these components. This improvement addresses the inherent limitations of standard vector network analyzers when measuring devices with extreme impedance values, resulting in enhanced measurement precision for high-impedance devices.

In response to the ongoing challenges associated with impedance measurement and device scaling, a team from IEMN conducted a comprehensive study and introduced an innovative solution. They proposed the use of a Wheatstone bridge structure with a high impedance, specifically ranging from 700 Ω to 3.5 kΩ. This bridge is fabricated using advanced micro-technology processes, allowing for the direct integration of a carbon nanotube with the measurement system. To ensure measurement accuracy, the device undergoes a calibration process utilizing three distinct kits: a balanced impedance bridge (Zc), an open circuit (O), and a short circuit (S) configuration. This approach enables precise characterization and calibration of high impedance nanodevices within the measurement setup [36].

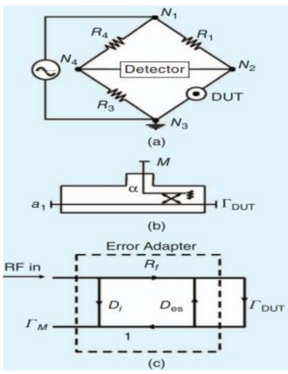

$$\Gamma_M = D_i + \frac{R_f\,\Gamma_{DUT}}{1 - D_{es}\,\Gamma_{DUT}}$$

Fig 1.51: (a) A schematic of the Wheatstone bridge structure. (b) A schematic of the directional coupler. (c) A flow graph of the Wheatstone bridge for the determination of Γ_M [36].

The sensitivity of radiofrequency (RF) measurements can be significantly improved by incorporating a high impedance nanodevice into a specifically designed structure. One effective approach involves utilizing a Wheatstone bridge configuration, as depicted in Fig. 1.51. This method is particularly advantageous in minimizing the impedance mismatch between the vector network analyzer and the device under test (DUT), which is often a source of measurement inaccuracies when dealing with high-impedance components.

In this setup, the Wheatstone bridge is constructed with a resistance value typically ranging from 700 Ω to 3 kΩ. The choice of resistance within this range is critical, as it serves to reduce the impedance mismatch between the VNA and the high impedance nanodevice being characterized. By optimizing the bridge resistance to better match the DUT, the measurement error is effectively minimized, resulting in more accurate and reliable characterization of high impedance nanodevices.

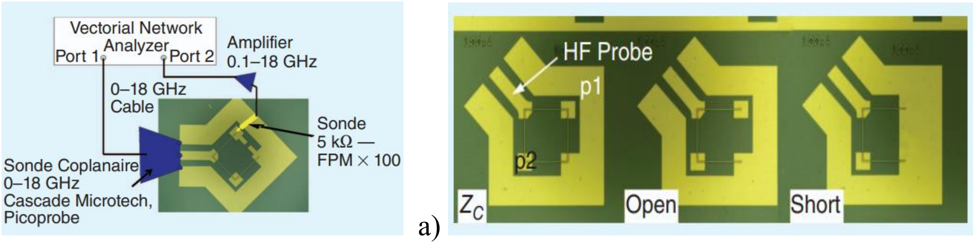

Fig. 1.52: a) The fabricated Wheatstone bridge structure for nanodevices characterization – b) Calibration kits used: Equilibrated bridge (Zc), open (CO), short (CC) [36].

To ensure precise measurements of nanodevices with high impedance, the system undergoes calibration using three distinct structures, each fabricated on the same wafer as the nanodevice under test. As shown in Fig. 1.52, these structures consist of Wheatstone bridges incorporating a short circuit (CC), an open circuit (CO), and a calibrated resistance (Zc). This approach allows for the appropriate calibration of the measurement setup, directly addressing potential sources of error and enhancing the reliability of the results.

Utilizing this calibration setup, accurate impedance measurements can be achieved for values as high as 11 kΩ. For instance, a Wheatstone bridge with a resistance of 3.5 kΩ enables the effective characterization of a single carbon nanotube, demonstrating the system's capability in handling high impedance nanodevices with improved measurement precision [37].

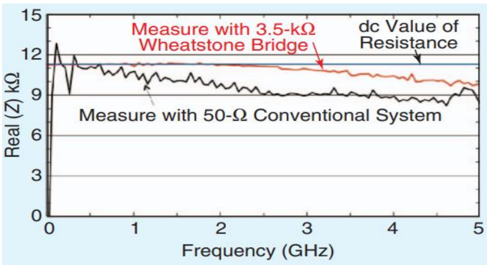

(a)

Frequency (GHz)	0–0.5	0.5–2	2–3.5	3.5–5
VNA 50 Ω (%)	<30	<15	<20	<30
Wheatstone Bridge (%)	<1	<1	<5	<15

(b)

Fig 1.53: The validation of calibration kit by measuring a 11.2-kΩ resistance: (a) comparison of measurement between conventional system and the method proposed; (b) comparison of measurement error in the whole frequency bandwidth [37].

The performance of the measurement system utilizing the Wheatstone bridge configuration was evaluated by comparing its results to those obtained from a conventional measurement system. The findings revealed that the Wheatstone bridge-based system achieved an accuracy better than 5% when compared to the dc value. This level of precision demonstrates a significant improvement over traditional methods, particularly in the context of high impedance measurements. The results, as shown in Fig. 1.53, confirm the effectiveness of the proposed approach in enhancing measurement accuracy for high impedance nanodevices.

A new method enables direct impedance measurement in microwave and millimeter-wave frequencies, offering substantial improvements over traditional techniques. Unlike traditional techniques that require the determination of impedance or admittance from the reflection coefficient, a process that can lead to accuracy issues, especially when measuring components with very high or very low impedance this method establishes a direct proportional relationship to the impedance of the device under test (DUT).

The system is specifically designed with its own calibration procedure to ensure measurement precision. The measurement setup utilizes two 90° hybrid couplers and two power splitters, although the configuration can also be implemented using two 180° hybrid couplers. This versatile design enables accurate direct impedance measurements across a wide range of frequencies without the limitations imposed by conventional reflection-based analysis [38, 39, 40].

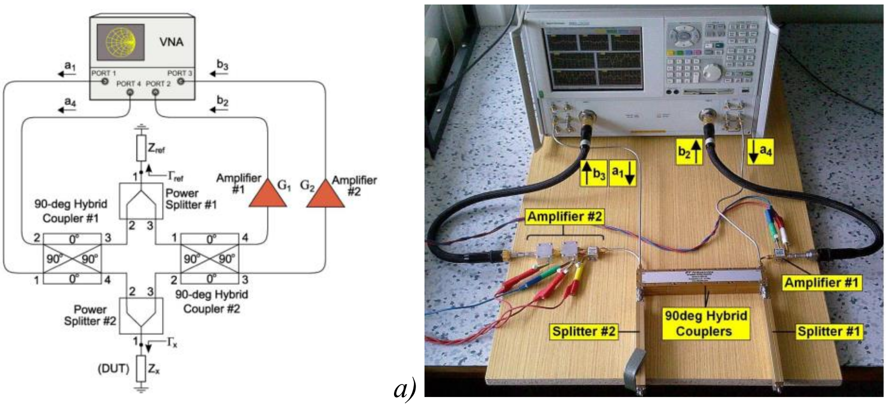

a) b)

Fig. 1.54: a) Idealized arrangement of the measurement system – b) Experimental setup of the measurement system using a two-port VNA with a configurable test set [38].

The measurement system operates by analyzing both the source and received waves within the setup, specifically considering source waves a1 and a4, and received waves b2 and b3, as depicted in Fig. 1.54. In this arrangement, the reflection coefficient Γ_{ref} represents the reference reflection coefficient associated with the reference impedance Z_{ref}, while Γ_x denotes the reflection coefficient corresponding to the input impedance Z_x of the device under test (DUT). Additionally, the system incorporates two amplifiers, with G1 and G2 indicating the voltage gains of amplifier #1 and amplifier #2, respectively.

Four distinct experimental setups have been implemented, each utilizing two reference components: open and short, as illustrated in Fig. 1.55. The configuration of the measurement system for the experiments corresponds to setup A. In this configuration, amplifier #1 operates at a low gain (G1 ≈ 10 dB), while amplifier #2 functions at a high gain (G2 ≈ 10 dB). The reference impedance in this scenario is nearly open, which makes the system particularly well-suited for measuring high impedances when the source port is assigned to port 1 of the vector network analyzer.

Conversely, for the measurement of low impedances, the system utilizes port 4 of the VNA as the source port. This flexible arrangement allows the setup to efficiently handle both high and low impedance measurements by selecting the appropriate source port and amplifier gain settings based on the desired measurement regime.

Setup	G_1	G_2	Γ_{ref}	Source Port	Z_x
A	Low	High	Open	1	High
				4	Low
B	Low	High	Short	1	Low
				4	High
C	High	Low	Open	1	Low
				4	High
D	High	Low	Short	1	High
				4	Low

Fig. 1.55: Operating regimes for measurement of low and high impedances [38].

A specialized technique has been proposed for near-field microscopy and the measurement of high-impedance components [42]. This innovative method integrates several key components to achieve precise measurements, particularly in challenging scenarios involving high impedance devices.

The measurement system is constructed around a vector network analyzer, which serves as the core instrument for characterizing the electrical properties of the device under test. A microwave probe is employed to facilitate the interaction between the VNA and the sample, allowing for localized measurements at microwave frequencies.

Central to the methodology is the inclusion of an interferometer within the measurement setup. The interferometer itself is comprised of a power divider, a phase shifter, and an attenuator, which together enable fine control of the measurement signals and enhance the accuracy of the impedance determination. The configuration of these elements is illustrated in Fig. 1.56.

By combining these components, the system can perform near-field microscopy while simultaneously enabling high-impedance measurements with improved precision and reliability.

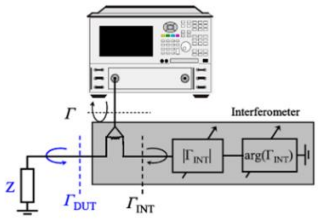

Fig. 1.56: Measurement system [41].

The concept underlying the measurement approach is the compensation of the reflection coefficient of the device under test (DUT) by using the interferometric reflection coefficient. This method involves adjusting the interferometric system so that its reflection coefficient counterbalances that of the DUT, as illustrated in Fig. 1.57. By achieving such compensation, the measurement system can accurately characterize the DUT electrical properties, particularly in scenarios requiring high precision. This technique is integral to the interferometric measurement principle and enhances the reliability of impedance measurements within the experimental setup.

$$\Gamma = \frac{1}{2}(\Gamma_{INT} + \Gamma_{DUT}) = 0 \quad \text{(E.1.71)}$$

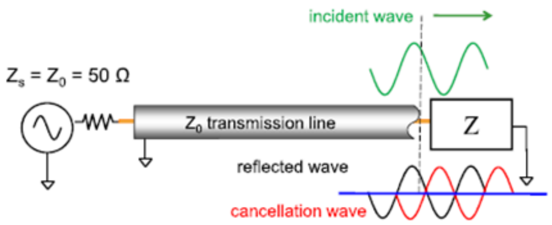

Fig. 1.57: Interferometric measurement principle [41].

A comprehensive investigation into extreme broadband impedance measurements was conducted using a multi-state reflectometer. This method enabled repeated and reliable measurements when characterizing high-impedance components, as referenced in [43]. The measurement system was specifically designed to incorporate both a power divider and a reference impedance device. These reference devices could be either mechanical or electronic in nature, thereby providing flexibility and adaptability depending on the experimental requirements. The overall configuration is depicted in Fig. 1.58.

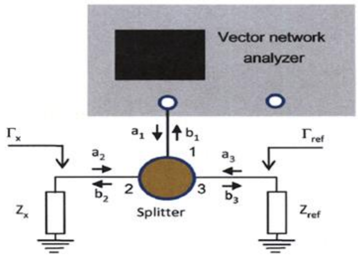

Fig. 1.58: Extreme impedance measurement system [43]

In the measurement system utilizing a multi-state reflectometer, the vector network analyzer is responsible for measuring the reflection coefficient at the port of the divider, denoted as Γm. This measurement is not isolated; rather, it is expressed as a function of two key parameters: the reflection coefficient of the reference device (Γ_{ref}) and the reflection coefficient of the component under test (Γ_x). By relating Γ_m to both Γ_{ref} and Γ_x, the system enables accurate characterization of the device under test, leveraging the known response of the reference to enhance measurement reliability and precision.

$$\Gamma_m = \frac{1}{2}(\Gamma_{ref} + \Gamma_x) \qquad \text{(E.1.72)}$$

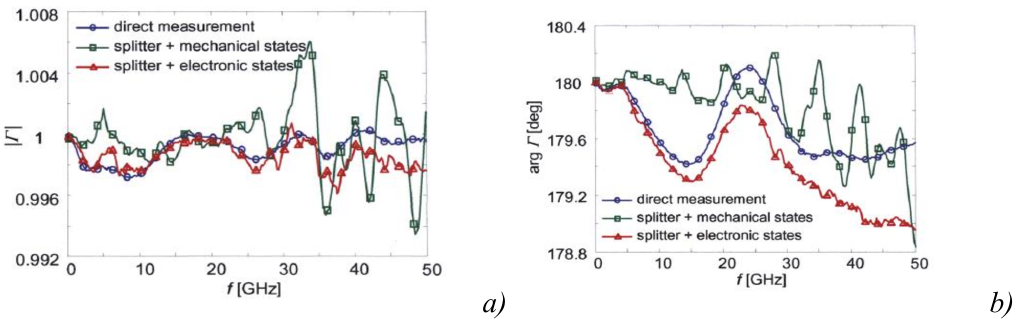

Fig. 1.59: Reflection coefficient of a short circuit - a) amplitude, b) phase [43]

The effectiveness of the described measurement approach was validated using a short-circuited component as the device under test. Experimental results demonstrated strong consistency between the measured and expected values for the electronic reference device, with only a 0.2% deviation observed in amplitude and a 0.6° deviation in phase. This high level of agreement indicates that the interferometric system provides precise measurements when evaluating electronic devices.

For the mechanical reference device, the measurements revealed a slightly higher discrepancy—specifically, a 1% deviation in amplitude and the same 0.6° deviation in phase. Although this represents a minor disparity compared to the electronic device, the results still affirm the reliability and robustness of the measurement setup for both electronic and mechanical reference standards. The corresponding results are illustrated in Fig. 1.59.

In addition to the previously described methods, additional studies have explored extreme impedance measurements utilizing interferometric techniques. The underlying principle across these approaches remains largely consistent. Whether the interferometric setup incorporates a power divider, as discussed in the earlier section, or utilizes configurations such as a hybrid divider and coupler, the measurement concept is fundamentally analogous. These variations in device integration, whether through the selection of a power divider or hybrid components, maintain the same basic approach for characterizing extreme impedance scenarios [5, 6].

3. On-wafer probe stations

On-wafer probe stations are highly precise instruments designed for the electrical testing and characterization of semiconductor devices directly on the chip or wafer. These instruments are essential tools in research, development, and production environments where direct access to the device under test is required.

Physically, the probe stations serve as the mechanical foundation within the measurement setup. They are used alongside Vector Network Analyzers, providing a stable and adaptable platform for positioning and manipulating coplanar probes during measurements. The robust mechanical design of the probe station ensures accurate alignment and contact with the device under test, which is critical for obtaining reliable measurement results.

Signal transmission from the measurement source to the on-wafer probes is achieved through the use of coaxial cables or rectangular waveguides. These transmission lines connect the ports of the VNA directly to the probe connectors, ensuring minimal signal loss and high fidelity in measurements. The integration of these components allows for efficient and repeatable electrical testing of semiconductor devices in various experimental setups [24].

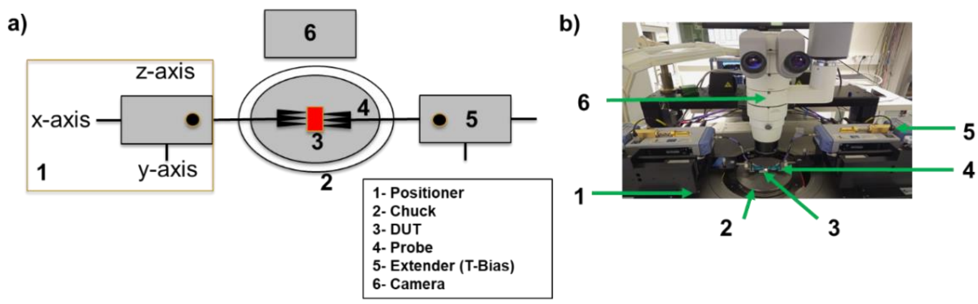

Fig. 1.60: a) Top view, (b) Probe station and building blocks.

In the block, there is the chuck, a planar metallic support positioned at the center of the station. The chuck serves a critical role in facilitating the accurate positioning and probing of the device under test (DUT) or substrates used for calibration, as depicted in Fig. 1.60. To securely hold the device in place during measurements, the chuck is equipped with a vacuum pump. This vacuum system operates by drawing air through small holes distributed across the chuck surface, effectively fixing the DUT or substrate in position.

The chuck's position can be precisely controlled along the x, y, and z axes by means of an integrated positioner. This allows for fine adjustments in all three spatial dimensions, ensuring exact alignment of the DUT under probe tips. Depending on the frequency range and the specific measurement requirements, the system can be further enhanced through the integration of millimetric heads or extenders, enabling measurements across a broader frequency spectrum.

A wide range of probe types is available to accommodate various excitation signals, from direct current (DC) up to millimeter wave frequencies. The selection of probe type also depends on the configuration of the probe tip and the style of the probe body. Each probe is fitted with a coaxial cable that connects it to the measurement instrumentation, attached via the probe's connector.

Inside the probe body, a precision coaxial cable establishes the electrical path between the radio frequency (RF) connector and the probe tip. To enhance measurement quality, absorber materials are strategically placed in different regions within the probe. These absorbers function to suppress unwanted electromagnetic mode propagation, as illustrated in Fig. 1.61, thereby improving the accuracy and reliability of the measurement results.

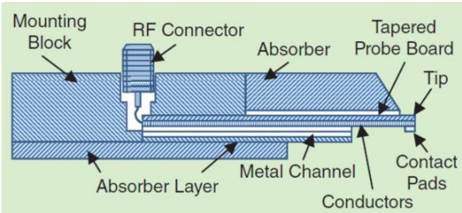

Fig. 1.61: Design of an on-wafer probe based on ceramic technology [53].

The most widely used probe tip configuration for radio frequency (RF) probes is the coplanar waveguide (CPW). This design is preferred because it can be engineered to match a characteristic impedance of 50 Ω across a broad frequency range, which is essential for ensuring consistent and accurate electrical measurements. The CPW probe tip often features a symmetric layout, commonly referred to as the ground-signal-ground (GSG) configuration. In this arrangement, a central signal strip is flanked by two ground planes, providing excellent isolation and minimizing unwanted signal interference.

On-wafer measurements and calibration procedures can be conducted on both microstrip and coplanar waveguide structures. However, the coplanar GSG configuration remains the most prevalent choice, primarily due to its effectiveness in maintaining impedance matching and its suitability for a wide spectrum of test scenarios.

One example of advanced probe technology is the Infinity probe, offered by FormFactor. This probe is engineered to deliver extremely low contact resistance when used on aluminum pads, which contributes to its ability to achieve highly reliable and repeatable RF measurement results. The Infinity probe is compatible with both coaxial and waveguide technologies, and its design minimizes unwanted coupling to nearby devices and transmission modes. This ensures that measurements are both precise and free from interference, supporting the highest standards of measurement accuracy in demanding RF testing environments.

Fig. 1.62: Some GSG probes from FormFactor [55].

The |Z| probe is engineered to deliver high-accuracy measurements by ensuring low contact resistance and superior impedance control. This probe is specifically designed to perform reliably in the most demanding test environments. Its robust construction makes it suitable for applications ranging from cryogenic testing where it helps characterize future computing integrated circuits (ICs) to high-temperature measurements conducted within closed systems, such as those required for automotive device testing.

The ACP (Air Coplanar Probe) is distinguished by its compliant tip, which facilitates accurate and repeatable on-wafer measurements. The design of the ACP probe tip enhances visibility and is optimized for low signal loss. This type of probe is renowned for its exceptional performance, combining precise probe mechanics with reliable measurement capabilities. As a result, it has become the most widely used microwave probe in on-wafer measurement applications today.

The T-Wave probe sets the industry standard for performance in on-wafer measurements of devices operating at millimeter and submillimeter wavelengths. T-Wave Probes are available in configurations that include both waveguide-banded probes and broadband (dual band) probes, allowing them to support a wide range of measurement requirements for high-frequency devices [55].

3.1. Key elements of probing station

The planarity and alignment of the probe tip are critical factors for ensuring precise on-wafer measurements. Achieving proper planarity minimizes measurement errors and guarantees that the probe maintains optimal contact with the device under test (DUT) throughout the measurement process.

The setup and installation of the entire probing system require careful technical handling. This process can introduce mechanical stress to the probe core, especially during the connection of radio frequency (RF) probes to positioners. Positioners can be operated manually, semi-automatically, or fully automatically, each offering different levels of control and precision over the probe movement.

Movement of the probes is managed through these positioners, which facilitate four main stages of motion: translation along the X and Y axes for horizontal movement, translation along the Z axis for vertical positioning, and rotation around the θ axis. These movement capabilities are essential for achieving the required probe alignment and planarity, as depicted in Fig. 1.63.

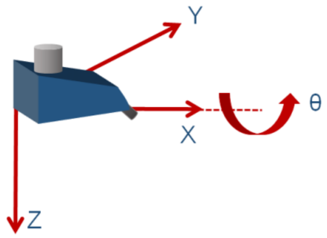

Fig. 1.63: Probe movement [54].

Improper handling of probes can result in misalignment of the probe tips along the z-direction, which directly affects the quality of measurements. It is crucial to carefully level the probes before commencing any measurement procedures to ensure optimal contact with the device under test. Even minor deviations caused by tilt, rotation, or translation of the probe can introduce significant offsets, ultimately reducing the accuracy of the results, as illustrated in Fig. 1.64. This sensitivity highlights the inherent challenges of on-wafer measurements, as the process is highly dependent on precise and skillful manipulation of the probes.

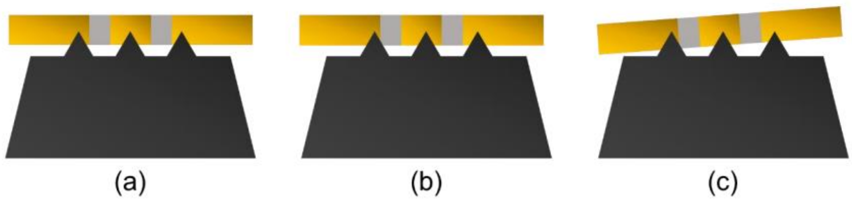

Fig. 1.64: Schematic of probe tips alignments (a) no offset (b) translation offset (c) rotation offset [54].

Manual probing stations often fall short in delivering the precision and accuracy required for advanced on-wafer measurement tasks. Due to inherent limitations in manual operation, such as difficulty in maintaining consistent probe alignment and planarity, measurement errors can arise, impacting the reliability of test results.

To address these challenges, the use of semi-automated and automated probing stations has become increasingly attractive. These advanced systems offer enhanced control over probe movement, allowing for more accurate and repeatable positioning of probes on the device under test (DUT). By minimizing human error and mechanical inconsistencies, semi-automated and automated probing solutions significantly improve the quality and reliability of on-wafer measurements.

3.2. Automated and nanorobotics probe station

Accurate S-parameter measurements for miniaturized RF and microwave devices present significant challenges, particularly regarding precision and consistency. Traditional manual probing techniques often fall short of the stringent requirements necessary for high-quality measurements, resulting in limitations that impact the reliability of test outcomes.

To overcome these obstacles, the development of a new generation of robotic and automated on-wafer probe stations has emerged as a promising alternative. These advanced systems are designed to provide improved measurement quality by delivering better precision and repeatability, addressing the shortcomings of conventional approaches.

Recent studies have concentrated on the development and optimization of such robotic and automated probe stations, with specification sheets detailing essential requirements and capabilities for these systems. Table 1.3 summarizes the key specifications related to the design and implementation of robotics and automated on-wafer probe stations, highlighting their potential to enhance the accuracy and reliability of S-parameter measurements for advanced RF and microwave devices.

Table 1.3: Specification Sheet regarding the development of robotics and automated on-wafer probe station [54].

Instrument specifications	- Automatic alignment of GSG probes on DUTs - Accurate and repeatable positioning - Low noise instrumentation - Compact solution - Easily integrable in industrial environment
Environmental specifications	- Controlled vibrations (early goal) - Controlled temperature and humidity (end goal)
Instrument design	- SolidWorks® mechanical design of different parts of the station: probe attachment pieces, camera bridge - Fabrication of the different elements at IEMN and external commercial companies
Instrument implementation	- Link the different elements efficiently
Software development	- Brainstorming on the technique to use - Explore each proposed idea and test its viability - Final program architecture - Develop each part of the program alone followed by tests and validation - Complete program
Testing	- Implementation of the automation program - Testing with no sensitive instruments (probes, DUTs) - Validation and test on the complete system

This new probing station utilizes SmarAct positioners, which feature advanced mechanical properties designed specifically for precise positioning tasks. The positioning stages incorporated in the station allow for both linear and rotational movements of the probe and chuck, enabling flexible and accurate alignment required for testing procedures (Fig. 1.65).

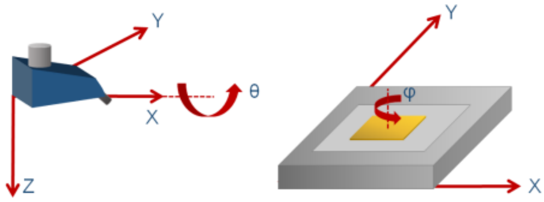

Fig. 1.65: Schematic representation of the probe and the chuck axis [54].

The SLC Linear Stages play a crucial role in enabling precise linear displacement within the probing station. These stages are engineered to facilitate movement in any required direction, which is essential for accurate alignment during testing procedures. The remote-control system, MCS2, is integrated with linear stages and provides an exceptionally high resolution of less than 1 nanometer for every directional movement. This high degree of precision ensures that even the smallest adjustments can be made reliably and consistently, supporting the station's advanced positioning capabilities.

In addition to their superior resolution, the SLC Linear Stages offer a displacement speed that exceeds 20 millimeters per second. This combination of speed and accuracy allows for efficient positioning during setup and calibration operations, contributing to the overall effectiveness and flexibility of the probing station (Fig. 1.66).

	Probe		Chuck	
Axis	X-Y	Z	X	Y
Reference	SL-2430	SLC-1730	SLC-24150	SLC-2475
Mechanical				
Scan Range [µm]	> 1.3	> 1.3	> 1.3	> 1.3
Travel [mm]	16	21	103	49
Dimensions [mm]	30 x 24 x 10.5	30 x 17 x 8.5	150 x 24 x 10.5	75 x 24 x 10.5
Weight [g]	36	20	180	90
Open-loop				
Velocity [mm/s]	> 20	> 20	> 20	> 20
Resolution MCS2 [nm]	< 1	< 1	< 1	< 1
Closed-loop				
Sensor Resolution MCS2 [nm]	1 (S)	1 (S)	1 (S)	1 (S)
Unidirectional Repeatability MCS2 [nm]	± 40 (S)	± 40 (S)	± 40 (S)	± 40 (S)

Fig. 1.66: SLC Linear Stages used for the probes and the chuck [54].

The SR Rotation Stages integrated into the probing station are responsible for enabling precise rotational movement of both the probe and the chuck. Notably, the two rotation axes possess different performance characteristics in terms of resolution and angular speed, as managed by the MCS2 remote-control system. Specifically, the rotational movement for the probe achieves an MCS2 resolution greater than 4 units and an angular speed exceeding 45 degrees per second. In contrast, the chuck rotation operates with an MCS2 resolution greater than 2 units and an angular speed surpassing 30 degrees per second. These differences are illustrated in Fig. 1.67, highlighting the tailored performance parameters designed to meet the distinct requirements of probe and chuck alignment within the probing station.

	Probe	Chuck
Axis	θ	ϕ
Reference	SR-2013	SR-4513
Mechanical		
Travel [°]	∞	∞
Dimensions [mm]	25.5 x 20 x 10.2	45 x 45 x 12.5
Weight [g]	11	89
Open-loop		
Angular Velocity [°/s]	> 45	> 30
Resolution MCS2 [µ°]	> 4	> 2
Closed-loop		
Sensor Resolution MCS2 [µ°]	25 (S)	15 (L, S)

Fig. 1.67: SR Rotation Stages used for the probes and the chuck [54].

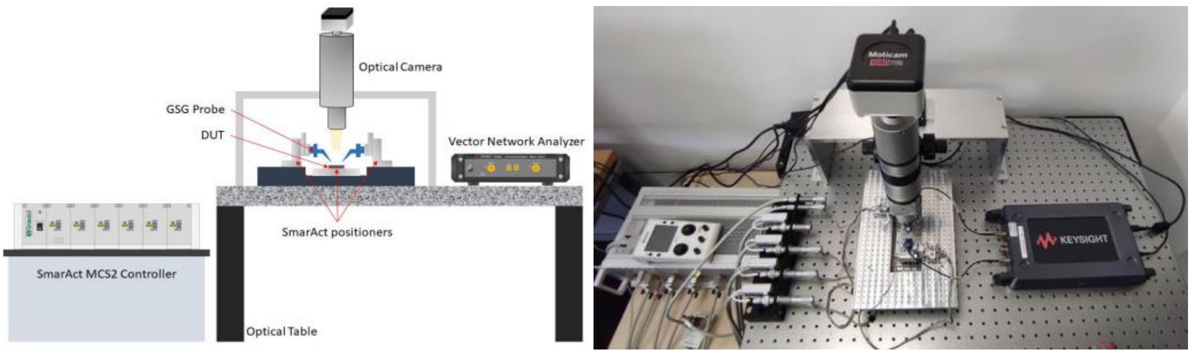

Fig. 1.68: View of the probing station [54].

With this setup, a one-port calibration was performed using a commercial Impedance Standard Substrate (ISS) over a frequency range spanning from 50 MHz to 50 GHz. The calibration was conducted with an Intermediate Frequency Bandwidth (IFBW) of 100 Hz and a Vector Network Analyzer output power set at -10 dBm, as depicted in Fig. 1.68. In total, ten individual measurements were carried out under these conditions [59].

$$\Delta|S_{11}| \approx \delta_1 + \tau_1|S_{11}| + \mu_1|S_{11}|^2 \tag{E.1.77}$$

As detailed in Section 1.4.23, the relationship between the corrected reflection coefficient (S11) and the actual reflection coefficient of the Device Under Test (DUT) can be described using the residual one-port error coefficients. This theoretical relationship allows for the derivation of the measurement uncertainty of S11, which is expressed mathematically in equation (E.1.77).

In the present study, this framework was applied to evaluate the performance of the automated probing system. The analysis demonstrated a significant improvement in measurement repeatability, with results showing a 1.4-fold enhancement compared to previous approaches. The uncertainty associated with S11 measurements using the current system was systematically compared to the uncertainties obtained with conventional measurement setups used in earlier studies. This comparison highlights the advantages of the new probing station in reducing measurement uncertainty and improving overall repeatability.

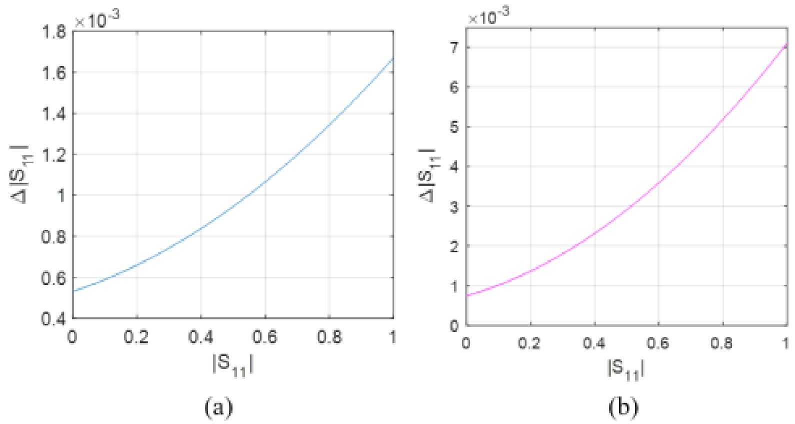

Fig. 1.69: Reflection coefficient magnitude uncertainties (a) solution proposed - (b) conventional probing [59].

Fig. 1.69 illustrates the reduction in uncertainty for one-port measurements when an automated probing station is utilized. This improvement is directly attributed to the automation process, which effectively minimizes the primary sources of error associated with probe movement. By reducing manual intervention, the system achieves more consistent and repeatable positioning of the probes, leading to greater reliability in measured results. The enhanced stability and precision of automated probe placement are critical factors in lowering measurement uncertainty and improving overall accuracy in the characterization process.

4. Miniaturization of devices and challenges on RF and microwave measurements

The rapid progress in semiconductor technology has been a key driver behind the ongoing miniaturization of electronic devices. This trend is largely fueled by the increasing need for devices that offer superior performance, reduced power consumption, and expanded functionality, all within increasingly compact designs. As a result, the landscape of electronic systems, especially those operating at radio frequency (RF) and microwave frequencies has been profoundly reshaped.

Modern electronic systems, ranging from mobile phones and Internet of Things (IoT) devices to advanced 5G and 6G communication modules and emerging quantum technologies, now incorporate highly sophisticated RF functionalities at both micro- and nanoscale dimensions. This shift toward greater integration density and smaller form factors has unlocked new possibilities for system capabilities and applications. However, it has also introduced significant complexities in the measurement and characterization of these devices, particularly as operating frequencies rise.

The miniaturization of RF and microwave devices presents a dual challenge. On one hand, it opens opportunities for innovation and enhanced device performance. On the other, it brings about technical hurdles related to the accurate measurement and analysis of device behavior at high frequencies. As device dimensions shrink, traditional measurement techniques often encounter limitations, requiring careful adaptation and the development of new strategies to ensure precise characterization. Understanding these implications is critical for researchers and engineers working to advance the field of RF and microwave technology.

This part explores how device miniaturization affects RF and microwave measurement methodologies. It highlights the main technical constraints associated with smaller device geometries and discusses the specialized approaches developed to overcome these barriers, ensuring continued progress in high-frequency electronic design and testing.

4.1. Devices Miniaturization

The miniaturization of electronic devices is fundamentally characterized by the integration of an increasing number of transistor nodes onto a single, smaller integrated circuit (IC). This densification process enables the IC to be seamlessly incorporated into its target system or device, allowing the final assembled product to perform its designated functions with enhanced efficiency and capability.

The significance of this technological shift was first articulated by Gordon Moore in 1965, who predicted that, "Cramming more components onto integrated circuits [would] lead to such wonders as home computers, automatic controls for automobiles and personal portable communications equipment." This vision set the stage for a transformative era in technology.

As a result, the industry has witnessed the emergence of a wide array of advanced devices, ranging from laptops and smartphones to new medical technologies. Subsequently, this revolution facilitated the proliferation of the Internet of Things (IoT), the advancement of 5G and 6G wireless communication devices, and the development of applications in augmented reality, virtual reality, and artificial intelligence. All these innovations have been made possible by the continuous trend toward smaller yet more powerful computing systems, as illustrated in Fig. 1.70.

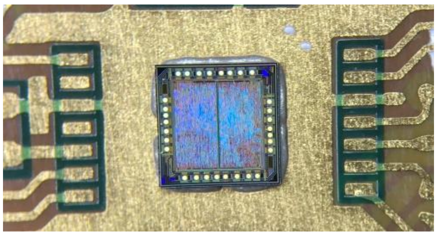

Fig. 1.70: A tiny "bare die" chip is placed onto a circuit board using a precise advanced electronics assembly process [57].

The prediction made by Gordon Moore has had a profound impact on the evolution of RF and microwave systems, primarily by enabling greater integration density through advancements in nanofabrication processes. As a direct result of these technological developments, it has become possible to incorporate a larger number of high-frequency components within increasingly compact modules.

For example, the latest generations of communication systems, such as those utilizing 5G and 6G technology, depend on the integration of complex high-frequency components into small, highly efficient modules. This trend is not limited to telecommunications; a wide range of modern applications including the Internet of Things (IoT), wireless communications, and quantum computing also require ultra-miniaturized devices to meet their stringent performance and size constraints.

4.2. Challenges in RF and Microwave Measurements

One of the main obstacles encountered in RF and microwave measurements as device dimensions are reduced is the issue of impedance mismatch. As electronic components become smaller, miniaturization leads to significant changes in their physical properties. Specifically, the metallic sections responsible for conducting RF signals experience increased resistivity at the nanoscale. This rise in resistivity is directly related to the decreased size of the conductors, as illustrated in Fig. 1.71.

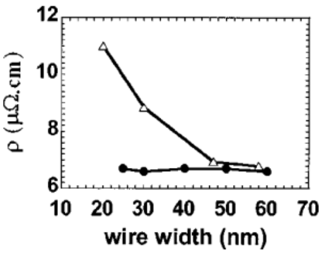

Fig. 1.71: Measured dependence of resistivity on wire width for a mean grain size of 20 nm (filled circles) and 40 nm (triangles) [32].

Unlike uniform macroscopic conductors, nanoscale conductors exhibit a grain structure characterized by distinct shapes and discontinuities. These discontinuities can have a significant impact on the electrical properties of the conductor, especially as device dimensions get smaller [32].

Impedance tuning becomes particularly important in high-frequency signal circuits at these scales. Proper impedance matching is essential for maximizing power transmission, ensuring that signal integrity is maintained and minimizing losses that can occur due to mismatches within the circuit.

4.3. Advances in Measurement Techniques

As electronic devices continue to shrink, on-wafer measurement techniques must evolve to enhance reliability. One of the primary parameters in this advancement is the probe contact and its precise positioning on the wafer. The reduction in pad size increases the difficulty of accurate probe placement, leading to higher risks of misalignment and increased contact resistance. These factors can distort measurement results, making it essential to investigate both planarity and repeatability effects. Recent studies have demonstrated that optimizing repeatability can be achieved by developing improved techniques for monitoring and controlling the contact condition of on-wafer RF probes with nanometer accuracy [58].

Miniaturization brings about parasitic inductance and capacitance in interconnects and pads, which can significantly influence measurement accuracy. While calibration helps correct for measurement system impacts, the extraction of parasitic contributions requires advanced de-embedding techniques. Additionally, meticulous on-wafer calibration is crucial and must utilize calibration standards designed at similar scales to the devices under test.

Miniaturization enables the achievement of higher frequencies due to shorter physical lengths for RF signal propagation. The optimal ratio between a L_P device physical size and the electrical wavelength should be maintained at less than one-twentieth of the λg wavelength ($L_P < \lambda g/20$ where λg is related to the frequency of interest f by ($\lambda g = c/f\sqrt{\varepsilon_r}$), ensuring favorable propagation conditions. As operating frequencies reach the millimeter wave and terahertz ranges, phenomena such as skin effect, radiation losses, and dispersion become increasingly significant.

The increased density of circuit elements leads to stronger electromagnetic coupling between adjacent components, affecting signal integrity through substrate modes, coupling, and reflections. These interactions can result in considerable performance shifts in small circuit devices, especially with temperature variations. High-frequency operations also introduce heating effects, necessitating controlled probing environments.

Modern measurement techniques must address various aspects to maintain accuracy. Advances in on-wafer probing technology, such as automated and nanorobotized probe stations, provide improved accuracy and precision in measurement results. The integration of artificial intelligence aids probe placement and defect detection, enhancing repeatability and reducing operator error.

Calibration approaches must also adapt, requiring the development of well-characterized nanoscale calibration standards. Designing these standards often involves 3D electromagnetic and analytical simulations that incorporate multiphysics considerations, such as electrical, thermal, and mechanical effects. Calibration routines, including algorithms and adopted measurement models, should be reviewed to account for coupling and neighborhood effects in miniaturized devices.

In summary, miniaturization, while a hallmark of technological progress, places substantial demands on RF and microwave measurement systems. As devices become smaller and operate at higher frequencies, accurate testing requires ongoing innovation in probing hardware, calibration methodologies, environmental control, and electromagnetic simulation tools. The development of sophisticated on-wafer probe stations and intelligent, adaptive measurement systems is essential to meet the stringent requirements of next-generation semiconductor technologies.

References 1

[1] WEN, Cheng P. *Coplanar waveguide: A surface strip transmission line suitable for nonreciprocal gyromagnetic device applications*. IEEE Transactions on Microwave Theory and Techniques, 1969, vol. 17, no 12, p. 1087-1090.

[2] BORET, Samuel. *Circuits intégrés monolithiques en technologie coplanaire pour applications de réception jusque 110 GHz*. 1999. Thèse de doctorat. Lille 1.

[3] C. Veyres and V. Fouad-Hanna, "*Extension of the application of conformal mapping techniques to coplanar lines with finite dimensions*," Int. J. of Electronics, no. 48, pp. 47–56, 1980.

[4] Collier, Richard J., and A. Douglas Skinner, eds. *Microwave measurements*. Vol. 12. IET, 2007.

[5] Teppati, Valeria, Andrea Ferrero, and Mohamed Sayed, eds. *Modern RF and microwave measurement techniques*. Cambridge University Press, 2013.

[6] https://www.ni.com/docs/fr-FR/bundle/ni-vna/page/vnahelp/error_and_uncertainty.html

[7] Zeier, Markus, Djamel Allal, and Rolf Judaschke. "Guidelines on the evaluation of vector network analysers (VNA)." *EURAMET Calibration Guide* 3.12 (2018): 507-521.

[8] Rytting, Doug. "Network analyzer error models and calibration methods." *White Paper, September* (1998).

[9] Engen, Glenn F., and Cletus A. Hoer. "Thru-reflect-line: An improved technique for calibrating the dual six-port automatic network analyzer." *IEEE transactions on microwave theory and techniques* 27.12 (1979): 987-993.

[10] Hoer, Cletus A., and Glenn F. Engen. "Calibrating a dual six-port or four-port for measuring two-ports with any connectors." *1986 IEEE MTT-S International Microwave Symposium Digest*. IEEE, 1986.

[11] Davidson, Andrew, Keith Jones, and Eric Strid. "LRM and LRRM calibrations with automatic determination of load inductance." *36th ARFTG conference digest*. Vol. 18. IEEE, 1990.

[12] Ferrero, Andrea, and Umberto Pisani. "Two-port network analyzer calibration using an unknown'thru'." *IEEE Microwave and guided wave letters* 2.12 (1992): 505-507.

[13] Basu, Saswata, and Leonard Hayden. "An SOLR calibration for accurate measurement of orthogonal on-wafer DUTs." *1997 IEEE MTT-S International Microwave Symposium Digest*. Vol. 3. IEEE, 1997.

[14] Ferrero, Andrea, and Umberto Pisani. "QSOLT: A new fast calibration algorithm for two port S parameter measurements." *38th ARFTG Conference Digest*. Vol. 20. IEEE, 1991.

[15] Fitzpatrick, Jim. "Error models for systems measurement." (1978).

[16] Rumiantsev, Andrej, and Nick Ridler. "VNA calibration." *IEEE Microwave magazine* 9.3 (2008): 86-99.

[17] DeGroot, Donald C., Jeffrey A. Jargon, and Roger B. Marks. "Multiline TRL revealed." *60th ARFTG Conference Digest, Fall 2002.*. IEEE, 2002.

[18] https://ziadhatab.github.io/posts/trl-calibration/

[19] Marks, R. and Williams, D. (1992), A General Waveguide Circuit Theory, Journal of Research (NIST JRES), National Institute of Standards and Technology, Gaithersburg, MD, doi: 10.6028/jres.097.024

[20] F. Purroy and L. Pradell, "New theoretical analysis of the LRRM calibration technique for vector network analyzers," *in IEEE Transactions on Instrumentation and Measurement*, vol. 50, no. 5, pp. 1307-1314, Oct. 2001, doi: 10.1109/19.963202.

[21] Eul, H-J., and B. Schiek. "Thru-match-reflect: One result of a rigorous theory for de-embedding and network analyzer calibration." *1988 18th European Microwave Conference*. IEEE, 1988.

[22] DOERNER, Ralf et RUMIANTSEV, Andrej. Verification of the wafer-level LRM+ calibration technique for GaAs applications up to 110 GHz. In : 65th ARFTG Conference Digest, 2005. Spring 2005. IEEE, 2005. p. 5 pp.
[23] SCHOLZ, René F., KORNDORFER, F., SENAPATI, Biswanath, et al. Advanced technique for broadband on-wafer RF device characterization. In : ARFTG 63rd Conference, Spring 2004. IEEE, 2004. p. 83-90.
[24] Lourandakis, Errikos. *On-wafer microwave measurements and de-embedding*. Artech House, 2016.
[25] Koolen, M. C. A. M., J. A. M. Geelen, and M. P. J. G. Versleijen. "An improved de-embedding technique for on-wafer high-frequency characterization." *Proc. Bipolar Circuits Technol. Meeting*. 1991.
[26] Cho, Ming-Hsiang, et al. "A cascade open-short-thru (COST) de-embedding method for microwave on-wafer characterization and automatic measurement." *IEICE Transactions on Electronics* 88.5 (2005): 845-850.
[27] Kim, Ju-Young, Min-Kwon Choi, and Seonghearn Lee. "A “Thru-Short-Open” de-embedding method for accurate on-wafer RF measurements of nano-scale MOSFETs." *Journal of Semiconductor Technology and Science* 12.1 (2012): 53-58.
[28] Ito, Hiroyuki, and Kazuya Masuy. "A simple through-only de-embedding method for on-wafer S-parameter measurements up to 110 GHz." *2008 IEEE MTT-S International Microwave Symposium Digest*. IEEE, 2008.
[29] LI, Qian et MELDE, Kathleen L. The impact of on-wafer calibration method on the measured results of coplanar waveguide circuits. *IEEE transactions on advanced packaging*, 2009, vol. 33, no 1, p. 285-292.
[30] KIM, Kichul, WALLIS, T. Mitch, RICE, Paul, et al. A framework for broadband characterization of individual nanowires. *IEEE microwave and wireless components letters*, 2010, vol. 20, no 3, p. 178-180.
[31] Hsu, Chuan-Lun, Gustavo Ardila, and Philippe Benech. "High frequency characterization and modeling of single metallic nanowire." *2012 International Semiconductor Conference Dresden-Grenoble (ISCDG)*. IEEE, 2012.
[32] Durkan, C., and M. E. Welland. "Size effects in the electrical resistivity of polycrystalline nanowires." *Physical review B* 61.20 (2000): 14215.
[33] Gomez-Rojas, Luis, et al. "RF response of single-walled carbon nanotubes." *Nano letters* 7.9 (2007): 2672-2675.
[34] Daffe, K., et al. "On-Wafer Broadband Microwave Measurement of High Impedance Devices-CPW Test Structures with Integrated Metallic Nano-Resistances." *2018 48th European Microwave Conference (EuMC)*. IEEE, 2018.
[35] ROMANO, Raffaele, MUBARAK, Faisal, SPIRITO, Marco, et al. The HΓ-VNA, an interferometric approach for the accurate measurement of extreme impedances. In : 2019 93rd ARFTG Microwave Measurement Conference (ARFTG). IEEE, 2019. p. 1-6
[36] Happy, Henri, et al. "Measurement techniques for RF nanoelectronic devices: new equipment to overcome the problems of impedance and scale mismatch." *IEEE Microwave Magazine* 15.1 (2014): 30-39.
[37] Nougaret, L., et al. "Gigahertz characterization of a single carbon nanotube." *Applied Physics Letters* 96.4 (2010).
[38] Randus, Martin, and Karel Hoffmann. "A method for direct impedance measurement in microwave and millimeter-wave bands." *IEEE transactions on microwave theory and techniques* 59.8 (2011): 2123-2130.
[39] Randus, Martin, and Karel Hoffmann. "A novel method for direct impedance measurement in microwave and mm-wave bands." *75th ARFTG Microwave Measurement Conference*. IEEE, 2010.

[40] RANDUS, Martin et HOFFMANN, Karel. A simple method for extreme impedances measurement-experimental testing. In : 2008 *72nd ARFTG Microwave Measurement Symposium*. IEEE, 2008. p. 40-44.
[41] BAKLI, Hind, HADDADI, Kamel, et LASRI, Tuami. Interferometric technique for scanning near-field microwave microscopy applications. *IEEE Transactions on Instrumentation and Measurement*, 2014, vol. 63, no 5, p. 1281-1286.
[42] HADDADI, Kamel et LASRI, Tuami. Interferometric technique for microwave measurement of high impedances. In : 2012 *IEEE/MTT-S International Microwave Symposium Digest*. IEEE, 2012. p. 1-3.
[43] LEWANDOWSKI, Arkadiusz, LEGOLVAN, Denis, GINLEY, Ronald A., et al. Wideband measurement of extreme impedances with a multistate reflectometer. In : 2008 *72nd ARFTG Microwave Measurement Symposium*. IEEE, 2008. p. 45-49.
[44] VOTSI, Haris, LI, Chong, AAEN, Peter H., et al. An active interferometric method for extreme impedance on-wafer device measurements. IEEE Microwave and Wireless Components Letters, 2017, vol. 27, no 11, p. 1034-1036.
[45] VLACHOGIANNAKIS, Gerasimos, SHIVAMURTHY, Harshitha Thippur, DEL PINO, Maria Alonso, et al. An I/Q-mixer-steering interferometric technique for high-sensitivity measurement of extreme impedances. In : 2015 IEEE MTT-S International Microwave Symposium. IEEE, 2015. p. 1-4.
[46] Stenarson, J., and K. Yhland. "A new assessment method for the residual errors in SOLT and SOLR calibrated VNAs." *2007 69th ARFTG Conference*. IEEE, 2007.
[47] https://qucs.sourceforge.net/tech/node75.html
[48] M. V. Schneider, ``Microstrip Lines for Microwave Integrated Circuits," *The Bell System Technical Journal*, vol. 48, pp. 1421-1444, May 1969.
[49] H. A. Wheeler, ``Transmission-Line Properties of Parallel Strips Separated by a Dielectric Sheet," *IEEE Transactions on Microwave Theory and Techniques*, vol. 13, no. 2, pp. 172-185, Mar. 1965.
[50] E. Hammerstad and Ø. Jensen, ``Accurate Models for Microstrip Computer-Aided Design," *Symposium on Microwave Theory and Techniques*, pp. 407-409, June 1980.
[51] https://markimicrowave.com/technical-resources/application-notes/get-connected-a-brief-waveguide-introduction/
[52] https://www.vcelink.com/products/coaxial-cable-connector
[53] Rumiantsev, Andrej, and Ralf Doerner. "RF probe technology: History and selected topics." *IEEE Microwave Magazine* 14.7 (2013): 46-58.
[54] Mokhtari, Cerine. *Development of a Nano-robotics and Automated Microwave On-Wafer Probe Station*. Diss. Université de Lille, 2023.
[55] https://www.formfactor.com/products/probes/
[56] Pozar, D. M., Microwave Engineering, New York: John Wiley & Sons, 2011.
[57]https://www.jabil.com/blog/miniaturization-key-to-fabricating-the-future.html#:~:text=Miniaturization%20in%20electronic%20devices%20involves,is%20made%20tinier%20yet%20mightier.
[58] Daffé, Khadim, et al. "RF wafer probing with improved contact repeatability using nanometer positioning." *2016 87th ARFTG Microwave Measurement Conference (ARFTG)*. IEEE, 2016.
[59] C. Mokhtari *et al*., "New Generation of On-Wafer Microwave Probe Station for Precision GSG Probing," *2022 24th International Microwave and Radar Conference (MIKON)*, Gdansk, Poland, 2022, pp. 1-4, doi: 10.23919/MIKON54314.2022.9925009.

Introduction

The electronics component industry is continually faced with the challenge of miniaturization. As the size of electronic devices decreases, this reduction inevitably affects their electrical performance. To evaluate these changes, design engineers must conduct thorough electrical characterization campaigns, utilizing advanced measurement instruments such as the Vector Network Analyzer (VNA).

VNA is an essential tool for assessing a component's ability to transmit or reflect electromagnetic signals. It operates by injecting an electromagnetic wave into the device under test and measuring the ratios between transmitted or reflected waves and the incident wave. These ratios are known as scattering parameters, or S-parameters.

Typically, measurements with a VNA are referenced to a characteristic impedance of 50 Ω. This value is chosen because it represents the nominal operating point at which the instrument offers its best sensitivity and accuracy. Before conducting measurements, it is crucial to calibrate the VNA to correct systematic errors. Calibration is performed using traceable standards, which can be created in various technologies including coaxial, rectangular, or planar formats.

Given the trend towards miniaturization, planar technology has become highly suitable and is increasingly in demand. Conventional calibration standards are usually designed to match the reference impedance of 50 Ω. However, as components become smaller, their impedance can shift to values far from this standard, presenting significant measurement challenges.

The sensitivity of the VNA, optimized for environments close to 50 Ω, may suffer when attempting to characterize devices with impedances that deviate markedly from this nominal value. This highlights the importance of adapting conventional calibration standards to the scale of nanodevices, ensuring accurate and reliable measurements.

This chapter is dedicated to the design and manufacture of nanoscale calibration components. The discussion is organized around three fundamental aspects: the selection of the standard structure, the design process, and the realization process of these components.

1. Choice of Standards Structure

1.1. Choice of Coplanar Technology

Planar topology represents the predominant technology used in the design of electronics, radio frequency (RF), and microwave circuits. The evolution of monolithic integrated circuits [1] has propelled continuous advancements within these fields, particularly in addressing the complex challenges associated with microwave measurements of miniaturized components on-wafer.

Within planar technology, several transmission line structures are employed, including the parallel plate line, slot line, microstrip line, and coplanar waveguide line (CPW) [2]. Among these, microstrip and coplanar waveguide lines are especially common due to their versatility and practicality in both circuit design and fabrication.

Microstrip and CPW lines support quasi-TEM modes, enabling efficient signal transmission. These structures allow for the integration of both passive and active components directly onto their surfaces. They provide flexibility in accommodating shunt or series circuit elements, enhancing design possibilities. The electrical characteristics of these transmission lines are directly influenced by their cross-sectional dimensions, which can be precisely controlled during fabrication.

In this work, the choice of CPW technology is supported by several advantages:

- Unlike Microstrip lines, CPW lines do not require the creation of via holes.

- CPW line is much less sensitive to substrate thickness than Microstrip line [3].
- CPW ribbons can have narrow width with appreciable value of characteristic impedance.
- CPW grounds presents less inductance than Microstrip with its via connections.

The various advantages outlined above make coplanar waveguide (CPW) structures highly suitable for numerous applications within high-frequency circuit design. One notable feature of CPW technology is its Ground-Signal-Ground (GSG) configuration. This arrangement is particularly beneficial during measurement processes, as it allows for straightforward and reliable connections with vector network analyzers. The VNA is linked to the circuit through GSG probes, which are in turn connected via coaxial cables. This setup streamlines measurement procedures, enhances accuracy, and supports the effective characterization of microwave and RF components.

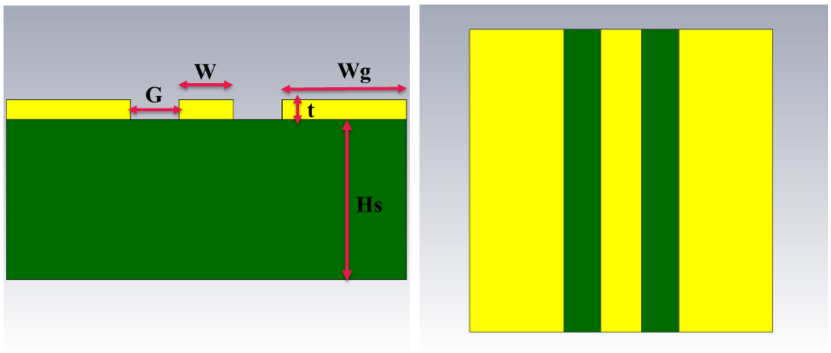

Fig. 2.1: CPW structure (front and top view).

1.2. Choice of Materials

Material parameters are fundamental in achieving high-performance and high-quality structures, especially for high-frequency circuit design. The selection of materials must adhere to stringent criteria, focusing particularly on minimizing both conductive and dielectric losses.

Substrate: Two types of dielectric substrates are employed in parallel for this study: Alumina (Al_2O_3) and High-Resistivity Silicon (HR-Si), each with a defined thickness Hs.

- Alumina (Al_2O_3): This material is characterized by a relative permittivity (ε_r) of 9.9 and an extremely low loss tangent of 0.0001, making it particularly well-suited for microwave applications requiring low dielectric losses.
- High-Resistivity Silicon (HR-Si): With a relative permittivity (ε_r) of 11.9 and a conductivity (σ) of 0.00025 S/m, HR-Si offers low loss characteristics while providing enhanced compatibility with silicon-based microfabrication processes.

Conductor: Gold is frequently chosen as the primary conductive material due to its low resistivity and chemical stability. Its excellent electrical conductivity ($\sigma = 4.56 \times 10^7$ S/m) ensures minimal signal loss, which is critical for microwave and RF applications. The gold layer is deposited with a specific thickness, denoted as *t*, to optimize electrical performance.

Resistive and Adhesion Layer: To ensure strong adhesion between the gold conductor and the substrate, as well as to create localized resistive elements where required, a layer of titanium (Ti) is deposited beneath the gold. Titanium is chosen for its reliable adhesion properties and its moderate conductivity ($\sigma = 5.661 \times 10^5$ S/m, as referenced from IEMN). The thickness of the titanium layer is denoted as *e*.

Fig. 2.2: Cross-section of CPW line.

1.3. Choice of Dimensions

After selecting the technology and materials, careful consideration must be given to determining the appropriate dimensions for the structure. The design process must address the requirement of minimizing the size, targeting reductions down to the nanometer scale. However, certain constraints must be considered, particularly those related to probing capabilities and technological feasibility.

Currently, ground-signal-ground (GSG) probes cannot directly access nanoscale components due to their physical limitations. Specifically, the minimum pitch size for GSG probes is typically 50 µm or greater, and their contact pads measure 25 µm by 35 µm. These dimensions restrict the ability to probe sections at the nanoscale, effectively making it impossible to directly access the nano section with standard probes.

To overcome these limitations, the structure is divided into two distinct sections: a microscale section and a nanoscale section. The microscale section is specifically optimized to accommodate GSG probes, with a pitch range from 50 µm to 100 µm and is matched to a 50 Ω impedance to ensure compatibility and performance. The nanoscale section, depicted in Fig. 2.3, allows for further miniaturization, while the microscale section serves as an interface for reliable electrical contact and measurement.

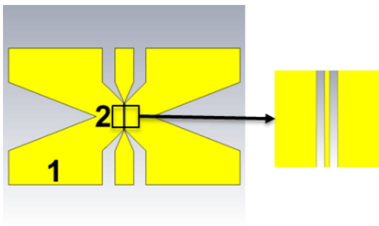

Fig. 2.3: Two sections (micro and nano) of the CPW structure.

The dimensions of the microscale section for each substrate type are determined based on the requirement for 50 Ω impedance matching. By utilizing an analytical model, it is possible to predetermine the characteristic impedance of the coplanar waveguide (CPW) line as soon as the cross-sectional dimensions are selected. For example, electromagnetic simulation tools such as CST Microwave Studio allow for the calculation of the impedance value of the proposed structure using the specified dimensional parameters. Table 2.1 presents the initial dimensional parameters for the micrometric section of the CPW structure on both alumina and high-resistivity silicon substrates.

Table 2.1: Dimensional parameters of the microscale part cross-section.

Substrates	Alumina ($\varepsilon_r = 9.9$)	HR Silicon ($\varepsilon_r = 11.9$)
Trace (W)	27 µm	27 µm
Gap (G, g)	14.5 µm	18.86 µm
Ground plane (Wg)	144 µm	135.28 µm
Metal thickness (t)	500 nm	500 nm
Substrate height (Hs)	350 µm	350 µm
Titanium thickness (e)	25 nm	25 nm

Characteristic impedance (Zc)	50 Ω	50 Ω

In the nanoscale section, the CST model presents a significant limitation when it comes to evaluating the analytical characteristic impedance of the coplanar waveguide (CPW) line. This restriction arises due to a specific condition that must be met between the gap (g) and the metal thickness (t). Specifically, the model requires that the ratio of t to g satisfies the condition $t/g > 0.1$, as illustrated in Fig. 2.4. If this requirement is not fulfilled, the model cannot accurately assess the characteristic impedance, which restricts the range of geometrical parameters that can be explored in nanoscale designs.

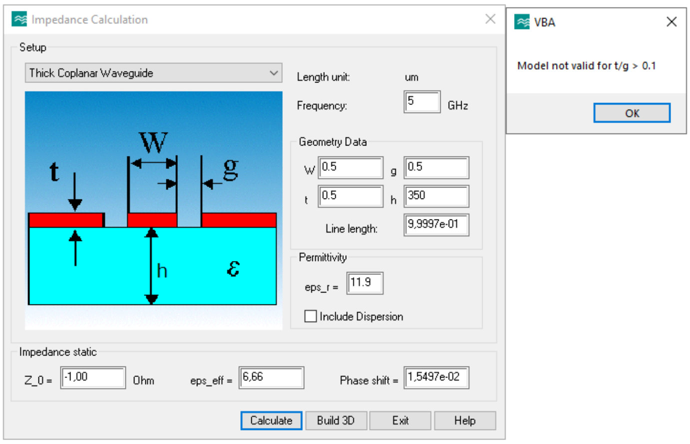

Fig. 2.4: Condition of impedance calculation of CST Studio Suite.

In this section, a trace width (W) of 500 nm, a metal thickness (t) of 500 nm, and a substrate height (Hs) of 350 µm were predefined for both types of dielectrics considered. The primary objective was to determine an appropriate gap (g) value that would result in a characteristic impedance close to 50 Ω. Achieving this target required a systematic analysis that simultaneously accounted for all relevant parameters.

To address this, the model was employed by varying the cross-sectional dimensions within permissible limits, while maintaining the aspect ratio between the trace width and the gap, and ensuring the impedance remained at 50 Ω. By systematically adjusting these dimensions up to the boundary condition, a relationship was established between the trace width and the gap. This relationship enabled extrapolation to the desired dimensions for the design under consideration.

Table 2.2 presents the variation of the shape ratio ($a = W/G$) between the trace width (W) and the gap (G), which maintains the impedance at 50 Ω for the Alumina substrate.

Table 2.2: The shape ration trace width - gap keeping the impedance.

Zc (Ω)	**50**	**50**	**50**	**50**	**50**	**50**	**50**	**50**	**50**	**50**	**50**	**50**	**50**	**50**	**50.68**	**51**
w	**13.5**	**13**	**12.5**	**12**	**11.5**	**11**	**10.5**	**10**	**9.5**	**9**	**8.5**	**8**	**7.5**	**7**	**6.5**	**0.5**
a	**1.64**	**1.62**	**1.61**	**1.59**	**1.58**	**1.56**	**1.54**	**1.52**	**1.51**	**148**	**1.46**	**1.43**	**1.41**	**1.37**	**1.29**	**0.68**

As the calculation progresses, a critical point is reached at a trace width of 6.5 µm and a shape ratio of 1.299, corresponding to a gap of 5.03 µm. At this dimension, the condition ($t/g > 0.1$) is nearly satisfied. This indicates that the geometric constraints become increasingly significant as the structure is miniaturized.

Consequently, it is evident that reducing the classic coplanar waveguide (CPW) structure to the nanoscale, while maintaining a characteristic impedance of 50 ohms, is fundamentally challenged by these limitations. The near fulfillment of the (t/g > 0.1) condition signifies a threshold beyond which further miniaturization may compromise the intended electrical performance.

$$y = 0.8263 * x^{0.2655}$$
$$R^2 = 0.9978$$

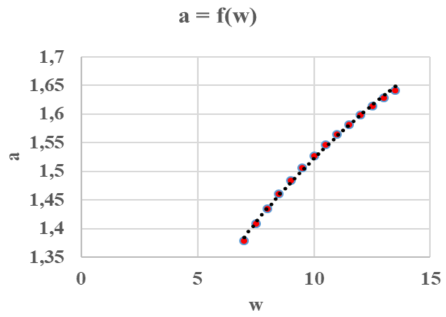

$$a = 0.8263 * W^{0.2655}$$
$$G = W/a$$

Fig. 2.5: The relationship between trace width W and gap G.

The primary objective is to extrapolate the existing data down to the nanoscale, utilizing the values provided in Table 2.2. Fig. 2.5, which was generated using Excel, plays a crucial role in this process. By applying the trend curve equation (E.2.1) with a high correlation coefficient (R^2 = 0.9978), it becomes possible to determine reduced dimensions through extrapolation. This approach ensures that the reduction in scale maintains consistency with the established data trends.

$$\frac{W}{G} = 0.8263 * W^{0.2655} \tag{E.2.1}$$

To further analyze the miniaturization of the coplanar waveguide (CPW) structure, the relation established in equation (E.2.1) is employed to extrapolate the data to nanoscale dimensions. Specifically, a trace width (W) of 500 nm is selected as the target value. By applying this width to equation (E.2.1), the corresponding gap (G) values for each substrate are determined.

For Alumina, the calculated gap is 727 nm, while for high-resistivity (HR) Silicon, the gap is found to be 900 nm. These calculated values are consistent with the trend observed in the earlier data and follow the extrapolation approach outlined previously.

A summary of the resulting cross-sectional dimensions for the micro and nano components of both substrates is presented in Table 2.3. This table provides a clear comparison of the trace widths and gap values for Alumina and HR-Silicon at both scales.

Table 2.3: The first considered cross-sectional dimensions of parts 1 and 2.

Cross sections	**Alumina**		**HR Silicon**	
Parts	Parti 1	Part 2	Part 1	Part 2
Trace (W)	27 µm	500 nm	27 µm	500 nm
Gap (G)	14.5 µm	727 nm	18.86 µm	900 nm
Metal thickness (Gold)	500 nm	500 nm	500 nm	500 nm
Height (Substrate)	350 µm		350 µm	

2. Design and realization of calibration structures

The accuracy of measurements in radio frequency (RF) and microwave domains is fundamentally influenced by the quality of calibration performed on measurement instruments. Precise calibration ensures that measurement results are both reliable and reproducible, which is critical for effective characterization and analysis of RF and microwave devices.

Calibration structures (kits) play a key role in this process. These kits are composed of carefully characterized reference standards, each designed to enable correction of systematic errors that may arise from the measurement system. Such errors might include losses, reflections, or impedance mismatches, all of which can negatively affect the integrity of measurement data.

The design of calibration kits is a multifaceted task that must consider a variety of factors. Technological specificities, physical layout, and fabrication constraints are all critical elements that influence the final performance of the kits. Additionally, the kits must meet stringent requirements to align with the needs of the intended applications.

To ensure the effectiveness of calibration kits, a thorough validation process is conducted. This involves performing electromagnetic simulations, applying analytical models, and implementing calibration algorithms. Each step is essential in verifying that the kits achieve the necessary accuracy and reliability for RF and microwave measurement systems.

2.1. Electromagnetic simulations of structures

2.1.1. Tools and parameters of simulations

RF and microwave devices are commonly measured using a Vector Network Analyzer, which utilizes the concept of S-parameters. S-parameters, or scattering parameters, are complex matrices of numerical values. These matrices are typically organized in the standard Touchstone format, which facilitates both measurements and simulations carried out with instruments or simulation tools.

A critical aspect of RF and microwave device characterization is the definition of the frequency band in which the devices operate. The relationship between frequency (*f*) and wavelength (λ) is described by the equation ($f.\lambda\sqrt{\varepsilon_r} = c$), where εr represents the relative permittivity and c is the speed of light. This equation demonstrates that higher frequencies correspond to shorter wavelengths.

The propagation of signals is particularly relevant when the physical length (L) of the transmission line is comparable to the wavelength. In such cases, the transmission line's behavior must be carefully considered. Transmission lines are classified according to their physical length in relation to the wavelength or the frequency of the signal they are designed to carry, as detailed in Table 2.4.

Table 2.4: Transmission lines depending on the physical length - wavelength ratio.

Transmissions lines	Short	Medium	long
Physical length - wavelength ratio	$L < \frac{1}{10}\lambda$	$\frac{1}{10}\lambda < L < \frac{1}{5}\lambda$	$L > \frac{1}{5}\lambda$

Recent technological advancements have driven the development of miniaturized, high-speed, and high-performance systems. Notably, wireless communication and Internet of Things (IoT) applications have become increasingly compact while operating at higher frequencies.

To address the demands of these modern applications, the working frequency band for this study was extended from 250 MHz to 110 GHz. The initial phase of component design involved comprehensive 3D electromagnetic simulations using CST Studio Suite. CST Studio Suite provides a suite of 3D simulation tools tailored to various study requirements, including CST Microwave Studio, CST EM Studio, CST Cable Studio, CST Particle Studio, and CST Multiphysics Studio [4].

For the design of structures, particular attention was given to CST Microwave Studio. This module offers versatile simulation capabilities, including:

- Time Domain Solver: Utilizes a transient solver for efficient calculations on both lossy and lossless structures. The solver can analyze the entire frequency band of interest by calculating S-parameters from the Discrete Fourier Transform (DFT) of time signals. It employs the Finite Integration Technique (FIT).
- Frequency Domain Solver: Performs adaptive sampling and supports both tetrahedral and hexahedral meshes. This solver includes two variations for resonant structure analysis: one dedicated to calculating S-parameters and another that evaluates electromagnetic fields, which may require additional computation time [4].

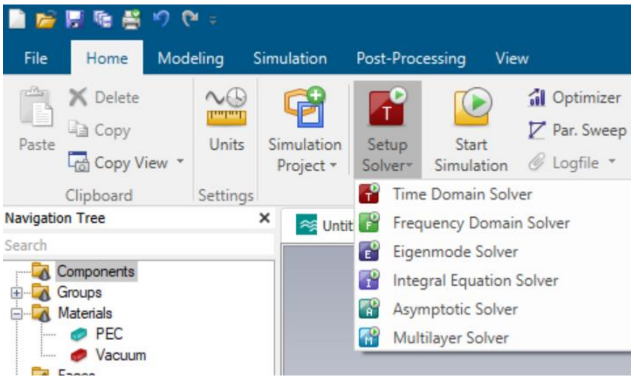

Fig. 2.6: CST Microwave Studio interface.

The time domain solver in CST Microwave Studio is highly suitable for a wide range of high-frequency applications, including connectors, transmission lines, filters, and antennas. One of its key advantages is the ability to capture the entire broadband frequency response of a simulated device in a single calculation run. This efficiency makes the time domain solver particularly well-matched for coaxial and thin planar structures, such as thin coplanar waveguide (CPW) lines.

A distinctive feature of the time domain solver is its use of hexahedral meshing, as illustrated in Fig. 2.7. This meshing approach approximates the curves and bends of planar surfaces by varying the angles between the quadrilateral faces within the mesh. As a result, it is possible to achieve a flat surface with high precision while maintaining a low density of nodes and elements along that surface. Furthermore, the hexahedral mesh can be independently defined in the x, y, or z directions, allowing for flexible and efficient modeling of diverse geometries.

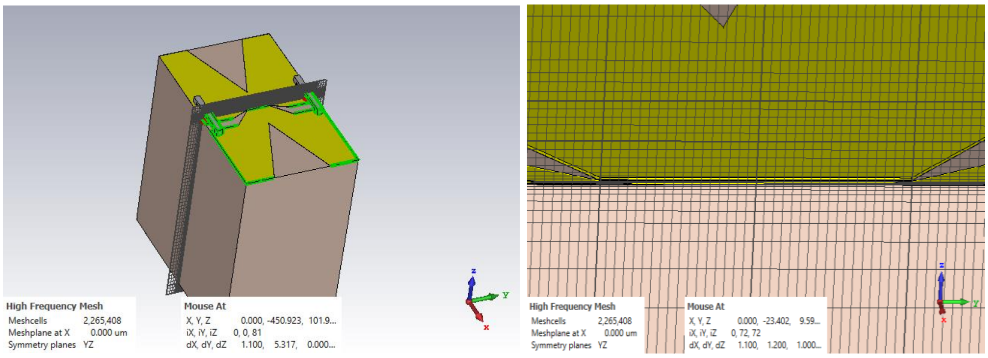

Fig. 2.7: Hexahedral meshing of time domain solver (CPW and Coaxial line) in CST.

The mesh properties within CST Microwave Studio play a critical role in determining the accuracy and efficiency of electromagnetic simulations. The most significant parameter is the Maximum cell, which specifies the largest permitted cell size within the calculation domain (see Fig. 2.8). This value is directly linked to the geometrical dimensions of the structure under investigation.

For high-frequency applications, the highest frequency of interest is a key factor because it dictates the smallest wavelength that must be resolved. Consequently, the maximum cell size is set so that the mesh can accurately represent the smallest wavelength present in the simulation. This establishes the number of cells per wavelength, which in turn sets the upper limit for cell size relative to the wavelength.

The choice of maximum cell size has a substantial impact on both the quality of the simulation results and the total computation time. Increasing the number of cells per wavelength enhances simulation accuracy but also leads to longer calculation times. The spatial sampling rate for signals within the structure is defined by this parameter, ensuring that electromagnetic phenomena are properly captured throughout the model [4].

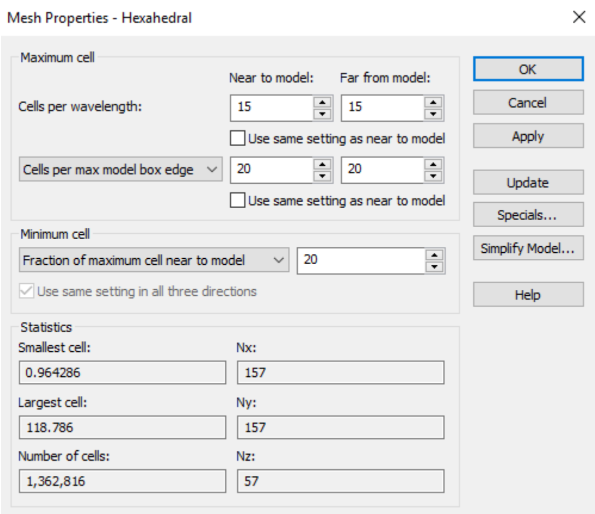

Fig. 2.8: Mesh proprieties with hexahedral meshing in CST.

The number of cells along the maximum edge of the model box is determined by the maximum cell size, which is calculated by dividing the length of the largest edge of the model's bounding box by a specific number. This number is dictated by the geometric details present within the structure, ensuring that the mesh resolution accurately represents the physical features of the model. The background region is excluded from this calculation, and it is important to verify that the bounding box is properly defined and not empty. The maximum cell size parameter ensures that the mesh is neither too coarse nor too refined for the features of interest.

To prevent unnecessary mesh refinement caused by very small geometric features, such as thin regions or narrow gaps, a minimum cell size is also specified. This avoids excessive computational cost while still capturing critical details, as illustrated in Fig. 2.8.

Another essential simulation parameter is the definition of boundary conditions. Because the software operates within a finite computational domain, these settings must be established before running the simulation. The boundary conditions dialog box allows users to specify the type of boundaries and, if applicable, symmetry planes for the model. These parameters ensure that the solver accurately represents the interaction between the simulated structure and its surroundings, as shown in Fig. 2.9.

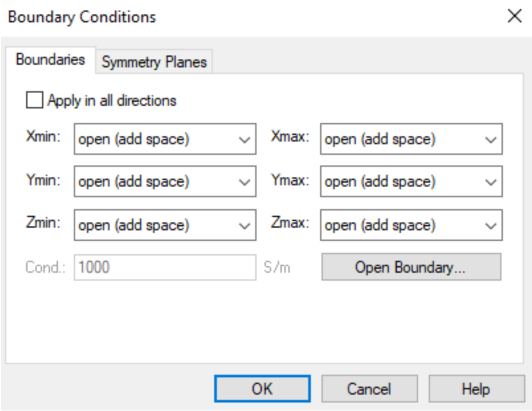

Fig. 2.9: Boundary conditions in CST.

In high-frequency electromagnetic simulations, the selection and definition of boundary conditions are critical for accurately modeling the behavior of fields within the computational domain. There are seven primary types of boundary conditions that may be applied, each tailored to represent different physical scenarios and to optimize simulation efficiency:

- Electric Boundary: This condition assumes a perfect electric conductor at the boundary. As a result, the tangential components of the electric field and the normal components of the magnetic flux are set to zero at this interface.
- Magnetic Boundary: Used to model a perfect magnetic conductor, this boundary sets the tangential magnetic fields and the normal electric fluxes to zero at the surface.
- Open Boundary: Implemented using a perfectly matched layer (PML), this boundary simulates the extension of the geometry to infinity. It allows electromagnetic waves to exit the domain with minimal reflection, making it suitable for problems where outgoing waves must be absorbed efficiently.
- Open (Add Space) Boundary: Like the Open boundary, this option introduces additional space around the simulated structure, which is particularly useful for far-field calculations in antenna simulations. Users can specify either a minimum distance to the structure by selecting a frequency center or by defining an absolute distance value.
- Periodic Boundary: This boundary connects two opposing faces of the domain with a user-defined phase shift, effectively simulating an infinitely repeating structure in that direction. It is typically used for structures with inherent periodicity.
- Conducting Wall Boundary: This boundary condition represents a wall made of lossy metal material, introducing realistic energy dissipation effects at the boundary.
- Unit Cell Boundary: Closely related to the periodic boundary, the unit cell boundary condition allows for the definition of two-dimensional periodicity, including in directions other than those aligned with the coordinate axes.

If the structure under study exhibits symmetry, symmetry plane parameters can be defined. Utilizing these symmetry planes can significantly reduce simulation time and computational resources by effectively halving the number of initial mesh cells that need to be calculated.

In addition to boundary condition configuration, several specialized tools are available for the design, modeling, and optimization of high-frequency devices. Among these, the Advanced Design System (ADS) stands out as a comprehensive electronic design automation software suite tailored for RF, microwave, high-speed digital, and power electronics applications. ADS offers standards-based design and verification capabilities, including wireless libraries and circuit-system-electromagnetic (EM) co-simulation within a unified platform.

The advanced features of ADS facilitate the design process for wireless components such as power amplifiers and RF front-end modules. The software enables users to create and analyze both circuit and system-level designs, as well as to visualize simulation data for further evaluation and refinement [5].

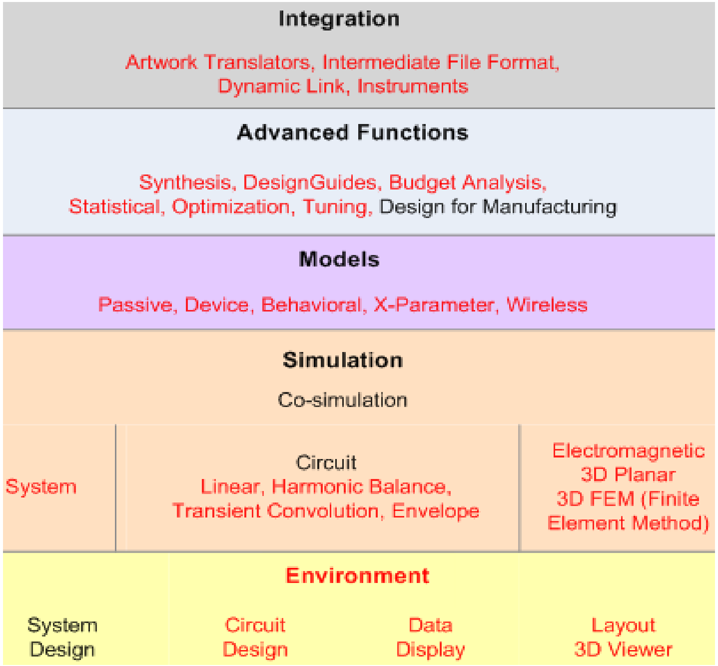

Fig. 2.10: Advanced Design System (ADS).

In this work, these two electromagnetic simulation tools have been employed for the design and modeling of various structures. These tools play a crucial role in accurately representing and analyzing the behavior of the structures under study. Additionally, MATLAB and Python software are utilized for post-processing the data obtained from simulations, as well as for executing calibration algorithms necessary for precise measurement and evaluation.

A brief investigation has been conducted into the different excitation methods available for coplanar waveguide (CPW) structures within CST simulation software. There are three primary excitation techniques: using a ground-signal-ground (GSG) probe, a bridge, or a waveguide port. Fig. 2.11 illustrates a simulated tapered line measuring 200 µm, demonstrating these three excitation methods.

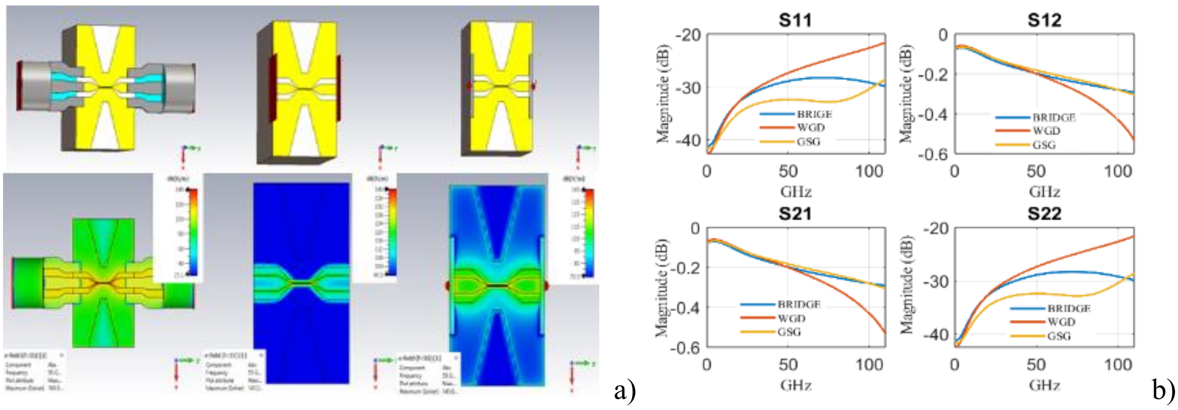

Fig. 2.11: Excitation types – left (E-field map), Right (line S-parameters).

When utilizing waveguide port excitation in simulations, it is important to note that higher order modes may emerge at frequencies above several gigahertz, particularly around 40 GHz. These modes, often referred to as box modes, are a consequence of the physical dimensions of the ports themselves.

Alternatively, employing bridge or lumped port excitation results in the presence of a pure coplanar waveguide (CPW) mode. This configuration does not account for the effects of the probes in actual measurements, allowing for a simplified analysis of the CPW structure.

The ground-signal-ground (GSG) probe excitation method offers a more realistic simulation by incorporating neighborhood effects. However, this approach demands greater memory capacity due to the increased complexity of the model [6].

2.1.2. Design of calibration structures

2.1.2.1. First design of structures

Building upon the previously described model line structure, a range of components has been developed to support both calibration and verification processes in radio frequency (RF) and microwave measurements (Fig. 2.12). These components are designed as either one-port or two-port structures, tailored to address various measurement scenarios and requirements. These kits have been implemented on two types of substrates: Alumina and High-Resistivity (HR) Silicon. The choice of these substrates allows the components to meet stringent standards for precision and reliability, which are essential for accurate RF and microwave characterization.

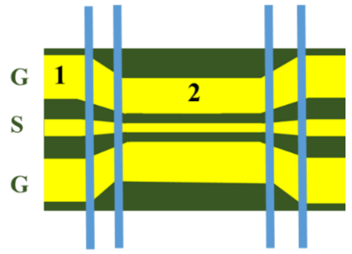

Fig. 2.12: prototype structure.

Fig. 2.13 presents the simulated S-parameters for a series of tapered lines with varying lengths. The analysis reveals a clear trend: as the line length and frequency increase, there is a noticeable degradation in transmission performance, accompanied by a rise in reflection. Specifically, the shortest line, known as the THRU line, measures 200 µm, while the longest line extends to 1650 µm.

Across the entire frequency range evaluated, which spans from 0.25 GHz to 110 GHz, the maximum reflection coefficients (S11) are observed to be -26.26 dB for the shortest line and -13.6 dB for the longest line, indicating greater reflection losses in longer lines. In terms of transmission, the S21 coefficient reaches a minimum value of -0.26 dB for the short line, whereas the longest line exhibits a more pronounced loss, with a minimum S21 value of -5.6 dB.

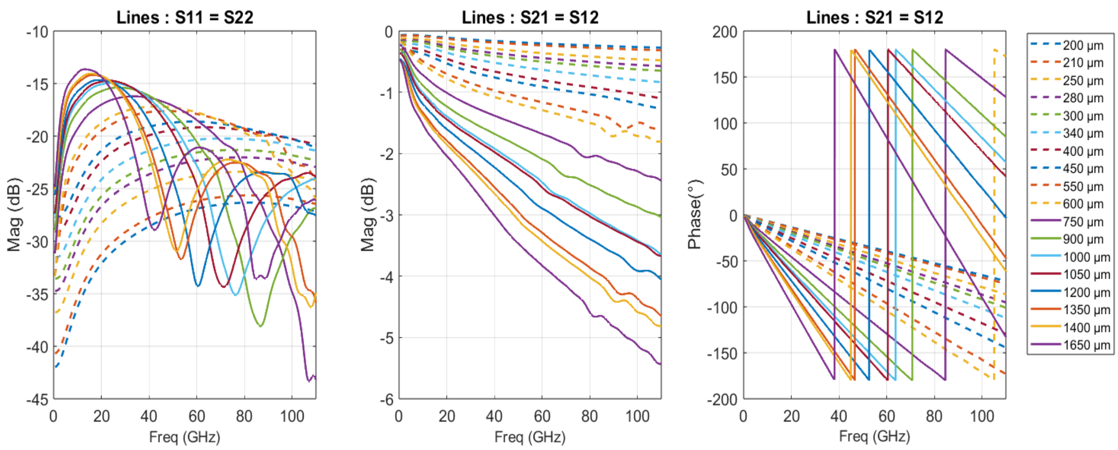

Fig. 2.13: Simulated S-parameters of tapered lines with length varying from 200 µm to 1650 µm.

The primary structure designed for high reflection within the calibration kit is the open circuit, commonly referred to as the Open standard. This Open standard is configured to have a length that is exactly half that of the Thru line, serving as a baseline for comparison with other open-circuit structures.

In addition to the primary Open standard, a series of supplementary open-circuit structures have been developed by incrementally increasing their lengths relative to the main Open standard. By introducing distinct length offsets for each of these additional components, it is possible to conduct a detailed and systematic analysis of how reflection characteristics vary as a function of the physical dimensions of the open-circuit standard. This approach enables an in-depth assessment of the influence of structure length on reflection behavior, providing valuable insights into the optimization of calibration kit performance for a range of frequencies and measurement conditions.

Simulation results reveal a consistent trend: the reflection coefficient (S11) exhibits a reduction in amplitude with increasing electrical delay and frequency. This behavior is illustrated in Fig. 2.14, which demonstrates how both the extension in length and the rise in frequency contribute to a progressive decrease in the magnitude of the reflected signal.

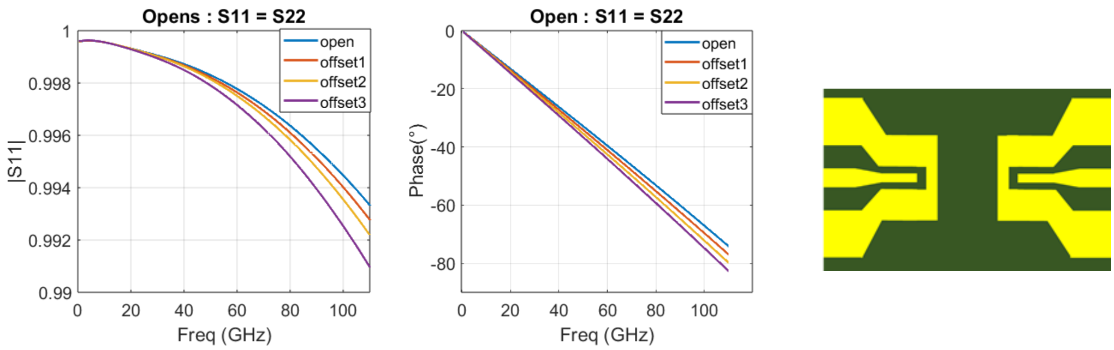

Fig. 2.14: Simulated S-parameters of tapered Open standards.

Short-circuit structures, commonly referred to as Short standards, are developed using a methodology that closely parallels the approach used for open-circuit structures. These standards are constructed to facilitate accurate reflection measurements within the calibration kit.

In terms of performance, the reflection coefficient (S11) for the Short standards demonstrate a pattern like that observed in the Open standards. Specifically, as both the physical length of the Short standard and the frequency of operation increase, there is a consistent reduction in the amplitude of S11. This decreasing trend is depicted in Fig. 2.15 and can be attributed to the combined effects of ohmic and dielectric losses within the structure.

The systematic design and analysis of these Short standards are essential for ensuring reliable calibration, as they provide a well-characterized reference for high-reflection conditions. Their behavior under varying lengths and frequencies offers valuable insights into the influence of physical and material properties on reflection performance.

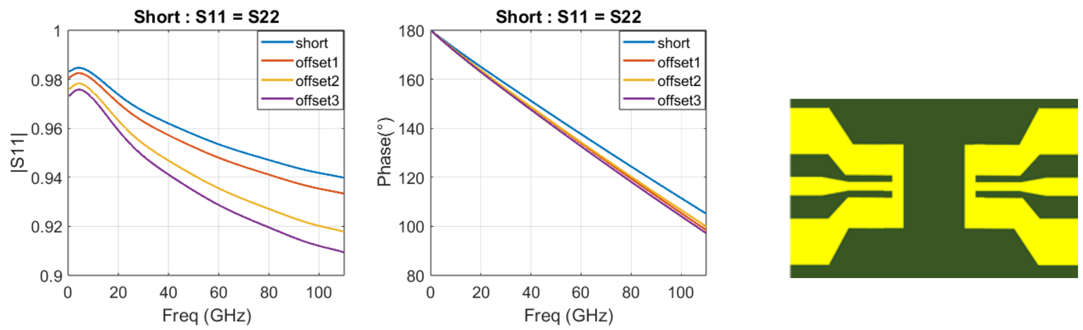

Fig. 2.15: Simulated S-parameters of tapered Short standards.

The components classified as matched loads, also referred to as Match or Load standards, are specifically engineered to facilitate the implementation of various calibration methods, including SOLT (Short-Open-Load-Thru), LRM (Line-Reflect-Match), and LRRM (Line-Reflect-Reflect-Match). Their design methodology closely parallels that employed for the reflective structures previously discussed. As depicted in Fig. 2.16, these matched loads are fabricated using a systematic approach that ensures consistency with other calibration standards within the kit.

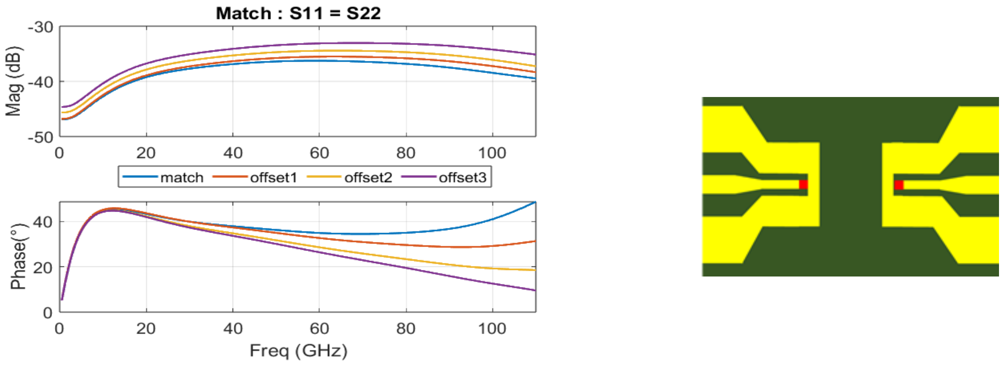

Fig. 2.16: Simulated S-parameters of tapered Load standards.

The verification kits are composed of several key components that serve distinct roles in the calibration process. These include attenuators, mismatched lines, and both one-port and two-port components featuring high series impedance. Each component is selected to provide a specific test condition, enabling comprehensive evaluation of calibration accuracy across a range of scenarios. These elements are integrated into the verification process to ensure that the kit offers robust and reliable performance under varying measurement conditions.

2.1.2.2. Calibration algorithm implementation and validation

Several calibration methods have been explored and are integrated with the developed calibration standards. These methods have been implemented within MATLAB software, utilizing simulation data derived from the various structures designed for this study. The structures serve dual roles, functioning both as reference standards and as test components within the calibration framework.

Fig. 2.17 illustrates the foundational assumptions considered during the simulation of measuring a component with a vector network analyzer, following calibration using the established standards. This figure consolidates all essential components required for the successful execution of the calibration procedure, providing a clear representation of the measurement process post-calibration.

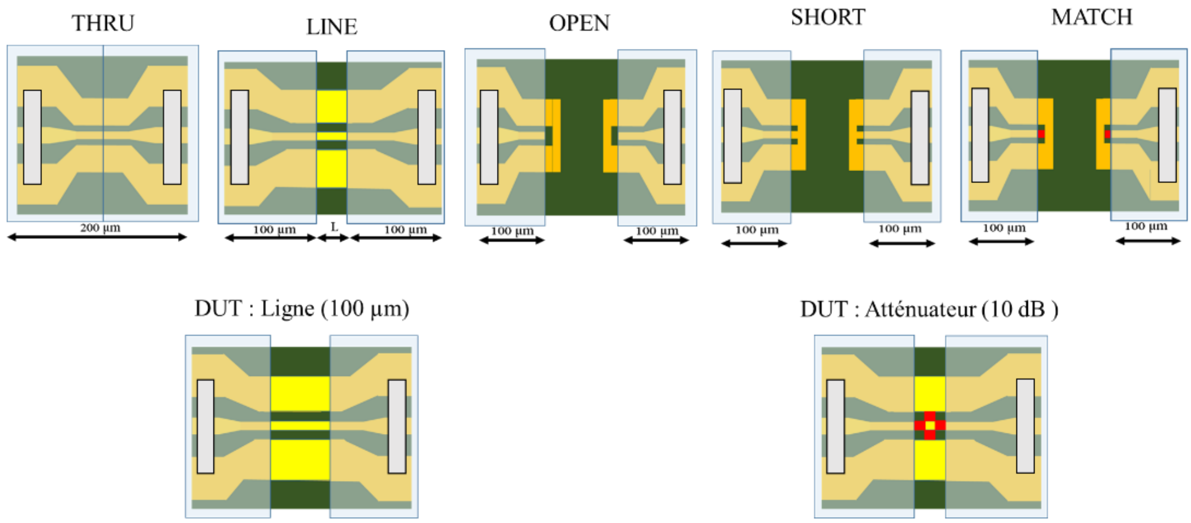

Fig. 2.17: Considerations for implementing calibration algorithms.

The Thru standard is conceptualized as a cascade consisting of two error boxes. In this model, the S-parameters obtained from simulation are treated as raw measurement data, representing the combined response of the system. This approach provides a foundational reference for calibration procedures, as the error boxes encapsulate all systematic imperfections present in the measurement setup.

When introducing a Line standard or any Device Under Test (DUT), the device is considered as being inserted between these error boxes. The error boxes themselves include the excitation bridges, which are depicted in grey color and serve as the measurement ports. This arrangement allows for a clear and systematic separation of the device intrinsic response from the errors introduced by the measurement system, facilitating accurate calibration and characterization.

a) Electrical characteristics of line

Coplanar Waveguide (CPW) lines possess unique attributes among waveguide structures, particularly in terms of their electrical properties. The characteristic impedance and the effective permittivity of CPW lines are determined by several factors. These include the dimensions of the cross section such as the width of the signal conductor, the width of the slots, the thickness of the metallic layer, and the height of the substrate as well as the intrinsic properties of the materials used [7].

A crucial aspect of accurate measurement lies in the calibration technique employed. Thru-Reflect-Line (TRL) calibration is particularly effective, as it enables the shifting of measurement reference planes directly to the ports of the Device Under Test (DUT) by utilizing the properties of the line itself [8]. The success of this calibration method is fundamentally dependent on precise knowledge of the line propagation constant and its characteristic impedance, the latter of which serves as the reference impedance for the component being evaluated.

The electrical characteristics of CPW lines can be determined through various approaches. One option is to use simulation software to extract these characteristics, or to calculate them based on the S-parameters obtained from such simulations and the corresponding analytical relationships. Alternatively, real measurements can be conducted using at least two lines of different lengths. By comparing the data from these two lines, the propagation constant can be evaluated. Subsequently, the line impedance is established after measuring the line capacitance [9]. This approach enables a thorough comparison of the properties observed in nanoscale (tapered) lines versus those in microscale (normal) lines, highlighting the influence of dimensional scaling on CPW performance.

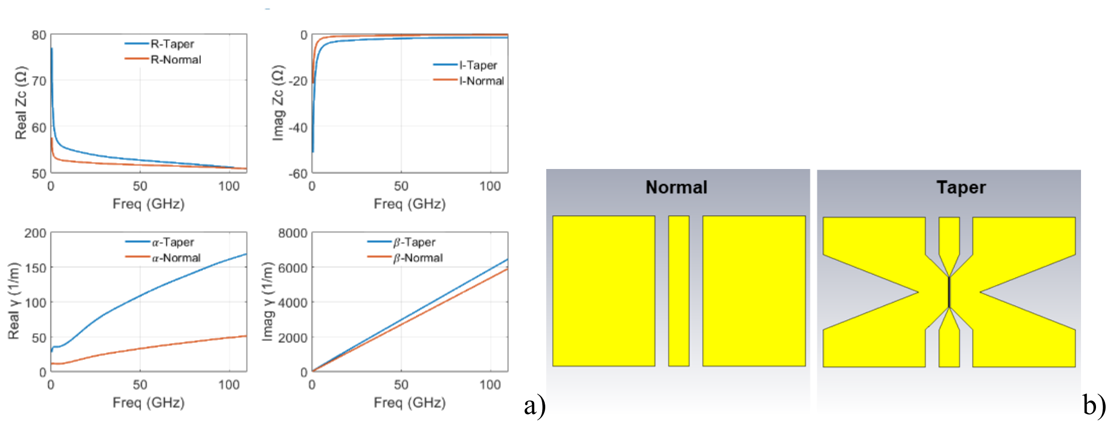

Fig. 2.18: a) Lines characteristics: propagation constant and characteristic impedance, b) Tapered and normal line.

Fig. 2.18 presents detailed information regarding the propagation constant and characteristic impedance of the lines, highlighting both their real and imaginary components. The imaginary part of the propagation constant, also referred to as the attenuation constant, indicates the extent to which the signal is attenuated as it travels along the line. This attenuation increases with frequency and is significantly more pronounced in the tapered line compared to the normal line. In contrast, the real part of the propagation constant, known as the phase constant, corresponds to the phase change experienced by the signal as it propagates.

Regarding the characteristic impedance, its real part remains close to 50 Ω, which is typical for such lines and confirms consistency with standard analytical models. The imaginary part of the characteristic impedance arises from conductor losses, reflecting the dissipative effects inherent in the line structure.

To facilitate a meaningful comparison of the responses of structures fabricated on two different substrates, it is necessary to account for their differing permittivity values. Although the substrates do not share the same physical properties, they must exhibit identical electrical lengths for the results to be comparable. This requirement dictates that the length of the line on alumina must be approximately 1.087 times greater than that on high-resistivity (HR) silicon. The difference in permittivity between the substrates means that the physical dimensions of the components must be adjusted accordingly, ensuring that both possess the same electrical length and enabling a consistent evaluation of their respective performance.

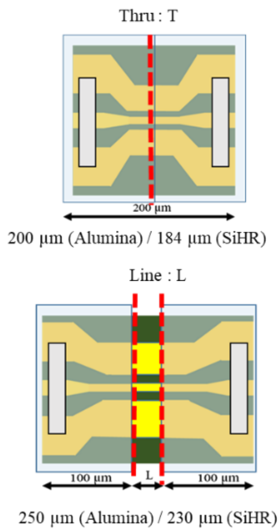

Fig. 2.19: Procedure for determining propagation characteristics.

To accurately determine the propagation characteristics of the coplanar waveguide (CPW) lines for each substrate, a systematic procedure was followed. This involved analyzing two lines fabricated with different lengths on the respective substrates. By conducting measurements on both lines, it was possible to extract the propagation constant γ, which characterizes how signals attenuate and phase-shift as they travel along the transmission line. The procedure is visually depicted in Fig. 2.19, which outlines the steps for evaluating the propagation constant using two distinct line structures. This approach ensures that the propagation characteristics are accurately determined for each substrate under investigation.

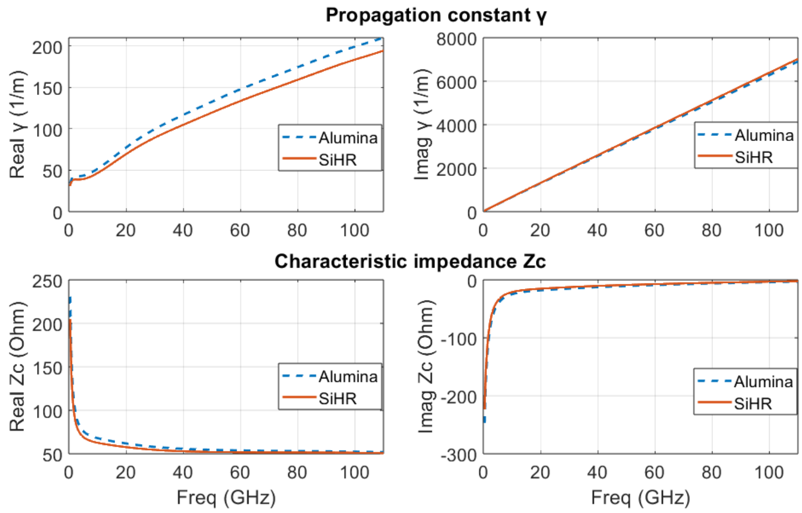

Fig. 2.20: Propagation characteristics – propagation constant γ and characteristic impedance Zc.

The propagation constant, denoted as γ, is a critical parameter in evaluating the performance of coplanar waveguide (CPW) lines. It consists of two components: a real part and an imaginary part. The real part of γ corresponds to the attenuation constant, which quantifies the extent of signal loss as it travels along the transmission line. Notably, this attenuation constant is influenced by both the operating frequency and the physical dimensions of the line. As the frequency increases, or as the dimensions of the line are reduced, the attenuation constant rises, indicating greater signal loss under these conditions.

The imaginary part of the propagation constant, on the other hand, represents the phase constant. This component describes the phase shift experienced by the signal as it propagates along the line, providing essential information about the behavior of the transmission path at various frequencies.

Turning to the characteristic impedance, noted as Zc, analysis reveals that its real part remains close to 50 Ω for both substrates under consideration. This consistency with the standard value is a strong indicator of the accuracy and validity of the analytical approach utilized in the evaluation process. The maintenance of this typical impedance value confirms that the structures behave as expected from a theoretical standpoint.

In contrast, the imaginary part of the characteristic impedance is attributed to ohmic losses within the conductor. These losses arise from the inherent resistance of the line material, reflecting the dissipative effects that impact signal transmission. Together, the real and imaginary components of γ and Zc provide a comprehensive understanding of the electrical properties and performance limitations of CPW lines fabricated on different substrates.

b) Calibration algorithm implementation and validation

To rigorously assess the structures, various calibration methods were implemented and evaluated through simulation. Standard structures served as the basis for this process, with simulation data generated for each. The calibration algorithms applied included the Thru-Reflect-Line (TRL), Line-Reflect-Reflect-Match (LRRM), and Line-Reflect-Match (LRM) methods. All simulations and analyses were conducted within MATLAB, enabling a detailed comparison of the algorithms' effectiveness.

Two representative components were selected to undergo this calibration process: a transmission line and a 10 dB attenuator, as depicted in Fig. 2.17. For the transmission line, simulations were carried out both for the complete structure including the so-called error boxes and for the device under test (DUT) alone, corresponding to the yellow-highlighted section. This dual approach allowed for a direct comparison between the uncorrected S-parameters (which include the influence of error boxes) and the corrected S-parameters obtained after calibration. Ultimately, the resulting calibrated S-parameters could be evaluated against the actual, intrinsic S-parameters of the DUT, providing insight into the accuracy and performance of each calibration method.

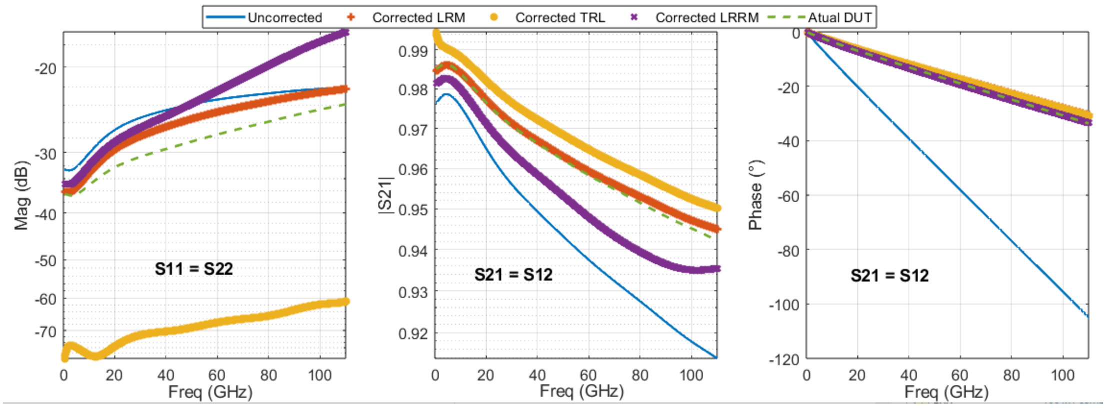

Fig. 2.21: S-parameters of line (before, after calibration, actual).

The primary objective of calibration, irrespective of the specific method implemented, is to mitigate the influence of error boxes (simulation approach). By employing calibration algorithms, the response can be corrected to more accurately reflect the intrinsic characteristics of the component.

A significant observation across all three calibration methods TRL, LRRM, and LRM is the change in the reflection coefficient, S11. This shift is a direct result of the unique procedures and assumptions inherent to each algorithm. Specifically, the LRM (Line-Reflect-Match) and LRRM (Line-Reflect-Reflect-Match) techniques are based on certain assumptions regarding the Reflect and Match standards. These standards, however, are not perfect, especially at higher frequencies, and as a consequence, the methods rely on approximations. Although both LRM and LRRM are self-determinative, these approximations can introduce discrepancies in the results.

In contrast, the TRL (Thru-Reflect-Line) method distinguishes itself by being an advanced and automated approach. It is less sensitive to the exact nature of the standards used, provided its fundamental conditions are satisfied. This robustness makes TRL an attractive option for accurate calibration, as it does not depend heavily on the ideality of the standards.

Regarding the transmission coefficient S21, its behavior remains relatively consistent across all calibration methods. Despite some minor discrepancies observed in the results (as illustrated in Fig. 2.21), the general trend and magnitude of S21 are preserved, demonstrating that each method is effective in capturing the essential transmission characteristics of the DUT.

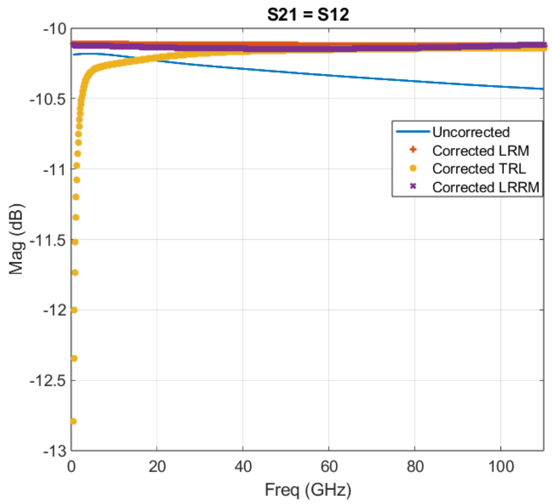

Fig. 2.22: S-parameters of 10dB attenuator (before, after calibration, actual).

Similarly to the transmission line case, a 10 dB attenuator was selected as the device under test (DUT) for calibration assessment. The calibration process revealed consistent observations with those previously noted for the transmission line, though minor differences emerged depending on the specific calibration method applied, as illustrated in Fig. 2.22. These discrepancies are attributable to variations in the standards utilized or to distinct features inherent to each algorithm's setup.

Additionally, several calibration algorithms were validated using the Advanced Design System (ADS). ADS provides a schematic interface that facilitates the modeling of circuit elements, including transmission lines, lumped components, and sources. The TRL calibration was implemented within ADS using the same considerations applied in CST Studio Suite. In this approach, error boxes were inserted between the sources and the DUT. This setup generates two sets of S-parameters: the actual S-parameters, representing the intrinsic response of the DUT, and the raw S-parameters, which include the influence of the error boxes, as shown in Fig. 2.23.

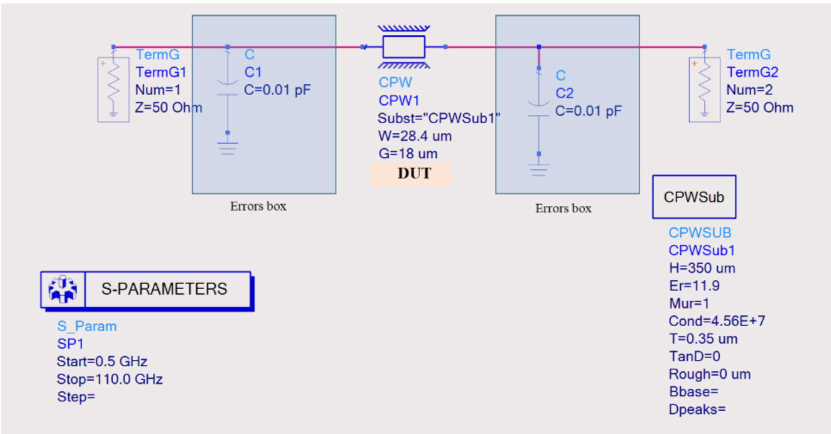

Fig. 2.23: Considerations using ADS.

Calibration in this context involves the extraction of two error boxes from the excitation ports. This is accomplished by employing thru, line, and reflect standards, which are essential for accurate calibration procedures. The application of these standards enables the isolation and correction of systematic errors introduced by the measurement system, ensuring that the S-parameters obtained reflect the true behavior of the device under test.

Through the implementation of these calibration steps, several key objectives of the project were achieved. Notably, components were designed that are suitable for use as S-parameter standards and verification devices at the nanometer scale. These components are paired with appropriate calibration algorithms to facilitate reliable measurements.

Ultimately, two distinct masks were developed, corresponding to the two substrates utilized in this project: Alumina and High-Resistivity Silicon. These masks serve as the templates for fabricating the calibration and verification components, ensuring the readiness of the designs for subsequent manufacturing processes.

2.1.2.3. Fabrication of calibration structures

After validating the structures and their corresponding calibration algorithms through simulations, the next critical step involved creating masks to facilitate the fabrication process. To accomplish this, KLayout, a widely used open-source software for layout visualization and editing was employed. It provides an intuitive platform for drawing, modifying, and transforming hierarchical layouts, which is essential for designing complex structures.

In addition to manual editing capabilities, KLayout offers scripting features that enable automated generation of layouts, making it a powerful tool for streamlining the design process. The software also supports thorough analysis of the layouts, ensuring design accuracy and readiness for subsequent fabrication steps. Fig. 2.24 illustrates the KLayout interface utilized during this phase.

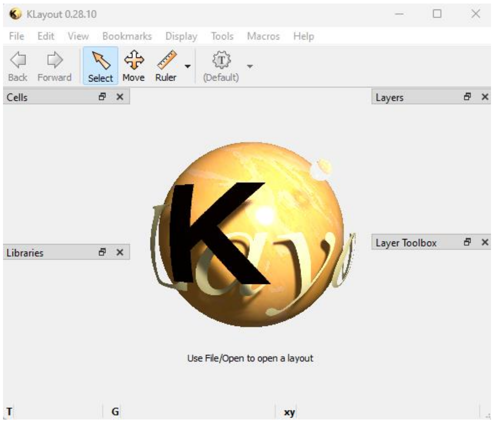

Fig. 2.24: KLayout interface.

The initial set of masks was developed to accommodate both types of substrates used in this project: Alumina (Al2O3) and High-Resistivity Silicon (HR-Silicon). For the Alumina substrate, the commercial specifications provided by the manufacturer were followed, including a diameter of 75.4 mm, a thickness of 350 µm, and a surface roughness (Ra) of less than 0.01 µm. The permittivity of Alumina falls within the range of 9 to 10.

Each mask was designed to integrate both micro- and nanoscale devices within a principal cell. To ensure the integrity and performance of the fabricated structures, it was necessary for every mask to adhere to certain guidelines, such as maintaining a minimum distance of 1000 µm between individual components.

Distinct patterns were specified for each fabrication level, including those for the metal conductor (gold), alignment marks, and resistive elements made from titanium. These design choices facilitate accurate alignment during fabrication and ensure reliable electrical performance of the finished devices.

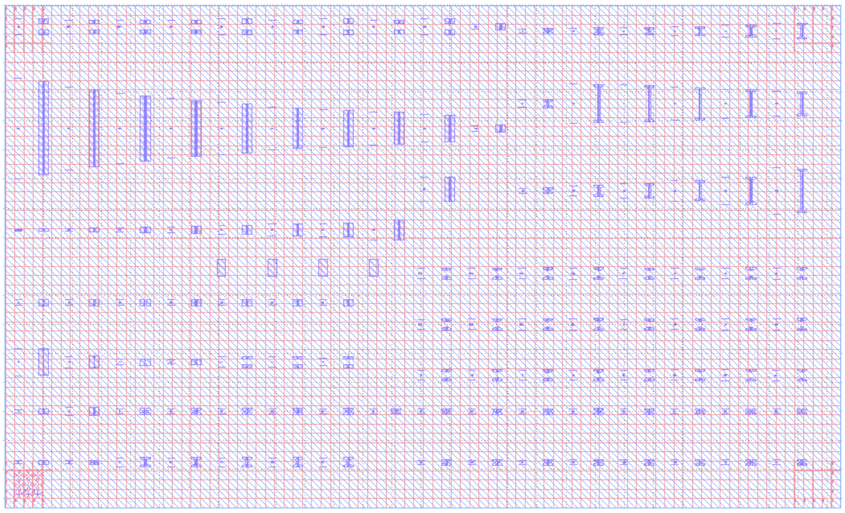

Fig. 2.25: First masks for calibration kits on Alumina and HR-Silicon with KLayout.

Fig. 2.25 is an example of the principal mask cell designed for this project. This cell incorporates all the essential components necessary for both calibration and verification procedures. By integrating these elements within a single layout, the mask cell ensures efficient use of substrate space and facilitates streamlined fabrication. The comprehensive arrangement includes micro- and nanoscale devices, as well as specific patterns for metal conductors, alignment marks, and resistive elements. Each component is strategically placed to comply with design guidelines, such as maintaining adequate spacing between devices, thereby supporting the reliability and performance of the final structures.

Although the actual fabrication process was not directly our responsibility, we maintained close collaboration with the manufacturing process engineer at IEMN. This partnership enabled us to gain valuable insights into certain aspects of structure realization throughout the project. The initial fabrication campaign was conducted simultaneously for both wafers, with the established procedures applied to each substrate accordingly.

The overall fabrication workflow can be divided into three distinct phases:

- **Phase I: First level – Fabrication of alignment marks**

The first phase of the fabrication process focused on creating alignment marks, which are essential for accurately positioning and locating different components throughout subsequent processing steps. This phase was systematically executed through six key steps to ensure precision and optimal adhesion of materials:

1. Wafer cleaning

The initial step involved thoroughly cleaning the wafer to remove organic impurities and ensure the surface was suitably prepared for resist adhesion. The wafer was sequentially cleaned using an acetone solution followed by an isopropanol (IPA) solution, with each cleaning step lasting five minutes. This procedure was critical for achieving a contaminant-free surface.

2. Resist Deposition (Spin-Coating) and Baking

Following cleaning, the wafer surface was treated with Hexamethyldisilane (HMDS) in "Open" mode to further enhance resist adhesion. The next stage involved the application of EL 13% resist, targeting a thickness of 600 nm. The resist was deposited using a spin-coating process, initially spinning at 1000 to 2900 rpm for 12 seconds with the lid closed, followed by 500 to 1000 rpm with the lid open. A brief soft bake was performed to dry the resin. Additionally, a layer of PMMA (polymethyl methacrylate) 3%

resist was applied to achieve a target thickness of 60 nm, ensuring the proper layering required for subsequent processing.

3. Electron Beam Lithography (EBL)

The third step utilized Electron Beam Lithography (EBL), in which a focused electron beam scanned the surface covered with the electron-sensitive resist [10]. This process, known as exposing, altered the solubility of the resist, thereby enabling selective removal of either exposed or non-exposed regions during development. EBL allowed for the precise definition of custom shapes, specifically forming the alignment marks that constituted the first level of the mask. These marks would later facilitate accurate alignment in following fabrication stages.

4. Development

Next, plasma etching is carried out to achieve the desired titanium layer thickness of 24 nm. This specific thickness yields a square resistance value of 48 Ω/□, ensuring the required electrical properties for the resistive elements.

5. Metallization

In the metallization step, a thin layer of titanium (10 nm) was first deposited onto the wafer to promote strong adhesion. Subsequently, a 100 nm layer of gold was applied, giving the alignment marks their distinct appearance. This dual-layer approach ensured both durability and visibility of the marks.

6. Lift-off

The final step in this phase was the lift-off process, which involved removing the excess resist and retaining only the precisely aligned metallic marks. This was accomplished by immersing the wafer in a bath at 70°C for 1 hour and 30 minutes. The result was a set of clean, well-defined alignment marks, ready to guide further fabrication steps.

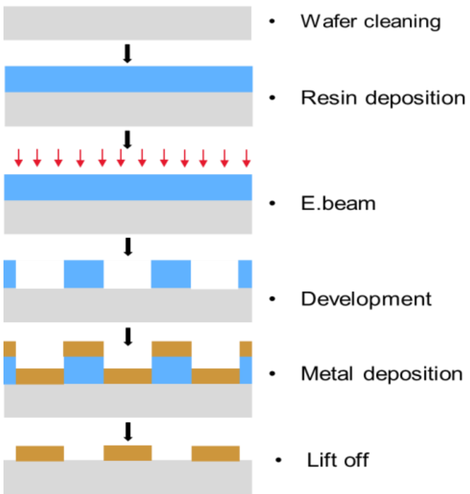

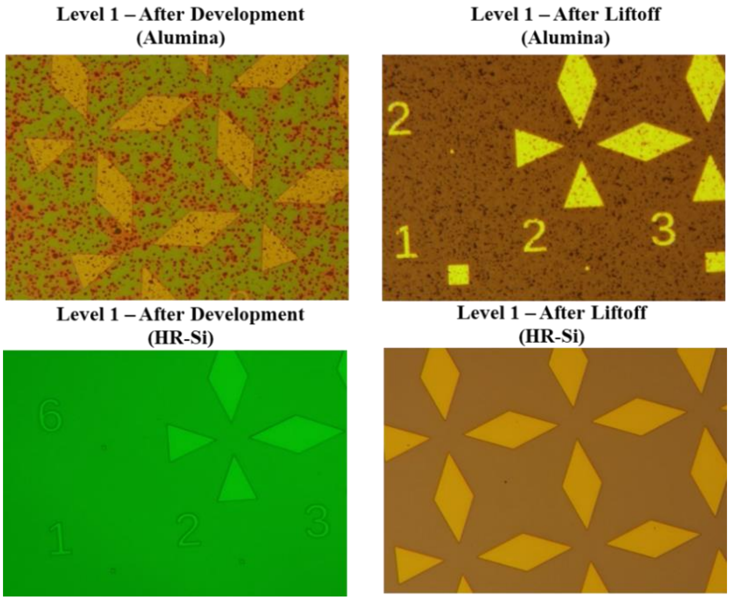

Fig. 2.26: Alumina and HR Silicon after phase I.

The images presented in Fig. 2.26 provide a clear indication of the pronounced roughness present on the alumina substrate. Upon examination of the scale associated with this surface roughness, it becomes evident that achieving miniaturized patterns on this substrate is not feasible. The significant unevenness poses a fundamental limitation, restricting the possibility of fabricating fine features during subsequent processing steps.

- **Phase II: Second level – Fabrication of Titanium Resistances**

The second level of the fabrication process focuses on creating resistive elements by depositing a thin layer of titanium. This phase consists of five sequential steps designed to ensure precise patterning and reliable performance of the titanium resistors:

1. Resist Deposition (Spin-Coating)

The process begins with a heat treatment to dehydrate the wafer. This is achieved by vacuum baking the substrate at an average temperature of 180°C for 10 minutes, which effectively eliminates any residual moisture. The dehydration step is critical and mirrors the procedure used in the fabrication of alignment marks during the previous phase. Once dehydration is complete, HMDS is deposited to promote adhesion of the resist.

2. Electron Beam Lithography (EBL)

Electron Beam Lithography is then employed to define the mask for level two, which corresponds specifically to the titanium resistors. The precise control offered by EBL enables the accurate formation of the desired patterns on the resist-coated surface.

3. Development

Following exposure, the wafer undergoes a development process. The resist is developed by immersing the wafer in a Methyl isobutyl ketone (MIBK) solution for one minute. This is immediately followed by a rinse in isopropyl alcohol (IPA) for 30 seconds to remove any remaining developer and to clean the wafer surface.

4. Titanium metallization

In this step, the plasma etching is handled to achieve 24 nm Titanium thickness with a square resistance value of 48 Ω/□.

5. Lift-off

The final step in this phase is the lift-off process. The wafer is immersed in a bath at 70°C for 1 hour and 30 minutes, which effectively removes any excess resist and leaves only the precisely aligned metallic marks. This step finalizes the formation of the titanium resistors, preparing the substrate for subsequent fabrication processes.

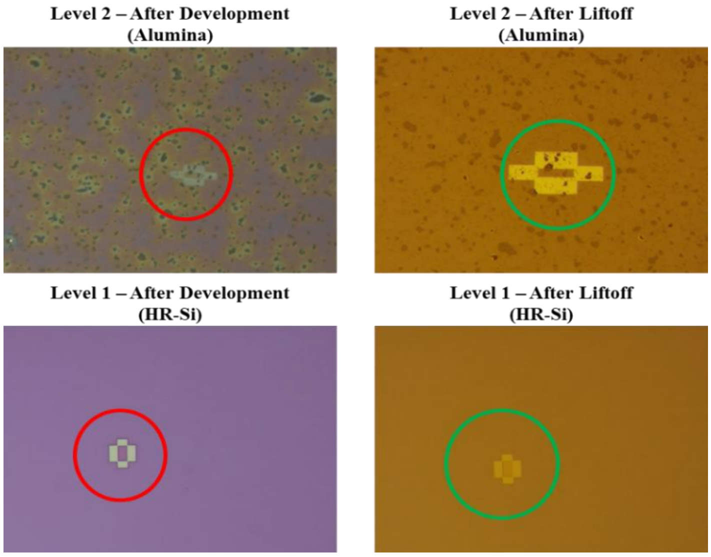

Fig. 2.27: Alumina and HR Silicon after phase II.

Fig. 2.27 illustrates the resistive components of an attenuator fabricated at the microscale for both Alumina and High-Resistivity (HR) Silicon substrates during phase II. In this stage, the Titanium elements are reduced to nanoscale dimensions. As a result of this miniaturization, surface roughness becomes a dominant factor, potentially affecting device performance and fabrication outcomes.

- **Phase III: Third Level – Fabrication of Gold Access Lines**

The third level of fabrication focuses on creating the access lines, which are essential components of the overall device structure. This process involves the sequential deposition of two metal layers: a thin titanium layer (25 nm) is first deposited to promote adhesion, followed by a gold layer (500 nm) to form the primary conductive pathway. The fabrication of these gold access lines is carried out in a series of five steps, mirroring the methodology applied in the previous phases (I and II). The depositions were made by evaporation.

Fig. 2.28 presents the outcomes of the last fabrication step for devices constructed at both the microscale and nanometric scale, using two types of substrates: Alumina and High-Resistivity (HR) Silicon. The results highlight the role of substrate surface characteristics in device fabrication success. While microscale structures can be achieved, their formation on Alumina proves challenging due to the substrate's pronounced graininess, which undermines the reliability of miniaturized components. Consequently, Alumina is not considered suitable for the fabrication of these small-scale devices.

In contrast, HR-Silicon demonstrates greater compatibility, supporting fabrication at both the micro and nanometric scales. However, the transition to nanoscale structures introduces additional challenges, as these devices are more susceptible to a range of defects. These limitations emphasize the necessity for further optimization in the fabrication process to enhance the quality and functionality of nanoscale components.

Level 3 – After Liftoff (Alumina)

Level 3 – After Liftoff (HR-Si)

Fig. 2.28: Alumina and HR Silicon after phase III.

The implementation of an optimization process became imperative in this phase, as attempts to fabricate nanometric components consistently resulted in failure, apart from a limited number of partially compliant structures. Recognizing these recurring challenges, discussions were undertaken to identify and evaluate alternative approaches that could enhance fabrication outcomes.

Ultimately, the chosen strategy involved a dual optimization pathway. The first aspect focused on dimensional optimization, specifically targeting the high-resistivity (HR) silicon substrate, which offers a smoother surface favorable for nanoscale fabrication. The second aspect addressed technical optimization within the fabrication process itself. It became clear that the thickness of the metallization layer was a decisive factor, directly affecting the practicality and reliability of the process. An excessively thick metallization layer posed the risk of exceeding the technological capabilities of the deposition equipment, which could jeopardize the successful realization of the intended nanoscale structures, as illustrated in Fig. 2.29.

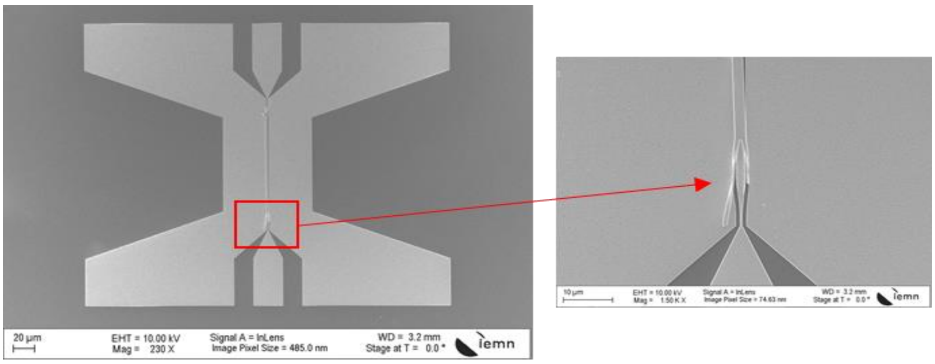

Fig. 2.29: Scanning electron microscope (SEM) view of a defective tapered line (1st fabrication run).

2.1.2.4. Optimization of dimensional parameters

While optimizing the fabrication process, particular attention was given to the dimensional parameters critical to the performance of the transmission line structures. Specifically, the width of the central strip (w), the metal thickness (e), and the gap between conductors (g) were systematically investigated. To thoroughly evaluate the influence of these variables, a simulation-driven methodology was employed, enabling a comprehensive analysis of how each parameter affects the characteristic impedance (Zc) of the transmission line.

During this assessment, each dimensional variable was individually scrutinized to determine its specific impact on the electromagnetic behavior of the structure. For example, by maintaining constant values for the width (w) and thickness (e) while varying the gap (g), the simulations revealed a clear trend: the characteristic impedance increases as the gap between the conductors becomes larger, as illustrated in Fig. 2.30. This insight is essential for guiding further optimizations and ensuring that the desired electrical properties are achieved in the final device.

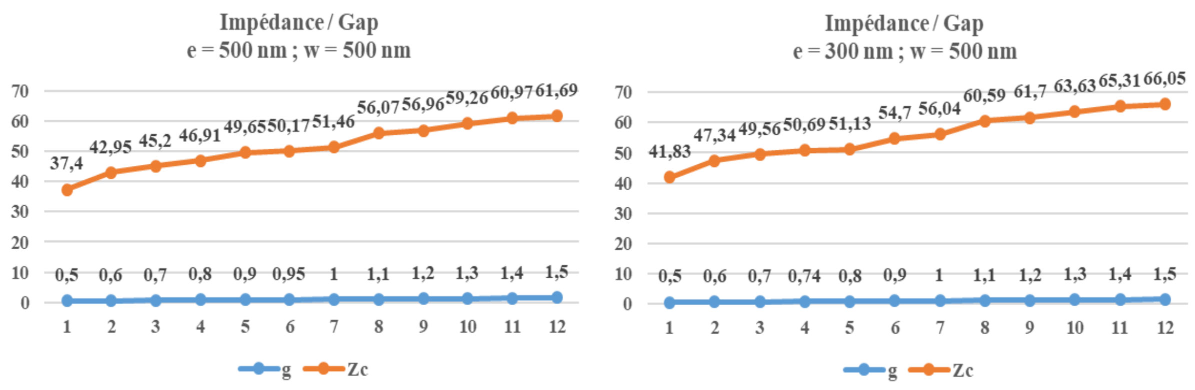

Fig. 2.30: Impact of the gap on the line characteristic impedance.

In Fig. 2.31, the relationship between the characteristic impedance (Zc) and the central trace width (w) was systematically evaluated. During this analysis, the metal thickness (e) and the gap (g) between conductors were kept constant to isolate the effect of varying the trace width.

The results revealed a clear trend: as the central trace or strip width (w) increases, the characteristic impedance (Zc) correspondingly decreases. This behavior underscores the importance of carefully controlling the trace width during the design and fabrication process, as it directly impacts the electrical properties of the transmission line structure.

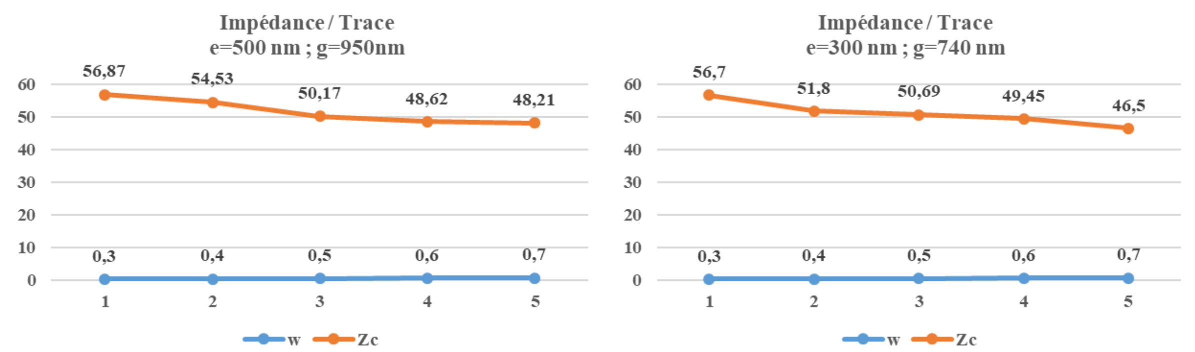

Fig. 2.31: Impact of the trace width on the line characteristic impedance.

In the final stage of the dimensional optimization process, the gap (g) and the width of the central strip (w) were held constant to isolate and analyze the effect of the metal thickness (e) on the characteristic impedance (Zc) of the transmission line. Through systematic evaluation, it was clearly demonstrated that increasing metal thickness leads to a decrease in the characteristic impedance. This inverse relationship, as depicted in Fig. 2.32, highlights the critical role of metallization thickness in achieving the desired impedance characteristics. By understanding and controlling this parameter, the fabrication process can be steered towards producing transmission line structures with optimal electrical performance.

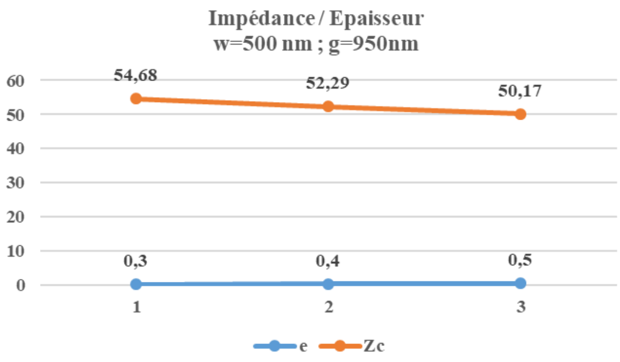

Fig. 2.32: Impact of the metal thickness on the line characteristic impedance.

The primary objective at this stage was to identify an appropriate balance among the dimensional parameters, specifically focusing on reducing the metallization thickness while ensuring that the transmission line maintains the target characteristic impedance of 50 **Ω**. Guided by the results of the systematic simulations and analyses described above, adjustments to the initial values were made to achieve the desired electrical properties. The revised dimensional parameters are presented in Table 2.4, reflecting the modifications applied to reach the optimal configuration.

Table 2.5: Dimensional parameters for optimization.

Parameters	Trace width w (nm)	Gap g (nm)	Metal thickness e (nm)
Initial	500	900	500
Final	500	850	350

To ensure the validity of the new dimensional parameters, straightforward verification was conducted using electromagnetic simulation. This simulation evaluated the dimensions specified in the table. The results, illustrated in Fig. 2.33, reveal that the characteristic impedance closely matches the target value of 50 **Ω** when the updated parameters (highlighted in red) are applied. This improved impedance alignment persists up to frequencies of 10 GHz, demonstrating the effectiveness of the revised design.

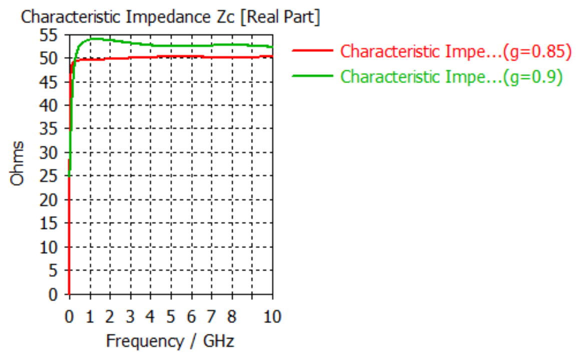

Fig. 2.33: Characteristic impedance for hold and new parameters values.

The results obtained for the updated dimensional parameters further confirm their effectiveness. Specifically, the newly selected set of values 500 nm for W (width), 850 nm for G (gap), and 350 nm for e (thickness) have been validated through simulation. This outcome demonstrates that these parameters provide the desired characteristic impedance, aligning closely with the target value. Therefore, the triplet (500 nm, 850 nm, 350 nm) can be considered optimal for the intended application, as verified by the electromagnetic analysis conducted.

2.1.2.5. Optimization of fabrication process

During the manufacturing stage, special attention was given to optimizing various steps of the process, with a particular focus on Electron Beam Lithography (EBL). The fabrication of nanoscale structures introduced notable technical challenges, primarily due to the need for high resolution. To address these challenges, precise control over the exposure time during EBL was essential to minimize proximity effects and achieve the desired resolution.

Additionally, the final liftoff step was carefully managed to ensure that the fabricated structures remained clean and free of residues. This step was critical in enabling high-yield fabrication, especially when operating at the resolution limits imposed by the available microfabrication technology.

To further refine the process, a specific dose test was conducted to establish optimal control over the EBL. In this test, the surface charge density was varied from 500 to 700 µC/cm2 in increments of 25 µC/cm2. This systematic approach allowed for the identification of a surface charge density of 625 µC/cm2 as the most suitable value, providing an effective compromise between resolution and process reliability.

Following these optimization efforts, the second fabrication run yielded well-defined structures, as illustrated in Fig. 2.34. In contrast to the initial run depicted in Fig. 2.23, where the signal trace width contacted the ground planes, the second realization demonstrated improved separation between these elements, indicating a significant enhancement in fabrication quality.

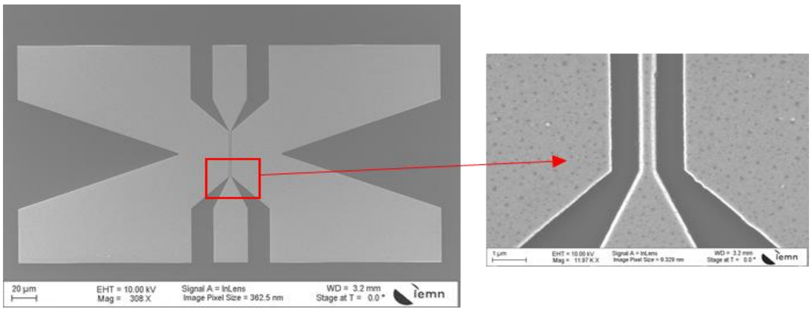

Fig. 2.34: Scanning electron microscope (SEM) view of a tapered TL (2nd fabrication run).

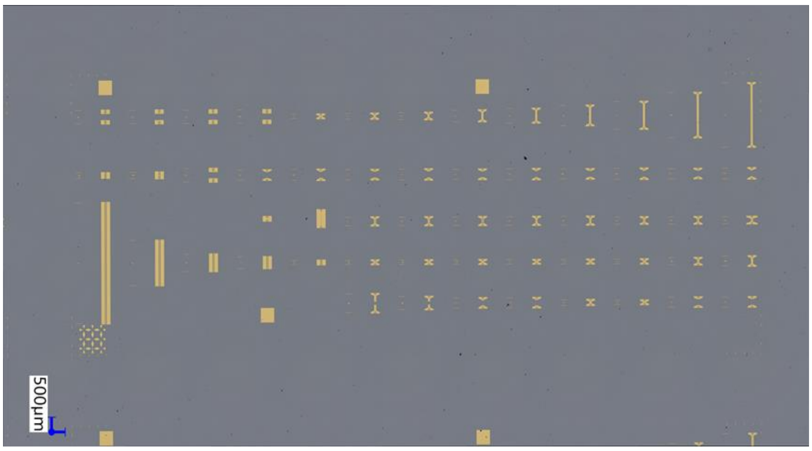

Fig. 2.35: HR silicon wafer with dedicated miniaturized CPW structures.

Fig. 2.35 presents an example cell from the second fabrication run, featuring a high-resistivity (HR) silicon wafer that contains both micro- and nanoscale structures designed for verification and calibration. Within this cell, the micrometer-scale devices were successfully fabricated and include several resistance elements, demonstrating effective implementation at the microscale.

However, several challenges emerged in the fabrication of nanoscale components. A number of these nanoscale elements exhibited defects, which were primarily associated with the length of the device and some resistive features, as depicted in Fig. 2.36. One specific issue encountered was the misalignment between the gold layer and the titanium resistance layer. Additionally, there were instances of overlapping between these two layers, particularly in the case of lumped element resistances. These issues highlight the complexities involved in achieving precise layer alignment and separation during the fabrication of nanoscale structures.

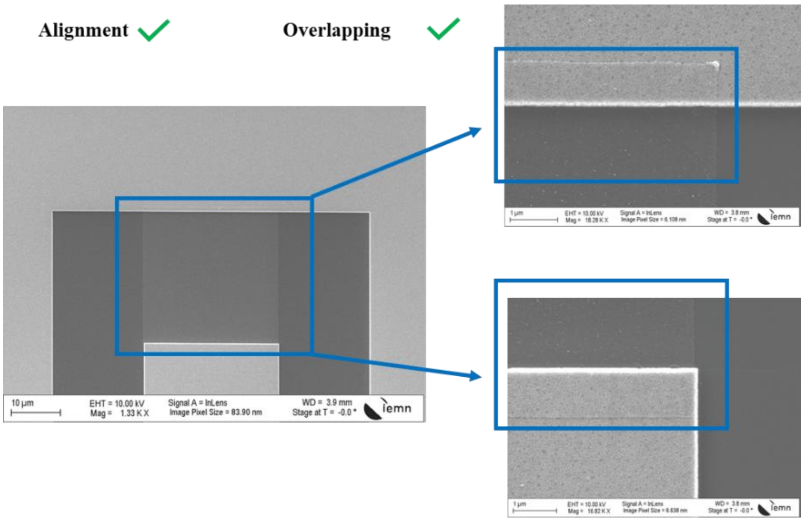

Fig. 2.36: Alignment and overlapping problem at microscale.

Fig. 2.37 displays a nanoscale load standard that was fabricated using a square resistance with a value of approximately 48 Ω per square. The creation of this standard highlights the critical importance of achieving precise focus during the Electron Beam Lithography (EBL) process. Any deviation in the EBL focus can have a significant impact on the resolution and quality of the nanoscale features. Furthermore, these observations underscore the necessity for meticulous control throughout the liftoff stage. Proper execution of the liftoff process is essential to ensure that the delicate nanoscale structures remain intact and free of unwanted residues, thereby preserving the electrical and structural integrity of the fabricated components.

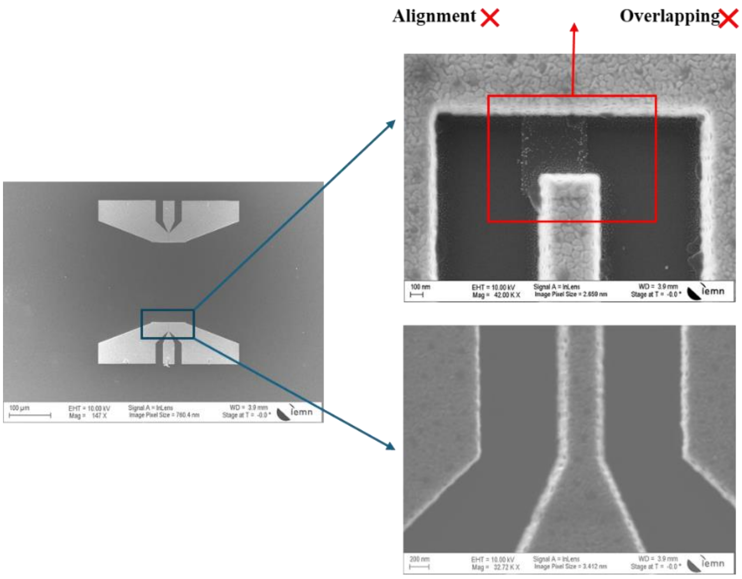

Fig. 2.37: Alignment and overlapping problem at nanoscale.

While the fabrication process demonstrated significant improvements for micrometer-scale devices, the realization of multiple long nanoscale coplanar waveguide (CPW) lines on a single wafer posed additional difficulties. Specifically, managing the electron beam lithography (EBL) process for these numerous and extended nanoscale structures became increasingly complex due to inherent limitations in the electron beam distribution. As the number and length of nanoscale CPW lines increased, precise and uniform exposure across the wafer became harder to achieve, which directly impacted the fidelity and consistency of the resulting features.

Conclusion

This work adopted a methodical process, beginning with the careful selection of standard structures and progressing to the design and optimization of calibration kits specifically tailored for microwave measurements. The initial decisions regarding the choice of technology, materials, and dimensions played a critical role in achieving the desired outcomes of miniaturization, high performance, and reproducibility.

During the design phase, rigorous electromagnetic simulations were conducted using specialized tools and clearly defined parameters. An initial set of structures was modeled and subsequently used to implement and validate the calibration algorithm, which leveraged the electrical characteristics of the transmission lines. The fabrication of prototypes allowed for a concrete assessment of the designed structures' behavior and highlighted areas requiring further optimization.

Subsequent optimization efforts focused on both the physical dimensions and the fabrication process itself, with the aim of improving the accuracy, repeatability, and robustness of the developed calibration kits. Through these advancements, this study establishes a solid foundation for more advanced applications in the measurement of complex RF devices and supports future progress in on-wafer S-parameter measurements at the nanoscale.

References 2

[1] Pengelly, R. S. (1975, September). Broadband Lumped Element X-Band GaAS FET Amplifiers. In *1975 5th European Microwave Conference* (pp. 301-305). IEEE.

[2] U-yen, K., D. Chuss, and E. J. Wollack. "Planar transmission line technologies." *Int. Conf. Technology Development for a CMB Probe of Inflation, Boulder, Colorado, USA*. 2008.

[3] Yoon, Yeong J., and Brace Kim. "A new formula for effective dielectric constant in multi-dielectric layer microstrip structure." *IEEE 9th Topical Meeting on Electrical Performance of Electronic Packaging (Cat. No. 00TH8524)*. IEEE, 2000.

[4] https://www.3ds.com/products/simulia

[5] qthelp://ads.2021update2/doc/adstour/ADS_Overview.html

[6] ARFTG94 B2 - Calibration Substrate Design for Accurate mm-Wave Probe-Tip Calibration (https://www.youtube.com/watch?v=-EnatD4RpAU)

[7] R. N. Simons, "Coplanar waveguide circuits, components, and systems," *John Wiley & Sons*, 2004.

[8] https://www.klayout.de/

[9] Williams, D. F., & Marks, R. B. (1991). Transmission line capacitance measurement. IEEE Microwave and guided wave letters, 1(9), 243-245.

[10] https://en.wikipedia.org/wiki/Electron-beam_lithography

Introduction

The radio frequency (RF) and microwave characterization of electronic devices plays a vital role in the development and performance evaluation of electronic systems. Before proceeding with device characterization, it is essential to calibrate the measurement system using traceable standards, which helps to correct systematic errors and ensure the accuracy of the results.

With the ongoing trend toward miniaturization and higher operating frequencies in technology, on-wafer measurements using advanced probe stations have become increasingly important. These methods offer a rapid solution that eliminates the need for intermediate packaging steps, enabling the direct and accurate assessment of both active and passive devices immediately following fabrication.

This chapter offers a clear and structured overview of the various device characterization methods, placing particular emphasis on techniques tailored to RF and microwave measurements. It begins by outlining the principal characterization methods employed in both industrial and research settings. The chapter then describes the architecture of a typical measurement setup, which integrates direct current (DC) and high frequency (RF) measurement instruments. Subsequently, the discussion turns to the specific measurement techniques and associated equipment, followed by an analysis of the experimental results, including an estimate of measurement uncertainties.

Finally, the chapter presents a comparison between the measured performance of the devices and existing standards or references. This comparison enables an evaluation of the compliance and reliability of the tested devices. Overall, the chapter aims to provide a thorough and rigorous overview of the on-wafer measurement process, aligning with the precision, repeatability, and standardization demands that are critical in RF and microwave applications.

1. DC and RF measurement setup

Establishing an appropriate measurement bench is essential for achieving accurate and repeatable on-wafer electrical characterizations. This process depends on the integration of specialized instruments and maintaining a carefully controlled testing environment. Such a setup accommodates both direct current (DC) and radio frequency (RF) measurements on miniaturized components that are directly accessible on the wafer surface.

At the heart of the on-wafer measurement system is the probe station. The probe station enables the precise placement of contact tips, or probes, onto the designated test pads of the component under test. Modern probe stations are equipped with advanced features to enhance measurement precision and flexibility. These features include a heated chuck, which facilitates temperature-dependent measurements; an optical or camera-based microscope, which provides accurate visual alignment of the probes; and micrometer or nanometer-driven translation stages, which allow for fine adjustment of probe positions. Together, these elements ensure reliable electrical contact and enable high-precision measurements directly on the wafer.

The probes are specifically designed to operate within defined frequency ranges. This frequency specialization ensures optimal performance for both DC and RF measurements, minimizing signal loss and reflections. By selecting probes tailored to the desired measurement frequencies, the accuracy and reliability of on-wafer characterization are maintained. The careful matching of probe capabilities with measurement requirements is a critical factor in achieving precise electrical contact and high-quality measurement results.

- DC probes are specifically designed for the application of static voltages or currents to the device under test and for the measurement of slow electrical responses, such as those associated with biasing and resistances. The typical configuration utilizes four probe tips. In this setup, two

of the tips are dedicated to injecting current from an external source into the test structure. The remaining two probes are positioned at a defined distance from the current injection points and are used to measure the potential difference, or voltage, across that separation. This arrangement is illustrated in Fig. 3.1.
This four-point probing technique enables precise resistance measurements by minimizing the influence of contact and lead resistances, thereby ensuring greater accuracy in the assessment of the device's true electrical properties.

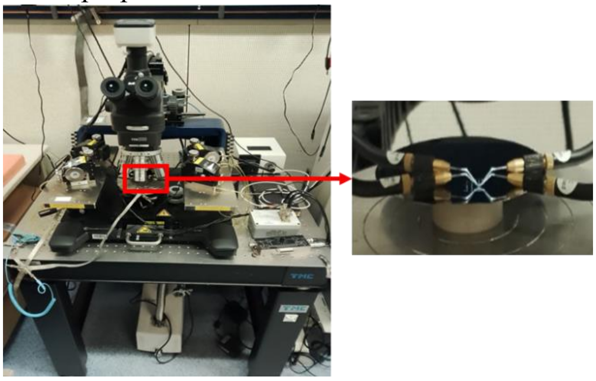

Fig. 3.1: DC measurement with four tips probes.

- RF probes are essential components in on-wafer measurement systems, specifically designed for the transmission of high-frequency signals while ensuring minimal signal loss. These probes are frequently constructed in a coplanar configuration, most commonly the Ground–Signal–Ground (GSG) type. This configuration is chosen because it optimizes impedance matching and effectively reduces signal reflections, thereby enhancing the accuracy and reliability of high-frequency measurements, as shown in Fig. 3.2.
  Although RF probes are primarily intended for use in radio frequency applications, their design versatility also allows them to be employed for direct current (DC) measurements. This flexibility enables a single probe setup to address both DC and RF characterization needs, streamlining the measurement process and improving overall efficiency in device characterization workflows.

Fig. 3.2: DC measurement with GSG probes.

The high-frequency measurement system used in this work consists of two primary components: a vector network analyzer and a probe station. Together, these elements form an integrated setup that supports highly precise on-wafer measurements. The probe station allows for accurate positioning and electrical contact with the wafer under test, while the VNA serves as the core instrument for characterizing the electrical properties of devices at high frequencies.

In this study, an on-wafer measurement system is employed in conjunction with a ZVA67 Rohde & Schwarz VNA, which is equipped with millimeter-wave extenders. This configuration, illustrated in Fig. 3.3, enables broadband frequency measurements ranging from 250 MHz up to 110 GHz. Such a wide frequency range is critical for thorough and accurate characterization of miniaturized components directly on the wafer surface, ensuring the reliability and comprehensiveness of the measurement results.

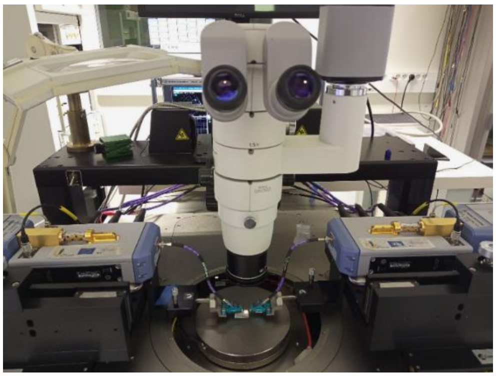

Fig. 3.3: Semi-automatic broadband On-wafer measurement system up to 110 GHz.

The measurement instrument used in this system is functionally equivalent to the R&S®ZVA110. It is comprised of an R&S®ZVA67 four-port base unit, which is augmented by two R&S®ZVA-Z110E W-band converters. These converters are equipped with electronic attenuators and diplexers, enhancing the overall measurement capability. The complete setup provides two test ports, each outfitted with 1 mm connectors located at the diplexer outputs. This configuration allows for flexible measurement across a broad frequency spectrum. Specifically, within the frequency range of 10 MHz to 67 GHz, the test signal is generated by the R&S®ZVA67 four-port network analyzer and directed to the 1 mm test ports through the diplexers. For measurements extending from 67 GHz up to 110 GHz, the system automatically switches the routing of the test signal. In this higher frequency range, the diplexers operate in conjunction with the converters to guide the test signal to the test ports via the converters and diplexers [1]. This systematic switching ensures seamless coverage across the full frequency range required for advanced on-wafer measurements.

2. Recommended tricks for On-wafer RF and Microwave Measurements

On-wafer measurements are inherently complex and face significant challenges related to achieving high accuracy and reliability in the results. Multiple factors influence the quality of these measurements, with variables stemming from both the measurement system itself and the human operator. Ongoing efforts in the field focus on developing autonomous instruments that can reduce operator influence and enhance measurement precision [2], [3], [4], [5].

A precise characterization of RF and microwave devices on the wafer demands the use of well-designed measurement systems. Such systems are essential for ensuring accuracy, repeatability, and the minimization of parasitic effects that can compromise data integrity. Proper installation of these measurement systems is critical and requires a combination of careful planning, precise alignment, and strict environmental controls.

This section outlines the key steps involved in establishing a reliable on-wafer measurement setup. The process emphasizes the importance of each phase, from planning and alignment to maintaining appropriate environmental conditions, to support the highest levels of accuracy and repeatability in RF and microwave device characterization.

- **Equipment setup**

The measurement system required for precise on-wafer RF and microwave characterization comprises several essential elements. Each component plays a distinct role in supporting the accuracy and reliability of measurement results.

A Vector Network Analyzer with the necessary frequency range forms the core of the measurement system. The VNA is responsible for generating and analyzing high-frequency signals, enabling the characterization of devices under test (DUT) with precision.

High-frequency signals are delivered to the DUT using specialized RF probes. The choice of probe depends on the configuration of the DUT. Common probes include Ground-Signal-Ground (GSG), Ground-Signal (GS), Ground-Signal-Signal-Ground (GSSG), and Ground-Signal-Ground-Signal-Ground (GSGSG) probes. Leading suppliers of these probes include FormFactor® and MPI®.

The probe station is designed to facilitate precise positioning and electrical contact with the wafer. Stations may be manual, semi-automated, or fully automated, and often feature micro or nano-positioners for enhanced alignment accuracy.

Specialized high-frequency cables are used to connect system components. These cables are selected based on their dimensions and performance characteristics, such as phase stability and low signal loss, which are critical for high-frequency measurements.

To assist with positioning and visualization during measurements, a display unit is connected to the system. This unit typically includes a high-resolution camera for detailed observation of the probe tips and DUT alignment.

Accurate measurements require systematic error correction, which is achieved by integrating a calibration substrate into the system. The most common type is an Impedance Standard Substrate (ISS), which provides reference standards for calibration procedures.

Fig. 3.4 provides an illustration of the fully assembled high-frequency measurement system, showcasing the integration of these key components.

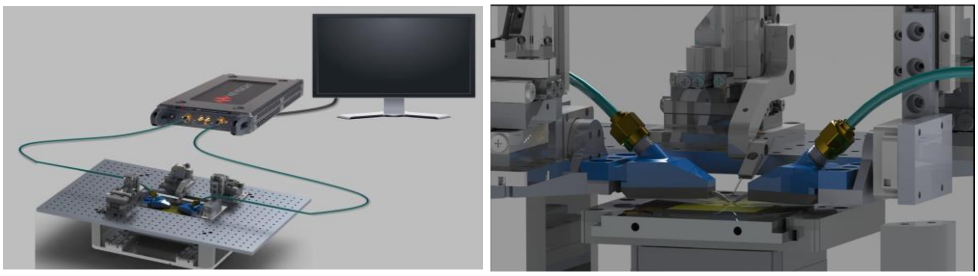

Fig. 3.4: Elements of high frequency measurement system.

In addition to the physical setup, the measurement system also incorporates essential software components that facilitate data acquisition and analysis. Typically, the Vector Network Analyzer is interfaced with a personal computer (PC), where specialized data processing software is installed to handle measurement data efficiently.

A variety of commercial software solutions are available for this purpose. These programs are designed to support advanced calibration routines and device modeling, ensuring the accuracy and reliability of the measurement results. Notable examples include vendor-specific and third-party software such as Keysight IC-CAP, Cascade WinCal, NIST MultiCal, and Anritsu software suites. Each of these platforms offers distinct capabilities for calibration and post-measurement data processing, thereby enhancing the overall functionality of the measurement system.

- **Mechanical integration**

Assembling the measurement system involves careful mechanical integration of all components to ensure reliable and precise operation. Each cable, adapter, connector, and the entire probe station must be securely mounted, as shown in Fig. 3.5. Attention to detail during assembly helps to prevent signal loss and mechanical issues that could compromise measurement accuracy.

It is essential to thoroughly verify the condition and positioning of critical elements, including the probes, wafer chuck, and positioners. Proper alignment and secure placement of these components are fundamental for achieving accurate contact with the device under test (DUT).

The use of a torque wrench is highly recommended during the assembly process. This tool enables the operator to apply the correct amount of force when connecting mechanical parts, preventing potential damage caused by overtightening or insufficient tightening. By following these practices, the integrity and performance of the high-frequency measurement system are maintained throughout the measurement process.

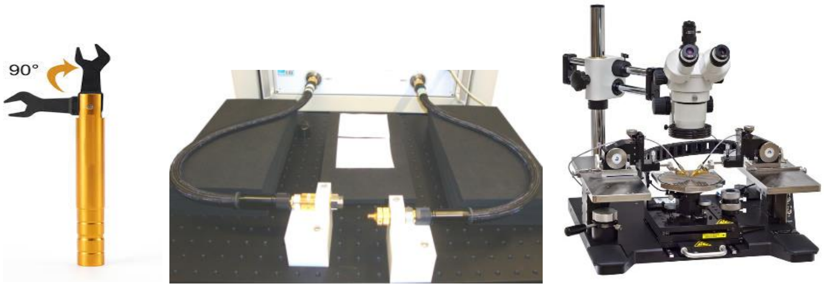

Fig. 3.5: Integration of the measurement equipment [6]-[7].

- **Configuration of Measurement system**

Measurement environment plays a critical role in ensuring the accuracy and reliability of precision measurements. Key factors such as mechanical vibrations, temperature, and humidity must be carefully managed to minimize potential sources of error.

It is recommended to maintain the measurement environment at the standard laboratory temperature for electrical measurements, which is 23°C. Consistent temperature control is essential, as fluctuations can affect the characteristics of calibration standards and introduce additional errors during Vector Network Analyzer calibration. In practical terms, temperature deviations of up to ±1°C from the standard value generally do not impact on the performance of typical VNA calibration standards [1].

Humidity also influences measurement outcomes, though its impact on VNA measurements tends to be minimal if extreme conditions are avoided. A relative humidity level of 40% ± 20% is recommended for optimal operation. Excessively high humidity can lead to unwanted condensation, while very low humidity increases the risk of electrostatic discharge, which may damage sensitive equipment such as VNA.

In addition to temperature and humidity, mechanical vibrations should be minimized within the measurement environment. Proper isolation and stabilization of equipment help prevent disturbances that could compromise measurement precision.

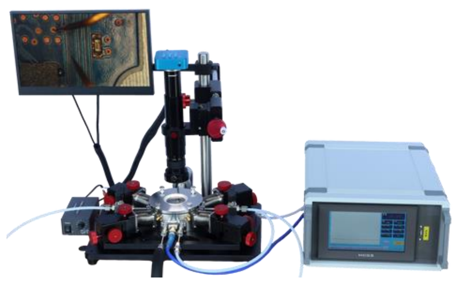

Fig. 3.6: Mini Vacuum Probe System with Temperature Control [10].

The mini vacuum probe system, as illustrated in Fig. 3.6, is equipped with advanced temperature control capabilities. This system enables precise operation across a wide temperature range, from −190°C up to 400°C, by providing both heating and cooling functions. Such temperature versatility supports a variety of measurement scenarios, accommodating both cryogenic and high-temperature testing requirements.

High-frequency test environments are typically sensitive to electromagnetic interference, which can adversely affect measurement accuracy. Minimizing electromagnetic interference is essential, as it helps to reduce unwanted coupling effects that may arise during testing [9]. Ensuring proper shielding and maintaining a controlled environment are important practices for achieving reliable results.

The alignment and contact of probes with the device under test (DUT) play a crucial role in the outcome of on-wafer measurements. Careful verification of probe positioning and proper engagement with the contact pads are critical steps in the measurement process [11]. Several parameters can impact the overall performance, including probe overtravel and skating.

Overtravel refers to the continued downward movement of the probe tip after it initially contacts the wafer surface. Skating is defined as the lateral movement or distance the probe tip travels along the surface of the contact pads during this overtravel [12], as depicted in Fig. 3.7. Both overtravel and skating must be carefully controlled to maintain the integrity of the contact and ensure consistent, accurate measurement results.

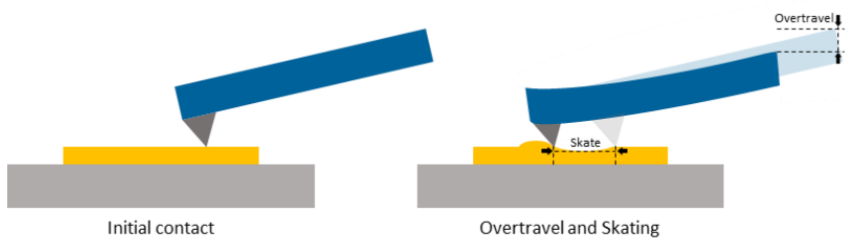

Fig. 3.7: Representation of the overtravel and the skating of a probe tip [11].

An essential aspect of conducting accurate RF and microwave measurements involves establishing an effective measurement protocol. The process begins by configuring the Vector Network Analyzer with appropriate measurement parameters. These parameters include selecting the desired frequency sweep range, setting the required output power level, adjusting the intermediate frequency bandwidth (IFBW), determining the number of measurement points, and configuring the averaging settings. Each of these parameters must be carefully chosen to align with the specific requirements of the measurement scenario.

Once the VNA parameters are set, the operator must decide whether to perform a calibration of the measurement system. Calibration can be accomplished using recognized calibration standards, with a selection of well-established calibration algorithms available. Common calibration methods include Short-Open-Load-Thru (SOLT), Line-Reflect-Reflect-Match (LRRM), Line-Reflect-Match (LRM), Thru-Reflect-Line (TRL), and Multiline TRL. Alternatively, the operator may opt to proceed with uncalibrated measurements, depending on the objectives and required accuracy.

On-wafer measurements present distinct challenges and demand adherence to good laboratory practices to ensure reliable outcomes. It is important to regularly check and clean the measurement probes, and to replace them, if necessary, to maintain optimal contact quality with the device under test. Additionally, drift effects which can compromise measurement accuracy over time should be addressed by periodically recalibrating the measurement system.

By ensuring that the on-wafer measurement setup is properly installed and maintained, users can achieve reliable RF and microwave characterization. Following structured planning, rigorous calibration, and consistent maintenance protocols fosters repeatability and accuracy across measurement campaigns.

3. Measurements and Results with bench up to 110 GHz

This section details the results obtained from measurements conducted using a semi-automatic RF/mm-wave characterization bench, which can operate at frequencies up to 110 GHz, as shown in Fig. 3.3. The measurement system is equipped with high-precision positioners, a vector network analyzer, and waveguide or coaxial probes that are suitable for the targeted frequency range.

The semi-automatic configuration of the bench plays a crucial role in ensuring the repeatability of measurements and minimizing variability introduced by the operator during both calibration and measurement processes.

- Vector Network Analyzer: Rohde & Schwarz® ZVA67 with mm-wave frequency extenders was used to cover the broad frequency span required for characterization.
- Frequency Band: The measurement campaign was carried out across a frequency range from 0.25 GHz to 110 GHz, accommodating both RF and mm-wave regimes.
- Intermediate Frequency Bandwidth (IFBW): The IFBW was set to 50 Hz, providing a balance between measurement speed and noise performance.
- VNA Output Power: The output power of the VNA was set to –15 dBm, which is suitable for sensitive device testing within the specified frequency range.
- Number of Frequency Points: A total of 440 frequency points were configured, with 201 points utilized in the dataset presented in this work.
- Impedance Standard Substrate (ISS): Calibrations were performed using a CascadeMicrotech® 138-357 ISS to ensure measurement accuracy and consistency.
- Environmental Conditions: All measurements were conducted in a controlled environment, with temperature maintained between 20.7°C and 23.0°C, and relative humidity kept between 38.8% and 42.0%.

3.1. DC measurements

Direct current (DC) measurements in this study are conducted to evaluate the electrical characteristics of coplanar waveguide (CPW) lines. These measurements are critical for quantifying parameters such as resistance, conductivity, and various distributed properties, including linear capacitance, inductance, and conductance. Unlike alternating current (AC) measurements, which involve a current that periodically reverses direction, DC measurements focus on circuits powered by a constant, unidirectional current source.

Two primary methods are employed to perform DC measurements in this work. The first method involves the use of the four tips technique, which enables precise measurement of resistance and related properties by minimizing contact resistance effects. The second method utilizes a configuration in which an RF bias tee is integrated into the probe station, allowing for the simultaneous application of DC and high-frequency signals. These setups are depicted in Fig. 3.1 and Fig. 3.2, respectively.

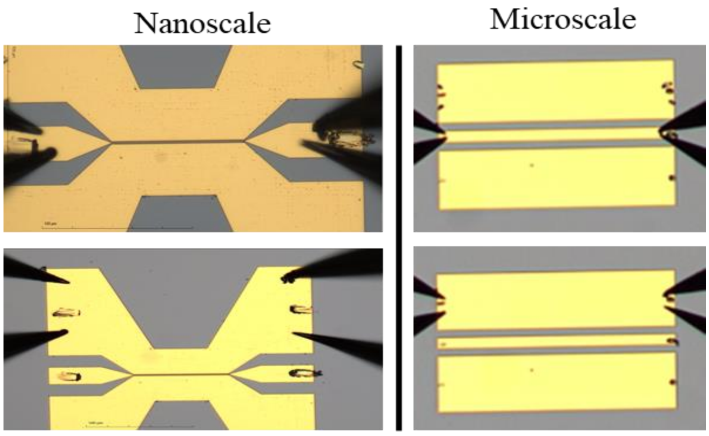

Fig. 3.8: DC measurement with four tips technique.

Fig. 3.8 illustrates the procedure for conducting direct current (DC) measurements on coplanar waveguide (CPW) lines through the application of the four tips technique. This approach was utilized for both nanoscale and microscale CPW structures, which were fabricated using gold. The measurement configuration involves the evaluation of both the center strip serving as the signal pathway and the ground plane for each structure. During testing, a current is injected into the CPW line, and the resulting voltage is recorded.

The resistance for each CPW structure is calculated using Ohm's law, represented by the equation U = R · I, where U denotes the measured voltage, R is the resistance, and I is the injected current. In these experiments, a current of approximately 100 mA is introduced into the CPW line. This technique enables accurate assessment of the electrical properties for both the signal and ground planes.

The effective DC resistance of the CPW line, referred to as Reff., is determined by the combined contributions from the strip resistance (Rs.) and the ground plane resistance (Rg). This relationship is defined mathematically by equation (E.3.1):

$$R_{eff} = R_s + R_g/2 \tag{E.3.1}$$

The measurement process focused on evaluating two coplanar waveguide (CPW) lines at the nanoscale and microscale levels. This dual-scale analysis was essential for accurately determining the specific linear resistance associated with each structure.

To obtain the specific linear resistance, the resistance values of both CPW lines were first measured. The difference between these resistance values was then calculated, as was the difference in lengths between the two respective lines. By dividing the difference in resistance by the corresponding difference in length, the specific linear resistance for each scale was determined.

A summary of the calculated specific linear resistance values for both the micro- and nanometric CPW structures is presented in Table 3.1.

Table 3.1: Results of DC measurement with methods of four tips.

	Nanoscale		difference	**Microscale**		difference
Length (µm)	250	300	50	200	4200	3550
R_s (Ω)	17.04	26.04	9	1.74	12.15	10.21
R_g (Ω)	0.32	0.42	0.1	0.34	2.36	2.02
R_{eff} (Ω)	17.2	26.25	9.05	1.91	11.33	11.42
R linear (Ω/m)			1.81×10^5			3.22×10^3

We can notice that the contribution of ground planes resistance is not very significant compared to signal resistance. The driven linear DC resistances are for nano and micro CPW lines are 1.81×10^5 Ω/m and 3.22×10^3 Ω/m respectively.

In addition, metal conductivity can be extracted by employing an empirical relationship that links the resistance (R), length (l), conductivity (σ), and section surface area (S), as given by equation (E.3.2). Given that the resistance of the strip is more pronounced than that of the ground planes, the section area of the signal trace is used as the reference surface for calculating the gold conductivity. This approach ensures that the extracted conductivity value accurately reflects the properties of the signal line, acknowledging its dominant contribution to the overall resistance.

$$R = \frac{L}{\sigma . S} \quad \text{(E.3.2)}$$

The section surface areas of the traces are determined by multiplying the trace width (w) by the gold thickness (t). For the nano and micro CPW (coplanar waveguide) lines, these calculated surface areas are 1.75×10^{-13} m^2 and 9.45×10^{-12} m^2, respectively. Based on these values, the corresponding conductivities are found to be 3.175×10^7 S/m for the nano CPW line and 3.61×10^7 S/m for the micro CPW line.

Additionally, DC measurements were performed using a probe station equipped with an RF bias tee. This setup allows for the direct measurement of the effective DC resistance across the entire CPW lines, providing practical values for comparison with the calculated resistances and conductivities.

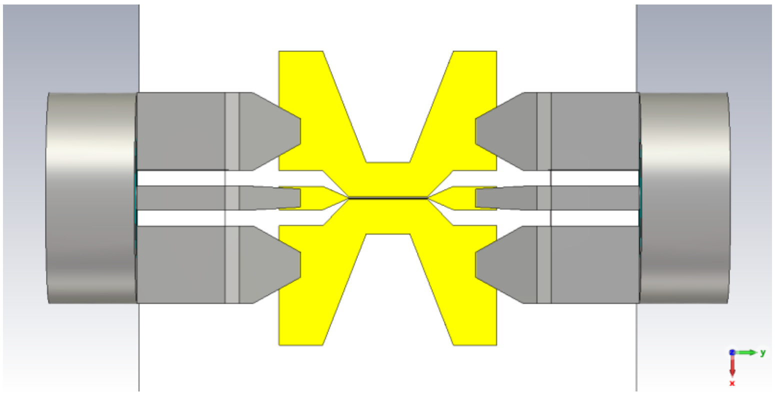

Fig. 3.9: Top view of CPW line with GSG probe in CST.

The distinction between this approach and the previous technique lies in the specific contribution to internal resistance. While this method introduces a certain amount of internal resistance approximately 1.8 Ω it is important to note that this contribution, though present, is not the main factor influencing the overall performance. The difference in internal resistance sets this technique apart, even though its effect remains relatively modest when compared to other elements in the system.

Table 3.2: Results of DC measurement with probe station (RF bias tee).

Lignes (Micro)	N1	N2	N3	N4	N5	N6	
L(m)	2.00E-04	2.50E-04	3.00E-04	4.50E-04	7.50E-04	2.25E-03	
R(Ω)	3.75	4	4.5	5.2	5.8	9.4	
Lignes (Nano)	L1	L2	L3	L4	L5	L6	L7
L(m)	2.00E-04	2.50E-04	3.00E-04	4.50E-04	5.50E-04	7.50E-04	1.00E-03
R(Ω)	11.6	20.4	29.2	55	73	109	153

A graphical analysis of the data clearly demonstrates the relationship between DC resistance and the length of the transmission line, as depicted in Fig. 3.10. The plotted trend shows that DC resistance is directly and explicitly dependent on the line length, indicating a linear relationship between these two parameters.

By examining the slope of the trend curve also referred to as the tangent or slope it becomes possible to determine the linear resistance of the line. This slope corresponds directly to the coefficient in the equation representing the curve. Through this approach, the distributed or linear DC resistance can be automatically extracted from the graphical data without the need for additional calculations.

The analysis yields specific values for the linear DC resistance of coplanar waveguide (CPW) lines at different scales. For micrometer-scale CPW lines, the calculated linear DC resistance is 2543.2 Ω/m. In contrast, for nanoscale CPW lines, the value is significantly higher, at 177111 Ω/m.

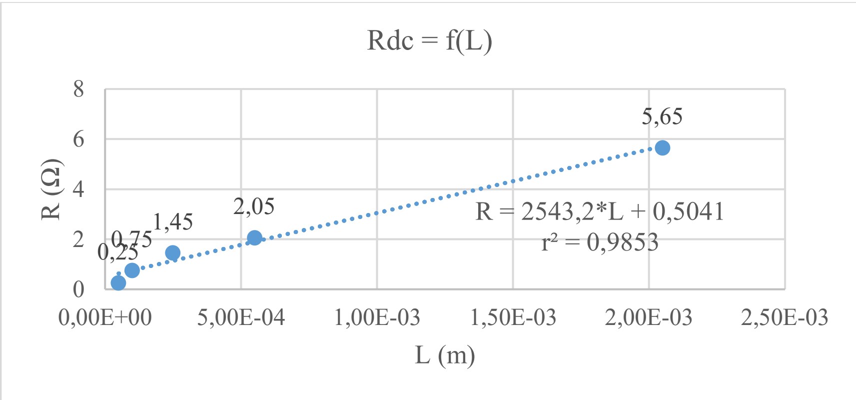

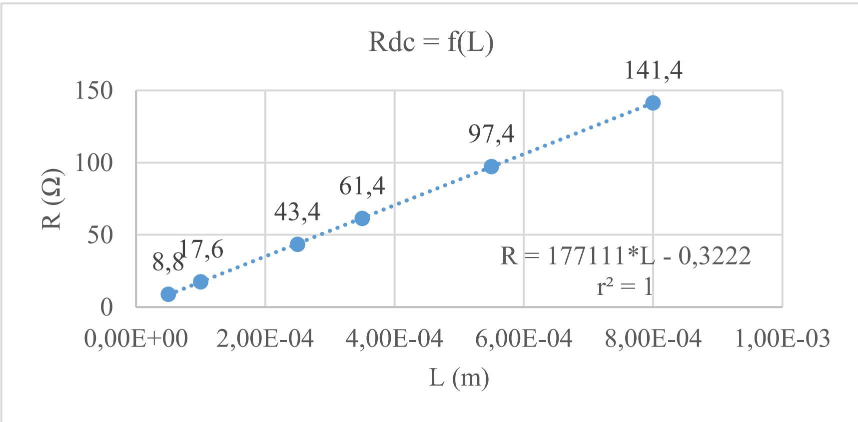

Fig. 3.10: DC resistance with line length at micro and nanoscale.

An additional noteworthy aspect of the findings presented in Fig. 3.10 is the ability to determine the conductivity of the transmission lines using the same equation (E.3.2) applied earlier. In this context, the extraction of conductivity is less direct, as it is embedded within the coefficient of the curve equation derived from the graphical analysis. This coefficient corresponds to the factor $\frac{1}{\sigma . S}$ in equation (E.3.2).

By analyzing this relationship, the conductivity values for both micro- and nanoscale transmission lines were estimated. Specifically, the conductivity for the micrometer-scale transmission line is approximately 4.16×10^7 S/m, while for the nanoscale transmission line, it is about 3.24×10^7 S/m. These values provide further insight into the electrical properties of the respective transmission lines and are consistent with the established relationship between conductivity, resistance, and dimensional parameters as described by the governing equation.

3.2. Extraction of electrical characteristics CPW line

Transmission lines play a critical role in microwave and millimeter-wave circuits, with coplanar waveguides (CPWs) being particularly prevalent. The planar structure of CPWs makes them especially advantageous for integration with both active and passive circuit components. This compatibility extends to monolithic microwave integrated circuit (MMIC) technology, where CPWs are favored for their efficient integration, reduced radiation losses, broadband performance, and ease of access for probing.

Transmission lines, including CPWs, can be modeled as networks of distributed elements. These elements linear resistance (R), inductance (L), capacitance (C), and linear conductance (G) collectively define the electrical properties of the line. Understanding and accurately characterizing these electrical characteristics is essential for the effective design and optimization of CPW-based devices.

Key electrical characteristics of interest include the propagation constant (γ), effective permittivity ($\varepsilon_{r,eff}$), characteristic impedance (Z_0), and losses attributed to both the conductor and the dielectric material. The investigation of these parameters is fundamental to predicting and enhancing the performance of CPWs in various applications.

There are multiple methods available for accessing and determining the propagation characteristics of CPW lines. These approaches provide valuable insights for engineers and designers aiming to develop high-performance microwave and millimeter-wave circuits utilizing coplanar waveguides.

a. Analytical Method

Analytical models are essential tools for evaluating the electrical characteristics of coplanar waveguide (CPW) transmission lines. These models rely on mathematical functions that take into account both the dimensional and material parameters of the structure. Specifically, they require detailed information about the cross-sectional dimensions of the CPW line, as well as the physical properties of the materials involved, including the conductivity (σ) of the conductor and the dielectric constant (ε) and loss tangent ($\tan\delta_\varepsilon$) of the substrate. Reference [13] provides a comprehensive overview of these requirements. Fig. 3.11 illustrates the necessary parameters needed to accurately assess the electrical characteristics of a CPW transmission line.

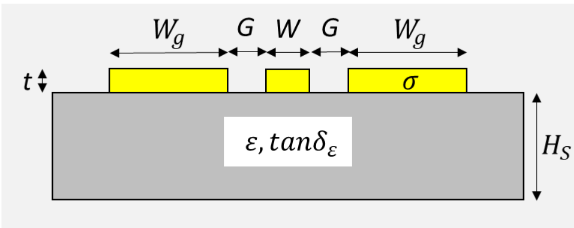

Fig. 3.11: Dimensional and material parameters of CPW line.

The analytical models employed for evaluating coplanar waveguide (CPW) transmission lines utilize a quasi-static analysis, primarily relying on conformal mapping techniques. These models incorporate elliptic integral functions that consider both the air and substrate regions of the transmission line. By doing so, they enable the determination of the line's linear distributed elements, such as resistance, inductance, capacitance, and conductance. As a result, they also facilitate the calculation of important parameters like characteristic impedance and propagation constant, as referenced in [13–15].

Furthermore, these analytical approaches allow for the integration of additional effects into the calculation framework. Specifically, they can be extended to include considerations such as losses, conductor surface roughness, dispersion, and radiation effects that vary with frequency, as described in references [16–18].

To practically implement these analytical models, a MATLAB script was developed based on the methodologies outlined in the cited literature. This script was used to compute the electrical parameters of the CPW transmission line at both micro and nanoscale dimensions. The calculations were carried out using the final section dimensions, which are detailed in Table 2.4 of Chapter 2.

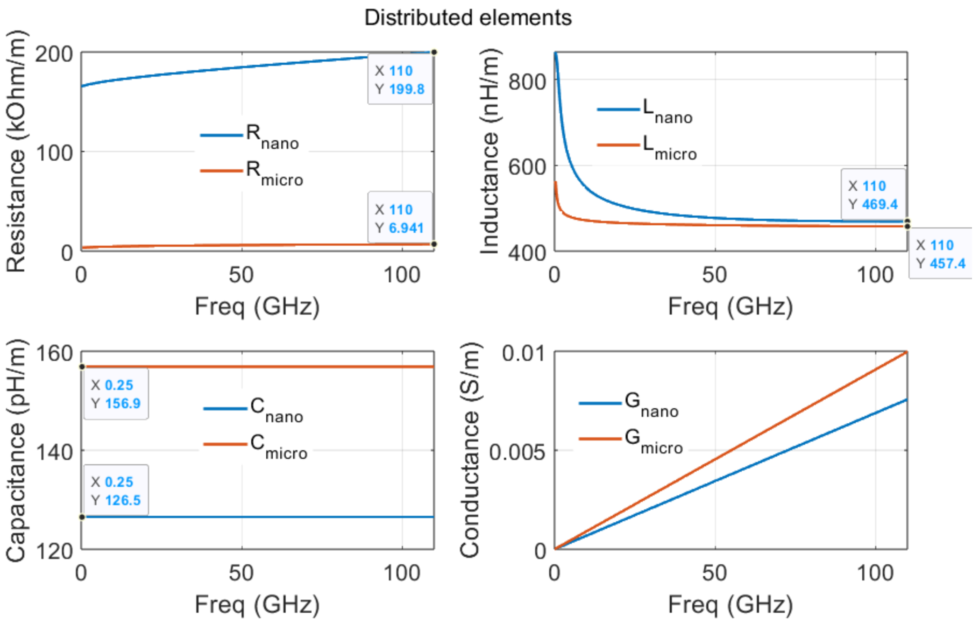

Fig. 3.12: Distributed elements of CPW line at nano and micro level from analytic CPW model.

Fig. 3.12 provides an analytical evaluation of the linear distributed elements specifically resistance, inductance, capacitance, and conductance for both micro and nano-scale coplanar waveguide (CPW) transmission lines. The results reveal notable differences between the two scales.

Firstly, the resistance and inductance values are higher in the nano CPW line compared to those observed in the micro CPW line. This indicates that as the dimensions of the transmission line decrease to the nanometric level, both resistive and inductive effects become more pronounced.

In contrast, the capacitance and conductance of the nano CPW line are lower than those of the micro CPW line. It should be noted that while conductance remains low at both scales, its value is still reduced at the nanoscale. These differences in electrical parameters play a significant role in defining the overall behavior of CPW lines at varying dimensions.

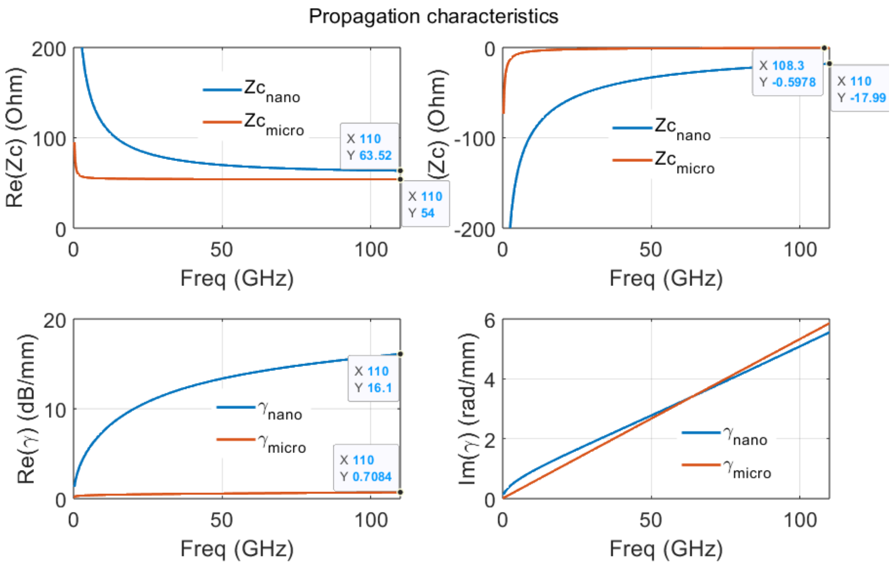

Fig. 3.13: Characteristic impedance and propagation constant at nano and microscale from analytic CPW model.

Fig. 3.13 presents a detailed comparison of the propagation characteristics for coplanar waveguide (CPW) transmission lines, as determined by the analytic model. One of the key parameters, the characteristic impedance (Zc), is found to be noticeably higher at the nanoscale compared to the microscale. Specifically, the real part of the characteristic impedance, which reflects the effective resistance of the transmission line, is 54 Ω at a frequency of 110 GHz for the microscale CPW. In contrast, this value rises to approximately 63.52 Ω at the nanometric scale. This increase highlights the more pronounced resistive nature of the line as its dimensions are reduced.

The imaginary component of the characteristic impedance is indicative of ohmic losses within the CPW structure. These losses become more significant at the nanoscale, contributing to the overall attenuation of the signal.

Turning to the propagation constant (γ), the real part, known as the attenuation constant, is relatively larger at the nanometric scale. This reflects the greater signal attenuation experienced by the nano CPW line. On the other hand, the imaginary part of the propagation constant, which corresponds to the phase constant, exhibits a distinctive "pinch" for the nanoscale CPW. This phenomenon results from the delay introduced by impedance mismatches and the higher impedance present at lower frequencies in nano-sized lines.

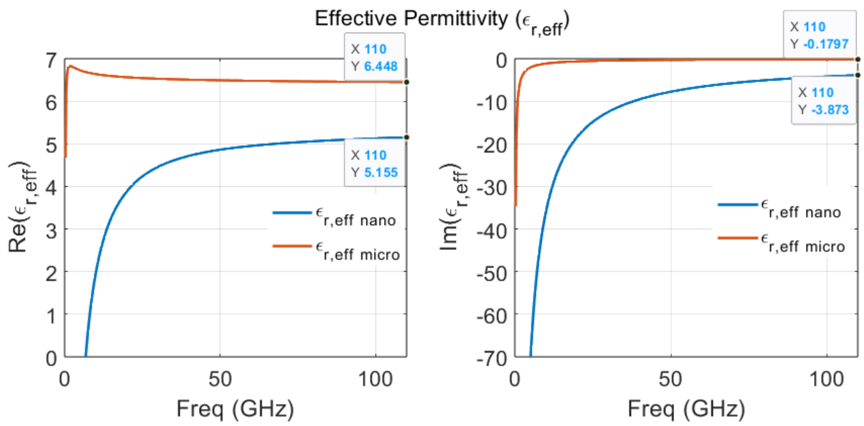

Fig. 3.14: Effective permittivity at nano and microscale from analytic CPW model.

The effective permittivity, denoted as $\varepsilon_{r,eff}$., for both micro and nanoscale coplanar waveguide (CPW) structures is depicted in Fig. 3.14. This parameter characterizes the dielectric environment experienced by the electromagnetic waves propagating through the transmission lines.

Of particular importance is the imaginary component of the effective permittivity, which represents the effect of dielectric losses within the structure. Notably, these losses are more pronounced at the nanoscale, indicating that signal attenuation due to the dielectric medium is a significant factor when the dimensions of the CPW line are reduced.

Effective permittivity can be derived from the propagation constant, using specific formulas. This relationship allows for a quantitative assessment of how the dielectric properties influence the propagation characteristics of the CPW transmission line.

$$\varepsilon_{reff} = -(\frac{c}{2\pi f}\gamma)^2 \tag{E.3.3}$$

The observed difference in the real part of the characteristic impedance between nano and micro CPW lines can primarily be attributed to variations in the shape ratio of their cross-sections. As depicted in Fig. 3.15, the cross-sectional geometry of the CPW line plays a significant role in determining its electrical properties. Changes in the width-to-height ratio or the aspect ratio of the conductors and gaps can lead to notable discrepancies in the resistance and impedance values. This geometric influence becomes especially pronounced when comparing microscale and nanoscale structures, where even slight alterations in dimensions may result in marked changes in the overall impedance characteristics of the transmission line.

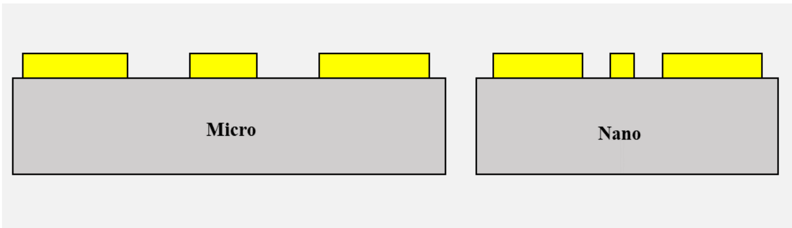

Fig. 3.15: Shape ratio of cross-section between micro and nano CPW lines.

Another approach to understanding the propagation characteristics of coplanar waveguide (CPW) transmission lines is through the analysis of S-parameters, which are directly related to signal behavior along the line. Specifically, the transmission coefficient (S21) and reflection coefficient (S11) serve as key indicators of line performance at different scales.

Fig. 3.16 displays the S21 and S11 coefficients for both nano and micro CPW structures. At the nanometric scale, the transmission coefficient S21 is observed to be lower, indicating greater attenuation of the signal as it propagates through the line. Conversely, the reflection coefficient S11 is higher at this scale, reflecting increased signal reflection, which is typically a result of impedance mismatches and more significant losses inherent to the nano-sized geometry. These trends in S-parameter values reinforce the previously discussed findings regarding greater attenuation and resistive effects in nanoscale CPW transmission lines.

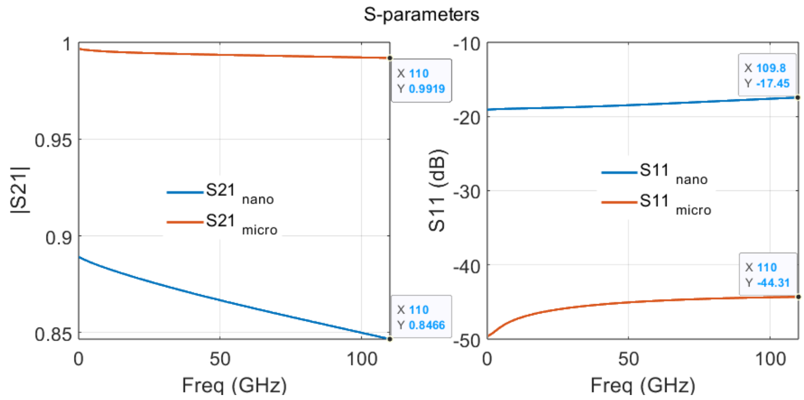

Fig. 3.16: S-parameters 100 µm length CPW line at micro and nanoscale from analytic CPW model.

As previously discussed, signal attenuation is significantly greater in nanoscale coplanar waveguide (CPW) transmission lines compared to their microscale counterparts. This heightened attenuation at the nanoscale is closely associated with increased dielectric losses and more pronounced resistive and impedance effects, all of which become more impactful as the dimensions of the CPW line are reduced.

Analytical models for CPW structures provide a valuable means of investigating and predicting the propagation characteristics of these transmission lines. Through these models, it is possible to gain a quantitative understanding of how changes in geometry and dielectric properties can influence signal behavior. Despite the incorporation of increasingly sophisticated factors to more accurately reflect real-world scenarios, analytical results often show discrepancies when compared to actual or simulated outcomes. This highlights the inherent limitations of purely analytical approaches, particularly as structural dimensions approach the nanoscale.

b. Full Wave Analysis Method

This technique involves conducting either circuit-level or three-dimensional electromagnetic simulations to analyze and design high-frequency structures. A variety of simulation tools are available for this purpose, each offering robust capabilities to accurately model and predict the behavior of complex transmission lines. Notable examples of such tools include CST Studio Suite, HFSS ENSYS, COMSOL Multiphysics, and Advanced Design System (ADS).

In practice, work is often carried out using both CST Studio Suite and ADS to leverage the strengths of each environment. Figure 3.17 presents a visual representation of CPW line simulations within these two software platforms, illustrating how both tools can be employed to investigate the electrical characteristics of transmission lines at different scales.

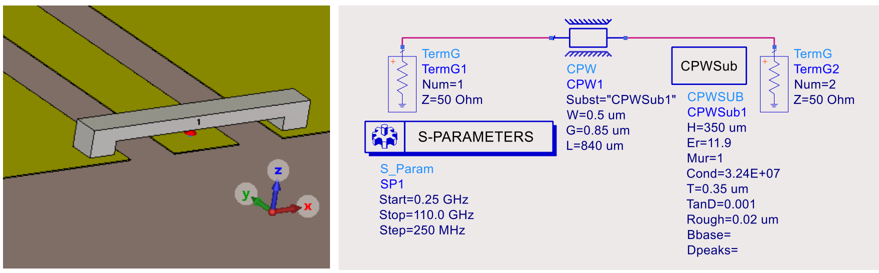

Fig. 3.17: Simulated CPW line in ADS and CST.

Accessing the electrical characteristics of a transmission line is straightforward when using advanced simulation software such as CST Studio Suite. After the initial steps of modeling the transmission line structure, users define essential parameters including boundary conditions, the desired frequency range, and the type of mesh to be utilized for the simulation. Once these conditions are properly set, the software allows for direct extraction of critical transmission line parameters from the simulation results. These parameters include the characteristic impedance, propagation constant, effective permittivity, and the distributed elements of the transmission line. This integrated workflow streamlines the analysis process and provides comprehensive insight into the electrical behavior of the modeled structure.

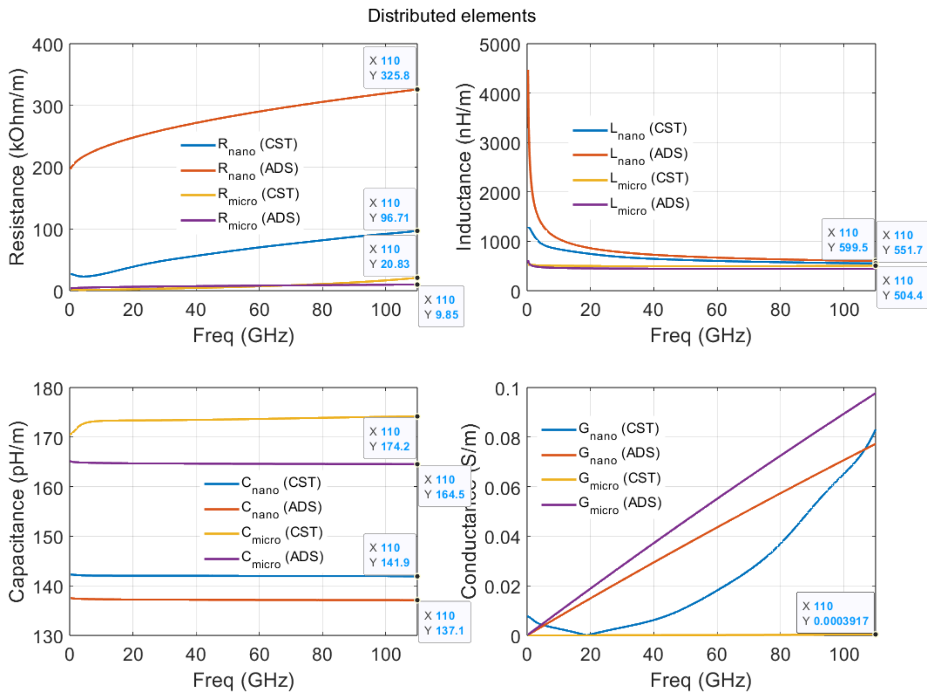

Fig. 3.18: Distributed elements of CPW line at nano and micro level from CST and ADS simulation.

The distributed elements of the coplanar waveguide (CPW) structure, including linear resistance, inductance, capacitance, and conductance, can be directly determined from the S-parameters response of the line through full wave simulation. Fig. 3.18 illustrates these distributed parameters for both micro- and nanoscale CPW lines. Consistent with observations from analytical models discussed in the previous section, the linear resistance and inductance values are notably higher at the nanoscale compared to the microscale.

Similarly, the characteristic impedance and propagation constant of the transmission line can be extracted from simulation results. The comparison between simulation and analytical approaches reveals that the results are generally in good agreement. Specifically, Fig. 3.19 presents the real part of the characteristic impedance for nanoscale CPW lines, showing values of 70.49 Ω (CST) and 62.84 Ω (ADS). For micrometric CPW structures, the corresponding real parts are 53.84 Ω and 51.84 Ω as obtained from CST and ADS, respectively.

However, there is a significant difference in the real part of the propagation constant for the nano transmission line when comparing results from three-dimensional (3D) simulation and circuit simulation. The attenuation value extracted from ADS is considerably higher at the nanoscale, a phenomenon that is not as pronounced at the micrometric level though it remains discernible in both ADS and CST results, as shown in the figure. This discrepancy indicates that 3D simulation accounts for geometry-related effects that influence distributed line elements such as linear capacitance, conductance, resistance, and inductance.

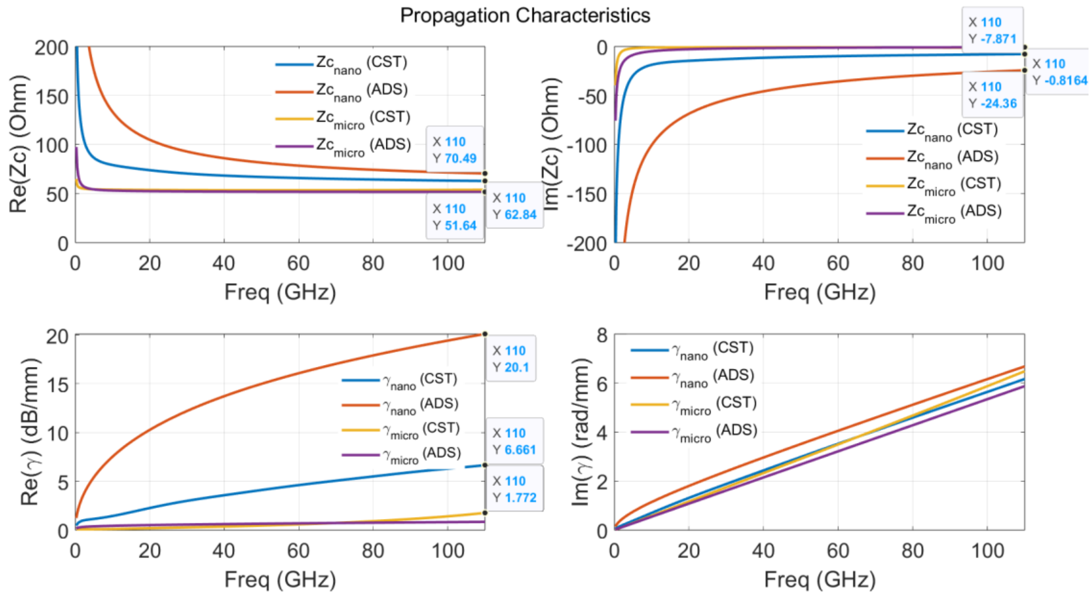

Fig. 3.19: Characteristic impedance and propagation constant at nano and microscale from CST and ADS.

A key consideration in interpreting these simulation results is the issue of impedance mismatch, which arises when there is a difference between the source impedance and the characteristic impedance of the transmission line. This mismatch can lead to significant effects, especially in high-frequency applications. When the source impedance does not match the line's characteristic impedance, reflected signals are generated at the point of discontinuity, resulting in increased reflection coefficients (S11) and decreased transmission coefficients (S21). These phenomena are particularly evident in the simulation results, where pronounced reflections and reduced transmission are observed, especially at the nanoscale. Such impedance mismatches can adversely affect the accuracy of extracted transmission line parameters, emphasizing the need for careful design and calibration to ensure optimal performance and reliable data from electromagnetic simulations.

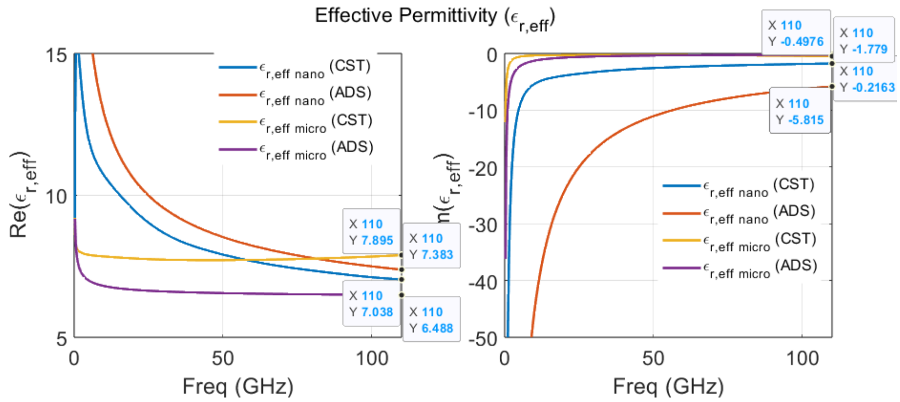

Fig. 3.20: Effective permittivity at nano and microscale from CST and ADS.

The effective permittivity of the coplanar waveguide (CPW) line demonstrates a similar trend to other transmission line parameters, as its value is derived directly from the propagation constant. This relationship means that any variations observed in the propagation constant due to factors such as line geometry or simulation environment are reflected in the calculated effective permittivity.

Fig. 3.20 presents both the real and imaginary components of the effective permittivity for CPW lines at both the micro- and nanoscale levels. These values are obtained from simulations conducted using CST Studio Suite and ADS, allowing for a direct comparison between the results produced by the two software tools. The figure illustrates how effective permittivity evolves depending on the scale of the structure and the simulation methodology, providing valuable insight into the dielectric behavior of the CPW line across different regimes.

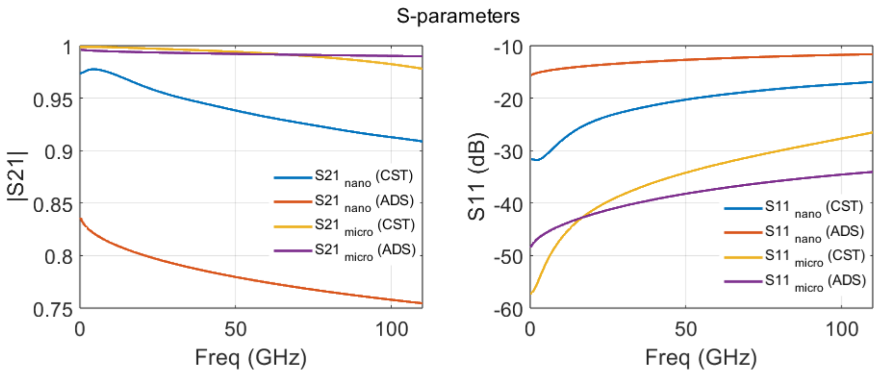

Fig. 3.21: S-parameters 100 µm length CPW line at micro and nanoscale from CST and ADS.

Fig. 3.21 presents a comparison of the S-parameters for coplanar waveguide (CPW) lines at both micro- and nanoscale dimensions, as obtained from CST Studio Suite and ADS simulations. At the microscale, the results from both simulation tools are nearly identical, with the transmission coefficient (S21) and the reflection coefficient (S11) showing close agreement across the two platforms. This consistency reflects a reliable simulation environment for microscale structures, where both CST and ADS yield comparable outcomes.

In contrast, at the nanoscale, notable discrepancies emerge between the two simulation approaches. While both CST and ADS demonstrate high reflection (S11) and low transmission (S21) coefficients, these effects are more pronounced in the ADS results. The pronounced increase in reflection and corresponding decrease in transmission observed in the ADS data highlight the significant impact of impedance mismatch, as well as differences in the port excitation mode utilized in three-dimensional simulations. These findings underscore the importance of carefully considering both simulation methodology and impedance matching, particularly when analyzing nanoscale transmission line structures.

c. Measurement-Based Method

The measurement-based approach offers a realistic means of extracting the propagation quantities of transmission lines. This process relies on S-parameter measurements acquired with a vector network analyzer. These measured S-parameters can then be transformed into the relevant transmission line parameters by employing calibration or de-embedding techniques, such as the Thru-Reflect-Line (TRL) or multiline-TRL methods.

The TRL method is regarded as one of the most effective procedures for both determining the key characteristics of transmission lines and calibrating a VNA. It achieves this by correcting systematic errors that may arise during measurement. Through this calibration, the actual transmission characteristics such as characteristic impedance (Zc), propagation constant (γ), and effective relative permittivity (ε_{reff}) can be accurately determined. These parameters are fundamental in radio frequency (RF) and microwave engineering for understanding the performance of transmission lines.

The propagation constant (γ) and effective relative permittivity (ε_{reff}) can be directly extracted from measured S-parameters of two transmission lines with different lengths. This is accomplished by using a VNA in conjunction with a TRL-based calibration and extraction method, as described in [19]. The characteristic impedance is then obtained using the approach proposed by Mark and Williams, which utilizes the propagation constant, as well as capacitance measurements, as outlined in [20] and [21].

The entire on-wafer measurement procedure employs a two-port measurement model, illustrated in Fig. 3.22, and is typically described by Equation (E.3.4). This equation defines the relationship between the measured data and the intrinsic characteristics of the Device Under Test (DUT). In this context, the matrix M represents the measured scattering matrix of the DUT, referenced to the system's measurement planes. The matrices X and Y account for systematic errors introduced upstream and downstream of the DUT, respectively, which may result from imperfections in the measurement setup—such as connectors, adapters, or cables. The term TDUT denotes the true response of the DUT, corrected for these systematic errors.

$$M = X \cdot T_{DUT} \cdot Y \quad \text{(E. 3.4)}$$

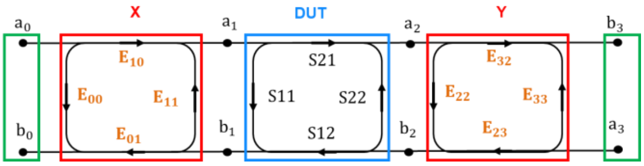

Fig. 3.22: Two-port measurement model.

The uses the reflective component enables to complete the determination of systematic error terms (Fig. 3.23). It defines the measurement reference plane at the middle of the Thru line with reference impedance corresponding to Z_c. Another advantage for this method is the possibility to shift the reference plane and to change reference impedance. The multiline-TRL is overcome the limitation in frequency band of the TRL offering more accuracy in the calibration and extraction of propagation characteristics of transmission line.

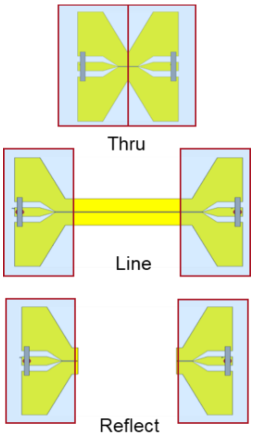

Fig. 3.23: TRL process.

In this context, measured raw S-parameters data with setup in Fig. 3.3 were subsequently processed using both standard TRL and multiline TRL calibration techniques. The multiline TRL approach employed nine transmission lines with lengths ranging from 200 µm (serving as the thru standard) to 2250 µm, along with a short-circuit reflect standard positioned at the center of the thru.

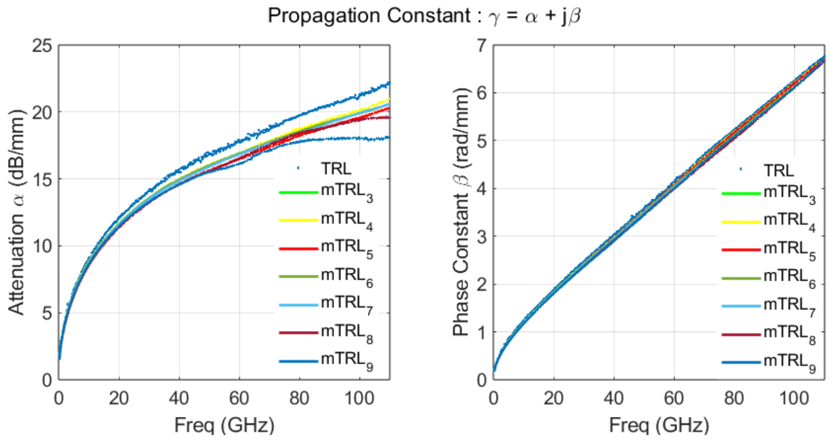

Fig. 3.24: Propagation constant of the nanoscale structures (real and imaginary parts).

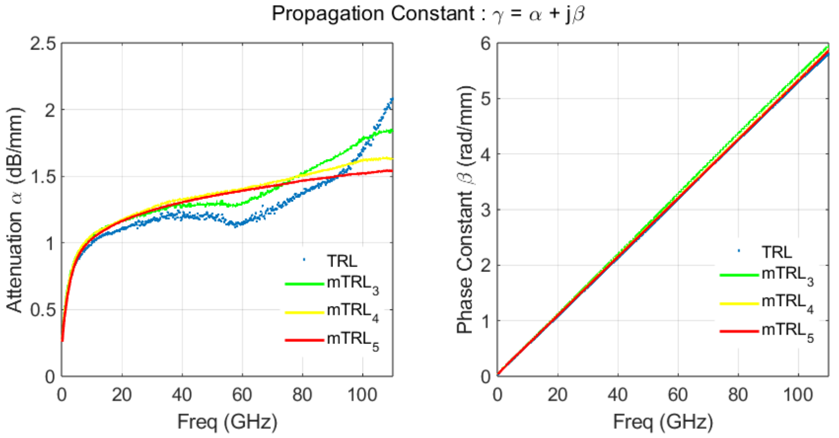

Fig. 3.25: Propagation constant of the microscale structures (real and imaginary parts).

Fig. 3.24 and Fig. 3.25 present the propagation constants of the nanoscale and microscale CPW structures, respectively. In both cases, the multiline-TRL (mTRL) method demonstrates superior precision, particularly when a sufficient number of transmission lines is used. From low frequencies up to approximately 20 GHz, the attenuation constant α obtained using both TRL and mTRL methods is nearly identical; however, notable discrepancies emerge at higher frequencies. These deviations in attenuation are primarily attributed to the increasing influence of measurement noise and dispersion phenomena. In contrast, the phase constant remains practically unaffected, showing excellent agreement across methods. This consistency is also reflected in the effective permittivity, derived from Equation (E.3.3), which is used to identify the minimum and maximum values for further analysis.

In addition to experimental characterization, electromagnetic simulations are performed using both Keysight Advanced Design System (ADS) and an analytical approach. The latter is based on the Heinrich model, which analytically describes coplanar waveguides (CPWs) by incorporating cross-sectional dimensions, such as the signal line width (W), gap (G), ground width (Wg), and metal thickness (t), along with material properties like conductor conductivity (σ) and substrate permittivity (ε_r). This enables the calculation of the distributed transmission line parameters: per-unit-length resistance (R), inductance (L), capacitance (C), and conductance (G) [13]. Recent developments have extended the Heinrich model by including additional physical effects such as surface roughness, radiation losses, and frequency-dependent dispersion to improve agreement with experimental data [16], [17], [18].

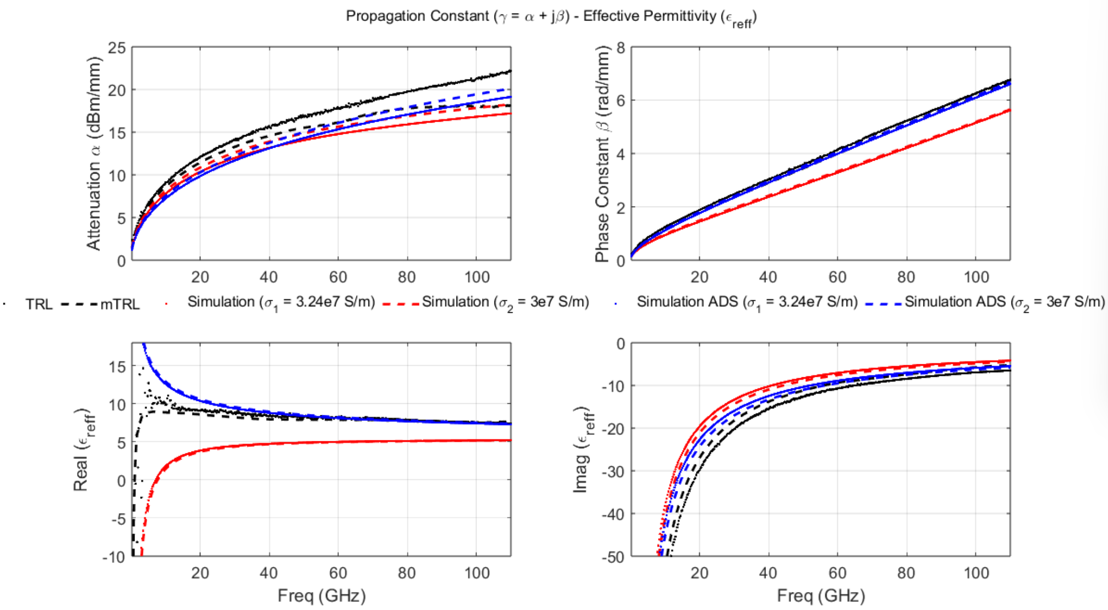

Fig. 3.26: Propagation constant and effective permittivity of the microscale structures (real and imaginary parts).

The measured DC conductivity (σ=3.24×10^7 S/m) and the theoretical value (σ=3×10^7 S/m) were incorporated into the simulations. The propagation constant and effective permittivity, experimentally extracted using TRL and multiline TRL methods, were compared with those obtained from both ADS and analytical simulations (Fig. 3.256). The comparison reveals notable discrepancies, particularly in the attenuation constant, despite the use of an advanced CPW model that accounts for radiation and dispersion effects. These deviations highlight the limitations of existing models and the sensitivity of attenuation to complex frequency-dependent phenomena.

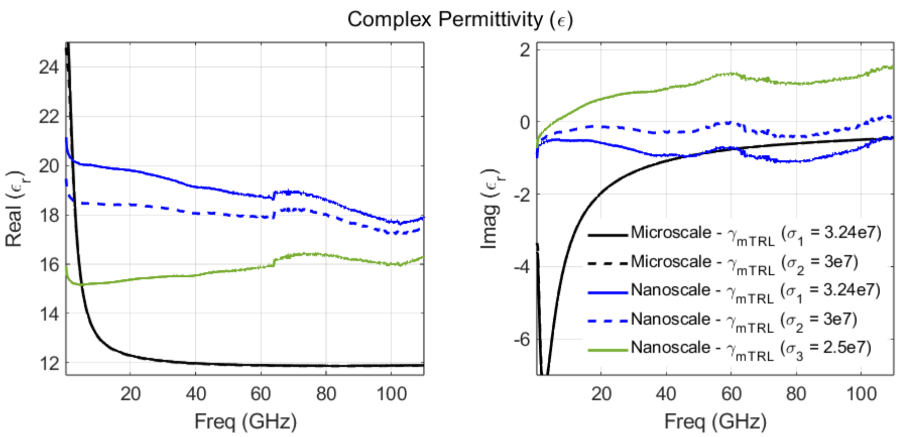

Fig. 3.27: Extracted complex permittivity of the micro and nanoscale structures.

The quasi-TEM analytical model proposed in [11] enables the determination of the distributed parameters, as resistance (R), inductance (L), capacitance (C), and conductance (G) of a CPW TL, based on the cross-sectional geometry, metal conductivity (σ), relative permittivity (ε_r), and loss tangent (tanδ) of the substrate. By combining the analytically derived values of R and L with the experimentally measured propagation constant γ, it is possible to extract the per-unit-length capacitance C_m and conductance G_m, as described in Equation (E.3.5) and discussed in [22], [23].

$$G_m + i\omega C_m = \gamma^2/(R + j\omega L) \qquad \text{(E.3.5)}$$

With the determined values of C_m and G_m, it becomes possible to calculate the relative permittivity ε_r and the loss tangent tanδ, using Equations (4) and (5). These expressions incorporate the factors F_{low} and F_{up}, which are derived from the analytical model introduced in [13].

$$\varepsilon_r = \frac{C_m}{2\varepsilon_0 F_{low}} - \frac{F_{up}}{F_{low}} \tag{E.3.6}$$

$$tan\delta = \frac{G_m}{2\omega\varepsilon_0\varepsilon_r F_{low}} \tag{E.3.7}$$

Following this procedure, the complex permittivity of the substrate was evaluated for both micro- and nanometric scale structures. Three conductivity values were considered in the analysis: the first, $\sigma 1=3.24\times10^7$ S/m, was obtained from direct current (DC) measurements performed on the nanostructures, while the other two $\sigma 2=3.00\times10^7$ and $\sigma 3=2.50\times10^7$ S/m —correspond to theoretical assumptions.

Fig. 3.27 presents the extracted complex permittivity ε_r. The complex permittivity of the silicon substrate is determined following the methodology described in [22], [23], with the real part estimated at approximately 11.89. However, when this same approach is applied to nanometric structures, the extracted permittivity deviates from the expected value. Specifically, a real part ranging between 15.17 and 16.34 is observed. This discrepancy may be attributed, on the one hand, to differences in cross-sectional ratios between micro- and nanometric structures, as outlined in Heinrich analytical model [13]. On the other hand, deviations may also result from fabrication-induced variations that affect the electrical characteristics of the transmission line. The characteristic impedance is determined from the propagation constant γ, linear capacitance C_m and linear conductance G_m.

$$Z_c = \frac{\gamma}{(G_m + j\omega C_m)} \tag{E.3.8}$$

In addition, the model described in [24], combined with 3D electromagnetic simulations performed using CST Microwave Studio, allows for the calculation of theoretical per-unit-length capacitance and conductance values for both micro- and nanometric CPW transmission lines. Based on [24], capacitance values of 164.208 pF/m and 125.698 pF/m are obtained for the micro- and nanometric structures, respectively. The corresponding CST simulation results yield capacitances of 168 pF/m for the micrometric line and 142 pF/m for the nanometric line. It is worth noting that the linear conductance term can be neglected in both cases, as $G \ll \omega C$.

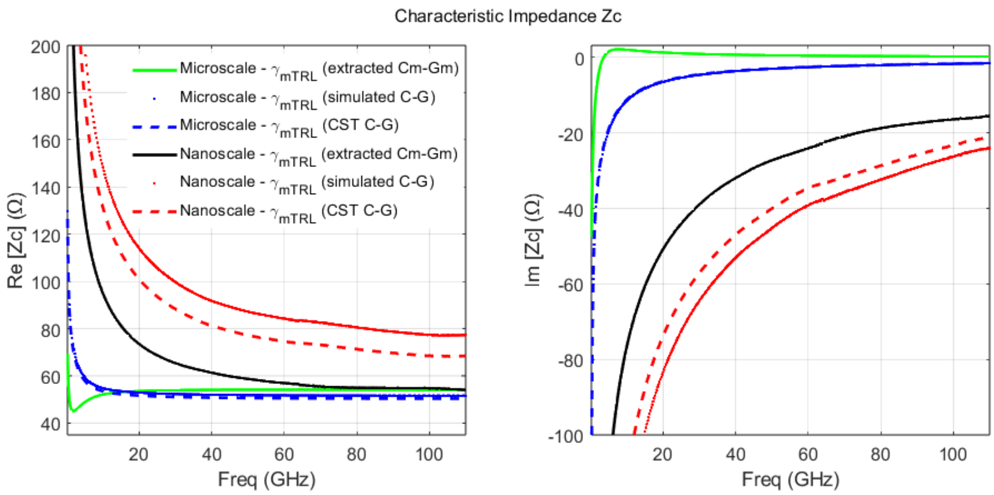

Fig. 3.28: Characteristic impedance of the micro and nanoscale structures.

The measured propagation constants are associated to the values of capacitance obtained from [22], [23], [24] and CST simulations to derive the characteristic impedance. For micro CPW line, the impedance at 110 GHz is 54 Ω against 51.6 and 50.37Ω of CST and analytical capacitance. It is coherent with respect to relation (6) because in reality there are phenomena such as dispersion and radiation that can influence the distributed elements (*RLCG*) of the line. Similarly, there is a significant difference in the impedance of the nano CPW line, 54.04 Ω against 77.36 and 68.48Ω at 110 GHz (Fig. 3.28). This disparity is due to the lack of perfect control of linear capacity. At least this approach makes it possible to determine impedance.

This study reveals notable differences between the two configurations, particularly a significant increase in dielectric losses and more pronounced attenuation in the nanometric lines. It demonstrates the feasibility of establishing a correlation between theoretical models and experimental results for the characterization of coplanar transmission lines. However, the findings also emphasize the limitations of classical analytical models, which fail to fully capture the physical phenomena emerging at nanometric scales.

We aim to leverage the relatively high attenuation in the real part of the propagation constant, allowing us to apply the TRL algorithm to any pair of lines at the nanoscale. Before running the TRL algorithm, we extract the electromagnetic properties and compare the propagation constant ($\gamma = \alpha + i\beta$) and effective permittivity, between conventional and nanoscale structures (Fig. 3.29).

Table 3.3: Length of the TLs.

Lines	L1	L2	L3	L4	L5	L6	L7	L8	L9
Length (µm)	200	250	300	450	550	750	1000	1600	2250

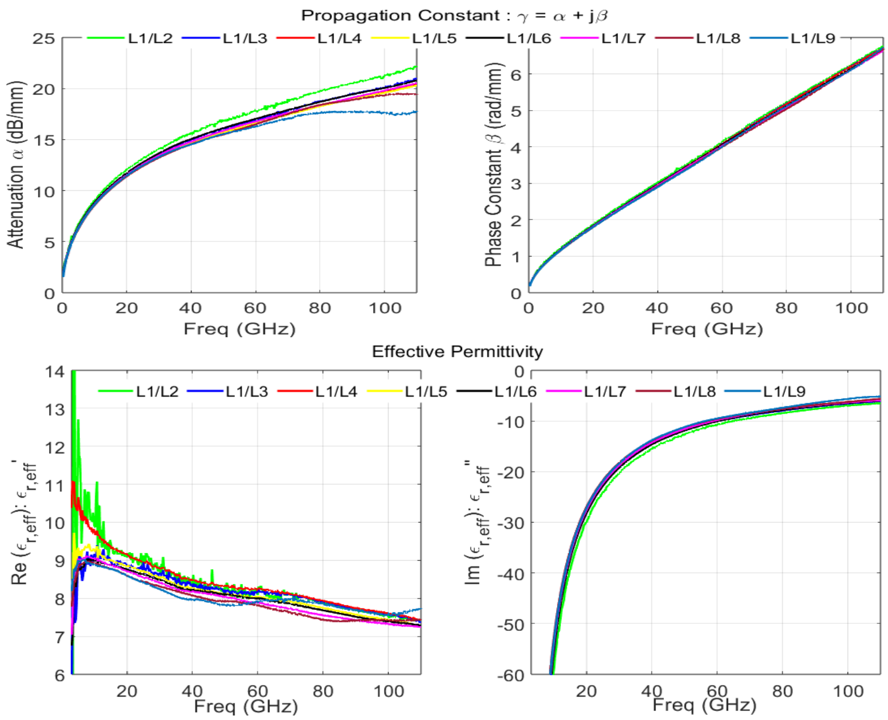

Fig. 3.29. Extracted propagation constant and Effective permittivity at nanoscale considering CPW TLs with different lengths.

The phase constant β is nearly identical across all cases, as shown in the right graph of the first figure. However, the attenuation constant α is almost the same for line pairs below 20 GHz but begins to show significant variation beyond this frequency. This divergence in attenuation behavior can be attributed to increasing noise and dispersion effects at higher frequencies. Additionally, errors in the measured length differences of line pairs may further contribute to this variation.

The second figure illustrates effective permittivity, with its real and imaginary components plotted as functions of frequency. The real part of the effective permittivity, $\varepsilon_{r,eff}{}'$ exhibits fluctuations at lower frequencies before stabilizing at higher frequencies. Meanwhile, the imaginary part, $\varepsilon_{r,eff}{}''$ follows a monotonic trend, decreasing significantly as the frequency increases. These variations highlight the frequency-dependent nature of the material's electromagnetic properties, influenced by both dispersion and measurement uncertainties.

Due to the attenuation of the real part of the propagation constant, the TRL algorithm remains valid for any pair of lines.

3.3. Correction of raw data of Devices Under Test

A 300 µm coplanar waveguide (CPW) transmission line (TL) was selected as the device under test (DUT) for detailed measurement and analysis. In the context of TRL (thru-reflect-line) calibration, the measurement reference plane is carefully established at the center of the thru standard. This configuration incorporates both halves of the thru structure within the error boxes, effectively capturing all systematic contributions originating from the vector network analyzer, including cables and probes. As a result, the TRL calibration method provides robust de-embedding, isolating the measurement reference plane from extraneous systematic errors.

Fig. 3.30 displays the measured transmission amplitude and phase of the transmission coefficient (S21) for the DUT following the application of both the ISS LRRM (impedance standard substrate line-reflect-reflect-match) calibration and the TRL calibration. These experimental results are further compared with simulation data generated using Keysight ADS software.

The ISS LRRM calibration results demonstrate higher observed attenuation. This outcome is expected, as the ISS calibration approach considers the entire structure between the probe tips, thereby including additional factors such as contact resistance and parasitic effects. In contrast, the TRL calibration technique more precisely isolates the response of the DUT itself by referencing the calibration plane within the nanoscale CPW TL structure. This targeted approach allows for a more accurate representation of the DUT's intrinsic transmission characteristics, minimizing the influence of external parasitic elements on the measurement.

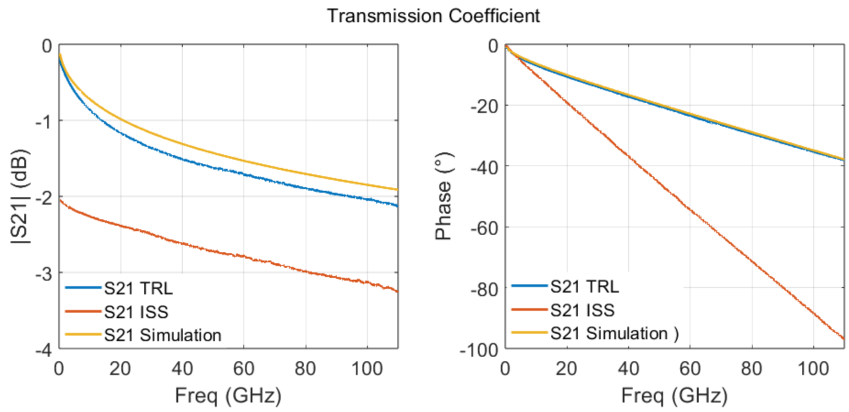

Fig. 3.30. Measured and simulated transmission coefficient S_{21} for the 300 µm CPW TL. The left plot shows the magnitude $|S_{21}|$ in dB, while the right plot presents the phase response (in degrees) as a function of frequency. The results compare the transmission coefficient obtained using the TRL calibration, ISS LRRM calibration, and Keysight ADS simulation.

The differences observed between the TRL-calibrated measurements and the simulation results can be primarily attributed to several sources of error within the fabrication and measurement processes. One significant factor is the presence of fabrication-induced imperfections, such as scratches on the coplanar waveguide (CPW) lines. These physical defects have the potential to locally alter the transmission characteristics of the lines, thereby introducing deviations from the idealized behavior predicted by simulations.

Another contributing factor is the observed lower-than-expected conductivity of the deposited metal used in the CPW structures. Reduced conductivity increases the insertion loss experienced by the transmission line, further contributing to the difference between measured and simulated data. These combined effects underscore the importance of precise fabrication and material quality in achieving measurement results that closely match simulation predictions.

The process of correcting the raw measurement data encompasses various devices under test (DUTs), including reflective structures and selected transmission lines (TLs). As demonstrated in Fig. 3.31, it becomes clear that utilizing long transmission lines at the nanoscale is not advantageous due to the substantial losses and attenuation encountered. Specifically, the transmission coefficient S21 exhibits a pronounced decrease as the line length increases, which highlights the significant influence of both conductor and dielectric losses at these reduced scales.

These findings emphasize the challenges associated with nanoscale transmission line measurements and the necessity of accounting for fabrication imperfections and material properties in both experimental and simulation analyses.

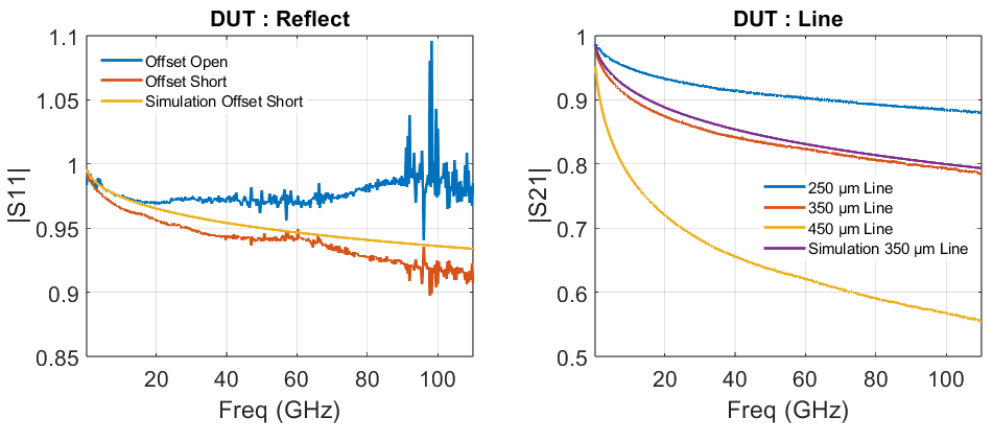

Fig. 3.31: Corrected S-parameters of Reflects and Lines at nanoscale.

The reflection responses (S11) of the open and short circuit devices under test (DUTs) are observed to be more susceptible to fluctuations. This increased sensitivity can be attributed to the placement of these two reflect standards, which are positioned at 15 μm from the thru standard. Such proximity makes them particularly responsive to variations in probe positioning and movement during the measurement process.

Due to this heightened sensitivity, the open and short circuit standards are considered uncertainty-prone structures within the measurement setup. Their behavior is therefore of significant interest when evaluating the overall uncertainty budget associated with the measurement procedure. By closely examining these standards, valuable insights can be gained regarding the sources and extent of uncertainty, ultimately contributing to a more comprehensive understanding of the measurement system's reliability and accuracy.

3.4. Reproducibility of Measurements

Reproducibility is defined as the capability to achieve consistent measurement results of the same quantity, even when certain conditions are varied. In the field of metrology, reproducibility serves as a foundational principle, ensuring reliability and integrity in the measurement process. The conditions that can influence reproducibility include differences among operators, variations in instruments, changes in laboratory environments, differing times at which measurements are taken, and other procedural or environmental factors.

Achieving reproducibility is essential for several reasons. It provides confidence in the accuracy of measurement results and supports the validation of scientific and technical claims. Furthermore, reproducibility is crucial for enabling meaningful interlaboratory comparisons and plays a significant role in maintaining quality control within manufacturing settings.

In the context of this study, particular attention is given to environmental factors that may impact reproducibility. These factors include humidity, temperature fluctuations, inherent system noise, instrument drift, and the timing of measurements. To assess the effect of these variables, two separate measurement sessions were conducted. The analysis focuses on how these environmental conditions influence the consistency and reliability of the obtained results.

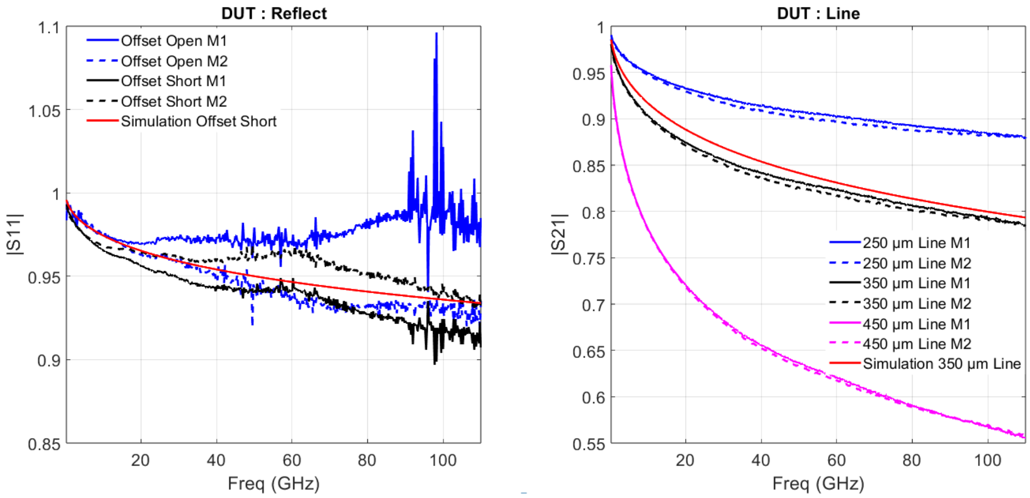

Fig. 3.32: S-parameters of DUTs (Reflect / Line).

Fig. 3.32 displays the S-parameter responses for three different types of devices under test (DUTs): an open circuit, a short circuit, and a transmission line. These measurements were conducted over two separate sessions, labeled M1 and M2. For reference and comparison, the figure also includes S-parameters obtained from ADS simulations.

Despite the overall reproducibility of the measurements, discrepancies between the results from sessions M1 and M2 are apparent. These differences are particularly pronounced in the reflection coefficient (S11), where greater fluctuations are observed during session M1 for both the open and short circuit DUTs. In contrast, the transmission coefficient (S21) exhibits consistent behavior across the two sessions, with only minor variations detected.

The observed discrepancies can be primarily attributed to system noise and drift effects present in the vector network analyzer and extenders. Additionally, small changes in environmental temperature may have contributed to the minor differences observed between the sessions.

It is also important to consider the effect of probing during the measurement process. Contact between the probe and the DUT can introduce surface scratches, which in turn lead to changes in the electrical access path length. This effect is particularly significant for reflective devices, such as open and short circuits, making them more sensitive to measurement conditions and resulting in greater uncertainty. In contrast, transmissive devices, such as transmission lines, are less affected by these variations and demonstrate higher measurement stability.

3.5. Experimental study on repeatability of nanoscale on-wafer calibration structures

Repeatability describes the extent to which a measurement process yields consistent outcomes when performed multiple times under identical conditions. In this context, repeatability is ensured by maintaining the same operator, using the same instrument, conducting measurements within the same laboratory, and performing each measurement with only a short delay between sessions.

The objective of this section is to examine how the positioning of probes and the chuck affects the repeatability of measurements. To systematically evaluate the impact of contact repeatability specifically related to the placement of both the probes and the chuck, eight separate measurements were performed, covering frequencies up to 110 GHz. During each measurement sequence, the probes were repositioned along the X, Y, and Z axes, and the chuck was moved vertically between consecutive measurements, as illustrated in Fig. 3.33.

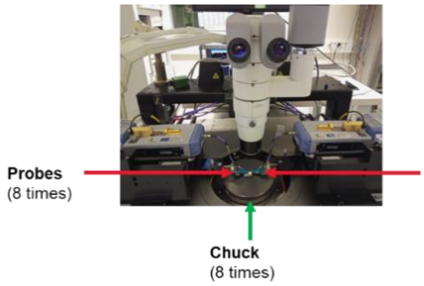

Fig. 3.33: Representation of the setup.

The analysis began with a focus on the two shortest coplanar waveguide transmission lines (L1 and L2) to assess how measurement uncertainties affect the determination of the propagation constant and effective permittivity, as illustrated in Fig. 3.34 and Fig. 3.35. The evaluation specifically examined the standard deviation associated with a broadening factor of k=2, which serves to highlight the roles of both the chuck and the probes in influencing the propagation characteristics of the transmission lines.

It was found that the probes have a more pronounced effect on these characteristics compared to the chuck. This heightened influence is primarily due to the cumulative impact of probes positioned at both ports 1 and 2. The effect is particularly observable in the attenuation coefficient (α), where the variability is considerably greater in the probe configuration. Such an outcome indicates increased sensitivity to the conditions at the probe contacts, the manner of signal injection, and the potential for impedance mismatches. In contrast, the influence of the chuck on these parameters remains relatively minor.

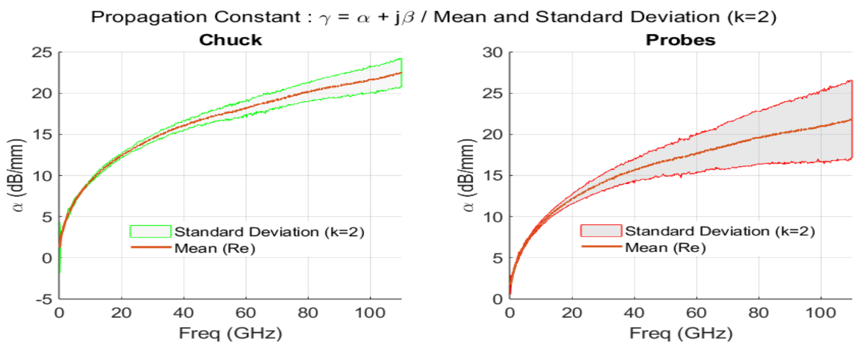

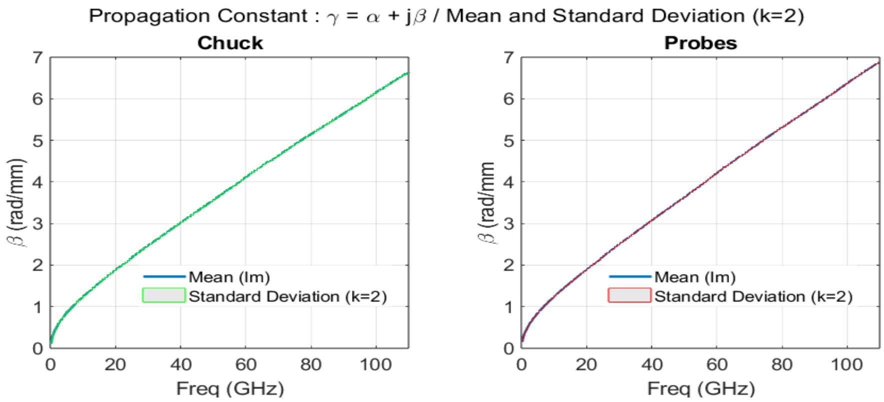

Fig. 3.34: Impact of probes and chuck repeatability on the determination of the propagation constant.

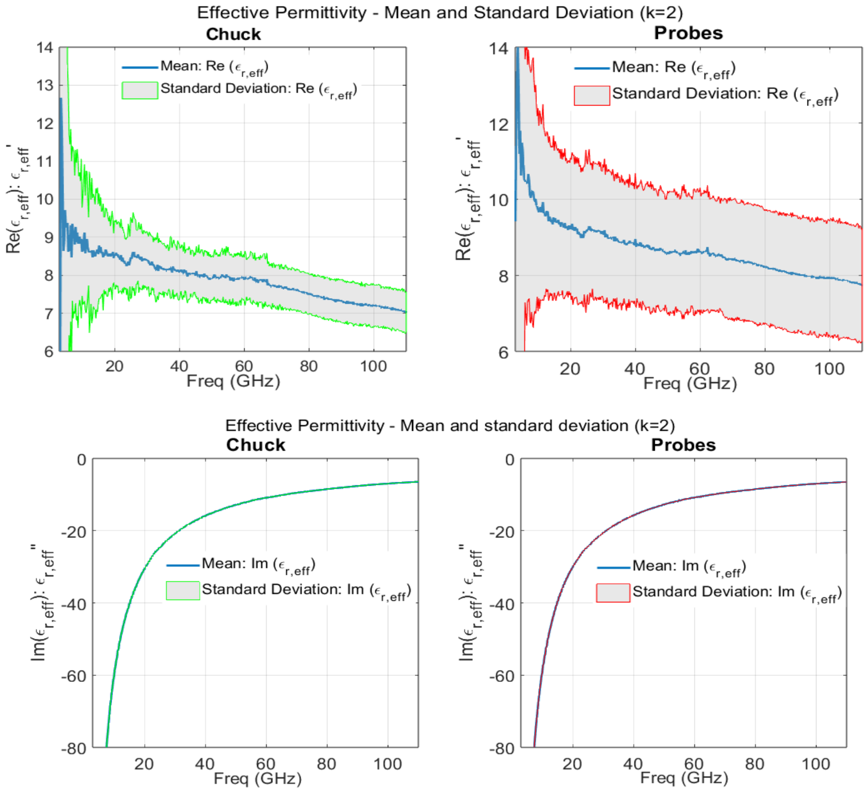

Fig. 3.35: Impact of probes and chuck repeatability on the determination of the effective permittivity.

Since the propagation constant is directly related to the effective permittivity, any disturbances introduced by the measurement setup will affect both these parameters similarly. This observation implies that variations in the measured permittivity are not only the result of localized effects but are also influenced by the overall interaction between the transmission line and its measurement environment. The standard deviation observed in the attenuation coefficient (α) across both the probe and chuck configurations demonstrates that the real part of the effective permittivity is consistently affected. This finding highlights the importance of implementing meticulous calibration and compensation strategies to minimize systematic errors, especially in high-frequency measurement scenarios.

Table 3.4 presents the measurement uncertainties arising from the repeatability of the chuck and probe positions during attenuation and effective permittivity determination at a frequency of 110 GHz. The probes add much more uncertainty than the chuck, as seen in both attenuation coefficient and effective permittivity measurements. This heightened sensitivity is due to the cumulative effects of probe placement at both ports and highlights the importance of consistent contact conditions for accurate high-frequency measurements. The standard deviations reported in the table further underscore the influence of probe variability, suggesting that meticulous calibration and careful handling are essential to minimize systematic errors in nanoscale on-wafer calibration structures

Table 3.4: Uncertainties Associated with Chuck and Probe Repeatability on attenuation end effective permittivity at 110 GHz

@ 110 GHz	Chuck	Probes
$\sigma(\alpha(\text{dB/mm}))$	1.7	4.725
$\sigma(Re(\varepsilon_{r,eff}))$	0.527	1.487

To further evaluate the effect of the chuck and probes on the S-parameters, a series of eight raw measurements were conducted on both TRL calibration structures and devices under test (DUTs), including short circuits and transmission lines. The means and standard deviations for these measurements were calculated using the TRL algorithm. Additionally, simulations were performed in the ADS circuit design environment, considering two distinct metal conductivity values: the first value (σ-1) was extracted from DC measurements, while the second value (σ-2) was based on theoretical expectations. These simulations are depicted in Fig. 3.36 and Fig. 3.37, allowing for a direct comparison between experimental results and modeled predictions.

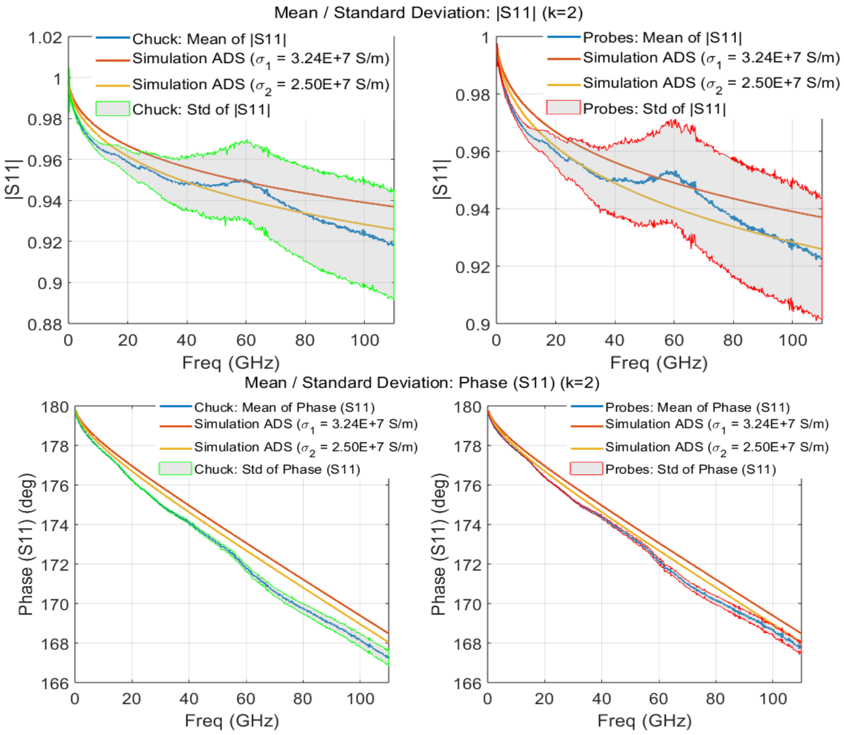

Fig. 3.36: Impact of probes and chuck repeatability on the determination of S_{11} (DUT = Short).

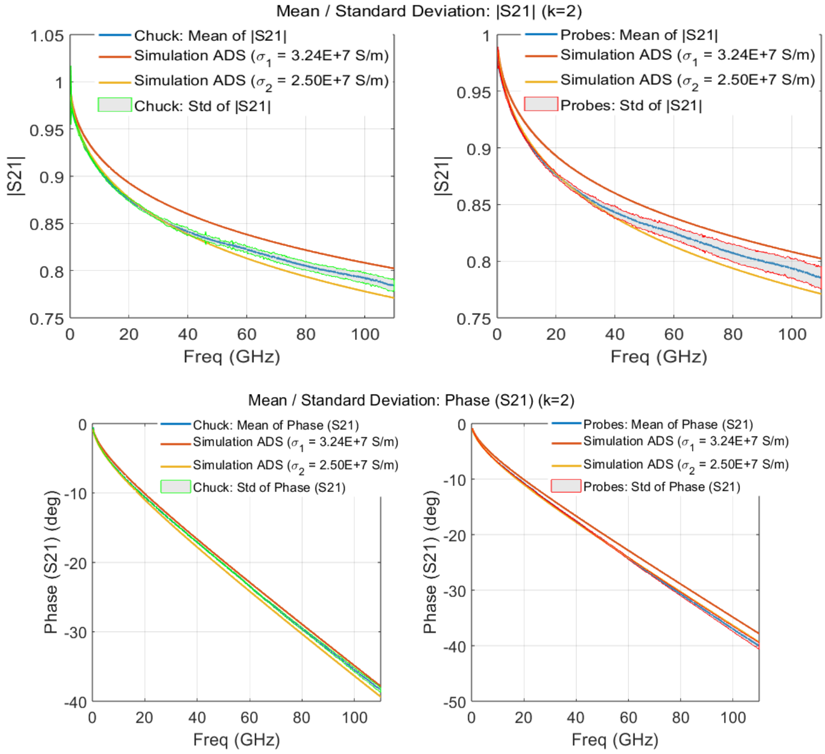

Fig. 3.37: Impact of probes and chuck repeatability on the determination of S-parameters (DUT = TL3).

The comparison between modeling and experimental measurements reveals clear discrepancies that stem from real-world variations in material properties, fabrication tolerances, and experimental uncertainties. Specifically, Fig. 3.36 illustrates how variability in both the probe and chuck significantly affects the determination of S11 when the device under test (DUT) is configured as a short circuit. The observed standard deviation in both the magnitude and phase of S11 highlights that even minor changes in contact conditions and the repeatability of measurements can lead to noticeable variations in the results.

It is important to note that modeling is typically based on idealized conditions and predefined conductivity values. However, actual measurements are subject to additional factors such as surface roughness, contact resistance, and environmental noise, all of which can introduce deviations from the ideal model. Extending the analysis to S21 (as shown in Fig. 3.37), the transmission parameter is similarly affected by these sources of uncertainty. While the measured data generally follows the trends predicted by simulation, discrepancies become more pronounced at higher frequencies. This behavior suggests that dispersion effects, increased losses, and small differences in the actual transmission line length compared to the modeled structure contribute to the observed variations.

Table 3.5 summarizes the uncertainties associated with the repeatability of both the chuck and probes when measuring S-parameters for a transmission line and a short circuit at 110 GHz. These uncertainties are quantified for the reflection coefficient S_{11} of the short circuit and for the transmission coefficient S_{21} of the line. The data clearly illustrates that both chuck and probe variability can introduce measurable deviations in the magnitude of S-parameters. Specifically, for the short circuit, the standard deviations for $|S_{11}|$ are 0.026 for the chuck and 0.02 for the probes. For the transmission line, the standard deviations for $|S_{21}|$ are 0.005 for the chuck and 0.01 for the probes. These values highlight the importance of ensuring consistent contact conditions and careful handling during high-frequency measurements to minimize the impact of mechanical repeatability on measurement accuracy.

Table 3.5: Uncertainties Associated with Chuck and Probe Repeatability on S-parameters at 110 GHz

Short	Chuck	Probes	**Ligne**	Chuck	Probes
σ(|S11|)	0.026	0.02	σ(|S21|)	0.005	0.01
σ(S11 deg)	0.37°	0.28°	σ(S21 deg)	0.35°	0.61°

Furthermore, imperfections in the calibration process and the limited precision of probe positioning also play a significant role in the inconsistencies observed in the measurements. Overall, this analysis of the influence of probes and the chuck on nanoscale calibration structures and verification devices using the TRL calibration method demonstrates that, although modeling provides a helpful theoretical foundation, practical measurement challenges must be carefully considered. The differences observed between simulation and experimental results emphasize the necessity for accurate material characterization, precise calibration techniques, and robust measurement setups to minimize uncertainty and improve the reliability of extracted parameters.

4. Analysis of results

The experimental investigation conducted using a probe station up to 110 GHz yields valuable insights into several critical aspects, including measurement quality, the validity of parameter extraction methods, and the stability of calibration procedures.

Initially, DC measurements were performed using two distinct approaches to quantify both the linear resistance of coplanar waveguide (CPW) lines and the electrical conductivity of the gold used in their fabrication. The results from these measurements demonstrated good agreement with expected conductivity values for microscale structures, with gold showing a conductivity of approximately 4.16×10^7 S/m. This value aligns closely with the standard reference conductivity of gold at 4.5×10^7 S/m typically used for bulk materials at room temperature.

However, as the analysis shifted to nanoscale structures, a notable decrease in gold conductivity was observed. The measured conductivity values dropped to around 3.17×10^7 S/m and 3.24×10^7 S/m for the nano-structured CPW lines. This reduction is primarily attributed to the effects of miniaturization, wherein surface roughness becomes increasingly significant and has a pronounced impact on the electrical properties of the material.

Moreover, at the nanoscale, the electrical properties of the structures are extremely sensitive to the fabrication process. Even minor process variations such as those occurring during the liftoff step can substantially alter the geometry and, consequently, the electrical behavior of the device. For example, the liftoff process can either leave behind or remove residues on the structure, leading to deviations from the intended design and affecting its overall performance. These geometric modifications are illustrated in Fig. 3.38, highlighting the importance of precise fabrication in ensuring consistent and reliable nanoscale device characteristics.

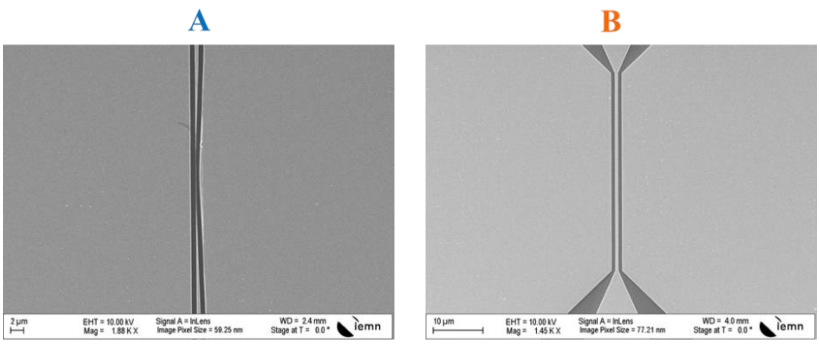

Fig.3.38: Default driven from liftoff.

To evaluate the impact of the liftoff process on the electrical performance of nano coplanar waveguide (CPW) lines, a series of simulations were conducted using CST software. In these simulations, specific variations were introduced to the dimensional parameters related to the cross-sectional geometry of the nano CPW line. The focus was placed on how changes in the ground plane dimensions and trace width parameters that are directly affected by the liftoff process can influence the overall behavior of the transmission line.

Six distinct cases were developed, each representing a different set of dimensional variations for the ground planes and trace width. These scenarios were chosen to systematically capture the possible effects that liftoff-induced alterations might have on the structure. Figure 3.39 presents detailed views of the various cross-sectional schemes that correspond to potential impacts resulting from the liftoff process. These schematic representations serve to highlight the range of geometric modifications that may occur and provide a foundation for analyzing how such changes affect the electrical characteristics of the transmission line.

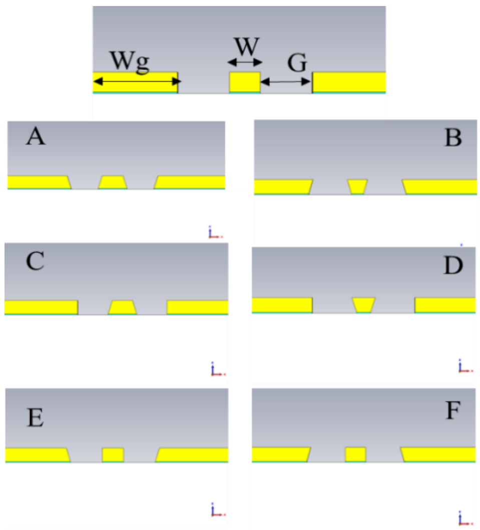

Fig. 3.39: Simulation of liftoff impact on nano CPW line.

The standard coplanar waveguide (CPW) structure, which serves as the reference for comparison in this analysis, is defined by specific geometric parameters. These parameters include the trace width (*W*), the gap between the signal trace and the ground planes (*G*), and the width of the ground planes themselves (*Wg*). The configuration of these dimensions is illustrated at the top of the referenced figure, providing a clear depiction of the baseline geometry against which the effects of liftoff-induced modifications and other dimensional variations are assessed.

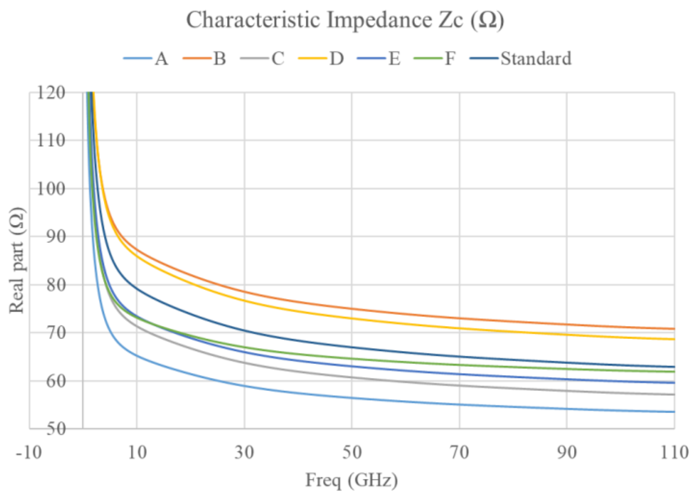

Fig. 3.40: The real of Characteristic impedance for different cases.

A detailed examination of Fig. 3.40 reveals that, in the specified order, cases A, C, E, and F display a lower real part of the characteristic impedance when compared to the standard coplanar waveguide (CPW) structure. Conversely, cases B and D exhibit the highest real part of impedance among the scenarios considered. The primary factor of interest in this comparison is the effective gap width between the signal trace and ground planes. Notably, as the gap increases, the impedance of the line also rises, underscoring the critical role of geometric parameters in determining electrical performance.

At high frequencies, the S-parameters measured from the CPW structure closely align with results from both full-wave electromagnetic simulation and analytical models. While there is general agreement, subtle discrepancies are observed between the CST simulation outcomes and the experimental measurements. These differences can be attributed to fabrication-related defects that alter the electrical properties of the structures, losses introduced by the measurement probes, and the port excitation type employed in the three-dimensional modeling process.

To further investigate the impact of the fabrication process, two test structures were fabricated with identical components but subjected to different fabrication procedures. The intent was to highlight the influence of processing steps, particularly the liftoff step, on the final device characteristics. As illustrated in Fig. 3.41, the transmission coefficient of two nominally identical nano CPW lines is compared, each resulting from a distinct fabrication process (referred to as fabrication 1 and fabrication 2). The liftoff procedure in fabrication 1 introduces a geometry change, as previously depicted in Fig. 3.38. This modification is reflected in the transmission performance: the CPW line produced by fabrication 2, in which the liftoff step does not alter the geometric structure, demonstrates superior signal transmission. This finding underscores the importance of precise and consistent fabrication processes in achieving optimal electrical performance for nanoscale transmission lines.

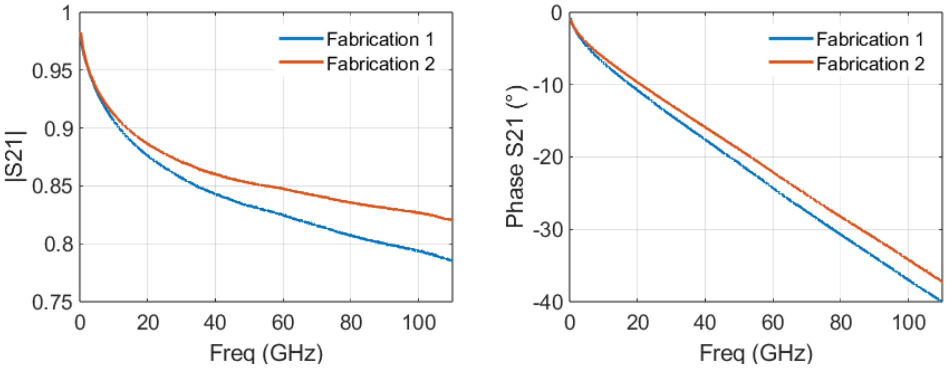

Fig. 3.41: Impact of fabrication on the response in transmission of nano CPW line.

Three distinct approaches were employed to extract the electrical characteristics of the coplanar waveguide (CPW) line: the analytical method, the electromagnetic (EM) simulation method, and the measurement-based method. In general, the results obtained from all three methods were found to be consistent with one another, indicating reliability and agreement across the different extraction techniques.

Despite this overall consistency, the measurement-based method stands out, particularly in its ability to more accurately represent the actual losses present in the CPW line. This advantage becomes especially significant at high frequencies, where various loss mechanisms such as surface roughness, dielectric losses, and discontinuities introduced during fabrication become increasingly dominant and can substantially affect device performance.

Further insight into these effects can be drawn from the analysis of propagation characteristics, including the propagation constant and effective permittivity. As illustrated in Fig. 3.42, these parameters clearly demonstrate the influence of the liftoff process signature on the electrical behavior of the nano CPW line. This observation highlights the critical impact that fabrication-induced variations have on high-frequency device performance and underscores the importance of precise process control in nanoscale transmission line fabrication.

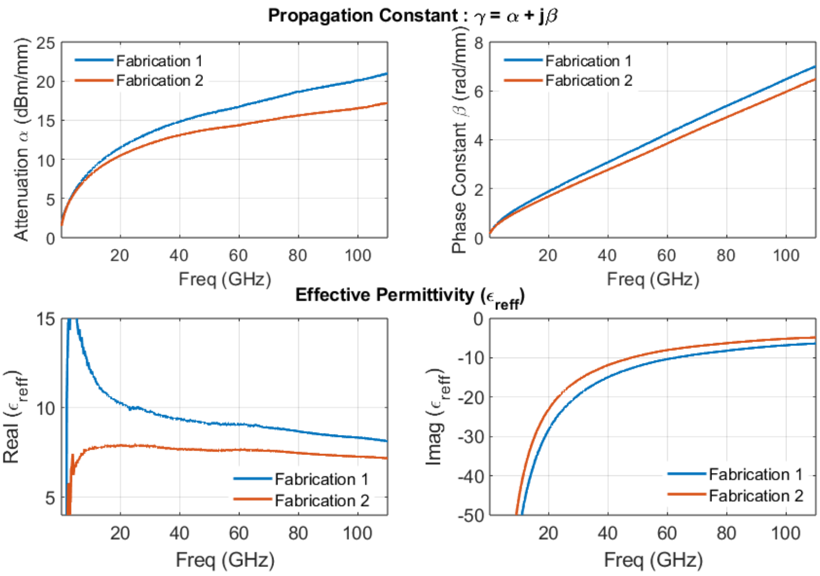

Fig. 3.42: Impact of fabrication on the propagation constant and effective permittivity of nano CPW line.

The application of systematic error correction through TRL or Multiline TRL calibration significantly influences the interpretation of Device Under Test (DUT) performance. By employing these calibration techniques, it becomes possible to access the true response of the DUT, as the measurement reference plane is shifted from the Vector Network Analyzer ports to the midpoint of the thru standard.

In on-wafer measurements, three distinct reference planes can be identified:

- VNA Ports: Data referred to the VNA ports represents raw, uncorrected measurements.
- Probe Tips: Data referenced to the probe tips is obtained through calibration techniques such as LRRM or SOLT, resulting in corrected data that accounts for the measurement chain up to the probe contacts.
- Wafer Level: Data referenced to the wafer level is achieved through the TRL calibration process, providing measurement results that are directly related to the on-wafer test structure.

For instance, as depicted in Fig. 3.29, the application of both ISS-LRRM and TRL calibrations results in two distinct DUT (line) responses. The ISS calibration positions the measurement reference plane very close to the probe tips, thereby encompassing the entire structure located between the probe contacts. This includes contributions from contact resistances and parasitic effects present at the probe interface. In contrast, TRL calibration establishes the calibration plane within the coplanar waveguide (CPW) nanoscale transmission line itself, isolating the DUT response more effectively.

Results obtained from calibration structures with nanometric dimensions confirm the feasibility of performing on-wafer calibration at this scale. However, several significant challenges are observed. These include extreme sensitivity to probe alignment, parasitic capacitance associated with measurement pads that is difficult to accurately model, and amplified errors at very high frequencies. While repeated calibrations on such small structures exhibit greater variability compared to larger structures, the variability remains manageable provided that a rigorous calibration protocol is followed.

5. Evaluation of uncertainties

5.1. Principle

The accuracy of S-parameter measurements can be affected by various influence quantities, including internal characteristics of the VNA (such as noise floor, trace noise, drift, and non-linearity), crosstalk, test port cable stability, connection repeatability, and the characterization of calibration standards. Several established methods exist to evaluate or quantify the contribution of each of these uncertainty sources [8]. Uncertainty evaluation is typically based on two main approaches:

The accuracy of S-parameter measurements is influenced by a range of factors, known as influencing quantities. These include internal characteristics of the Vector Network Analyzer, such as noise floor, trace noise, drift, and non-linearity, as well as external factors like crosstalk, test port cable stability, connection repeatability, and the characterization of calibration standards. To assess the contribution of each source of uncertainty, several established evaluation methods are available [8].

- The rigorous method, which involves uncertainty propagation through a complete measurement model. There two approaches with this method. On one side, the linear uncertainty propagation technique in which, according to the inputs quantities, variances and covariances are propagated through a linearized measurement model. The uncertainty in the measured value of the measurand is assumed to be characterized by a multivariate Gaussian Probability Density Function (PDF). The variance or covariance of this PDF is found by propagating variance-covariance information associated with the input quantity estimates through the measurement model. The result can be obtained through an analytical calculation [8].
  The other way to process uncertainty propagation consists of using Monte Carlo technique. For this last one, the distributions are propagated through the measurement model by making repeated draws from the PDFs of the input quantities. The result is a PDF of the quantity of

interest. Numerical methods with the generation of pseudo-random numbers are usually needed to obtain the result [8].

- The Ripple Method, which assumes that repeated calibrations using the same standards and calibration scheme, should yield identical S-parameter results for the DUT, while allowing for the estimation of measurement uncertainty through observed variations.

Although both methods aim to quantify the uncertainty associated with the same measurement result, they often yield different uncertainty estimates [8].

In this work, we specifically focus on the influence of calibration standards and adopt the rigorous method, which is particularly well suited for coplanar waveguide (CPW) structures and high-frequency applications. This approach relies on a comprehensive measurement model that encompasses the entire measurement chain from the VNA calibration using known standards to the subsequent error correction applied to the DUT measurement. The methodology is consistent with the principles outlined in the *Guide to the Expression of Uncertainty in Measurement* (GUM) [8].

The law of uncertainty propagation assumes perturbations follow multivariate Gaussian distributions and relies on an approximation of the underlying mathematical model used in the calibration process. As such, it is only applicable when the sources of uncertainty can be explicitly expressed within the calibration model. For example, in the well-known short-open-load-thru (SOLT) calibration technique, all calibration standards are explicitly defined and directly related to the calibration equations, making the application of the law of uncertainty propagation straightforward. However, for VNA self-calibration methods such as TRL, multiline TRL, and similar techniques, the use of partially defined calibration standards introduces challenges. The absence of a direct and explicit relationship between the calibration equations and the standards complicates the application of the law of uncertainty propagation [25].

To address this issue, it is possible to relate small variations in the S-parameter values of the calibration standards to corresponding changes in the VNA response, thereby allowing for the indirect evaluation of sensitivity coefficients associated with the error terms obtained through calibration [26], [27]. In [27], TRL calibration method is specifically considered. For a two-port VNA, the measurand (i.e., the actual response) is represented by a complex matrix Y comprising four S-parameters that characterize the two-port device under test. The 8-term error model, defined by eight error coefficients E, relates the instrument response X (i.e., the raw measurement) to the measurand through equation of measurement model (E.3.9).

$$X = f(Y; E) \tag{E.3.9}$$

The measurand is determined by applying the inverse of the measurement model equation given in (E.3.10).

$$Y = g(X; E) \tag{E.3.10}$$

The error coefficients E are determined by a calibration function, which uses the response vectors $\{Xi\}$ corresponding to a set of calibration standards with known values $\{Yi\}$. In practice, the values of the calibration standards are predetermined, so the calibration function takes the following form:

$$E = h(X_i, Y_i) \tag{E.3.11}$$

Where *i* indicates the calibration standard.

We tried to solve our problem using this procedure above. In practice, the measurement model is descripted by the relationship (E.3.12).

$$\boldsymbol{M_{dut}} = k.\boldsymbol{A}.\boldsymbol{T_{dut}}.\boldsymbol{B} = f(\boldsymbol{T_{dut}}, k, \boldsymbol{A}, \boldsymbol{B}) \tag{E.3.12}$$

Where A and B are the error boxes (i.e. E) containing errors terms or calibration coefficients. M_{dut} (i.e. X) And T_{dut} (i.e. Y) are respectively the measured value and measurand in T-parameters. The k factor is the seventh term of the normalized 8-term model. This means the relationship in (E.3.9) corresponds to the inverse of the equation (E.3.13), given by:

$$\boldsymbol{T_{dut}} = \frac{1}{k}.\left(\boldsymbol{A^{-1}}.\boldsymbol{M_{dut}}.\boldsymbol{B^{-1}}\right) = g(\boldsymbol{M_{dut}}, k^{-1}, \boldsymbol{A^{-1}}, \boldsymbol{B^{-1}}) \tag{E.3.13}$$

The use of thru, line and reflect standards with their measured and estimated values enables the knowledge of error terms (k, A and B).

$$(k, \boldsymbol{A}, \boldsymbol{B}) = h(\boldsymbol{M_i}, \boldsymbol{T_i}) = E \qquad i: \{thru, line, reflect\} \tag{E.3.14}$$

The procedure takes place as following:

A-TRL with measured standards

In our procedure, we account for both the means and uncertainties of the input quantities, collectively represented as $\{\mathrm{x}\}$. The Through-Reflect-Line (TRL) calibration method is employed to extract the calibration coefficients, including the uncertainty associated with each coefficient: $\{k\}_m$, $\{\boldsymbol{A}\}_m$ and $\{\boldsymbol{B}\}_m$. Alongside these, additional outputs such as the propagation constant $\{\gamma\}_m$, the effective permittivity $\{\varepsilon_{r,ef}\}_m$, and the reflection coefficient for the reflect standard $\{\Gamma_{ref}\}_m$ are determined.

To accomplish this, the procedure involves performing repeated measurements of the three calibration standards: thru, reflect, and line. Each standard is measured multiple times to obtain its mean value and associated uncertainty, denoted as $\{\boldsymbol{M_i}\}$ for each standard. These statistical values are then incorporated into the TRL calibration algorithm, which is executed in conjunction with a Monte Carlo (MC) simulation conducted over N iterations. This approach enables a comprehensive assessment of the measurement uncertainty.

The overall process is organized around two main models, each playing a distinct role in the accurate calibration and correction of measurement data.

The first model is centered on the use of the Through-Reflect-Line (TRL) calibration method, as described in equation (E.3.14). In this stage, repeated measurements are performed on the three calibration standards: thru, reflect, and line. The measured values obtained from these standards are used to determine the calibration coefficients, specifically the error terms k, A, and B, as well as other associated outputs such as the propagation constant, the effective permittivity, and the reflection coefficient for the reflect standard. Each standard is measured multiple times to calculate both the mean value and the associated uncertainty. These statistical results are then processed through the TRL calibration algorithm, which is executed alongside a Monte Carlo (MC) simulation across a specified number of iterations. This combined approach allows for a robust estimation of each calibration coefficient and a comprehensive assessment of their uncertainties.

The second model pertains to the correction step, which is governed by equation (E.3.13). In this phase, the error terms obtained from the TRL calibration (k, A, and B) are applied to the measured data for the device under test (DUT) or any verification device. This correction process adjusts the raw measurement data, accounting for systematic errors identified during calibration, and yields the corrected device response along with its standard deviation.

Equation (E.3.15) summarizes the quantities that serve as inputs and outputs for the TRL application when combined with MC analysis. Here, the subscript 'm' denotes measured values. The inputs include the S-parameters of the three measured standards (thru, line, and reflect), the line length difference between the thru and line standards, and their actual S-parameter values. The outputs consist of the calibration coefficients, the propagation characteristics, and the associated uncertainties for each parameter. This structure ensures that all relevant sources of uncertainty are incorporated into the calibration and subsequent correction steps.

The relationship between the calibration coefficients and the measured standards in the Through-Reflect-Line (TRL) calibration process, when combined with Monte Carlo uncertainty analysis, is expressed as follows:

$$\left(\{k\}_m, \{\boldsymbol{A}\}_m, \{\boldsymbol{B}\}_m, \{\gamma\}_m, \{\varepsilon_{r,ef}\}_m, \{\Gamma_{ref}\}_m\right) = TRL\left(\{\boldsymbol{S_{thru}}\}_m, \{\boldsymbol{S_{line}}\}_m, \{\boldsymbol{S_{ref}}\}_m, \{L_{len}\}, \boldsymbol{S_a}^{thru,line}\right) \quad \text{(E.3.15)}$$

Where on the right side we have the S-parameters of the three measured standards, the line length difference between the thru and line standards their actual S-parameters values. On left side, there are the outputs mentioned earlier (i.e. the calibration coefficients, the propagation characteristics with their corresponding uncertainties). Each of these output parameters is determined along with its associated uncertainty, as calculated through the Monte Carlo simulation. This structure ensures that all relevant sources of uncertainty are systematically incorporated into the calibration process, improving the reliability and accuracy of subsequent measurement corrections.

The correction of the DUT or any verification device is carried out according to (E.3.13) in which the error terms and estimate DUT response with standard deviation constitute the input quantities. It can be rewritten in this form as (E.3.16). The corrected DUT S-parameters are $\{\boldsymbol{S_{dut}}\}_{corrected,m}$.

The process of correcting the Device Under Test (DUT), or any verification device, is accomplished by applying equation (E.3.13). In this method, the error terms, which have been extracted from the TRL calibration, together with the estimated DUT response and its standard deviation, serve as the input quantities to the correction process.

This correction procedure can be expressed more explicitly as equation (E.3.16), which provides a clear formulation for obtaining the corrected S-parameters of the DUT. Specifically, the corrected S-parameters, denoted as $\{\boldsymbol{S_{dut}}\}_{corrected,m}$, are determined by applying the correction function to the measured S-parameters of the DUT, along with the calibration error terms k, $\boldsymbol{A}$, and $\boldsymbol{B}$. Mathematically, this relationship is represented as:

$$\left(\{\boldsymbol{S_{dut}}\}_{corrected,m}\right) = Correction(\{\boldsymbol{S_{dut}}\}_m, \{k\}_m, \{\boldsymbol{A}\}_m, \{\boldsymbol{B}\}_m) \quad \text{(E.3.16)}$$

In this formulation, the measured S-parameters of the DUT ($\{\boldsymbol{S_{dut}}\}_m$) are corrected by incorporating the calibration coefficients, which themselves have been assessed along with their uncertainties through the TRL calibration process and Monte Carlo analysis. As a result, the corrected S-parameters of the DUT not only account for systematic errors identified during calibration but also incorporate the associated uncertainty, enhancing the reliability of the measurement results.

B- TRL with CPW standards model

The second part of the procedure focuses on the generation of calibration standards through the use of an analytical coplanar waveguide (CPW) model [14]. This process relies on the specific dimensional and material parameters that define the coplanar structure, including the trace width (W), ground plane width (Wg), gap (G), conductor thickness (t), substrate permittivity (ε), line length (L_{len}), and conductor conductivity (σ). Reference to Fig. 3.43 provides a visual overview of these critical parameters.

To account for the uncertainties inherent in each of these dimensional and material parameters, a Monte Carlo analysis is employed. This analytical approach enables the systematic inclusion of parameter variations by simulating multiple realizations of the standards. Specifically, the Monte Carlo simulation is performed for a defined number of prints (*N*), ensuring that the generated standards reflect the full range of possible parameter values and their associated uncertainties.

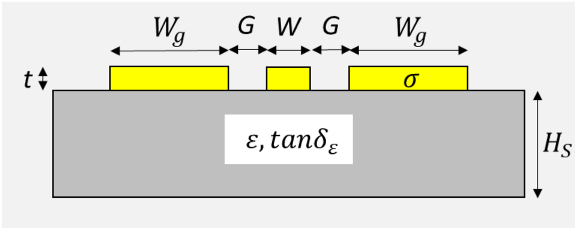

Fig. 3.43: Dimensional and material parameters of CPW line.

It is important to note that the S-parameters associated with the fabricated coplanar waveguide (CPW) standards as well as the Device Under Test (DUT) are inherently surrounded by uncertainty. These S-matrices are represented as $\{\boldsymbol{S_{thru,cpw}}\}$ for the thru standard, $\{\boldsymbol{S_{line,cpw}}\}$ for the line standard, $\{\boldsymbol{S_{ref,cpw}}\}$ for the reflect standard, and $\{\boldsymbol{S_{dut,cpw}}\}$ for the DUT, respectively. Each of these matrices encapsulates not only the actual values but also their associated uncertainties resulting from the fabrication and characterization processes.

Once the CPW standards have been created, complete with their actual S-parameter values and uncertainties, the next step involves generating pseudo measurements using these standards. This is achieved by applying the measurement model described in equation (E.3.12), where the mean error terms A, B, and k are derived from the execution of the TRL calibration using the mean values of the input parameters. Through this operation, the pseudo-measured standards and DUT from the CPW model are denoted as $\{M_{thru}\}_s$, $\{M_{line}\}_s$, $\{M_{ref}\}_s$ and $\{M_{dut}\}_s$, which correspond to transfer (T) matrices. These T matrices can subsequently be converted back into S-parameters for further analysis.

In practice, this procedure can be conducted for each standard or DUT, indexed by x, using the relation given in equation (E.3.17). The subscript 's' indicates that the process is carried out at the standard level, systematically incorporating the uncertainties present in the CPW fabricated standards into the measurement and calibration workflow.

$$\{M_x\}_s = k.\boldsymbol{A}.\{T_{x,cpw}\}.\boldsymbol{B} \tag{E.3.17}$$

Like the procedure applied with actual measurements, the use of TRL calibration with coplanar waveguide (CPW) standards yields a set of output parameters along with their associated uncertainties. These outputs specifically reflect the error terms including $\{k\}_s$, $\{\boldsymbol{A}\}_s$ and $\{\boldsymbol{B}\}_s$ as well as additional parameters such as $\{\gamma\}_s$, the effective permittivity $\{\varepsilon_{r,ef}\}_s$, and the reflection coefficient of the reflect standard $\{\Gamma_{ref}\}_s$. The uncertainties in these parameters are attributed to variations in the CPW standards themselves, encompassing both their dimensional and material properties. For the computation and correction of the Device Under Test (DUT) response, the same equation referenced in the previous section, specifically equation (E.3.28), is utilized to ensure consistency and systematic consideration of all identified error contributions.

$$\left(\{k\}_s, \{\boldsymbol{A}\}_s, \{\boldsymbol{B}\}_s, \{\gamma\}_s, \{\varepsilon_{r,ef}\}_s, \{\Gamma_{ref}\}_s\right) = TRL\left(\{\boldsymbol{S_{thru}}\}_s, \{\boldsymbol{S_{line}}\}_s, \{\boldsymbol{S_{ref}}\}_s, \{L_{len}\}, \boldsymbol{S_a}^{thru,line}\right) \tag{E.3.18}$$

In theory, the mean calibration coefficients obtained using the created standards should closely match the calibration coefficients $\boldsymbol{A}$, $\boldsymbol{B}$, and k derived from the TRL calibration performed with actual measurement data. This equivalence is foundational to ensuring that the simulation-based approach accurately reflects real measurement scenarios.

When the Device Under Test (DUT) can be adequately modeled using coplanar waveguide (CPW) parameters, it becomes feasible to generate simulated measurement data for the DUT. Subsequently, this simulated response can be corrected using an analogous equation to (E.3.16), specifically equation (E.3.19). This correction process allows for systematic treatment of measurement data, enabling accurate representation of the DUT's true behavior after accounting for calibration. Typical examples of DUTs that can be analyzed in this manner include components such as attenuators, transmission lines, and similar structures.

$$(\{\boldsymbol{S_{dut}}\}_{corrected}) = Correction(\{\boldsymbol{S_{dut}}\}_s, \{k\}_s, \{\boldsymbol{A}\}_s, \{\boldsymbol{B}\}_s) \qquad \text{(E.3.19)}$$

Fig. 3.44 illustrates the sequence of steps involved in implementing the TRL calibration method, with a specific focus on evaluating the individual contributions to measurement uncertainty. This approach distinguishes between uncertainty arising from the measurement instrument itself referred to as repeatability uncertainty and uncertainty introduced by the calibration standards, which encompasses both dimensional and material property variations. By systematically applying TRL calibration, it becomes possible to quantify the extent to which each of these factors influences the overall uncertainty in the S-parameter measurement process.

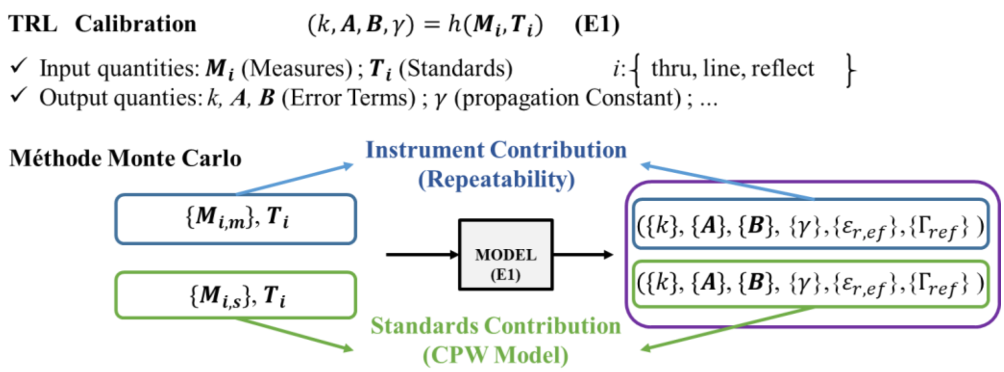

Fig. 3.44: Scheme to analyze repeatability and standards uncertainty contribution on TRL process.

In Fig. 3.45, the methodology is further extended to address the correction of the Device Under Test (DUT) response. This process incorporates both sources of uncertainty: the repeatability uncertainty associated with the measurement setup and the uncertainties attributed to the dimensional and material characteristics of the coplanar waveguide (CPW) standards. By integrating these two components, the correction scheme ensures that the adjusted DUT response accurately reflects the combined effects of instrument repeatability and standard variability, as modeled within the CPW framework.

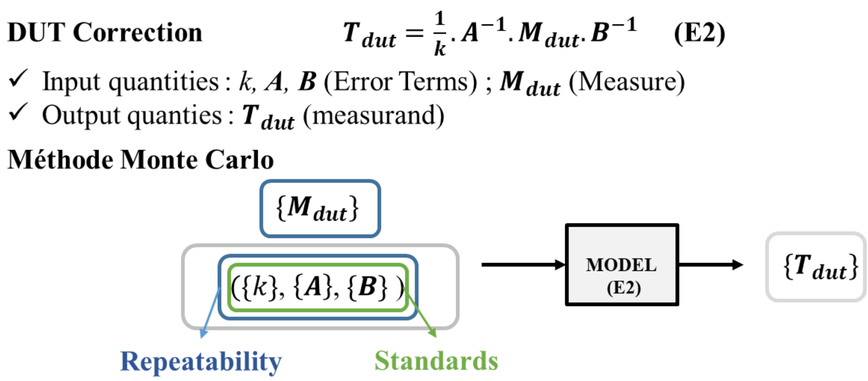

Fig. 3.45: Scheme to analyze repeatability and standards uncertainty contribution for the correction.

C- Evaluation of total uncertainty

Building a comprehensive uncertainty budget for S-parameter measurements begins with the identification of all influence quantities that may impact the accuracy of the measurement process. Recognizing these sources of uncertainty and evaluating their respective contributions forms a critical foundation for establishing reliable measurement confidence.

Within the context of S-parameter measurements, the principal influence quantities encompass both the inherent characteristics of the Vector Network Analyzer and external factors. The intrinsic properties of the VNA include elements such as trace noise, figure noise, non-linearity, and instrument drift. In addition to these, external factors such as the stability of cables, the repeatability of connections, and the isolation between ports also play significant roles in shaping the overall measurement uncertainty. Furthermore, the calibration standards themselves are recognized as major contributors to the uncertainty budget. Each of these influence quantities necessitates a dedicated approach for accurate characterization and incorporation into the uncertainty analysis.

For the purposes of this study, the evaluation of uncertainty is systematically divided into two primary categories: uncertainties associated with the calibration standards and uncertainties related to measurement repeatability. The latter implicitly captures the effects arising from connections, cables, and probes, thereby ensuring that these factors are adequately reflected in the overall assessment.

Following the methodology presented in [26], each output parameter in the S-parameter measurement process can be represented with its associated uncertainty, which accounts for both the contributions from the standards and from repeatability. Ultimately, the expressions for the error terms are provided in a form that clearly delineates the sources and magnitudes of uncertainty for each parameter under consideration.

$$\{\boldsymbol{A}\}_t = \overline{\boldsymbol{A}} + \{\boldsymbol{A}\}_m - \{\boldsymbol{A}\}_s \tag{E.3.20}$$

$$\{\boldsymbol{B}\}_t = \overline{\boldsymbol{B}} + \{\boldsymbol{B}\}_m - \{\boldsymbol{B}\}_s \tag{E.3.21}$$

$$\{k\}_t = \bar{k} + \{k\}_m - \{k\}_s \tag{E.3.22}$$

The propagation constant and effective permittivity are given as follows.

$$\{k\}_t = \bar{\gamma} + \{\gamma\}_m - \{\gamma\}_s \tag{E.3.23}$$

$$\{\varepsilon_{r,ef}\}_t = \overline{\varepsilon_{r,ef}} + \{\varepsilon_{r,ef}\}_m - \{\varepsilon_{r,ef}\}_s \tag{E.3.24}$$

The correction procedure for the Device Under Test (DUT) integrates the final expressions of the input quantities, each accompanied by their respective uncertainties, together with the measured response of the DUT and its standard deviation, as depicted in Fig. 3.45. This correction is performed through the application of equation (E.3.25), which utilizes the measured DUT response $\{\boldsymbol{S_{dut}}\}_m$ along with the calibration coefficients ($\{k\}_t$,$\{\boldsymbol{A}\}_t$ and $\{\boldsymbol{B}\}_t$).

Through this process, the resulting S-parameters for the DUT are determined as mean values that inherently account for uncertainties arising from both the calibration standards and the repeatability of the measurement process. In essence, the comprehensive expression for the corrected DUT response $\{\boldsymbol{S_{dut}}\}_t$ is formulated in accordance with equation (E.3.26), as referenced in [26]. This ensures that the final S-parameter values reflect all relevant uncertainty contributions, thereby supporting robust and reliable measurement results.

$$(\{\boldsymbol{S_{dut}}\}_t) = Correction(\{\boldsymbol{S_{dut}}\}_m, \{k\}_t, \{\boldsymbol{A}\}_t, \{\boldsymbol{B}\}_t) \tag{E.3.25}$$

$$\boldsymbol{S_{dut}} = \overline{\boldsymbol{S_{dut}}} \pm \boldsymbol{\sigma}[\boldsymbol{S_{dut}}] \tag{E.3.26}$$

Where $\overline{\boldsymbol{S_{dut}}}$ represents its mean S-parameters and $\boldsymbol{\sigma}[\boldsymbol{S_{dut}}]$ is the associated uncertainty due both to the repeatability and the standards.

5.2. Implementation

This section examines the evaluation of uncertainty arising from two primary sources: instrument repeatability and calibration standards. The instrument contribution is mainly attributed to the effects of the probes during the measurement process. To quantify this, repeatability measurements are performed using the measured data from the standards, which serve as the input quantities for the measurement model described in equation (E.3.13).

Five repeated measurements are conducted for each single standard thru, reflect, and line as well as for the Device Under Test (DUT). The means and standard deviations obtained from these repeated measurements are used as input data for the TRL (Thru-Reflect-Line) algorithm. This analysis incorporates Monte Carlo (MC) simulation, following equations (E.3.14) to (E.3.18), implemented in a Python program. For robust statistical analysis, the number of Monte Carlo runs is set to 20,000.

The standards are defined as follows: the thru standard is realized by a 200 µm coplanar waveguide (CPW) line, and the line standard has a length of 250 µm. The difference in length between these two standards is precisely 50 µm. The reflect standard is positioned at the midpoint of the thru standard.

The outputs of this uncertainty evaluation include the error boxes, the propagation constant, and the true reflection coefficient of the reflect standard. These results provide insight into the contributions of both measurement repeatability and standard definitions to the overall uncertainty in the calibration and measurement process.

Fig. 3.46 illustrates the uncertainty associated with the propagation constant as obtained from the described measurement and analysis process. The results indicate that the real component of the propagation constant demonstrates attenuation that progressively increases with frequency. This trend reflects the inherent frequency-dependent losses present in the measurement system.

Additionally, the effective permittivity can be determined from this analysis. By evaluating the measurement data and applying the Monte Carlo approach, the uncertainty in the effective permittivity is also quantified, offering insight into the reliability and consistency of the extracted material properties under repeated measurement conditions.

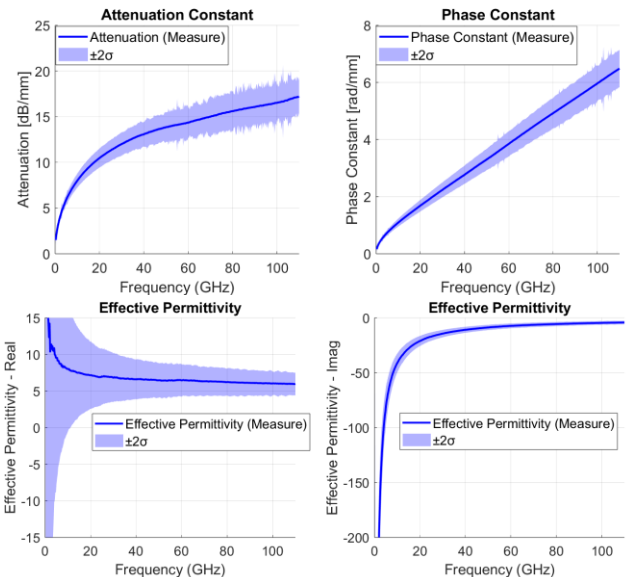

Fig. 3.46: Uncertainty on propagation constant and Effective permittivity (repeatability).

The reflection coefficient of the reflect standard is an essential output that is directly evaluated within the measurement model. In the context of calibration, this coefficient is particularly significant for the short standard, which is integral to the accuracy of the overall process. The reflection coefficient, commonly denoted as S11, is equal to S22 in the case of a reciprocal network, thereby providing a consistent measure of reflection characteristics for the standard.

The determination of the actual reflection coefficient for the short standard is achieved through repeatability measurements. These measurements allow for the quantification of uncertainty associated with the reflection coefficient, which is a critical factor in assessing the reliability of the calibration procedure. The resulting uncertainty is depicted in Fig. 3.47, which presents the variability inherent to the actual reflection coefficient of the short standard due to repeatability effects. This analysis underscores the importance of understanding and accounting for measurement repeatability in the calibration and subsequent use of the standard.

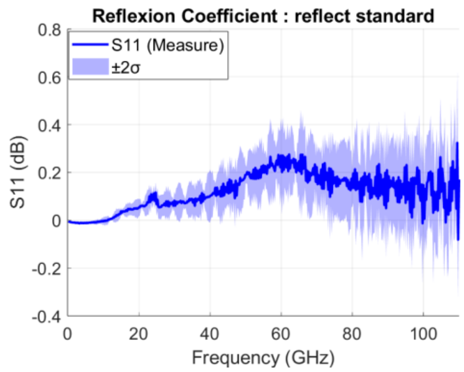

Fig. 3.47: Uncertainty on the actual reflection coefficient of short standard (repeatability).

Repeatability uncertainty is not limited to previously described outputs, such as the propagation constant and reflection coefficient. It also directly influences the calibration coefficients $\boldsymbol{A}$, $\boldsymbol{B}$, and k which represent directivity, source match, and both reflection and transmission tracking. These calibration parameters are integral to the measurement system's accuracy and are subject to variations arising from repeatability effects during the measurement process.

To systematically assess the effect of repeatability uncertainty on device corrections, three types of Devices Under Test (DUTs) were analyzed: a transmission line, a 20 µm-offset short circuit, and a load. For each DUT, corrections were performed using Monte Carlo simulations. Equation (E.3.12) was applied to each DUT, ensuring that the influence of repeatability on the correction procedure was comprehensively captured. This approach enabled the quantification of uncertainty associated with calibration coefficients and the corresponding corrected responses for each DUT, thereby providing a thorough evaluation of measurement reliability under repeated measurement conditions.

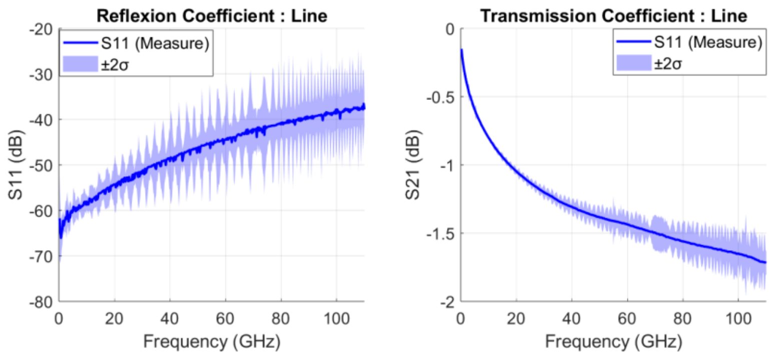

Fig. 3.48: Uncertainty on the reflection and transmission coefficients of corrected Line-DUT (repeatability).

Fig. 3.48 presents the corrected measurement response for a 300 µm coplanar waveguide (CPW) line, displaying both the reflection and transmission coefficients. This analysis highlights the influence of repeatability errors, with particular emphasis on the variability introduced by differences in probe positioning during the measurement process.

The results clearly demonstrate that even small inconsistencies in the placement of probes can have a significant effect on the measured reflection (S11) and transmission (S21) characteristics. These variations, in turn, impact the overall accuracy and reliability of the calibration and measurement process. By quantifying the uncertainty associated with these repeatability errors, the analysis underscores the necessity of careful probe handling and consistent measurement techniques to ensure dependable calibration outcomes.

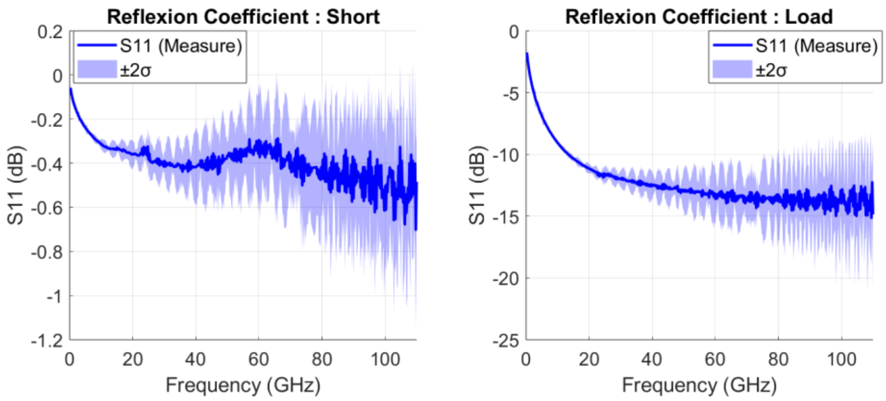

Fig. 3.49: Uncertainty on the reflection coefficients of offset short circuit and load (repeatability).

Fig. 3.49 presents the measured responses of both the dual shifted short circuit and the load under repeatability conditions. The reflection coefficient (S11) for the short circuit demonstrates noticeable fluctuations as the frequency increases. These variations are indicative of the sensitivity of the measurement system to probe positioning and other repeatability factors, which become more pronounced at higher frequencies.

In contrast, the load exhibits a distinctly different S11 behavior. At low frequencies, the value of S11 remains low, which can be attributed to the high characteristic impedance (Zc) of the transmission line. This high impedance results in a significant mismatch between the load resistance (68 Ω) and the line impedance, thus reducing the magnitude of the reflected signal. As the frequency increases, Zc gradually stabilizes, and the S11 response of the load correspondingly recovers. This trend underscores the frequency-dependent nature of the impedance matching and its impact on repeatability uncertainty in calibration and measurement processes.

A comparable approach was undertaken utilizing standards that were modeled based on the coplanar waveguide (CPW) structure and analyzed through the Monte Carlo (MC) simulation technique. As outlined in Section C, the dimensional and material characteristics were employed to accurately construct the standards, ensuring that their true electrical responses were represented.

Subsequently, simulated measurements were obtained by cascading these precisely constructed standards with the error boxes derived from the Through-Reflect-Line (TRL) calibration procedure. The error boxes used in this process were generated by applying the mean raw measurement values from the measured standards. This methodology enabled the generation of measurement data that closely reflected the actual behavior of the standards when subjected to the calibration environment, thereby supporting a rigorous assessment of measurement and calibration accuracy under repeatability conditions.

Table 3.6: CPW parameters.

Parameters	Mean	Std
w (μm)	0.5	0.106
wg (μm)	40	0.91
g (μm)	0.85	0.059
t (μm)	0.35	0.02
ε_r	11.9 + 0i	1.19 + 0.1i
σ (S/m)	3.64e7	0.324e7

The main objective of this section is to assess the uncertainty contribution of the CPW parameters. For this purpose, a TRL calibration is performed using the generated measurements, based on the model relationship (E.3.31). The corresponding output quantities include the error boxes, propagation constant, and other related parameters.

Fig. 3.50 shows the uncertainty on the propagation constant derived from the standards. As previously observed in Figure 3.46, the uncertainty increases with frequency roughly proportional to $\sqrt{f}$. However, in this case, the magnitude of uncertainty is larger.

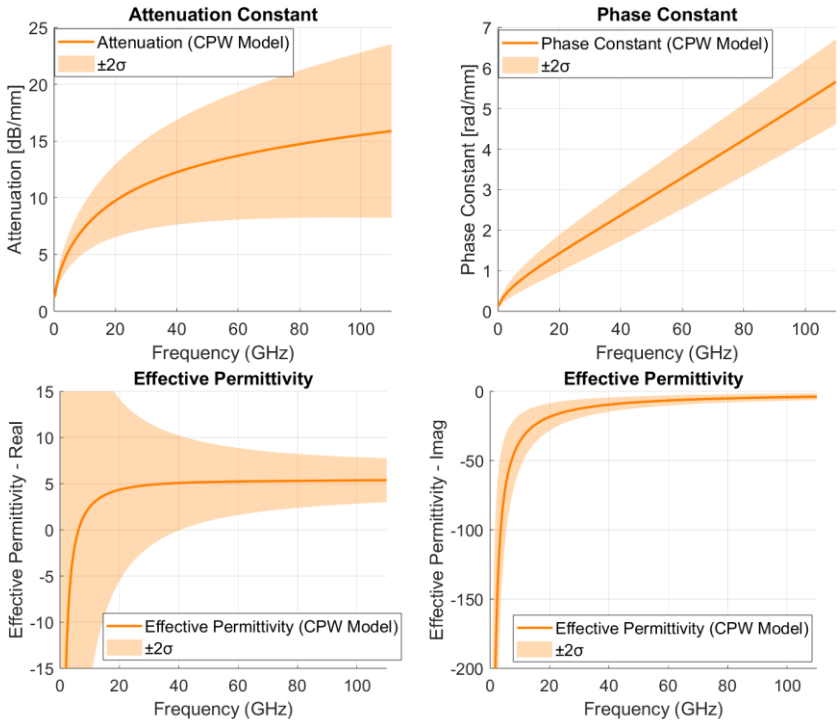

Fig. 3.50: Uncertainty on propagation constant and Effective permittivity (CPW standards).

In evaluating the overall uncertainty associated with coplanar waveguide (CPW) structures, it is critical to assess the individual contributions from each key parameter defining the CPW geometry and materials. The uncertainty analysis focuses on several specific parameters, including the cross-sectional dimensions, electrical conductivity, and dielectric constant of the substrate (Fig. 3.51).

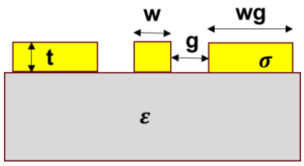

Fig. 3.51: Physical CPW parameters

A summary of these parameters and their respective uncertainty contributions is provided in Table 3.6. By evaluating the uncertainty associated with each parameter, it becomes possible to identify which aspects of the CPW design are most critical for accurate modeling and calibration. This insight is essential for optimizing measurement procedures and improving the reliability of results in CPW-related applications.

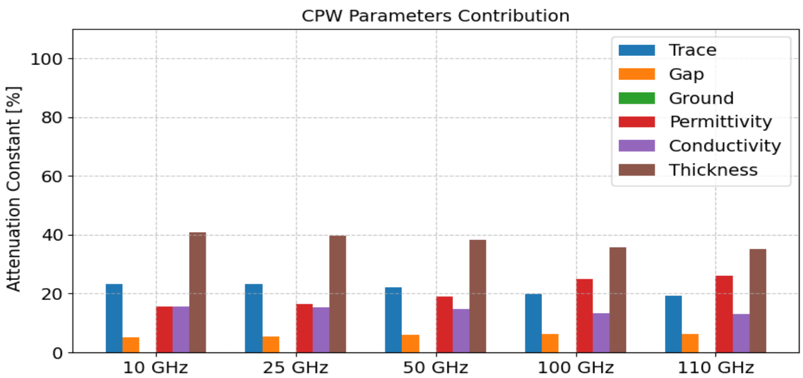

Fig. 3.52: Uncertainty contribution of CPW parameters.

The analysis of the histogram in Fig. 3.52 demonstrates that most coplanar waveguide (CPW) parameters play a significant role in the overall uncertainty, apart from the ground plane width, which has a minimal impact. Notably, the thickness of the metal layer emerges as the most influential factor, accounting for nearly 40% of the total uncertainty contribution. Table 3.7 further highlights the influence of individual physical parameters on the total uncertainty observed on the attenuation constant of CPW standards. In particular, the trace width, substrate permittivity, and electrical conductivity each contribute more than 18% to the overall uncertainty. This significant impact underscores the importance of accurately controlling and characterizing these parameters during the design and calibration processes. Understanding the relative contributions of these factors is essential for prioritizing measurement efforts and enhancing the precision of CPW-related applications.

Table 3.7: Contribution of physical parameters of standards.

Physical CWP parameters	Attenuation
Thickness (t)	40 %
Trace width (w)	20 %
Permittivity (ε)	- 20 %
Conductivity (σ)	15 %
Gap (g)	+ 5 %
Ground plane (wg)	low

The devices under test (DUTs) considered in this analysis are 300-µm line components. Their measurement correction was performed following the procedure outlined in equation (E.3.32). Figure 3.53 presents both the reflection coefficient (S11) and the transmission coefficient (S21) for the DUT. Across the examined frequency range, the S11 parameter remains very low, which is consistent with the negligible reflection expected from a line defined by the CPW model. This outcome confirms the effectiveness of the applied correction and the suitability of the CPW model for representing DUT behavior.

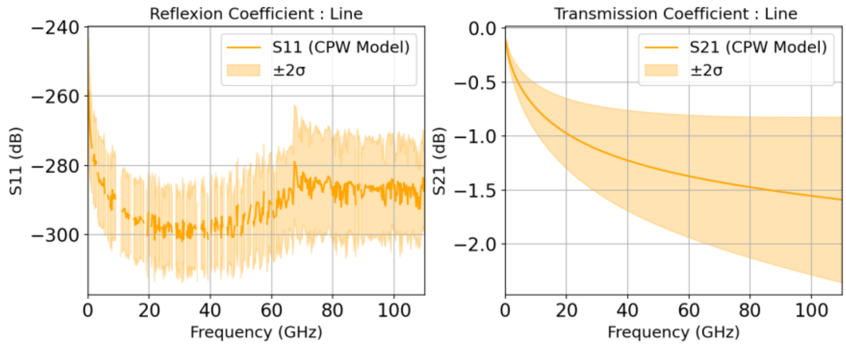

Fig. 3.53: Uncertainty on the reflection and transmission coefficients of Line (standards).

If the device under test (DUT) can be analytically represented using the coplanar waveguide (CPW) model, its measurement can be simulated and subsequently corrected based on the modeled parameters. To illustrate this principle, two representative one-port circuits were considered: a 20 µm-offset short and a load, with both configurations constructed according to the CPW approach.

In the case of the offset short, the actual reflection coefficient, denoted as ΓS, was assigned a value of -1. Although this assignment is idealized and does not capture the full complexity of a real-world short circuit, it effectively demonstrates the underlying concept of analytical modeling. A more accurate depiction would require a comprehensive descriptive model that reflects the physical properties and behavior of the circuit, as referenced in equation (E.3.38).

For the load configuration, the impedance was set to 68 Ω, determined from direct current (DC) measurements discussed in Chapter 4. While this value provides a practical example, it should be noted that it does not entirely represent the true operational characteristics of the load, which would necessitate a more realistic model, as described in equation (E.3.39).

The objective in presenting these examples is to demonstrate that an analytical approach is viable when the model used accurately describes the circuit in question. Within these equations, the propagation constant γ is derived from the CPW model after the relevant dimensional and material parameters have been assigned. This approach enables precise simulation and correction of DUT measurements, provided that the underlying model faithfully captures the circuit's behavior.

$$S_{11,short} = \Gamma_S e^{-2\gamma l} \; ; \; \Gamma_S = -1 \tag{E.3.38}$$

$$S_{11,load} = \Gamma_L e^{-2\gamma l} \; ; \; \Gamma_L = \frac{Z_L - Z_c}{Z_L + Z_c} \; ; \; Z_L = 68\Omega \tag{E.3.39}$$

Using the constructed offset short and load circuits, measurements were simulated to evaluate the device under test (DUT) behavior modeled by coplanar waveguide (CPW) parameters. After simulation, corrections were applied to the measurement data to account for dimensional and material variations inherent in the CPW structure.

The resulting reflection coefficients (S11) for both configurations, the offset short circuit and the 68 Ω load are displayed in Fig. 3.54. These results illustrate the distinct reflection characteristics of each standard, providing insight into the effectiveness of the analytical modeling and correction procedures applied to CPW-based DUTs.

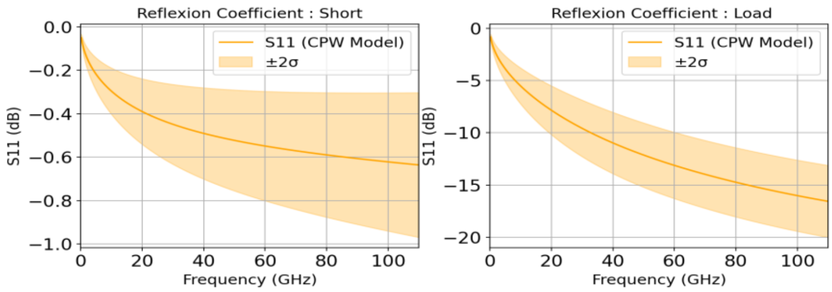

Fig. 3.54: Uncertainty on the reflection coefficients of offset short circuit and load (standards).

To provide a clear understanding of the factors contributing to measurement uncertainty, the results from both sources are presented side by side. Fig. 3.55 specifically highlights the differences in uncertainty contributions, enabling a direct comparison. When examining the mean values obtained from each procedure, it becomes evident that there are only marginal differences between them. This suggests that, overall, both methods yield comparable outcomes in terms of uncertainty.

It is important to note that the uncertainty associated with the attenuation constant is primarily influenced by the standards used in the measurement process. This finding underscores the pronounced sensitivity of coplanar waveguide (CPW) structures to variations in both dimensions and materials, especially at the nanoscale. Such sensitivity reinforces the need for precise modeling and careful consideration of all relevant parameters when working with CPW-based devices to ensure accurate characterization.

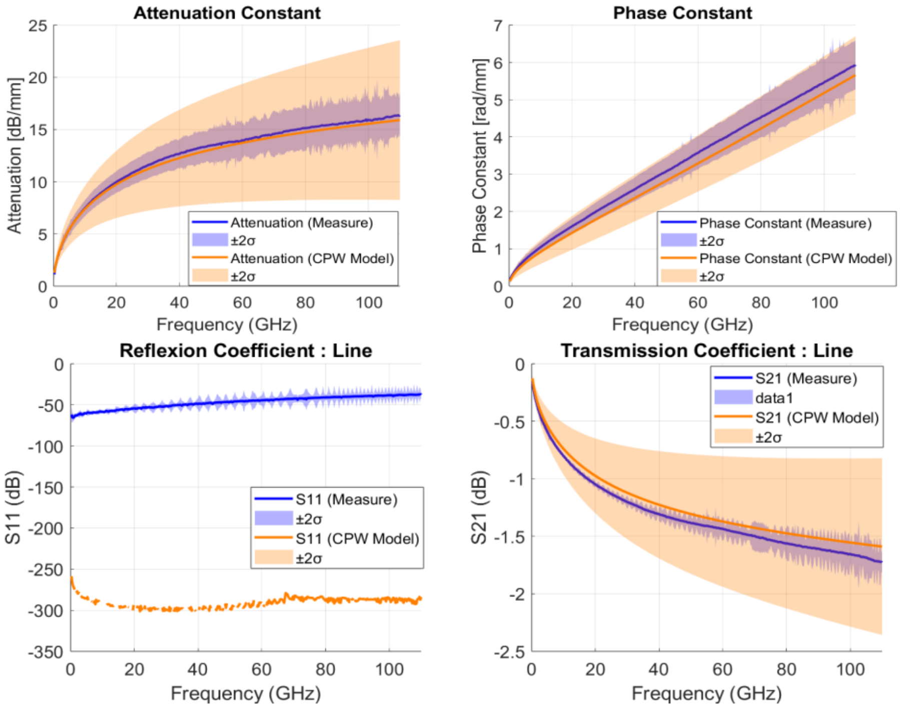

Fig. 3.55: Uncertainty on propagation constant and corrected DUT (repeatability - CPW standards).

The characteristic impedance, denoted as Zc, was assessed using three different approaches: measurement of the propagation constant, analytical calculation based on the coplanar waveguide (CPW) model, and 3D electromagnetic simulation with CST software. This comprehensive evaluation aimed to compare the accuracy and consistency of each method in characterizing the nanoscale CPW line.

At the frequency of 110 GHz, the results obtained from each method indicated close, yet distinguishable, values for the real part of the characteristic impedance. Specifically, the 3D CST simulation produced a real part of Zc equal to 62.93 Ω, while the direct measurement yielded a slightly lower value of 61.86 Ω. In contrast, the analytical CPW model predicted a somewhat higher value of 65.43 Ω. These findings highlight the impact of modeling and measurement techniques on the determination of characteristic impedance in high-frequency applications.

For the imaginary part of Zc, which is primarily associated with ohmic losses in the CPW structure, the 3D CST simulation provided the lowest value, approximately 7.74 Ω. This result, as illustrated in Fig. 3.56, emphasizes the sensitivity of loss characterization to the method employed and underscores the benefit of advanced simulation in capturing subtle loss mechanisms.

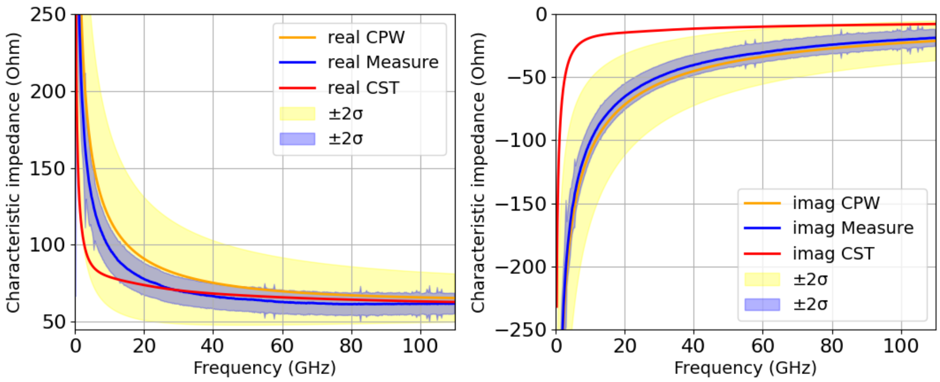

Fig. 3.56: Uncertainty on characteristic impedance (repeatability - CPW standards).

The uncertainty in the characteristic impedance of the coplanar waveguide (CPW) line, as determined by the CPW standards, incorporates two primary factors: the repeatability of the measurement process and the characteristic impedance values derived from 3D electromagnetic simulations. However, this combined uncertainty does not include imaginary part of the impedance. Table 3.8 presents a detailed comparison of the characteristic impedance (Zc) and the associated uncertainty for both the CPW standards and measurement repeatability at 110 GHz. The table summarizes the complex impedance values, including both the real and imaginary components, as well as the standard deviation representing uncertainty for each method.

For the CPW standards, the characteristic impedance is given as 65.33 - i 21.29 Ω, with an uncertainty of 7.80 Ω. In contrast, the measurement repeatability approach yields a characteristic impedance of 61.74 - i 18.80 Ω and a lower uncertainty of 3.37 Ω. These values directly reflect the impact of the measurement procedure and the influence of the standards used, further highlighting the sensitivity of the coplanar waveguide structure to the specific measurement conditions. The comparison demonstrates that, while both approaches produce closely related impedance values, the uncertainty associated with repeatability is notably smaller, indicating a higher degree of consistency in repeated measurements.

Table 3.8: Characteristic impedance and uncertainty for both repeatability and CPW standards

@ 110 GHz	**Zc (Ω)**	**σ(Zc) (Ω)**
CPW Standards	65,33 – i 21,29	7,80
Repeatability	61,74 – i 18,80	3,37

The alignment of these results provides a robust and reliable method for approximating the characteristic impedance of nanoscale CPW lines.

To calculate the overall uncertainty associated with each output parameter, the individual contributions from the measurement instrument (repeatability) and the calibration standards are combined using a squared-sum (root-sum-square) method. This approach ensures that both sources of uncertainty are appropriately accounted for in the final assessment. The specific mathematical formulations used to derive the output quantities in the Through-Reflect-Line (TRL) calibration and correction procedures are detailed in equations (E.3.33) to (E.3.37).

Fig. 3.57 illustrates the mean values of propagation constant and effective permittivity, along with their respective total uncertainties. These values reflect the combined influence of both repeatability and standard uncertainties. Additionally, these propagation characteristics have been evaluated through circuit-level simulations performed using Advanced Design System (ADS) software, further validating the uncertainty analysis.

Table 3.9: Uncertainty on attenuation constant and effective permittivity according to repeatability, CPW standards and combination

@ 110 GHz	**Repeatability**	**CPW Standards**	**Total (combined)**
σ(**Attenuation**)	1,075	3.825	4,888
$\sigma(Re(\boldsymbol{\varepsilon_{r,eff}}))$	0,774	1,173	1,365

Table 3.9 provides a comprehensive summary of the uncertainties associated with two key parameters: the attenuation constant σ(Attenuation) and the effective permittivity $\sigma(Re\ (\boldsymbol{\varepsilon_{r,eff}}))$. These uncertainties are systematically reported across three different assessment levels: repeatability, CPW standards, and their combined effect.

By organizing the data in this manner, the table enables a clear comparison of the contributions from measurement repeatability, the inherent uncertainty in the CPW standards, and the overall combined uncertainty. This structured presentation facilitates the evaluation of measurement consistency and calibration quality, highlighting the relative impact of each source of uncertainty on the final characterization results for both the attenuation constant and the effective permittivity.

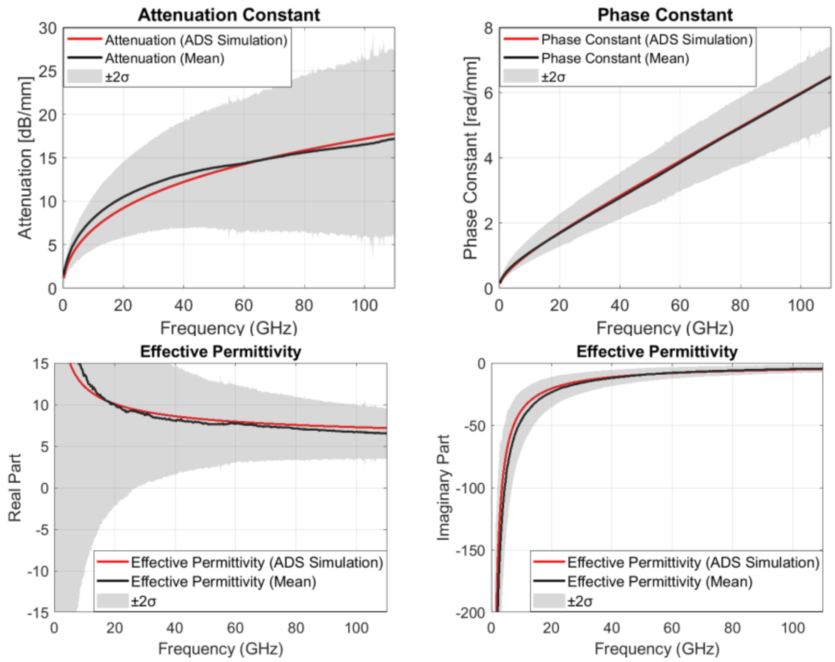

Fig. 3.57: Global uncertainty on propagation characteristics.

In this study, the S-parameters of the verification components, or Devices Under Test (DUTs), were systematically evaluated alongside their global uncertainty. The investigation included one transmission device, specifically a 100-µm coplanar waveguide (CPW) line, and two one-port devices: an offset short and a load. Each of these DUTs underwent repeated measurement and simulation using Advanced Design System (ADS) software to ensure comprehensive assessment and validation.

Fig. 3.58 presents the mean values of the reflection coefficient (S11) and the transmission coefficient (S21) in linear magnitude for the measured CPW line. The associated uncertainty is depicted using a coverage factor of k = 2, providing a clear representation of measurement confidence. The results indicate that the mean corrected S21 value obtained from direct measurement aligns closely with the value derived from simulation, with both measurements falling within the established uncertainty budget. This agreement demonstrates the consistency and reliability of the measurement and simulation methodologies applied in the characterization process.

A notable observation emerged regarding the reflection coefficient S11. In the simulation, the reference impedance was set to closely match the characteristic impedance of the CPW line. Consequently, this resulted in minimal reflection, with the S11 value approaching zero. This outcome underscores the importance of impedance matching in minimizing reflection and highlights the sensitivity of S-parameter measurements to reference impedance selection during simulation and measurement procedures.

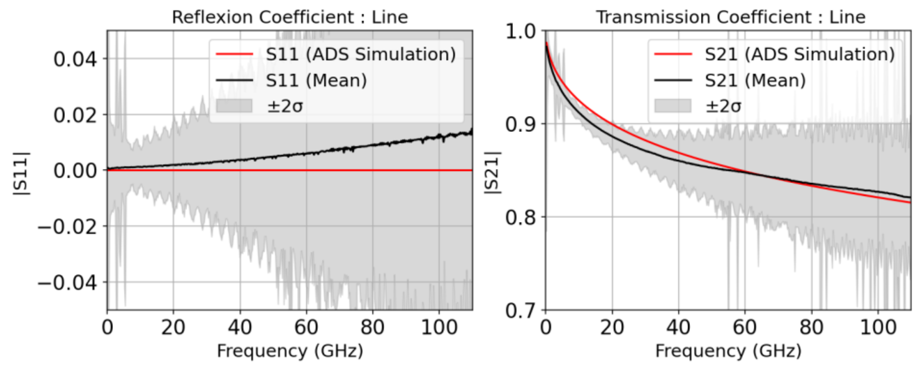

Fig. 3.58: Global uncertainty on the S-parameters of 300µm CPW line.

The 20 µm-offset short circuit and load were each subjected to a series of repeated measurements to rigorously assess their performance and measurement consistency. For both devices, the same correction methodology was applied as with the transmission line, ensuring that systematic errors were minimized and the data accurately reflected the intrinsic properties of the Devices Under Test (DUTs).

Following the correction process, further validation was achieved by simulating the respective circuits of these DUTs using Advanced Design System (ADS) software. This simulation step provided an additional layer of verification by allowing direct comparison between the measured and modeled behaviors of the offset short and load.

The results of these assessments are summarized in Fig. 3.59, which displays the reflection coefficients for both the 20 µm-offset short and the load. These reflection coefficients provide critical insight into the impedance characteristics and the quality of the calibration and measurement processes for these one-port devices.

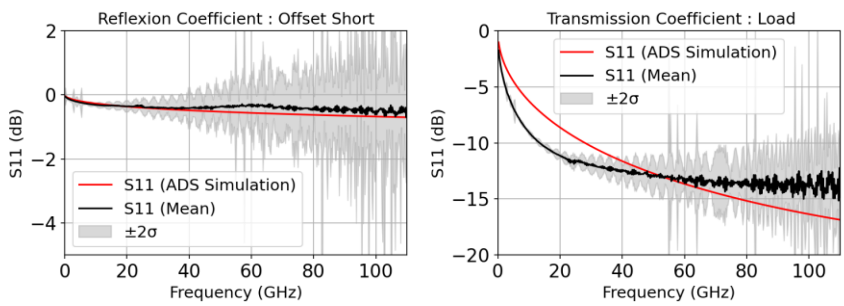

Fig. 3.59: Global uncertainty on the S-parameters of offset short and load.

Table 3.10 provides a detailed overview of the uncertainties associated with the corrected S-parameters for three distinct Devices Under Test (DUTs): a transmission line, a short circuit, and a load. These uncertainties are presented relative to three key assessment levels at 110 GHz: repeatability, CPW standards, and their combined effect. The summary allows for a clear comparison of the measurement consistency and calibration quality for each DUT, illustrating the influence of both individual and combined uncertainty sources on the overall characterization results.

Table 3.10: Uncertainties on corrected S parameters of DUTs according to repeatability, CPW Standards and combination

Line	**Repeatability**	**CPW Standards**	**Total (combined)**
$\sigma(\|S21\|)$	0.004	0.0365	0.0068
$\sigma(\|S11\|)$	0.0185	low	00262
Short	**Repeatability**	**CPW Standards**	**Total (combined)**
σ(S11 dB)	0.0930	0.1666	0.4720
Lord	**Repeatability**	**CPW Standards**	**Total (combined)**
σ(S11 dB)	2.981	1.7200	0.8183

The evaluation of the uncertainty budget is essential for gaining a comprehensive understanding of the different factors that influence measurement results. By carefully assessing the sources and magnitude of uncertainties, it is possible to identify the primary contributors to overall measurement variability and error.

This evaluation can be conducted using two principal methods: linear uncertainty propagation and Monte Carlo simulation. Linear uncertainty propagation involves analytically combining individual uncertainty components to estimate the total uncertainty. In contrast, Monte Carlo simulation employs statistical techniques, where repeated random sampling is used to model the combined effect of multiple uncertainty sources, thereby providing a more detailed representation of the uncertainty distribution.

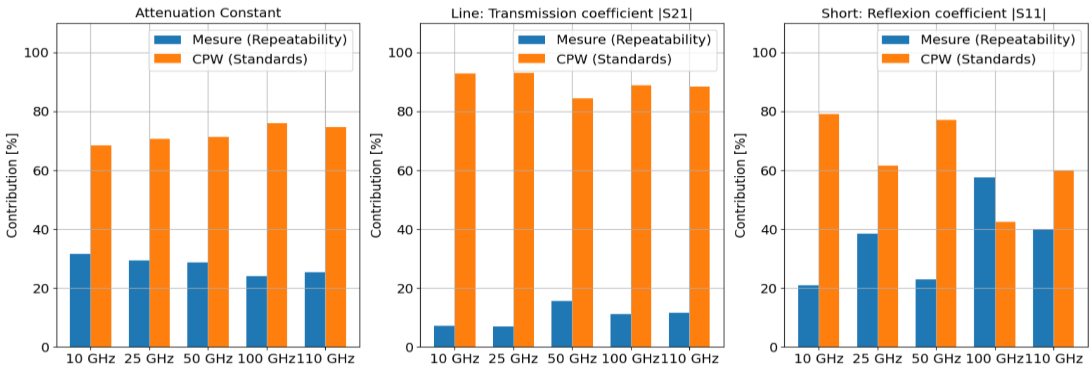

Fig. 3.60: Uncertainties contribution of repeatability and standards.

Fig. 3.60 provides a detailed examination of the primary factors influencing attenuation and S-parameters at specific frequency points within the measured band. The analysis reveals that, particularly at higher attenuation levels, calibration standards emerge as the dominant source of uncertainty. Specifically, these standards are responsible for more than 60% of the total uncertainty budget associated with attenuation measurements. Furthermore, in the context of the transmission reflection, calibration standards contribute to over 80% of the overall uncertainty as shown in Table 3.11. This significant impact underscores the critical role of calibration standards in the reliability and accuracy of S-parameter measurements across the evaluated frequency range.

Table 3.11: Uncertainties contribution at level repeatability and standards

Level	**Attenuation**	**S21**	S11
CPW standards	+ 65 %	80 %	+ 60 %
repeatability	30 %	15 %	- 40 %

Conclusion

This chapter has presented a comprehensive exploration of experimental RF and microwave characterization utilizing on-wafer measurement techniques, extending up to frequencies of 110 GHz. The discussion began with a detailed description of both the DC and RF measurement setups, accompanied by practical recommendations aimed at enhancing measurement quality, reducing parasitic effects, and promoting consistency throughout the experimental process.

The chapter concentrated on the investigation of coplanar waveguide (CPW) structures, employing three complementary approaches: analytical modeling, full-wave electromagnetic simulation, and measurement-based extraction. Each method provided consistent estimations of electrical parameters, which not only demonstrated the robustness of these approaches but also clarified their individual advantages and limitations.

A significant focus was placed on the correction of raw data obtained from Devices Under Test (DUTs). This correction process is critical for eliminating systematic errors that arise from the measurement environment and the configuration of the probe station. The reproducibility and repeatability of on-wafer measurements, particularly at the nanoscale, were examined experimentally. This examination underscored the impact of probe alignment, contact quality, and calibration strategy on the variability of measurement results.

An extensive uncertainty analysis was also conducted as part of this study. Two TRL calibration techniques were evaluated: one based on measured standards and the other on CPW line models. The overall uncertainty was quantified by integrating both systematic and random error contributions. This comprehensive evaluation provides deeper insight into the confidence level associated with the extracted parameters and establishes the experimental boundaries for future device characterizations.

In summary, this work demonstrates the critical importance of employing a rigorous methodology in high-frequency on-wafer measurements. By combining precise calibration procedures, effective error correction, and thorough uncertainty analysis, the study ensures that results in RF and microwave research are both reliable and reproducible.

References 3

[1] https://www.testequipmenthq.com/datasheets/Rohde-Schwarz-ZVA67-Datasheet.pdf

[2] Mokhtari, C., Lenoir, C., Sebbache, M., & Haddadi, K. (2023, August). Automated and robotic on-wafer probing station. In *2023 IEEE Symposium on Wireless Technology & Applications (ISWTA)* (pp. 99-102). IEEE.

[3] Mokhtari, C., Seck, D., Allal, D., Lenoir, C., Sebbache, M., Berthe, M., & Haddadi, K. (2023, June). Nanorobotics and Automatic On-Wafer Probe Station with Nanometer Positionning Accuracy. In *2023 IEEE MTT-S International Conference on Numerical Electromagnetic and Multiphysics Modeling and Optimization (NEMO)* (pp. 22-24). IEEE.

[4] Sakamaki, R., & Horibe, M. (2021, January). Automatic probing system with machine learning algorithm. In *2021 96th ARFTG Microwave Measurement Conference (ARFTG)* (pp. 1-4). IEEE.

[5] Vitali, D., Chillico, A., Samek, W., & Bengtsson, O. (2025). Improved On-Wafer Probing of High-Frequency Components Based on Optical Recognition of the Probe Positions. *IEEE Transactions on Microwave Theory and Techniques*.

[6] Zeier, M., Hoffmann, J., Hürlimann, P., Rüfenacht, J., Stalder, D., & Wollensack, M. (2018). Establishing traceability for the measurement of scattering parameters in coaxial line systems. *Metrologia*, *55*(1), S23.

[7] https://www.formfactor.com/product/probe-systems/150-mm-systems/mps150/

[8] Zeier, M., Allal, D., & Judaschke, R. (2018). Guidelines on the evaluation of vector network analysers (VNA). *EURAMET Calibration Guide*, *3*(12), 507-521.

[9] Nemashkalo, D., Koch, P., Moonen, N., & Leferink, F. (2024, September). S-Parameters Characterization for EMI Filters: Limitations. In *2024 International Symposium on Electromagnetic Compatibility–EMC Europe* (pp. 350-355). IEEE.

[10]https://www.micronanotools.com/products/manual-vacuum-probe-system-with-temperature-control

[11] Schmidt, R., Clochiatti, S., Mutlu, E., Weimann, N., Ferrero, A., Dieudonné, M., & Schreurs, D. M. P. (2022). Compensating probe misplacements in on-wafer S-parameters measurements. *IEEE Transactions on Microwave Theory and Techniques*, *70*(11), 5213-5223.

[12] Mokhtari, C. (2023). *Development of a Nano-robotics and Automated Microwave On-Wafer Probe Station* (Doctoral dissertation, Université de Lille).

[13] Heinrich, W. (1993). Quasi-TEM description of MMIC coplanar lines including conductor-loss effects. *IEEE transactions on microwave theory and techniques*, 41(1), 45-52.

[14] R. E. Collin, *Foundations for Microwave Engineering*, 2nd ed.New York: Mc Graw-Hill, 1992.

[15] https://qucs.sourceforge.net/tech/node86.html

[16] Gold, Gerald, et al. "High-frequency modeling of coplanar waveguides including surface roughness." *Advances in Radio Science* 17 (2019): 51-57.

[17] Schnieder, Frank, Thorsten Tischler, and Wolfgang Heinrich. "Modeling dispersion and radiation characteristics of conductor-backed CPW with finite ground width." *IEEE Transactions on Microwave Theory and Techniques* 51.1 (2003): 137-143.

[18] Phung, G. N., et al. "Improved modeling of radiation effects in coplanar waveguides with finite ground width." *2020 50th European Microwave Conference (EuMC)*. IEEE, 2021.

[19] Engen, G. F., & Hoer, C. A. (1979). Thru-reflect-line: An improved technique for calibrating the dual six-port automatic network analyzer. *IEEE transactions on microwave theory and techniques*, *27*(12), 987-993.

[20] Marks, R. B., & Williams, D. F. (1991). Characteristic impedance determination using propagation constant measurement. *IEEE Microwave and guided wave Letters*, *1*(6), 141-143.

[21] Williams, D. F., & Marks, R. B. (1991). Transmission line capacitance measurement. *IEEE Microwave and guided wave letters*, *1*(9), 243-245.

[22] U. Arz and J. Leinhos, "Broadband Permittivity Extraction from On-Wafer Scattering-Parameter Measurements," 2008 12th IEEE Workshop on Signal Propagation on Interconnects, Avignon, France, 2008, pp. 1-4, doi: 10.1109/SPI.2008.4558382.

[23] U. Arz and D. F. Williams, "Uncertainties in complex permittivity extraction from coplanar waveguide scattering-parameter data," 81st ARFTG Microwave Measurement Conference, Seattle, WA, USA, 2013, pp. 1-6, doi: 10.1109/ARFTG.2013.6579047.

[24] https://wcalc.sourceforge.net/cgi-wcalc.html

[25] Z. Hatab, M. E. Gadringer and W. Bösch, "Propagation of Linear Uncertainties Through Multiline Thru-Reflect-Line Calibration," in *IEEE Transactions on Instrumentation and Measurement*, vol. 72, pp. 1-9, 2023, Art no. 1007409, doi: 10.1109/TIM.2023.3296123.

[26] B. D. Hall, D. Allal, A. Litwin and F. Ziadé, "Evaluating the Uncertainty of Self-Calibrating VNA Procedures," *2018 Conference on Precision Electromagnetic Measurements (CPEM 2018)*, Paris, France, 2018, pp. 1-2, doi: 10.1109/CPEM.2018.8501006.

[27] Allal, Djamel, et al. "Propagation automatique des incertitudes: application aux techniques d'auto-étalonnage des analyseurs de réseau vectoriels." *17th International Congress of Metrology*. EDP Sciences, 2015.

Introduction

The precise measurement of high-impedance devices introduces a distinct set of challenges within the fields of RF and microwave metrology. In contrast to conventional low-impedance devices, high-impedance components including specialized sensors, certain miniature antennas, and integrated measurement structures tend to generate significant discontinuities and pronounced reflections when interfaced with standard transmission lines. These effects often compromise the effectiveness of classical calibration methods. Techniques such as SOLT (Short-Open-Load-Thru) or TRL (Thru-Reflect-Line), which are widely used for low-impedance measurements, frequently become inoperative or yield inaccurate results when applied to high-impedance scenarios.

This chapter offers a thorough exploration of the issues encountered during high-impedance measurements. It identifies calibration methods best suited for these challenging conditions and introduces experimentally validated, innovative approaches designed to enhance measurement robustness and accuracy. Such improvements are particularly relevant in contexts where advanced integration, miniaturization, or specialized material characterization is required.

The discussion begins with an analysis of the fundamental limitations inherent to high-impedance measurements. Following this, the chapter presents alternative calibration solutions, including adapted versions of the TRL technique, remote reference methodologies, and high-impedance multi-line calibrations. Each approach is supported by experimental validation on actual structures, demonstrating the practical effectiveness of the proposed solutions.

In summary, the chapter highlights future directions in embedded systems, passive RF sensors, and metrological challenges at quantum and biological scales. These perspectives aim to support precise measurement and calibration of high-impedance devices in complex, miniaturized electronics.

1. Issues specific to high-impedance measurements

Impedance matching is a fundamental challenge in RF circuit design, particularly when dealing with high-impedance devices. Efficient transmission of radio frequency power to a load depends on effective impedance matching. When mismatches occur, additional power losses and signal distortion can result, which is particularly detrimental in communication systems where signal attenuation must be minimized. As device miniaturization progresses, the customary impedance domain—traditionally centered around 50 Ω can shift to much higher values, further complicating measurement and matching tasks.

High-impedance measurements introduce a range of practical and theoretical difficulties. 50 Ω systems are poorly matched to high-impedance devices, usually those exceeding 1 kΩ. This condition leads to reflection coefficients that approach unity, making it challenging to accurately extract S-parameters. Such issues are especially pronounced in the high-frequency characterization of nanostructures, such as carbon nanotubes (CNTs) and single-walled carbon nanotubes (SWCNTs).

In addition to mismatch and reflection errors, high-impedance measurements are highly susceptible to parasitic effects, including capacitance, inductance, and contact resistance. These parasitic elements can significantly alter measurement outcomes, effectively reducing the sensitivity of the measurement system. As devices become smaller and more integrated, there is an increased need for advanced measurement techniques, such as the integration of additional interferometric modules to enhance accuracy and reliability.

From an S-parameter analysis perspective, high-impedance devices are typically characterized by their reflection coefficients, S_{11} or S_{22}, depending on the port configuration in two-port components. The complex load impedance (Z_L) can be calculated from the reflection coefficient using the following relationship:

$$Z_L = Z_r . \frac{1+S_{11}}{1-S_{11}} \quad \text{(E.4.1)}$$

where Zr denotes the reference impedance.

Conversely, if the load impedance and the reference impedance are known, the reflection coefficient can be determined using:

$$S_{11} = \frac{Z_L - Z_r}{Z_L + Z_r} \quad \text{(E.4.2)}$$

The Smith chart serves as an invaluable tool for interpreting high-impedance RF measurements. It enables visualization of normalized impedances and reflection coefficients, assisting in the implementation of impedance matching strategies. Three key points on the Smith chart are particularly relevant:

- $Z_L = 0$: This corresponds to a short circuit, where the incident signal is completely reflected, resulting in $S_{11} = -1$.
- $Z_L = Zr$: When the load impedance matches the reference impedance, there is no reflected signal ($S_{11} = 0$). This condition signifies perfect impedance matching, a critical goal in RF circuit design.
- $Z_L = \infty$: This represents an open circuit, where the signal cannot pass through the component, and the reflection coefficient approaches unity ($S_{11} = 1$).

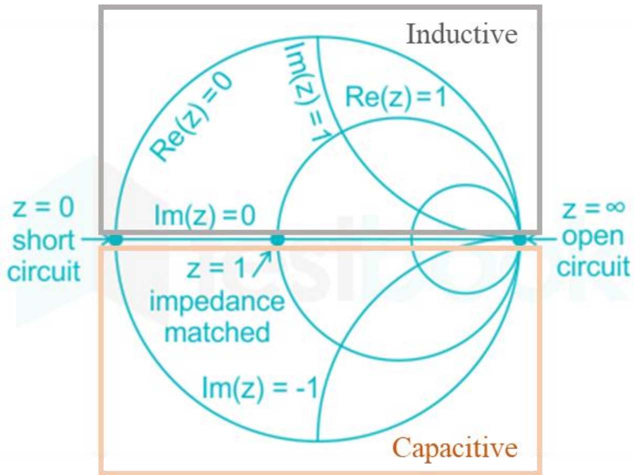

Fig. 4.1: Smith chart [4]

The Smith chart can be divided into two halves. The upper half represents inductive loads, while the lower half corresponds to capacitive loads. Purely resistive loads are located along the main horizontal axis that separates the two halves.

2. High and classical impedance measurements

A detailed account of the DC measurement process can be found in Chapter 3. The chapter describes two primary techniques: the first involves the four-tip method, while the second utilizes a probe station with RF tee bias. For conducting DC resistance measurements at both low (classical) and high impedance values, the latter technique has been selected.

2.1.1. DC low impedance value measurements

DC measurements for standard impedance values use specific offset short and load circuits. Fig. 4.2 shows the offsets of different short circuits and loads, each spaced by 10 µm increments from one element to the next.

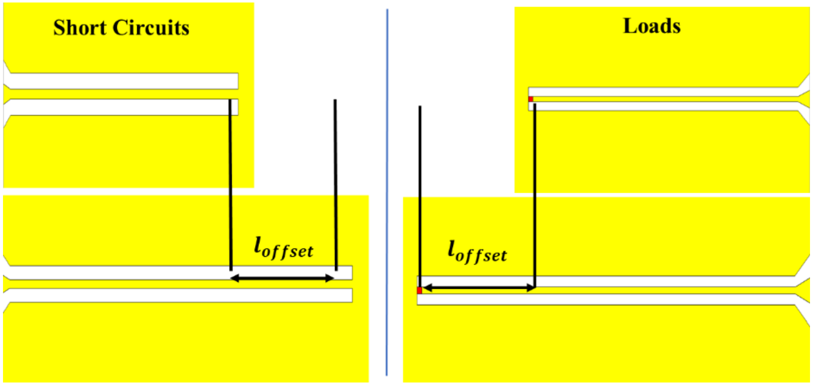

Fig. 4.2: Measured structures

Table 4.1 presents the mean and standard deviation of dc resistance for short circuits measured on two reticles.

Table 4.1: DC resistance of Short circuits

Resistance(Ω)	Length (m)	Mean	Standard deviation (µ)
S1	100.5e-6	5.9	0.3
S2	110.5e-6	7.6	0.4
S3	120.5e-6	9.1	0.3
S4	130.5e-6	11.8	0.1
S5	140.5e-6	12.7	0.1

A key element of measuring various offsets lies in facilitating the correlation between resistance values and section line lengths, thereby enabling the precise determination of a conductor's resistivity or conductivity.

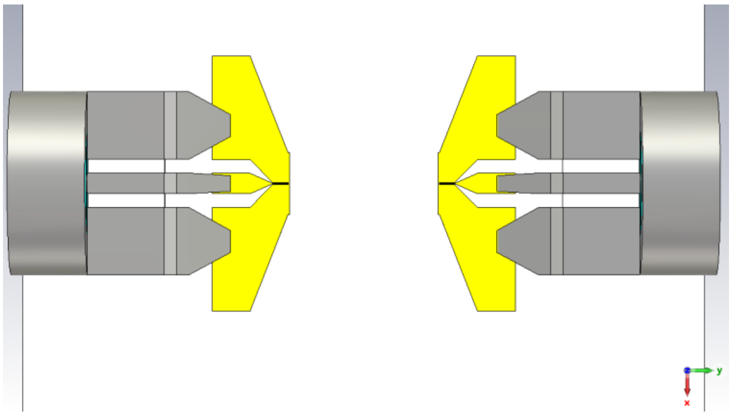

Fig. 4.3: Configuration of GSG probes tips for DC resistance measurement with CPW structures

Monte Carlo simulations comprising 10,000 iterations were conducted for two scenarios, utilizing the calculated mean and standard deviation values in linear regression analysis. In this MC simulation, a Gaussian distribution is used to model the uncertainties in the values of resistances and length. Each Monte Carlo run generates noisy data. The simple linear regression relies on the established relationship between resistance (R) and line length (l), which can be expressed as follows:

$$(R + \sigma(R)) = (r_0 + \sigma(r_0)) + (r_1 + \sigma(r_1)).(l + \sigma(l)) \quad \text{(E.4.3)}$$

Here, r_0 is the R-intercept and r_1 is the regression coefficient. Using this equation for all resistance measurements forms a system of linear equations (E.4.4), with resistance and line length as known inputs and standard deviations ($\sigma(R)$ and $\sigma(l)$). We used a constant uncertainty ($\sigma(l)$) for line lengths, reflecting a 1.5 µm probe placement offset. The regression outputs are the R-coordinate at the origin, not relevant here (r_0) and the slope (r_1).

$$\begin{pmatrix} R_1 + \sigma(R_1).rand(N) \\ R_2 + \sigma(R_2).rand(N) \\ R_3 + \sigma(R_3).rand(N) \\ R_4 + \sigma(R_4).rand(N) \\ R_5 + \sigma(R_5).rand(N) \end{pmatrix} = \begin{pmatrix} 1 & l_1 + \sigma(l_1).rand(N) \\ 1 & l_1 + \sigma(l_2).rand(N) \\ 1 & l_3 + \sigma(l_3).rand(N) \\ 1 & l_4 + \sigma(l_4).rand(N) \\ 1 & l_5 + \sigma(l_5).rand(N) \end{pmatrix} . \begin{pmatrix} r_0 + \sigma(r_0).rand(N) \\ r_1 + \sigma(r_1).rand(N) \end{pmatrix} \tag{E.4.4}$$

We examined two cases with this approach. In H1, we measured resistance from the probe tips to the ground plane through the CPW trace (see Fig. 4.3). In H2, we removed contributions from the probes and tapered sections by subtracting the resistance of S1 from each offset circuit measurement (S2–S5), allowing us to isolate the direct nanoscale portion of the CPW circuit.

Fig. 4.4 presents the linear regression between resistance and line length of short circuits from MC simulation in scenarios H1 and H2.

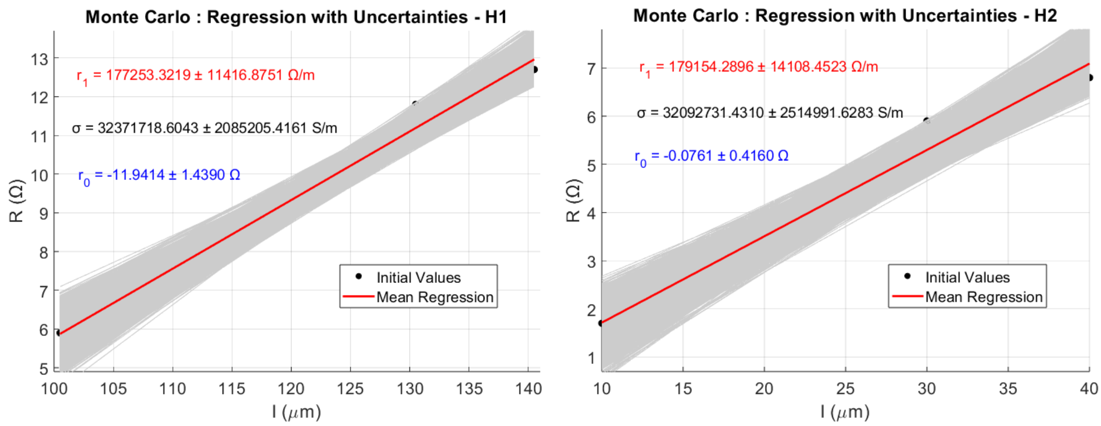

Fig. 4.4: Dc resistance of short circuits

If we consider only the direct relationship ($R= r_1.l$), the slope directly represents the linear DC resistance. This value indicates the metal's conductivity (σ_{cond}) or resistivity (ρ), as shown in equation (E.4.5).

$$r_1 = \frac{1}{\sigma_{cond}.S} = \frac{\rho}{S} \tag{E.4.5}$$

Fig. 4.4 shows the conductivity and linear DC resistance of the nano CPW lines: case H1 averages 32,371,718 S/m and 177,253 Ω/m; case H2 averages 32,092,731 S/m and 179,154 Ω/m.

Six offset structures, defined relative to the load and centered on the shortest line (thru), are used in loaded circuits. Their measured values are shown in Table 4.2.

Table 4.2: DC resistance of circuits with loads

Resistance(Ω)	Length (m)	Mean	Standard deviation (µ)
M1	100e-6	93	0
M2	110e-6	100.5	5.5
M3	120e-6	100.5	1.5
M4	130e-6	101.75	0.25
M5	150e-6	103	2
M6	160e-6	111	1
M7	170e-6	109	1

Handling measurements as in case H2 can result in the DC resistance of the load being excluded when M1 is eliminated from M2 or other offsets. To mitigate this, an approach similar to that used in case H1 is applied. The same system of equations from (E.4.3) is utilized, with the intercept at the origin interpreted as the resistance of the titanium load. The slope corresponds to the linear resistance of the line section.

The load resistance r_0, as illustrated in Fig. 4.5, is approximately 68.81 Ω with an associated uncertainty of 6.16 Ω.

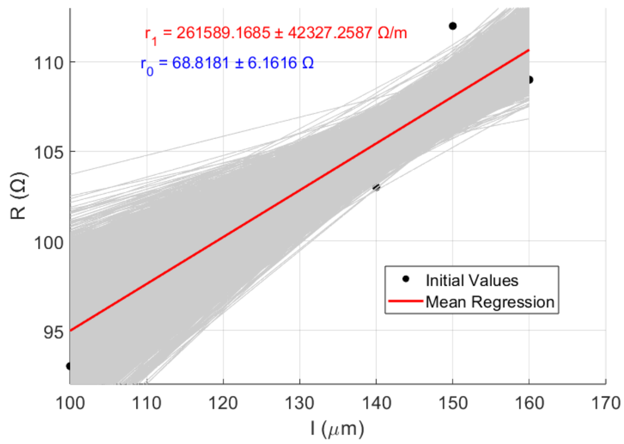

Fig. 4.5: Dc resistance of load

2.1.2. DC High impedance value measurements

This section examines two high-impedance devices: lines with series resistance and one-port series resistance loads, both made from titanium layers. Four resistance values (1 kΩ, 2 kΩ, 10 kΩ, and 20 kΩ) were used for each type. Fig. 4.6 shows the structures with series resistance across scaled sections.

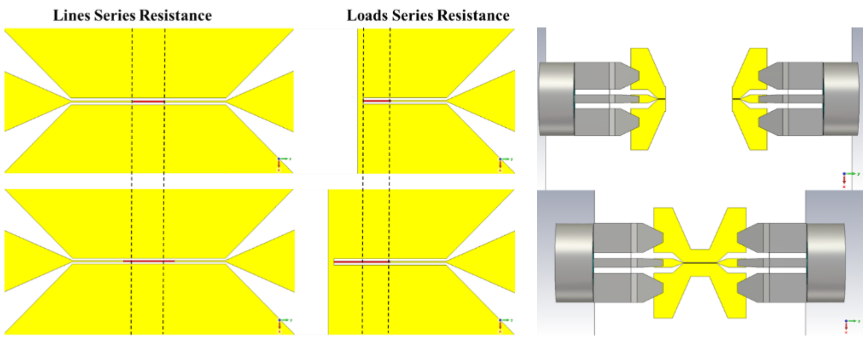

Fig. 4.6: Two-ports and one-port CPW structures with high series resistance.

GSG probe tips were used for DC measurements. The measured DC resistances differed from theoretical predictions. Table 4.2 summarizes the mean and standard deviation of these resistances for lines with series resistance (L1K, L2K, L10K, L20K) and one-port series resistance loads.

Table 4.3: DC resistance of circuits with high series resistance (lines-loads)

Resistance(Ω)	Length (m)	Mean (Ω)	Std (Ω)	Resistance(Ω)	Length (m)	Mean (Ω)	Std (Ω)
L1K	210e-6	1696	24	M1K	110e-6	1645	15
L2K	220e-6	3242.5	2.5	M2K	120e-6	3225	25
L10K	300e-6	15685	25	M10K	200e-6	15450	50
L20K	400e-6	30400	100	M20K	300e-6	29750	250

Series resistances are centered on the 200 µm CPW line, with effective length determined by the titanium layer sheet resistance. Loads are placed 100 µm from the access port.

The method used to assess low DC resistance via Monte Carlo simulations, as in case H2, is implemented here based on equation (E.4.4). Resistance and length values for the first component are subtracted from those of the remaining three components to isolate the resistance associated with the specific section length. Fig. 4.7 shows DC resistance as it relates to the resistive pattern length for both line (a) and load (b) configurations with series resistance.

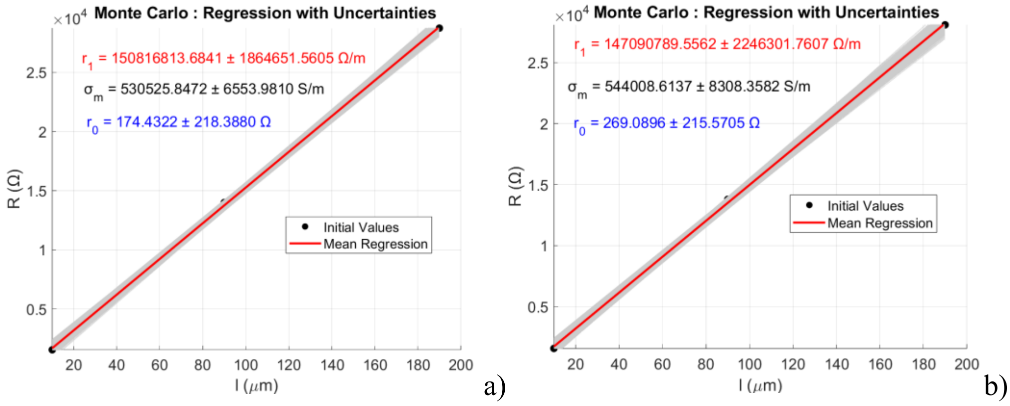

Fig. 4.7: DC resistance of lines and loads with series resistance.

The DC resistance to resistive layer length ratio enables calculation of titanium's linear resistance and conductivity. Conductivity is slightly greater for loads (about 544,008 S/m) than for lines (about 530,525 S/m).

3. Experimental validation of novel approaches

High-impedance components strongly reflect small-signal RF, making their properties identifiable through reflection coefficient analysis. The Smith chart enables quick RF device characterization; for example, highly reflective devices have an S11 near the main circle edge, indicating their type (resistive, capacitive, or inductive). Open and short circuits are typical examples of such devices.

This section examines the pronounced reflective characteristics of nano CPW structures by utilizing multiline TRL calibration, with the objective of advancing the development of structures appropriate for SOLT and driven calibration standards.

3.1. Standards calibration driven from multiline TRL calibration

The devices incorporating series resistances were measured at high frequencies using the setup described in Chapter 3. The set of devices consists of short and open circuits, loads and lines with different series resistances, as well as simple lines used for mTRL calibration.

Different offset shorts and opens were evaluated, with initial circuits (S1 and O1) centered on the thru standard. Additional shorts were generated by shifting the line section in 10 µm increments. Both raw measurement data and ADS simulations were analyzed. Fig. 4.8 shows the S11 reflection coefficients for the open and short circuits.

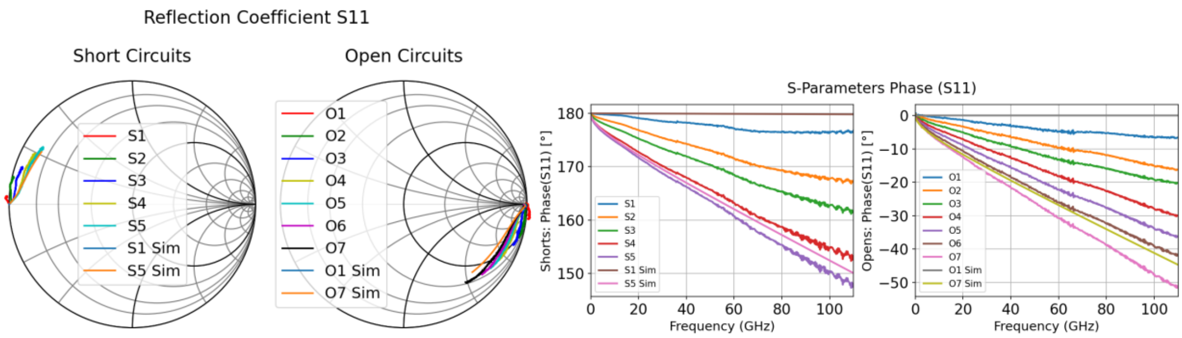

Fig. 4.8: S11 of Short and Open circuits

This result shows how shifted nano-transmission line sections impact the Smith chart and phase. Attenuation, which increases with frequency, is caused by line losses that depend on length.

The Smith chart provides a qualitative overview of DUT behavior, while impedance analysis using S11 and reference impedance Zr enables precise DUT specification. Equation (E.4.1) calculates impedance, with the reference set as the nano CPW line's characteristic impedance due to TRL calibration shifting the measurement plane. This impedance is determined by CST simulations, analytical models, and measurements. Figure 4.9 shows real and imaginary parts, with real values of 62.8 Ω, 65.3 Ω, and 61.8 Ω at 110 GHz.

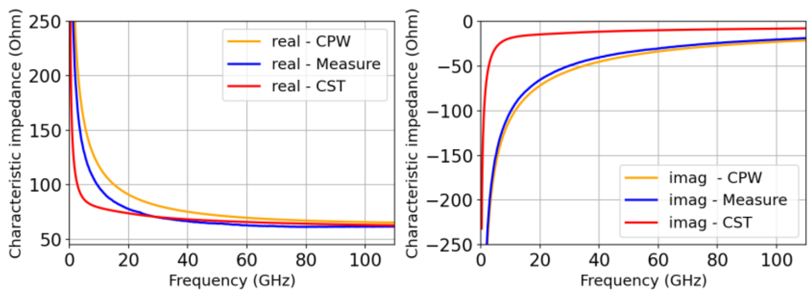

Fig. 4.9: Characteristic impedance of the nano CPW line

The analysis of short circuits considers the response of the effective section obtained via mTRL calibration in relation to the line impedance. Fig. 4.10 presents the corrected section for the short circuits.

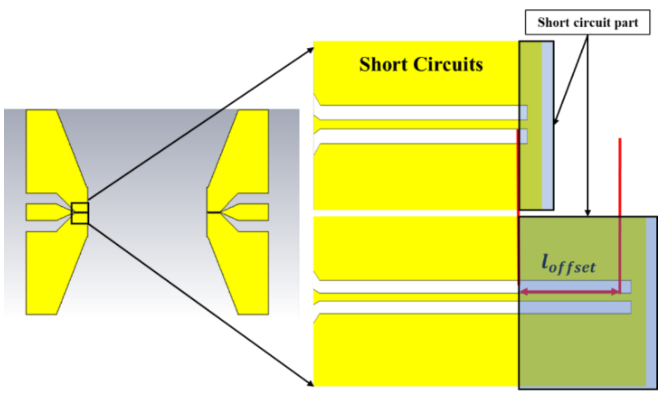

Fig. 4.10: Short circuit part in the impedance calculation

Fig. 4.11 provides insight into the behavior of the impedance for short circuits, displaying both the real and imaginary components. The data reveals that both components are positive across the measured frequency range. This observation is consistent with the expected analytical model for a short circuit, which is typically described as a resistor in series with an inductor. In this model, the real part of the impedance corresponds to the series resistance (R) of the transmission line section, which arises due to its finite conductivity. The imaginary part represents the inductive reactance, associated with the line's inductance (L). This relationship is mathematically expressed by equation (E.4.6), where the total short-circuit impedance is given by the sum of the resistance and the frequency-dependent inductive term.

$$Z_{Short} = R + i\omega L \tag{E.4.6}$$

The imaginary part of the impedance, or reactance, demonstrates a direct and linear relationship with frequency, steadily increasing throughout the measured frequency range. This linear trend is characteristic of the inductive behavior associated with the transmission line section. Additionally, the impedance measurements capture the influence of the offset introduced in the circuit configuration. As the offset increases, there is a corresponding rise in the total impedance observed. This effect highlights how both frequency and physical adjustments to the circuit layout contribute to the overall impedance response of the device under test.

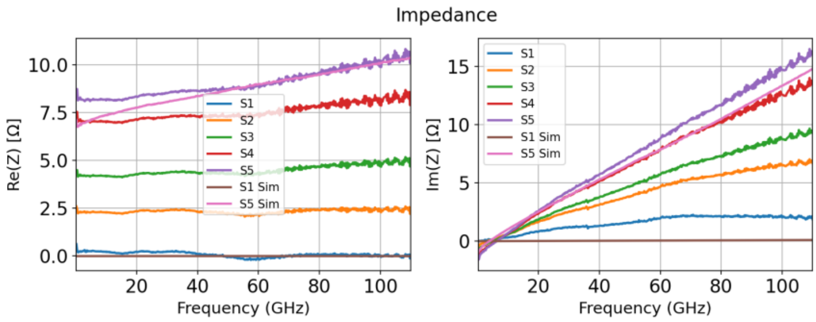

Fig. 4.11: Impedance of Short circuits

A detailed investigation was conducted on various shifted loads, labeled M1 through M7. Each of these loads features a series square resistance, which is fabricated from titanium. This resistive element serves as a connection between the signal trace and the ground plane, ensuring a controlled path for current flow. The specific configuration and implementation of this structure are depicted in Fig. 4.12. This arrangement allows for systematic study of the load behavior as a function of both the physical displacement and the electrical properties of the titanium resistor.

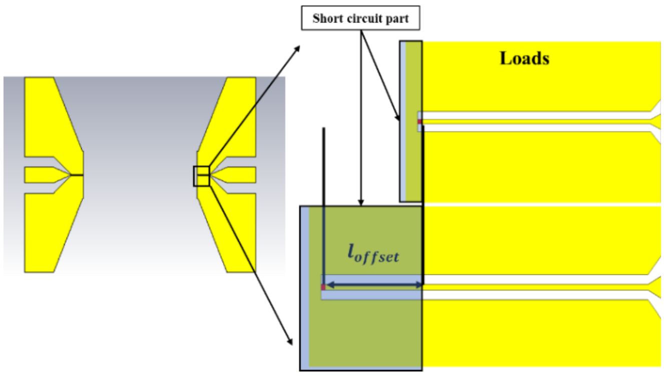

Fig. 4.12: Load part in the impedance calculation.

The DC value of the series resistance incorporated in the shifted load structures is approximately 68.8 Ω, with a standard deviation of ±6.2 Ω, as determined through analysis in the previous section. This titanium-based resistive element is integral to the connection between the signal trace and the ground plane, ensuring a controlled current path and enabling systematic investigation of load behavior.

Fig. 4.13 illustrates the reflection coefficient (S11) of the loads. This parameter provides insight into the impedance matching characteristics of the devices, particularly at low frequencies where a substantial reflection is observed due to the mismatch on one side. The reflection coefficient is influenced by both the load impedance and the reference impedance, specifically the characteristic impedance of the transmission line. These relationships are further described by the analytical models and equations presented in the surrounding sections.

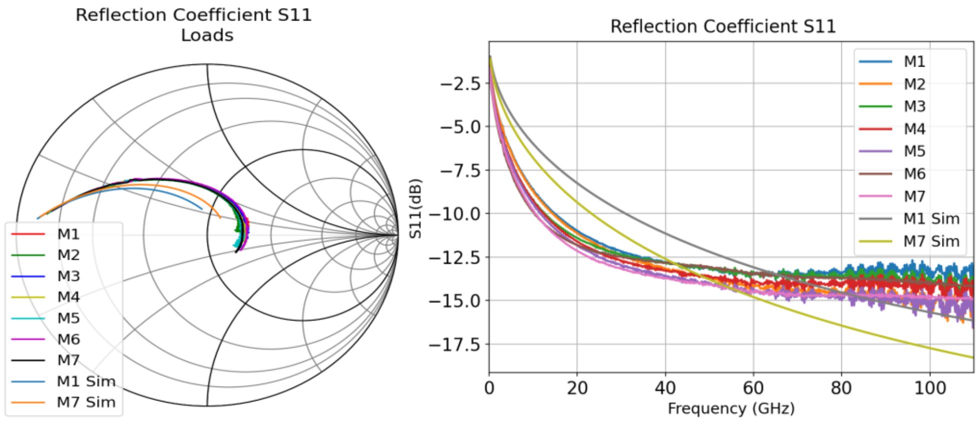

Fig. 4.13: Reflection coefficient of loads

The load devices demonstrate a pronounced reflection coefficient (S11) at low frequencies. This elevated S11 arises from impedance mismatch on one side of the device, which leads to significant signal reflection. The impedance mismatch is particularly notable in this frequency range, highlighting the importance of proper matching for minimizing reflections and ensuring efficient signal transmission.

According to equation (E.4.2), the reflection coefficient is influenced by both the load impedance and the reference impedance. The reference impedance, in this context, is the characteristic impedance of the transmission line to which the load is connected. This interplay between the load and reference impedances determines the degree of reflection observed.

The characteristic impedance itself is defined by equation (E.4.7). In this equation, the per-unit-length parameters of the transmission line resistance (R), inductance (L), capacitance (C), and conductance (G) are used to characterize the line impedance properties. Each of these parameters contributes to the overall impedance, impacting on how signals are transmitted and reflected along the line.

$$Z_c = \sqrt{\frac{R+i\omega L}{G+i\omega C}} \tag{E.4.7}$$

At low frequencies, the characteristic impedance of the transmission line exhibits a high value, which can be closely approximated by considering the dominant terms in the impedance expression. In this frequency regime, the linear resistance of the line is substantially greater, while the linear conductance remains low. This combination significantly influences the reflection coefficient, resulting in pronounced signal reflections due to the increased impedance mismatch.

As the frequency increases, the behavior of the characteristic impedance transitions. At high frequencies, the characteristic impedance approaches the value determined by the square root of the inductance over capacitance per unit length, L/C. In this regime, both the inductive and capacitive properties of the line become the primary contributors, and the characteristic impedance remains largely stable across the frequency spectrum. This stability in impedance at high frequencies leads to the reflection coefficient S11 reaching its anticipated value, as the impedance mismatch becomes less pronounced and the transmission line operates as expected.

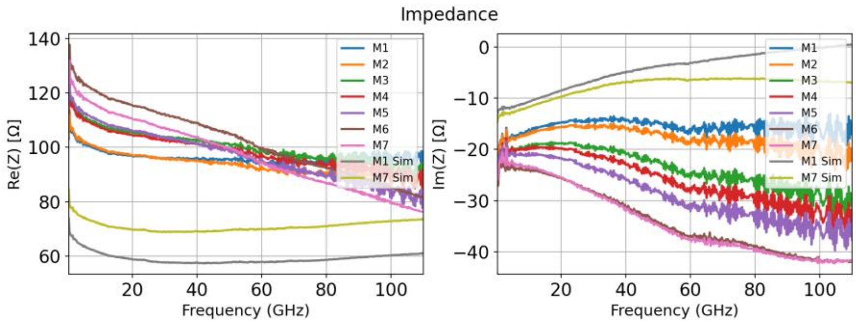

Fig. 4.14: Impedance of loads

The impedances of the load devices are determined using equation (E.4.2), which relies on the corrected reflection coefficient (S11) and the measured characteristic impedance of the transmission line. Figure 4.14 displays both the real and imaginary components of the load impedance. At lower frequencies, the real part of the impedance is observed to be in the range of several hundred ohms. This behavior is primarily attributed to the influence of the transmission line's characteristic impedance, as previously discussed in the document.

The high-impedance structures under investigation are composed of lines and loads that incorporate series resistances formed from titanium thin-film layers. These resistive elements span a range from 1 kΩ to 20 kΩ, providing a basis for systematic analysis of impedance effects. To ensure measurement accuracy, all devices are characterized and corrected using multiline TRL (mTRL) calibration techniques, which account for systematic errors in the measurement system.

For clarity in identification, the structures are designated as follows: lines are labeled with the prefix "LZ," while loads are denoted by "MZ." The accompanying indices indicate the nominal resistance values 1K, 2K, 10K, and 20K correspond to 1 kΩ, 2 kΩ, 10 kΩ, and 20 kΩ, respectively. The magnitude of the reflection coefficients for both line and load structures is depicted in Figure 4.15, providing a visual comparison of their impedance characteristics across the frequency spectrum.

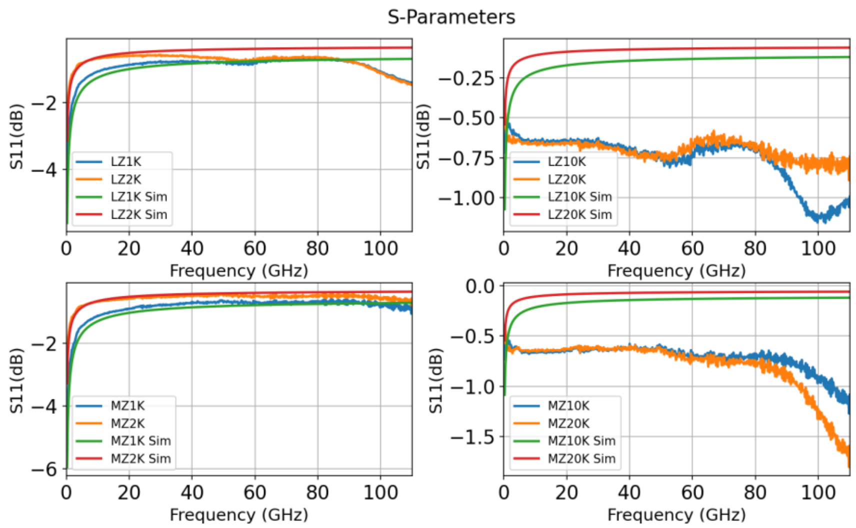

Fig. 4.15: Reflection coefficients of lines and loads with high series impedance.

In the analysis of the measured reflection coefficients (S11) for high-impedance coplanar waveguide (CPW) structures, the amplitude characteristics provide insight into the behavior of different device configurations across the frequency spectrum.

The top-left plot of Fig. 4.15 illustrates the amplitude of S11 for two lines structures, LZ1K and LZ2K, which incorporate series resistances of 1 kΩ and 2 kΩ, respectively. Up to 70 GHz, the difference between these two structures is clear: the S11 amplitude for the 2 kΩ line (LZ2K) is consistently higher than that of the 1 kΩ line (LZ1K), aligning with expectations based on their impedance values. However, beyond 70 GHz, the S11 curves for both lines converge, and the distinction between them is no longer apparent.

On the right side of the same figure, the reflection coefficients for lines with higher resistances, LZ10K and LZ20K, are shown. These two lines remain distinguishable up to approximately 50 GHz. Within this range, contrary to the anticipated trend, the S11 value for the 20 kΩ line (LZ20K) is actually smaller than that for the 10 kΩ line (LZ10K). After 50 GHz, the behavior reverses, with LZ20K exhibiting the highest S11 values in the frequency range.

For the one-port structures, which serve as loads, the reflection coefficient measurements further validate the simulation results. Specifically, the S11 values for MZ1K and MZ2K closely align with the outcomes predicted by simulation, indicating a strong agreement between experiment and modeled behavior for these lower-resistance load devices.

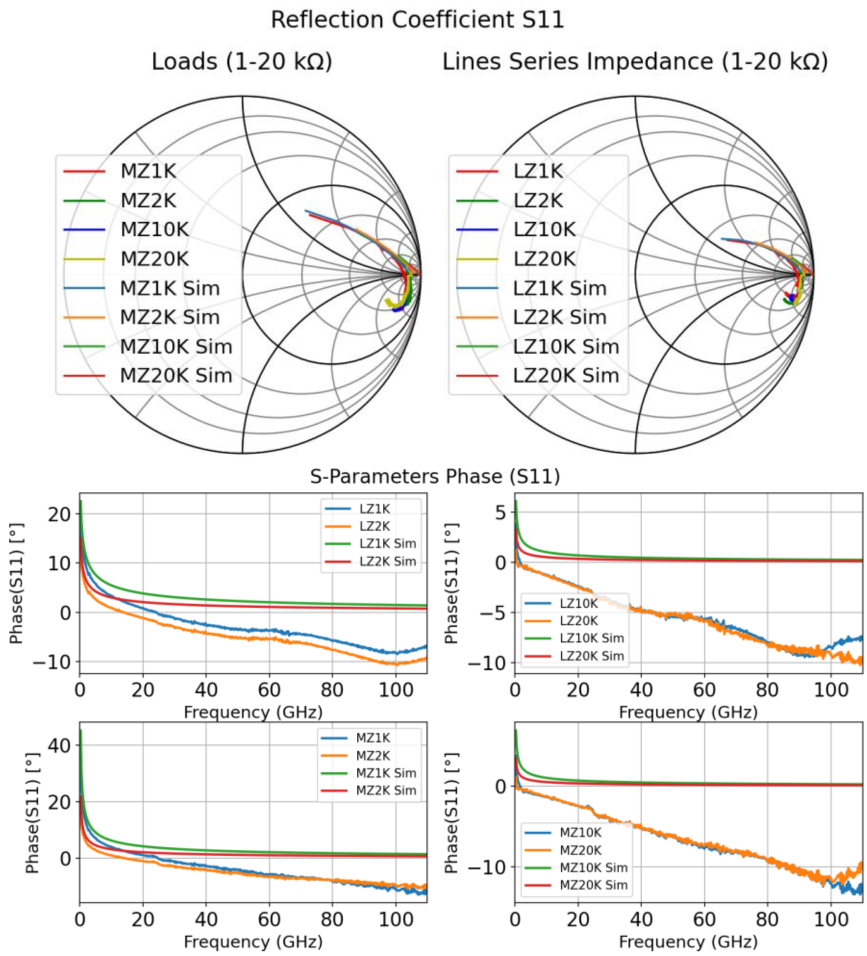

Fig.4.16: Reflection coefficients of loads and lines with series resistance in Smith chart and in phase

Fig. 4.16 provides a comprehensive view of the reflection coefficients measured for both one-port (load) and two-port (line) high-impedance coplanar waveguide (CPW) structures. Analysis of the S11 phase responses reveals that it is not possible to clearly distinguish between devices with resistance values of 1 kΩ versus 2 kΩ, or 10 kΩ versus 20 kΩ. This observation holds true for both simulated and experimentally measured data, indicating limited sensitivity of the S11 phase to incremental resistance changes within these ranges.

To further quantify the impedance characteristics of these structures, their impedances are calculated using the reflection coefficients in conjunction with the characteristic impedance of the transmission line, following the methodology previously described in this document. The resulting impedance values for the line structures incorporating series resistance are presented in Fig. 4.17, offering insight into the influence of series resistance on the overall line impedance.

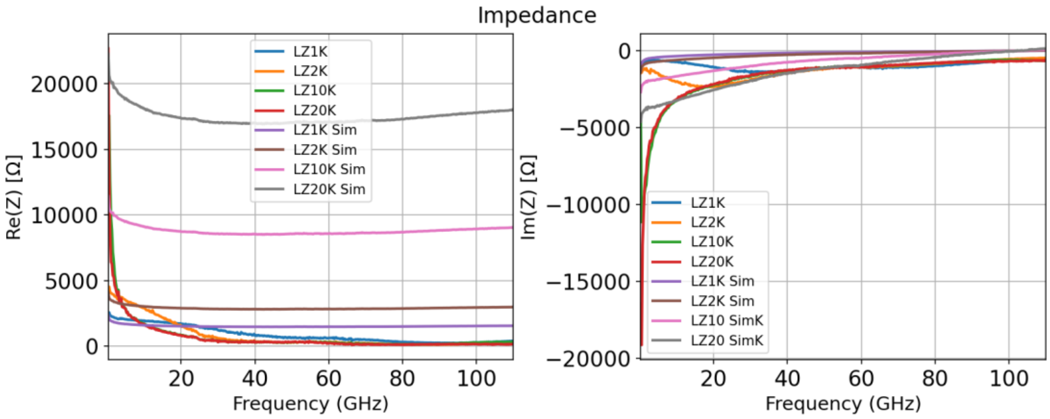

Fig. 4.17: Impedance of the lines with series resistance

A notable discrepancy exists between the measured and simulated impedance values for the high-impedance structures under investigation. While simulations indicate that the response of each high-impedance structure remains clearly distinguishable across the entire frequency spectrum, experimental results do not consistently reflect this separation especially at higher frequencies. This reduced distinction in measured data is primarily attributed to experimental limitations, with the sensitivity of the measurement instrument being a significant contributing factor.

This phenomenon is not limited to two-port line structures; it is also observed in the one-port high-impedance load devices, as shown in Fig. 4.18. The measured results for these loads demonstrate a similar challenge in differentiating between impedance values, further highlighting the impact of measurement system sensitivity on the accurate characterization of high-impedance devices.

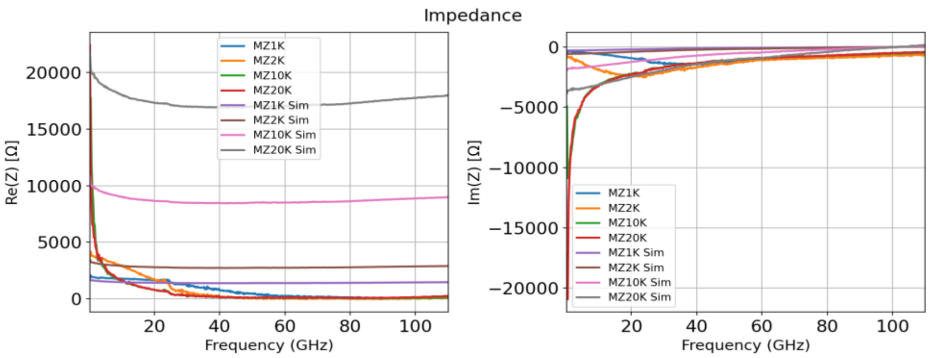

Fig. 4.18: Impedance of loads with series resistance

The characterization of high-impedance devices is particularly constrained by the sensitivity of the measurement system. As the impedance of the device under test (DUT) increases, the ability of the measurement apparatus to accurately capture the true response becomes limited. In such cases, noise emerges as a dominant factor, which can significantly distort the observed responses of the DUTs. This noise influence is especially pronounced at higher frequencies, where experimental limitations further exacerbate the challenge of distinguishing between different impedance values. Consequently, the reliability and accuracy of measurement outcomes for high-impedance structures are directly affected by these sensitivity constraints, underscoring the need for improvements in measurement techniques and instrumentation to ensure precise characterization.

3.2. Definition and implementation of SOLT calibration and derived calibration techniques

On-wafer S-parameter measurements at millimeter- and submillimeter-wave frequencies are particularly challenging due to the increased complexity in achieving precise and repeatable results. Calibration methods play a critical role in enhancing measurement accuracy and repeatability, provided that the calibration standards used are well-defined and thoroughly characterized. Nevertheless, the measurement instrument itself must exhibit sufficient performance capabilities to effectively compensate for frequency-dependent noise and the sensitivity limitations inherent to the components under test.

In this work, multiline Thru-Reflect-Line (TRL) calibration was employed to define specific structures that are suitable for implementing a range of calibration techniques. These include the widely used Short-Open-Load-Thru (SOLT) method as well as derivative approaches designed to further integrate offsets into the calibration standards. The additional calibration configurations applied consist of Short-Short-Short-Thru (SSST), Open-Open-Open-Thru (OOOT), High$_{Impedance}$-High$_{Impedance}$-High$_{Impedance}$-Thru (HHHT), and Short-Short-High$_{Impedance}$-Thru (SSHT). All of these calibration algorithms are fundamentally based on the SOLT methodology.

For consistency and comparability, the same wafer was utilized throughout these calibration procedures. Both corrected (mTRL) and raw measurement data were combined in the preparation of standards used in each additional calibration method. After establishing these standards, each selected device under test (DUT) was corrected using the corresponding calibration technique.

Fig. 4.19 presents the S-parameters measured for the DUTs according to the different calibration methods applied. The corrected DUTs included in this analysis consist of a transmission line and a line with series resistance of 10 kΩ (LZ10K). This comparative evaluation illustrates the impact of each calibration approach on the resulting S-parameter measurements, providing insight into the performance and suitability of each technique for high-frequency, on-wafer characterization.

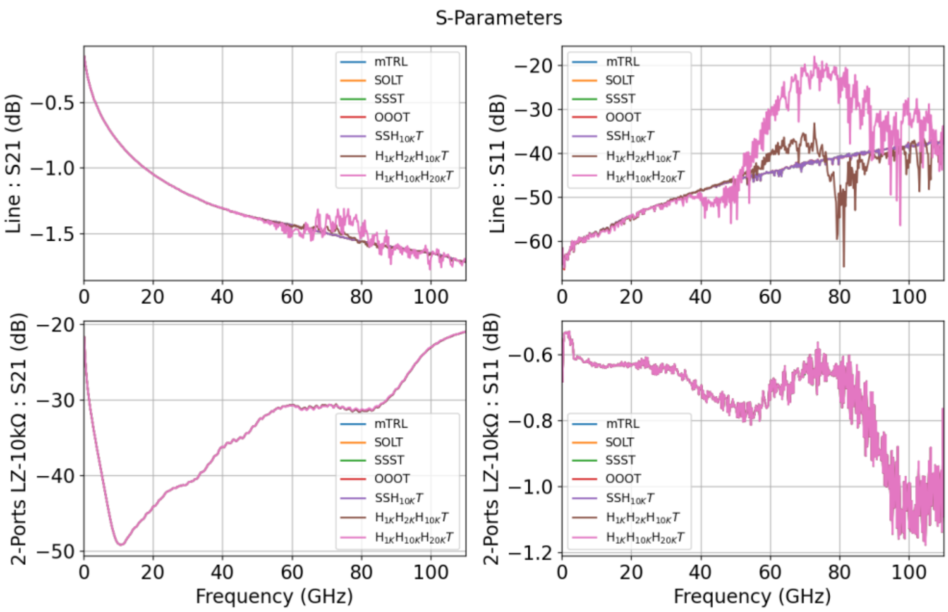

Fig. 4.19: S-parameters of DUTs considering different calibration methods.

Fig. 4.19 presents the corrected S-parameters of a short circuit, an open circuit, a 68 Ω load and 2kΩ load (MZ2K) according to the different calibration methods applied. This study show the impact of each calibration approach and depending on the type of DUT results can be identical.

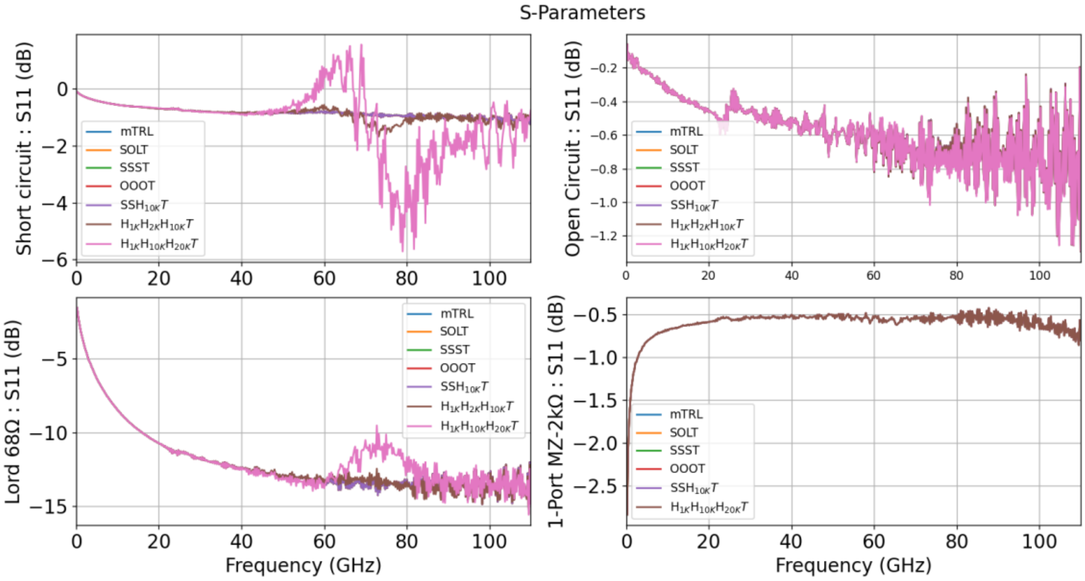

Fig. 4.20: S-parameters of DUTs considering different calibration methods.

Upon reviewing the measurement outcomes for the various calibration techniques, it is evident that nearly all results are virtually indistinguishable from one another, with the notable exception of the $\text{High}_{\text{Impedance}}$-$\text{High}_{\text{Impedance}}$-$\text{High}_{\text{Impedance}}$-Thru (HHHT) method. This distinction highlights the unique behavior or limitations associated with the HHHT approach compared to the other calibration algorithms applied. This phenomenon could be attributed to the fact that the values of the standards are close, as shown in Fig. 4.21. In fact, the HHHT algorithm is based on the resolution of a system of equations which requires the standards to be distinguished from one another. Imperfections in the production of high-impedance standards or instrument limits in relation to sensitivity could also account for this difference in results.

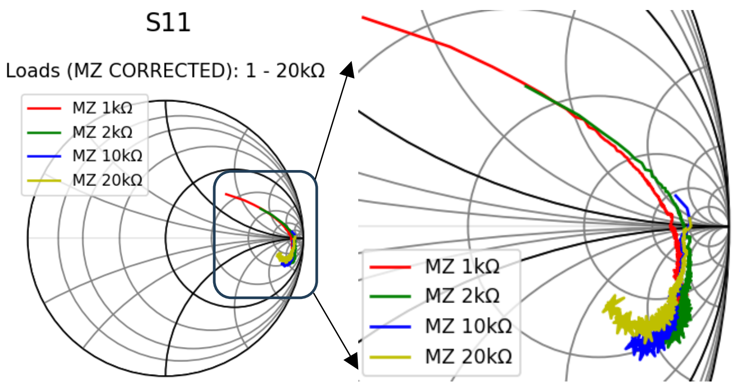

Fig. 4.21: Reflection coefficients of high impedance standards

Additionally, the effectiveness of the multiline Thru-Reflect-Line (TRL) calibration method becomes clear. The TRL technique not only delivers high accuracy in its own right but also serves as a robust foundation for the implementation of additional calibration strategies. By utilizing the corrected S-parameters obtained from TRL-calibrated structures, it is possible to reliably execute other derivative calibration methods, further enhancing the precision and consistency of on-wafer high-frequency measurements.

Conclusion

This chapter examines the distinctive challenges encountered in high-impedance measurements, with a focus on the inherent difficulty of achieving both accuracy and stability across a broad spectrum of impedance values. By revisiting the core principles underlying continuous impedance measurements for both low and high ranges, the discussion has underscored the limitations faced by conventional techniques, particularly when these are applied in high-frequency and high-impedance scenarios.

The experimental investigations provided validation for innovative calibration methods. In particular, the adoption of multiline Thru-Reflect-Line (TRL) calibration was demonstrated as an effective reference for establishing appropriate calibration standards. Furthermore, the chapter detailed the implementation and adaptation of Short-Open-Load-Thru (SOLT) calibration techniques to address these challenges.

The results from this work show that employing hybrid calibration strategies specifically tailored to the unique conditions of high-impedance and high-frequency measurements leads to notable improvements in both the robustness and reliability of the measurement outcomes.

References 4

[1] B. Mindan and L. Hong, "The Analysis of Impedance Matching Problem in RF Circuit Design," *2010 International Forum on Information Technology and Applications*, Kunming, China, 2010, pp. 350-353, doi: 10.1109/IFITA.2010.55.

[2] H. Happy, K. Haddadi, D. Theron, T. Lasri and G. Dambrine, "Measurement Techniques for RF Nanoelectronic Devices: New Equipment to Overcome the Problems of Impedance and Scale Mismatch," in *IEEE Microwave Magazine*, vol. 15, no. 1, pp. 30-39, Jan.-Feb. 2014, doi: 10.1109/MMM.2013.2288710.

[3] R. Romano, F. Mubarak, M. Spirito and L. Galatro, "The HΓ-VNA, an Interferometric Approach for the Accurate Measurement of Extreme Impedances," *2019 93rd ARFTG Microwave Measurement Conference (ARFTG)*, Boston, MA, USA, 2019, pp. 1-6, doi: 10.1109/ARFTG.2019.8739232.

[4] https://testbook.com/question-answer/the-smith-chart-is-a-graphical-way-for-solving--5ece7211f60d5d5714fe9c23

General conclusion and Perspectives

The research presented in this manuscript has tackled both fundamental and practical challenges involved in on-wafer RF and microwave measurements. Special attention was given to the increasing miniaturization of structures and high-impedance devices, which is driven by the heightened requirements for accuracy, repeatability, characterization, and calibration at frequencies up to 110 GHz.

A comprehensive review was first conducted, covering the essential principles of RF metrology, S-parameters, measurement systems, and the main sources of error in these processes. Techniques for calibration and de-embedding were examined, with a particular focus on the challenges inherent to on-wafer measurements of high-impedance devices and miniaturized structures. This examination highlighted significant technological and metrological issues that must be addressed in modern RF measurement scenarios.

The subsequent section of the manuscript described the design and fabrication of dedicated calibration kits. The selection of appropriate technologies, materials, and dimensions was outlined, followed by the use of electromagnetic simulation to support the design process. Implementation and validation of calibration algorithms were detailed, along with the development of structures specifically adapted for advanced on-wafer measurements. These steps ensured consistency between modeled and experimental data.

The third part of the work centered on the experimental realization of on-wafer characterization, encompassing setups from DC to RF up to 110 GHz. Practical protocols were developed to enhance measurement quality. The results achieved enabled correction of raw data, evaluation of reproducibility and repeatability, and quantification of uncertainties using various TRL calibration methods.

In the final section, new calibration methods tailored for high-impedance measurements were introduced. These included standards derived from multiline-TRL, as well as SOLT, SSST, OOOT, SSHT, and HHHT calibration kits. The implementation of these approaches has enabled improved characterization of devices that previously presented significant measurement challenges.

Overall, this work advances the field of wafer-level RF and microwave metrology by enhancing calibration procedures for nanoscale and high-impedance devices. It proposes innovative structures and methodologies that are well-suited to future technological nodes and offers a comprehensive framework for uncertainty evaluation in complex measurement environments. These results constitute a notable step forward for the RF and microwave metrology community, with applications spanning sensors, nanoelectronic devices, and components for millimeter-wave and terahertz communications.

Looking ahead, several avenues for future research are identified. One is the automation of calibration procedures using a nanorobotized measurement system. Adapting and validating the proposed calibration strategies at sub-THz and THz frequencies will also be vital, given the increased sensitivity to losses, dispersion, and parasitic effects at these frequencies. As miniaturization continues, there will be a need for more compact and automated measurement platforms incorporating embedded calibration standards and self-correction routines to further improve reliability and efficiency.

Another promising direction involves refining uncertainty evaluation through advanced statistical frameworks and machine learning techniques, enabling a deeper understanding of error behavior under practical measurement conditions. These advances could be particularly beneficial for applications involving modern technologies such as 2D-material transistors, MEMS devices, and bio-integrated sensors, all of which present high-impedance measurement challenges. Ultimately, the findings from this research could help establish new metrological guidelines and support worldwide standardization, benefiting both scientific and industrial communities in RF and microwave engineering.

Publication & Conferences

- **European Microwave Week (EuMW 2025):** oral presentation

Seck, D., Allal, D., Marlec, F., Lenoir, C., Sebbache, M., & Haddadi, K. (2025). *Experimental Study on the Repeatability of Nanoscale On-Wafer Calibration Structures on High Resistivity Silicon Substrate up to 110 GHz*.

- **URSI France 2025:** oral presentation

« *On-Wafer Calibration for Nanodevice Characterization up to 110 GHz* » Daouda Seck, José Morán-Meza, Florent Marlec, Clément Lenoir, Mohamed Sebbache, Djamel Allal, Kamel Haddadi

- **Congrès International de Métrologie (CIM 2025):** poster presentation

Seck, D., Allal, D., Marlec, F., Lenoir, C., Sebbache, M., & Haddadi, K. (2025). *Nanoscale Calibration Standards for On-Wafer S-Parameters measurements up to 110 GHz*. In EPJ Web of Conferences (Vol. 323, p. 12003). EDP Sciences**.**

- **Journées de Caractérisations Microondes et Matériaux (JCMM 2025):** poster presentation

« Structures de calibrage vectoriel à l'échelle nanométrique » D. Seck, D. Allal, K. Haddadi 2025.

- **International Symposium on Wireless Technology & Applications (ISWTA 2024):** oral presentation

D. Seck, D. Allal and K. Haddadi, "*On-Wafer TRL Calibration Design for Microwave Nanoscale and High Impedance Measurement*," 2024 IEEE Symposium on Wireless Technology & Applications (ISWTA), Kuala Lumpur, Malaysia, 2024, pp. 260-263, doi: 10.1109/ISWTA62130.2024.10651788.

- **Numerical Electromagnetic and Multiphysics Modeling and Optimization (NEMO 2024)**

« *Development of LRRM and TRL Calibration Kits for On-Wafer Microwave Measurements at the Nanoscale* » D. Seck, D. Allal, K. Haddadi 2024.

- **Journées Nationales des Micro-ondes (JNM 2024) :** oral presentation

« *Conception de kits TRL à l'échelle nano pour les mesures de paramètres S sur tranche en configuration masse-signal-masse* » D. Seck, D. Allal, K. Haddadi 2024.

- **Numerical Electromagnetic and Multiphysics Modeling and Optimization (NEMO 2023)**

Mokhtari, C., Seck, D., Allal, D., Lenoir, C., Sebbache, M., Berthe, M., & Haddadi, K. (2023, June). *Nanorobotics and Automatic On-Wafer Probe Station with Nanometer Positionning Accuracy*. In 2023 IEEE MTT-S International Conference on Numerical Electromagnetic and Multiphysics Modeling and Optimization (NEMO) (pp. 22-24). IEEE.

Appendices

Appendix 1: TRL algorithm

TRL (Thru-Reflect-Line) is a self-calibration algorithm that does not require exact knowledge of the standards. Engen and Hoer introduced it in 1974 [1]. It uses a thru line of length l_0, a second line of length l, and either an open or a short circuit as a reflect standard. Although it is not necessary to know all the standards precisely, the line lengths must be different and create a phase shift between 20° and 120°. The reflect standard should be lossless and exhibit a phase of ±90°, and must be symmetrical with respect to both ports. Using this method, one can determine the electrical properties of a transmission line, such as its propagation constant, characteristic impedance, etc.

The TRL method has the advantage of providing accurate calibration and good traceability by using primary standards like airlines [2]. However, it may suffer from frequency bandwidth limitations, since the choice of the Thru and Line standards must ensure a suitable length difference relative to the frequency of interest. To overcome these limitations, alternative techniques may be used.

TRL calibration involves evaluating the calibration errors of a network analyzer using three standards: a Thru (T), an open or short circuit (Reflect, R), and a line (L). There are eight error terms to determine, four on each side of the device under test (DUT): directivity (E_{00}, E_{33}), source match (E_{11}, E_{22}), and frequency responses in transmission (E_{10}, E_{23}) and reflection (E_{01}, E_{32}). It is possible to consider the error of crosstalk or isolation (E_{30}, E_{03}) that descripts leakage from port to port. The switch terms (Γ_F, Γ_R) result from the reflection of VNA port 2 when VNA port 1 is considered the source and vice versa (Fig. A1.1). According to the VNA architecture type, one may correct the switch terms before running TRL, by connecting any device of transmission between the ports and measuring the wave ratios as formulate in (E.A1.1)

$$\Gamma_F = \frac{a_3}{b_3}\Big|_{source:\,Port\ 1}\ ;\ \Gamma_R = \frac{a_0}{b_0}\Big|_{source:\,Port\ 2} \qquad \text{(E.A1.1)}$$

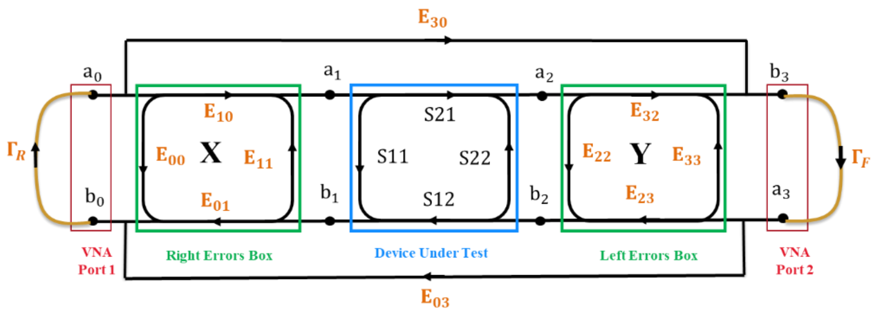

Fig. A1.1: Two-port measurement model

The error boxes $\boldsymbol{X}$ and $\boldsymbol{Y}$ with errors terms or calibration coefficients, represented by fictitious two-port networks, embed the DUT, which is modeled by an S-parameter network between the two ports of the Vector Network Analyzer. The purpose of the calibration is to extract these error boxes by removing their effects with an inverse operation (de-cascading), therefore shifting the measurement plane to the DUT. Fig. A1.1 shows signal flow graph of network cascade. The use of cascade or transfer matrix is very helpful for a simple analysis of measurement model.

The equation (E.A1.2) illustrates the measurement model that relates error boxes ($\boldsymbol{X}$, $\boldsymbol{Y}$), actual device response, $\boldsymbol{T_{DUT}}$ and measured device response, $\boldsymbol{M_{DUT}}$ at the VNA ports level.

$$\boldsymbol{M_{DUT}} = \boldsymbol{X}.\boldsymbol{T_{DUT}}.\boldsymbol{Y} \qquad \text{(E.A1.2)}$$

The conversion from S-parameters (S-Matrix) to T-parameters (T-matrix) and inversely, allows writing the following expressions:

$$\boldsymbol{T} = \frac{1}{S_{21}} \begin{bmatrix} S_{21}S_{12} - S_{11}S_{22} & S_{11} \\ -S_{22} & 1 \end{bmatrix} \; ; \; \boldsymbol{S} = \frac{1}{T_{22}} \begin{bmatrix} T_{12} & T_{11}T_{22} - T_{21}T_{12} \\ 1 & -T_{12} \end{bmatrix} \qquad \text{(E.A1.3)}$$

$$\boldsymbol{X} = r \begin{pmatrix} x_{11} & x_{12} \\ x_{21} & 1 \end{pmatrix} \; ; \; \boldsymbol{Y} = \rho \begin{pmatrix} y_{11} & y_{12} \\ y_{21} & 1 \end{pmatrix} \qquad \text{(E.A1.3)}$$

Reinjecting *X* and *Y* in the equation of the model (E.A1.2), we can obtain (E.A1.4). Then eight error terms become seven terms.

$$\boldsymbol{M} = r\rho \begin{pmatrix} x_{11} & x_{12} \\ x_{21} & 1 \end{pmatrix} . \boldsymbol{T} . \begin{pmatrix} y_{11} & y_{12} \\ y_{21} & 1 \end{pmatrix} = k \begin{pmatrix} x_{11} & x_{12} \\ x_{21} & 1 \end{pmatrix} . \boldsymbol{T} . \begin{pmatrix} y_{11} & y_{12} \\ y_{21} & 1 \end{pmatrix} = k \; \boldsymbol{A}.\boldsymbol{T}.\boldsymbol{B} \qquad \text{(E.A1.4)}$$

This section refers to [3]. The Thru-Reflect-Line process can be carried out in a few stages as in [3].

- Use of TRL kits to determine error boxes

The thru and line measurement allows determining the normalized calibration coefficients by solving an eigenvalue problem. The actual T-matrix of thru and line are respectively given by:

$$\boldsymbol{T_{thru}} = \begin{pmatrix} 1 & 0 \\ 0 & 1 \end{pmatrix} \; ; \; \boldsymbol{T_{line}} = \begin{pmatrix} e^{-\gamma l} & 0 \\ 0 & e^{\gamma l} \end{pmatrix} \qquad \text{(E.A1.5)}$$

Their measured responses correspond to the expressions:

$$\boldsymbol{M_{thru}} = k \; \boldsymbol{A}. \begin{pmatrix} 1 & 0 \\ 0 & 1 \end{pmatrix} . \boldsymbol{B} \qquad \text{(E.A1.6)}$$

$$\boldsymbol{M_{line}} = k \; \boldsymbol{A}. \begin{pmatrix} e^{-\gamma l} & 0 \\ 0 & e^{\gamma l} \end{pmatrix} . \boldsymbol{B} \qquad \text{(E.A1.7)}$$

Where l is difference length between line and thru standard and γ is the propagation constant. The multiplication of line measured T-matrix by the inverse of the thru measured T-matrix gives:

$$\boldsymbol{M_{line}}.\boldsymbol{M_{thru}}^{-1} = \boldsymbol{A}. \begin{pmatrix} e^{-\gamma l} & 0 \\ 0 & e^{\gamma l} \end{pmatrix} . \boldsymbol{A^{-1}} \qquad \text{(E.A1.8)}$$

The equation (E.A1.9) is typical of eigenvalue problem. In this case, $e^{-\gamma l}$ and $e^{\gamma l}$ are the eigenvalue and *A* contains the eigenvectors, as one can write:

$$\boldsymbol{M_{line}}.\boldsymbol{M_{thru}}^{-1}. \begin{pmatrix} x_{11} \\ x_{21} \end{pmatrix} = e^{-\gamma l} \begin{pmatrix} x_{11} \\ x_{21} \end{pmatrix} \; ; \; \boldsymbol{M_{line}}.\boldsymbol{M_{thru}}^{-1}. \begin{pmatrix} x_{12} \\ 1 \end{pmatrix} = e^{-\gamma l} \begin{pmatrix} x_{12} \\ 1 \end{pmatrix} \qquad \text{(E.A1.9)}$$

Normalizing the coefficients of first equation in (E.A1.9) holds:

$$\boldsymbol{M_{line}}.\boldsymbol{M_{thru}}^{-1}. \begin{pmatrix} 1 \\ \frac{x_{21}}{x_{11}} \end{pmatrix} = e^{-\gamma l} \begin{pmatrix} 1 \\ \frac{x_{21}}{x_{11}} \end{pmatrix} \; ; \; \boldsymbol{M_{line}}.\boldsymbol{M_{thru}}^{-1}. \begin{pmatrix} x_{12} \\ 1 \end{pmatrix} = e^{-\gamma l} \begin{pmatrix} x_{12} \\ 1 \end{pmatrix} \qquad \text{(E.A1.9)}$$

It may have two vectors, V_1 corresponding to $e^{-\gamma l}$ and V_2 to $e^{\gamma l}$, containing each two values, defined so that we can write:

$$\frac{x_{21}}{x_{11}} = \frac{V_1(2)}{V_1(1)} \; ; \; x_{12} = \frac{V_2(1)}{V_2(2)} \qquad \text{(E.A1.10)}$$

In the same way, the transpose of the multiplication of the inverse of the thru measured T-matrix by line measured T-matrix by gives:

$$(\boldsymbol{M_{thru}}^{-1}.\boldsymbol{M_{line}})^T = \boldsymbol{B}^T. \begin{pmatrix} e^{-\gamma l} & 0 \\ 0 & e^{\gamma l} \end{pmatrix} . (B^T)^{-1} \qquad \text{(E.A1.11)}$$

Normalizing the coefficients of first equation in (E.A1.9) holds:

$$(\boldsymbol{M_{thru}}^{-1}.\boldsymbol{M_{line}})^T. \begin{pmatrix} 1 \\ \frac{y_{12}}{y_{11}} \end{pmatrix} = e^{-\gamma l} \begin{pmatrix} 1 \\ \frac{y_{12}}{y_{11}} \end{pmatrix} \; ; \; (\boldsymbol{M_{thru}}^{-1}.\boldsymbol{M_{line}})^T. \begin{pmatrix} y_{21} \\ 1 \end{pmatrix} = e^{-\gamma l} \begin{pmatrix} y_{12} \\ 1 \end{pmatrix} \qquad \text{(E.A1.12)}$$

It may have two vectors, U_1 corresponding to $e^{-\gamma l}$ and U_2 to $e^{\gamma l}$, containing each two values, defined so that we can write:

$$\frac{y_{12}}{y_{11}} = \frac{U_1(2)}{U_1(1)} \; ; \; y_{21} = \frac{U_2(1)}{U_2(2)} \qquad \text{(E.A1.13)}$$

Until now, we have some ratios and calibration coefficients: $(x_{21}/\, x_{11} \; ; \; x_{12})$ and $(y_{12}/\, y_{11} \; ; \; y_{21})$. The last step on the error terms is to denormalize coefficients ratios and to find the k coefficient, which represents the seventh term.

Knowing that thru measurement is the direct cascade of error boxes, from (E.A1.4) ones can easily write:

$$\boldsymbol{M_{thru}} = k\begin{pmatrix} 1 & x_{12} \\ x_{21}/x_{11} & 1 \end{pmatrix}.\begin{pmatrix} x_{11} & 0 \\ 0 & 1 \end{pmatrix}.\begin{pmatrix} y_{11} & 0 \\ 0 & 1 \end{pmatrix}\begin{pmatrix} 1 & y_{12}/y_{11} \\ y_{21} & 1 \end{pmatrix} \quad \text{(E.A1.14)}$$

By inversing (E.A1.14), the equation (E.A1.15) can be driven and allows the determination of the quantities: $k.x_{11}y_{11}$, k hence, $x_{11}y_{11}$.

$$\begin{pmatrix} k.x_{11}y_{11} & 0 \\ 0 & k \end{pmatrix} = \begin{pmatrix} 1 & x_{12} \\ x_{21}/x_{11} & 1 \end{pmatrix}^{-1} \boldsymbol{M_{thru}} \cdot \begin{pmatrix} 1 & y_{12}/y_{11} \\ y_{21} & 1 \end{pmatrix}^{-1} \quad \text{(E.A1.15)}$$

The reflect standard enable to completely achieve all error terms. This may be symmetric and presents the same reflection coefficient at each port. Its actual reflect coefficient is Γ. Its measured coefficient at port 1 is Γ_x and Γ_y at port 2. The relationship between them is given:

$$\Gamma_x = \frac{x_{12}+x_{11}\Gamma}{1+x_{21}\Gamma} \rightarrow \Gamma = \frac{\Gamma_x - x_{12}}{x_{11}-x_{21}\Gamma_x} \quad \text{(E.A1.16)}$$

$$\Gamma_y = \frac{-y_{21}+y_{11}\Gamma}{1-y_{12}\Gamma} \rightarrow \Gamma = \frac{\Gamma_y + y_{21}}{y_{11}+y_{12}\Gamma_x} \quad \text{(E.A1.17)}$$

From the two last equations (E.A1.16) and (E.A1.18), we can derive the ratio, $x_{11}/y_{11,}$ which is equivalent to:

$$\frac{x_{11}}{y_{11}} = \frac{\Gamma_x - x_{12}}{1-\frac{x_{21}}{x_{11}}\Gamma_x}.\frac{1+\frac{y_{12}}{y_{11}}\Gamma_x}{\Gamma_y+y_{21}} \quad \text{(E.A1.18)}$$

Finally, we can obtain x_{11}, y_{11} using the expressions in (E.A1.19):

$$x_{11} = \pm\sqrt{\frac{x_{11}}{y_{11}}.x_{11}y_{11}}\ ;\ y_{11} = \frac{x_{11}y_{11}}{x_{11}} \quad \text{(E.A1.19)}$$

Little beat effort has to be done to distinguish right value of x_{11}. The sign ambiguity is overcame based on the concordance of the determined actual reflection coefficient of reflect standard to the expected value. If we use short or open standard this value is near to -1 or +1.
We resume all terms in the Table A1.1 to clearly explicit the error terms, in which the additional load match error terms are included when converting the model to twelve errors terms model.

Table A1.1: Errors terms or calibration coefficients

Error Terms	Forward	Reverse
Directivity: $E_{DF,R}$	$E_{DF} = x_{12}$	E_{DR} =-y_{21}
Source match: $E_{SF,R}$	$E_{SF} = x_{21}$	$E_{SR} = y_{12}$
Reflection tracking: $E_{RF,R}$	$E_{RF} = x_{11} - x_{12}.x_{21}$	$E_{RR} = y_{11} - y_{12}.y_{21}$
Transmission tracking: $E_{TF,R}$	$E_{TF} = \dfrac{1}{k(1-E_{DR}.\Gamma_F)}$	$E_{TR} = \dfrac{k.E_{RR}.E_{RF}}{(1-E_{DF}.\Gamma_R)}$
Load match: $E_{LF,R}$	$E_{LF} = E_{SR} + \dfrac{E_{RR}.\Gamma_F}{(1-E_{DR}.\Gamma_F)}$	$E_{LR} = E_{SF} + \dfrac{E_{RF}.\Gamma_R}{(1-E_{DF}.\Gamma_R)}$

- Propagation constant and effective permittivity extraction

The propagation constant γ is extractible from the eigenvalue problem solving. Supposing that the first eigenvalue $\lambda_1$is associated with $e^{-\gamma l}$ and the second λ_2 with $e^{\gamma l}$, then defining the ratio, λ_2/λ_1, we can write:

$$e^{2\lambda l} = \lambda_2/\lambda_1 \quad \text{(E.A1.20)}$$

Applying logarithm function, (E.A1.21) becomes:

$$2\lambda l + i2\pi n = \log\left(\lambda_2/\lambda_1\right) \quad \text{(E.A1.21)}$$

Here, it is important to account the wrap factor to determine accurately γ. For doing this, ones can make estimation on the propagation constant, γ_{est}, then find the integer n as follows:

$$n = round\left(\frac{Imag(\log\left(\frac{\lambda_2}{\lambda_1}\right) - 2\gamma_{est}.l}{2\pi}\right) \quad \text{(E.A1.22)}$$

The unwrapped γ is given by:

$$\gamma^{unwrap} = \frac{\log\left(\frac{\lambda_2}{\lambda_1}\right) - i2\pi n}{2l} \tag{E.A1.24}$$

The effective permittivity is related to propagation constant by the expression:

- Perform calibration

After determining errors boxes $\boldsymbol{X}$ and $\boldsymbol{Y}$, we can carry out the calibration through measurement model equation (E.A1.2), descripted earlier in the section. Typically, this consists of extracting these systematic errors to achieve true response of the DUT by inverting this equation, as following:

$$\boldsymbol{T_{DUT}} = \boldsymbol{X^{-1}}.\boldsymbol{M_{DUT}}.\boldsymbol{Y^{-1}} \tag{E.A1.2}$$

The TRL calibration presents many advantages. It does not need the entire knowledge of standards and belongs to self-determination methods. From this, one can build new traceable standards. Other aspect of this technique is that is possible to shift the measurement reference plane from the center of the thru standard to a distance, and to transform the reference impedance.

Appendix 2: LRM algorithm

The Line-Reflect-Match (LRM) was discovered in the 1980s [4]. Like TRL, it replaces the second line standard with a matched load (Match). It is a self-calibration method that does not require prior knowledge of all standards, except for the match standard, which must be well-defined and symmetrical at both ports. Its impedance consists of a DC resistance *Rdc* close to 50 Ohms in series with a reactance *L* that depends on frequency, allowing the method to achieve a wider bandwidth than TRL. This method has been significantly improved and is now referred to as LRM+ [5], [6].

Like any algorithm, LRM begins with the definition of the theoretical transfer matrices representing the standards. Specifically, we have the true matrices T_1 for the line standard, T_2 for the reflect standard, and T_3 for the match standard, which correspond to the measured transfer matrices M_1, M_2, and M_3, respectively, in that order. It is recalled that the measured transfer matrix M_i and the theoretical matrix T_i are related by:

$$M_i = X.T_i.Y \tag{E.A2.1}$$

Where *X* and *Y* are systematic error boxes that are given by:

$$X = r\begin{pmatrix} x_{11} & x_{12} \\ x_{21} & 1 \end{pmatrix} \tag{E.A2.2}$$

$$Y = \rho\begin{pmatrix} y_{11} & y_{12} \\ y_{21} & 1 \end{pmatrix} \tag{E.A2.3}$$

- The knowledge of the propagation constant γ and the line length *l* is required for the line standard. Its actual matrix is:

$$T_1 = \begin{pmatrix} e^{-\gamma l} & 0 \\ 0 & e^{\gamma l} \end{pmatrix} \tag{E.A2.4}$$

- The reflect standard can be an unknown Open or Short with a phase of ±90°. It must be highly reflective (with minimal loss) and have identical reflection coefficient at both ports. Its actual and measured T-parameters are:

$$T_2 = \frac{1}{S_{21}^r}\begin{pmatrix} -\Gamma_r^2 & \Gamma_r \\ -\Gamma_r & 1 \end{pmatrix}; \quad M_2 = \frac{1}{S_{21}^{rM}}\begin{pmatrix} S_{21}^{rM}.S_{21}^{rM} - S_{11}^{rM}.S_{22}^{rM} & S_{11}^{rM} \\ -S_{22}^{rM} & 1 \end{pmatrix} \tag{E.A2.5}$$

- The real part of the match standard impedance should be sufficiently close to the system impedance Z_0, and the unknown reactance *Ls* should be small. The true and measured T-matrices of the match standard are:

$$T_3 = \frac{1}{S_{21}^m}\begin{pmatrix} -\Gamma_m^2 & \Gamma_m \\ -\Gamma_m & 1 \end{pmatrix};\ M_3 = \frac{1}{S_{21}^{mM}}\begin{pmatrix} S_{21}^{mM}.S_{21}^{mM} - S_{11}^{mM}.S_{22}^{mM} & S_{11}^{mM} \\ -S_{22}^{mM} & 1 \end{pmatrix} \quad \text{(E.A2.6)}$$

The method is based on the redundancy of equations to overcome certain unknown parameters and singularities; to achieve this, the matrices are combined with each other. Thus, the matrix products of line with reflect (T_{21}) and line with match (T_{31}), corresponding to the measured data matrices M_{21} and M_{31}, are performed to yield:

$$T_{21} = T_2.T_1^{-1} = \frac{1}{S_{21}^r}\begin{pmatrix} -\Gamma_r^2 e^{\gamma l} & \Gamma_r e^{-\gamma l} \\ -\Gamma_r e^{\gamma l} & e^{-\gamma l} \end{pmatrix};\ M_{21} = M_2.M_1^{-1} = \begin{pmatrix} M_{21}^{11} & M_{21}^{12} \\ M_{21}^{21} & M_{21}^{11} \end{pmatrix} \quad \text{(E.A2.7)}$$

$$T_{31} = T_3.T_1^{-1} = \frac{1}{S_{21}^m}\begin{pmatrix} -\Gamma_m^2 e^{\gamma l} & \Gamma_m e^{-\gamma l} \\ -\Gamma_m e^{\gamma l} & e^{-\gamma l} \end{pmatrix};\ M_{31} = M_3.M_1^{-1} = \begin{pmatrix} M_{31}^{11} & M_{31}^{12} \\ M_{31}^{21} & M_{31}^{11} \end{pmatrix} \quad \text{(E.A2.8)}$$

Moreover, the following relationships can be demonstrated and reveal the criterion of similar matrices:

$$M_{21}.X = X.T_{21} \quad ; \quad M_{31}.X = X.T_{31} \quad \text{(E.A2.9)}$$

$$Y.M_{12} = T_{21}.Y \quad ; \quad Y.M_{13} = T_{13}.Y \quad \text{(E.A2.10)}$$

The matrices M_{21} and T_{21}, M_{31} and T_{31} in equations (E.A2.9) are similar. By applying the algebraic properties of similar matrices, the preservation of trace and determinant in particular, the following relationships can be established:

$$M_{21}^{11} + M_{21}^{22} = \frac{1}{S_{21}^r}(e^{-\gamma l} - \Gamma_r^2 e^{\gamma l}) \quad \text{(E.A2.11)}$$

$$M_{31}^{11} + M_{31}^{22} = \frac{1}{S_{21}^m}(e^{-\gamma l} - \Gamma_m^2 e^{\gamma l}) \quad \text{(E.A212)}$$

In principle, reflect and match are not transmission standards (S_{21}^r= 0, S_{21}^m= 0); equations (E.A2.11) and (E.A2.12) allow these singularities to be overcame and facilitate normalization.

$$\frac{1}{S_{21}^r} = \frac{M_{21}^{11}+M_{21}^{22}}{(e^{-\gamma l}-\Gamma_r^2 e^{\gamma l})} \quad \text{(E.A2.13)}$$

$$\frac{1}{S_{21}^m} = \frac{M_{31}^{11}+M_{31}^{22}}{(e^{-\gamma l}-\Gamma_r^2 e^{\gamma l})} \quad \text{(E.A2.14)}$$

The coefficient Γ_r is unknown; it can be determined by combining the similar matrices.

$$T_{32} = T_{31}.T_{21}^{-1} = \begin{pmatrix} T_{32}^{11} & T_{32}^{12} \\ T_{32}^{21} & T_{32}^{22} \end{pmatrix} \quad \text{(E.A2.15)}$$

$$\mathrm{M}_{32} = \mathrm{M}_{31}.\mathrm{M}_{21}^{-1} = \begin{pmatrix} \mathrm{M}_{32}^{11} & \mathrm{M}_{32}^{12} \\ \mathrm{M}_{32}^{21} & \mathrm{M}_{32}^{11} \end{pmatrix} \quad \text{(E.A2.16)}$$

By applying the property of trace preservation between these two matrices, we arrive at the following equation.

$$\left(K_{31}^{21}.\Gamma_m^2.e^{2\gamma l} + 1 - K_{31}^{21}\right).\Gamma_r^2 - 2\Gamma_m.\Gamma_r + (1 - K_{31}^{21}).\Gamma_m^2 + K_{31}^{21}.e^{-2\gamma l} = 0 \quad \text{(E.A2.17)}$$

Where K_{31}^{21} is a constant derived from measured data.

$$K_{31}^{21} = \frac{M_{31}^{11}.M_{21}^{22} - M_{31}^{21}.M_{21}^{21} - M_{31}^{21}.M_{21}^{12} + M_{21}^{22}.M_{31}^{11}}{(M_{31}^{11}+M_{31}^{22})+(M_{21}^{11}+M_{21}^{22})} \quad \text{(E.A2.18)}$$

In equation (E.A2.17), the reflection coefficient of the match (Γ_m) is not precisely known due to its reactance Ls, nor is the reflection coefficient Γ_r of the Reflect. A useful trick is to do estimation on the match by assuming $\Gamma_m = 0$, which gives the estimated reflection coefficient of the reflect standard as:

$$\Gamma_{re} = \pm\sqrt{\frac{K_{31}^{21}.e^{-2\gamma l}}{K_{31}^{21}-1}} \quad \text{(E.A2.19)}$$

The estimated and actual reflection coefficients of reflect standard are related by:

$$\Gamma_r = \pm\frac{\Gamma_m-\Gamma_{re}}{1-\Gamma_m\Gamma_{re}e^{2\gamma l}} \quad \text{(E.A2.20)}$$

The expression for the match reflection coefficient is given by:

$$\Gamma_m = \frac{Z_m-Z_0}{Z_m+Z_0} = \frac{Rdc+i\omega Ls-Z_0}{Rdc+i\omega Ls+Z_0} \quad \text{(E.A2.21)}$$

By considering a reflect with a magnitude close to 1 and Rdc = Z_0, (E.A2.20) and (E.A2.21) it is possible to accurately determine the reactance Ls, as shown in the second-degree equation below.

$$(\Gamma_{re}\Gamma_r e^{2\gamma l} + 1 - \Gamma_m - \Gamma_{re}).(i\omega \boldsymbol{Ls})^2 + 2Z_0(\Gamma_{re}.\Gamma_r.e^{2\gamma l} - 1).(i\omega \boldsymbol{Ls}) - 4Z_0(\Gamma_{re} - \Gamma_r) = 0 \quad \text{(E.A2.22)}$$

Appendix 3: SOLT algorithm

SOLT calibration is one of the most widely used calibration methods. It is based on the use of standards (Short-Open-Load-Thru), which respectively refer to short circuit, open circuit, matched load, and direct connection [2]. These standards must be well-defined and characterized by models and data. With this knowledge, they can be measured or tested using a VNA in order to determine the error terms. The use of all four standards allows for the extraction of directivity, source match, reflection and transmission tracking, and even isolation or crosstalk errors.

This method aims to determine the system calibration coefficients described in the previous section. Once the S-O-L-T standards are properly defined, the error terms can be evaluated. Virtual networks inserted between the VNA and the device under test represent these terms (Fig. A2.1).

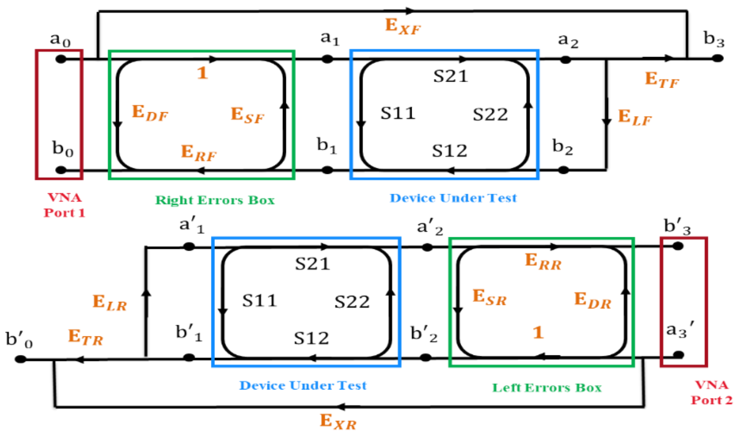

Fig. A3.1: Two-port measurement model (12-errors terms).

By analyzing and applying Mason's rules to the network diagram shown in Fig. A3.1, the equation relating the error terms at port 1 can be written.

$$\Gamma_M = E_{DF} + \frac{1.E_{RF}.\Gamma}{1-E_{SF}.\Gamma} \quad \text{(E.A3.1)}$$

By setting $\Delta_{e1} = E_{DF} \cdot E_{SF} - 1.E_{RF}$, equation (E.A3.1) becomes:

$$\Gamma_M = \frac{E_{DF} - \Delta_{e1}.\Gamma}{1 - E_{SF}.\Gamma} \qquad \text{(E.A3.1)}$$

Finally, the measured value, the true value, and the error terms in reflection are related by the following equation.

$$E_{DF} + \Gamma.\Gamma_{\mathrm{M}}.E_{SF} - \Gamma.\Delta_{\mathrm{e1}} = \Gamma_{\mathrm{M}} \qquad \text{(E.A3.3)}$$

This last equation involves three unknowns, namely the error terms (E_{DF}, E_{SF}, E_{RF}), which are solved by performing a series of three measurements using different components or standards, typically Short, Open, and Load. This leads to the following system of linear equations (E.A.4):

$$\begin{cases} E_{DF} + \Gamma_1.\Gamma_{M1}.E_{SF} - \Gamma_1\Delta_{e1} = \Gamma_{M1} \\ E_{DF} + \Gamma_2.\Gamma_{M2}.E_{SF} - \Gamma_2\Delta_{e1} = \Gamma_{M2} \\ E_{DF} + \Gamma_3.\Gamma_{M3}.E_{SF} - \Gamma_3\Delta_{e1} = \Gamma_{M3} \end{cases} \qquad \text{(E.A.4)}$$

This procedure is repeated at the second port, in the reverse direction, to determine the error terms (E_{DR}, E_{SR}, E_{RR}). After calibration, a one-port device connected to port 1 can be measured, and its true value Γ is expressed as a function of the measured value Γ_m and the error terms obtained during calibration, as shown in equation (E.A2.5).

$$\Gamma = \frac{\Gamma_M - e_{00}}{\Gamma_M e_{11} - \Delta_{e1}} \qquad \text{(E.A2.5)}$$

The measurement of the Load standard at each port, on one hand, and the thru standard, on the other hand, allows for the determination of the error terms (E_{TF}, E_{TR}, E_{LF}, E_{LR}, E_{XF}, E_{XR}).

$$E_{XF} = S_{21}^{dual\ Load} \qquad \text{(E.A3.6)}$$

$$E_{XR} = S_{12}^{dual\ Load} \qquad \text{(E.A3.7)}$$

$$E_{LF} = \frac{S_{11}^{thru} - E_{DF}}{(S_{11}^{thru}.E_{SF} - \Delta_{e1}).e^{-\gamma l}} \qquad \text{(E.A3.8)}$$

$$E_{LR} = \frac{S_{22}^{thru} - E_{DR}}{(S_{22}^{Thru}E_{SR} - \Delta_{e2}).e^{-\gamma l}} \qquad \text{(E.A3.9)}$$

$$E_{TF} = \left(S_{21}^{thru} - E_{XF}\right).\left[e^{\gamma l} - E_{SF}.E_{LF}.e^{-\gamma l}\right] \qquad \text{(E.A3.10)}$$

$$E_{TR} = \left(S_{12}^{thru} - E_{XR}\right).\left[e^{\gamma l} - E_{SR}.E_{LR}.e^{-\gamma l}\right] \qquad \text{(E.A3.11)}$$

Once all the error terms are known, the S-parameters for the two-port device under test can be extracted by using the following equations:

$$D = \left(1 + \left(\frac{S_{11M} - E_{DF}}{E_{RF}}\right)E_{SF}\right)\left(1 + \left(\frac{S_{22M} - E_{DR}}{E_{RR}}\right)E_{SR}\right) - \left(\frac{S_{21} - E_{XF}}{E_{TF}}\right)\left(\frac{S_{12} - E_{XR}}{E_{TR}}\right)E_{LF}.E_{LR} \qquad \text{(E.A3.12)}$$

$$S_{11} = \frac{\left(\frac{S_{11M} - E_{DF}}{E_{RF}}\right)\left(1 + \left(\frac{S_{22M} - E_{DR}}{E_{RR}}\right)E_{SR}\right) - \left(\frac{S_{21} - E_{XF}}{E_{TF}}\right)\left(\frac{S_{12} - E_{XR}}{E_{TR}}\right)E_{LF}}{D} \qquad \text{(E.A3.13)}$$

$$S_{21} = \frac{\left(\frac{S_{21} - E_{XF}}{E_{TF}}\right)\left(1 + \left(\frac{S_{22M} - E_{DR}}{E_{RR}}\right)(E_{SR} - E_{LF})\right)}{D} \qquad \text{(E.A3.14)}$$

$$S_{22} = \frac{\left(\frac{S_{22M} - E_{DR}}{E_{RR}}\right)\left(1 + \left(\frac{S_{11M} - E_{DF}}{E_{RF}}\right)E_{SF}\right) - \left(\frac{S_{21} - E_{XF}}{E_{TF}}\right)\left(\frac{S_{12} - E_{XR}}{E_{TR}}\right)E_{LR}}{D} \qquad \text{(E.A3.15)}$$

$$S_{12} = \frac{\left(\frac{S_{12}-E_{XR}}{E_{TR}}\right)\left(1+\left(\frac{S_{11M}-E_{DF}}{E_{RF}}\right)(E_{SF}-E_{LR})\right)}{D} \quad \text{(E.A3.16)}$$

Appendix 4: LRRM algorithm

Line-Reflect-Reflect-Match method was developed by WinCal. As LRM technique, it is based on certain considerations regarding its standards. The values of the open, short, and match standards are initially unknown; they are estimated and optimized. The redundancy in the algorithm equations makes it possible to determine the error terms using both measurement data and estimated values. It is much more robust with respect to issues related to contact repeatability and probe tip alignment.

Appendix 5: Network theory

Two types of networks are considered in microwave analysis: linear networks and nonlinear networks. With a linear network, the input and output frequencies are identical. The output spectrum does not undergo distortion. In the case of a nonlinear network, the output spectrum shows distortion due to harmonics. The input frequency can be altered, this is the case, for example, with a frequency mixer. Other examples include diodes, transistors, etc.

In general, to characterize a linear two-port network, several types of parameters are used depending on the area of interest. These include, notably, Z, Y, ABCD, S, and T parameters, among others.

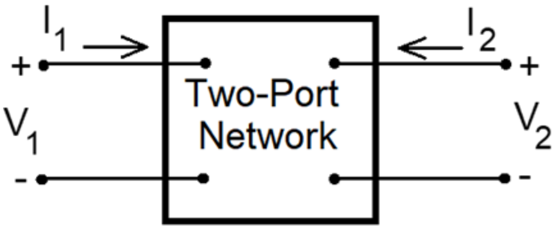

Fig. A5.1: Two port network

Z-parameters

Impedance parameters, commonly referred to as Z-parameters, serve as a fundamental tool in the analysis of linear electrical circuits. These parameters are particularly advantageous when it comes to evaluating series impedances within a network. By focusing on the relationship between current and voltage at each port of a two-port network, Z-parameters provide a systematic way to characterize the network's behavior.

The Z-parameters are organized into what is known as the Z-matrix. Each element of this matrix is derived from the relationships observed between the currents and voltages at the two access points, or ports, of the network. This approach enables engineers to assess how the network will respond to various electrical inputs, making the Z-matrix an essential component in the study and design of linear circuits.

$$V_1 = Z_{11}I_1 + Z_{12}I_2 \quad \text{(E.A5.1)}$$

$$V_2 = Z_{21}I_1 + Z_{22}I_2 \quad \text{(E.A5.2)}$$

$$Z = \begin{pmatrix} Z_{11} & Z_{12} \\ Z_{21} & Z_{22} \end{pmatrix} = \begin{pmatrix} \frac{V_1}{I_1}|I_2 = 0 & \frac{V_1}{I_2}|I_1 = 0 \\ \frac{V_2}{I_1}|I_2 = 0 & \frac{V_2}{I_2}|I_1 = 0 \end{pmatrix} \quad \text{(E.A5.3)}$$

Equation (E.A5.3) reveals that to determine every element of the Z-matrix, open-circuit terminations at the network's ports are required. However, implementing open circuits in practice, especially at high frequencies, is challenging. This difficulty arises because the open-circuit model introduces parasitic capacitance, which can impact the accuracy of the measurements. As frequency increases, these parasitic effects become more pronounced, making it increasingly difficult to ensure a true open-circuit condition during testing.

Despite these measurement challenges, it remains possible to represent the equivalent electrical circuit of a two-port network by utilizing the cascaded elements of the Z-parameter matrix. This approach allows for the systematic modeling of the network's behavior based on the relationships defined by the Z-parameters, providing insight into how the network will respond under various operating conditions.

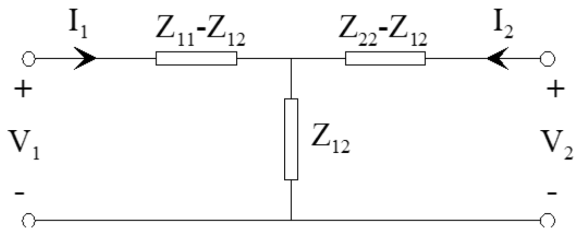

Fig. A5.2: Electrical representation of Z- parameters

if a two-port network is reciprocal, the Z-parameters are symmetric. Reciprocity in this context means that the transfer impedance from port 1 to port 2 is equal to the transfer impedance from port 2 to port 1. Mathematically, this condition is expressed as $Z_{21} = Z_{12}$.

When this reciprocal condition holds, the general Z-parameter representation of the network can be further simplified. The schematic depiction provided in Fig. A5.3 illustrates this simplified form, where the symmetry between Z21 and Z12 is clearly reflected in the network's equivalent circuit. This allows for a more straightforward analysis and understanding of the network's electrical behavior.

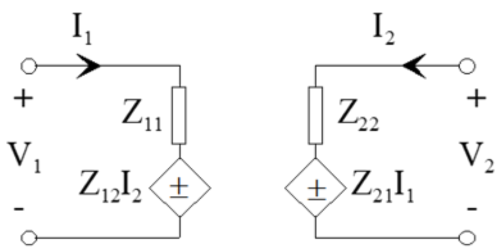

Fig. A5.3: Electrical representation of reciprocal Z- parameters

Y-parameters

In contrast to the Z-matrix, which is mainly used for analyzing series impedances in linear circuits, Y-parameters also known as admittance parameters are particularly useful when examining parallel capacitance within a two-port network. The analysis with Y-parameters centers on the relationship between current and voltage at each port. By considering how currents and voltages behave at the network's ports, Y-parameters provide a complementary perspective to Z-parameters, especially in scenarios where parallel elements dominate the network's behavior.

$$I_1 = Y_{11}V_1 + Y_{12}V_2 \tag{E.A5.4}$$

$$\mathrm{I}_2 = \mathrm{Y}_{21}V_1 + \mathrm{Y}_{22}\mathrm{V}_2 \tag{E.A5.5}$$

$$Y = \begin{pmatrix} Y_{11} & Y_{12} \\ Y_{21} & Y_{22} \end{pmatrix} = \begin{pmatrix} \frac{I_1}{V_1}|V_2 = 0 & \frac{I_1}{V_2}|V_1 = 0 \\ \frac{I_2}{V_1}|V_2 = 0 & \frac{I_2}{V_2}|V_1 = 0 \end{pmatrix} \tag{E.A5.6}$$

To determine the elements of the Y matrix, also known as the admittance matrix, it is necessary to apply short circuits at the network's ports. However, implementing short circuits at high frequencies presents practical difficulties because the short-circuit model introduces parasitic inductance, which can interfere with accurate measurements and analysis.

Despite these challenges, admittance parameters serve as an alternative method for representing an electrical two-port network. This representation is illustrated in Fig. A5.4, where the Y-parameters provide a framework for analyzing the relationship between the currents and voltages at each port, particularly in networks dominated by parallel elements.

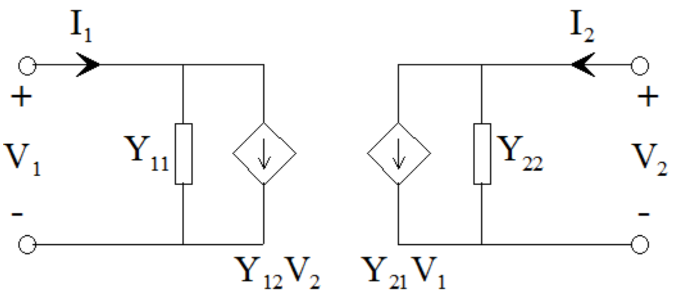

Fig. A5.4: Electrical representation of Y-parameters

When the two-port network is reciprocal, meaning that the admittance parameter Y21 is equal to Y12, the analysis of the network can be further simplified. In this case, the mutual admittance between the two ports is identical in both directions, reflecting the reciprocal behavior of the network. This symmetry allows for a more straightforward representation, which is depicted in Fig. A5.5. The reciprocal condition reduces the complexity of the network's mathematical model, making it easier to analyze and interpret the relationship between the ports using Y-parameters.

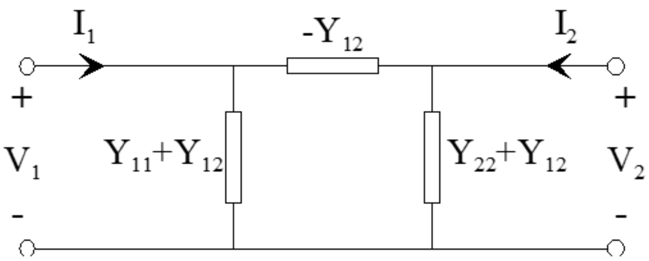

Fig. A5.5: Electrical representation of reciprocal Y-parameters

ABCD-parameters

The ABCD matrix, also known as the transmission matrix, is a fundamental tool for representing a two-port electrical network. This matrix provides a systematic way to describe how voltages and currents at the input of the network relate to those at the output. Specifically, the ABCD parameters encapsulate the linear equations that express the relationships between the input and output voltages and currents within the two-port network.

Each letter in the ABCD matrix A, B, C, and D corresponds to a specific matrix element. These elements are defined by the system of linear equations that connect the input and output variables. By using the ABCD matrix, engineers can conveniently analyze complex networks and determine how signals are transmitted from one port to another within the network.

$$V_1 = A.V_2 + B.I_2 \tag{E.A5.7}$$

$$I_1 = C.V_2 + D.I_2 \tag{E.A5.8}$$

$$ABCD = \begin{pmatrix} A & B \\ C & D \end{pmatrix} = \begin{pmatrix} \frac{V_1}{V_2}|I_2 = 0 & \frac{V_1}{I_2}|I_1 = 0 \\ \frac{V_2}{V_2}|I_2 = 0 & \frac{I_1}{I_2}|I_1 = 0 \end{pmatrix} \quad \text{(E.A5.9)}$$

The advantage of using ABCD-parameters is their ability to simplify the analysis of cascaded two-port networks. When multiple two-port networks are connected in series, their overall behavior can be determined by multiplying their respective ABCD matrices. This property makes ABCD-parameters especially valuable in high-frequency signal analysis, where complex systems are often constructed by cascading several network stages.

For example, consider two network circuits arranged in a cascade configuration. The overall ABCD matrix for the combined system is obtained by multiplying the ABCD matrices of the individual networks, as demonstrated by equation (E.A5.10) and illustrated in Fig. A5.6. This matrix multiplication approach provides a systematic method for evaluating the collective response of cascaded networks, allowing engineers to efficiently analyze signal transmission through multi-stage systems.

$$[ABCD] = [ABCD]_1 * [ABCD]_2 \quad \text{(E.A5.10)}$$

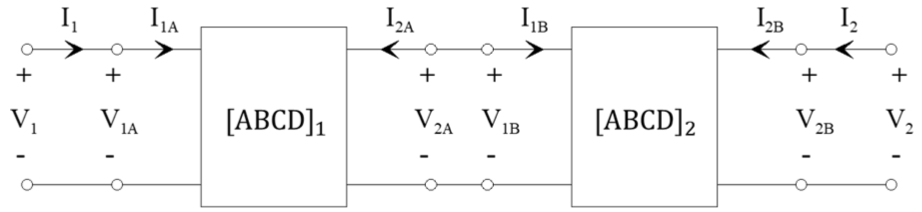

Fig. A5.6: Cascade of ABCD matrices

S-parameters

S-parameters, also known as scattering parameters, are dimensionless complex values that characterize the reflection and transmission behavior of a network with one or more ports. These parameters describe how power waves originating from a source interact with the network, specifically by quantifying how much power is reflected towards the source and how much is transmitted through the network.

Each S-parameter represents a ratio of power waves: either between the incident wave and the reflected wave, or between the incident wave and the transmitted wave. This makes S-parameters an essential tool for analyzing signal flow and impedance matching in radio frequency (RF) and microwave engineering, where they help engineers understand how a network responds to signals at different ports.

For a two-port network, the elements of the S matrix are defined by specific mathematical expressions. These elements detail the relationships between the incident and outgoing power waves at each port, effectively mapping the network's scattering characteristics. The S matrix thus provides a comprehensive description of how signals propagate and interact within the two-port system:

$$b_1 = S_{11}a_1 + S_{12}a_2 \quad \text{(E.A5.11)}$$

$$\mathrm{b}_2 = \mathrm{S}_{21}a_1 + \mathrm{S}_{22}a_2 \quad \text{(E.A5.12)}$$

$$S = \begin{pmatrix} S_{11} & S_{12} \\ S_{21} & S_{22} \end{pmatrix} = \begin{pmatrix} \frac{b_1}{a_1}|a_2 = 0 & \frac{b_1}{a_2}|a_1 = 0 \\ \frac{b_2}{a_1}|a_2 = 0 & \frac{b_2}{a_2}|a_1 = 0 \end{pmatrix} \quad \text{(E.A5.13)}$$

T-parameters

T-parameters, also known as transfer parameters, are fundamentally like S-parameters in that both are derived from ratios of power waves associated with a two-port network. However, T-parameters present distinct advantages when analyzing cascaded two-port networks. Specifically, when two-port networks are arranged in cascade, their respective T-matrices can be simply multiplied to yield the overall network's T-matrix. This property greatly simplifies the analysis of cascaded circuits.

Additionally, a straightforward mathematical transformation exists between S-parameters and T-parameters, allowing easy conversion between these two representations. The ability to cascade T-parameter matrices is frequently leveraged in de-embedding routines, which are used to isolate the characteristics of a specific network within a larger measurement setup.

Another notable advantage of T-parameters is that, unlike the ABCD matrix, there is no requirement to specify the reference impedance of the circuit. This makes T-parameters particularly convenient in situations where impedance matching is complex or variable.

The relationship between the power waves and the elements of the T-matrix is described by the following equations:

$$a_1 = T_{11}b_2 + T_{12}a_2 \tag{E.A5.14}$$

$$\mathrm{b}_1 = \mathrm{T}_{21}b_2 + \mathrm{T}_{22}a_2 \tag{E.A5.15}$$

$$T = \begin{pmatrix} T_{11} & T_{12} \\ T_{21} & T_{22} \end{pmatrix} = \begin{pmatrix} \frac{a_1}{b_2}|a_2 = 0 & \frac{a_1}{a_2}|b_2 = 0 \\ \frac{b_1}{b_2}|a_2 = 0 & \frac{b_1}{a_2}|b_2 = 0 \end{pmatrix} \tag{E.A5.16}$$

All these network parameters such as S-parameters, T-parameters, Z-parameters, Y-parameters, and ABCD-parameters are interrelated and can be mathematically converted from one form to another. Table of matrices conversion provides a comprehensive guide for converting elements between these different parameter matrices. By using this table, it is possible to express the characteristics of a two-port network in any of the commonly used matrix forms, facilitating flexible analysis and design of complex networks.

Table of Matrices Conversion

Parameters	S-parameters	T-parameters	Z-parameters	Y-parameters	ABCD-parameters
S_{11}	-	$\frac{T_{12}}{T_{22}}$	$\frac{(Z_{11}-Z_0)(Z_{22}+Z_0)-Z_{12}Z_{21}}{\Delta Z}$	$-\frac{(Y_{11}-Y_0)(Y_{22}+Y_0)-Y_{12}Y_{21}}{\Delta Y}$	$\frac{A+\frac{B}{Z_0}-CZ_0-D}{A+\frac{B}{Z_0}+CZ_0+D}$
S_{12}	-	$\frac{T_{11}T_{22}-T_{12}T_{21}}{T_{22}}$	$\frac{2Z_{12}Z_0}{\Delta Z}$	$\frac{-2Y_{12}Y_0}{\Delta Y}$	$\frac{AD-BC}{A+\frac{B}{Z_0}+CZ_0+D}$
S_{21}	-	$\frac{1}{T_{22}}$	$\frac{2Z_{21}Z_0}{\Delta Z}$	$\frac{-2Y_{21}Y_0}{\Delta Y}$	$\frac{2}{A+\frac{B}{Z_0}+CZ_0+D}$
S_{22}	-	$-\frac{T_{21}}{T_{22}}$	$\frac{(Z_{11}+Z_0)(Z_{22}-Z_0)-Z_{12}Z_{21}}{\Delta Z}$	$-\frac{(Y_{11}+Y_0)(Y_{22}-Y_0)-Y_{12}Y_{21}}{\Delta Y}$	$\frac{-A+\frac{B}{Z_0}-CZ_0+D}{A+\frac{B}{Z_0}+CZ_0+D}$
T_{11}	$\frac{S_{12}S_{21}-S_{11}S_{22}}{S_{21}}$	-	$\frac{(Z_{11}+Z_0)(Z_{22}+Z_0)-Z_{12}Z_{21}}{2Z_{21}Z_0}$	$\frac{-(Y_{11}+Y_0)(Y_{22}+Y_0)+Y_{12}Y_{21}}{2Y_{21}Y_0}$	$\frac{A+\frac{B}{Z_0}+CZ_0+D}{2}$
T_{12}	$\frac{S_{11}}{S_{21}}$	-	$-\frac{(Z_{11}+Z_0)(Z_{22}-Z_0)-Z_{12}Z_{21}}{2Z_{21}Z_0}$	$\frac{-(Y_{11}+Y_0)(Y_{22}-Y_0)+Y_{12}Y_{21}}{2Y_{21}.Y_0}$	$\frac{A-\frac{B}{Z_0}+CZ_0-D}{2}$
T_{21}	$-\frac{S_{22}}{S_{21}}$	-	$\frac{(Z_{11}-Z_0)(Z_{22}+Z_0)-Z_{12}Z_{21}}{2Z_{21}Z_0}$	$\frac{(Y_{11}-Y_0)(Y_{22}+Y_0)-Y_{12}Y_{21}}{2Y_{21}Y_0}$	$\frac{A+\frac{B}{Z_0}+CZ_0-D}{2}$
T_{22}	$\frac{1}{S_{21}}$	-	$-\frac{(Z_{11}-Z_0)(Z_{22}-Z_0)-Z_{12}Z_{21}}{2Z_{21}Z_0}$	$\frac{(Y_{11}-Y_0)(Y_{22}-Y_0)+Y_{12}Y_{21}}{2Y_{21}Y_0}$	$\frac{A-\frac{B}{Z_0}-CZ_0+D}{2}$
Z_{11}	$\frac{Z_0(1+S_{11})(1-S_{22})+S_{12}S_{21}}{(1-S_{11})(1-S_{22})-S_{12}S_{21}}$	$\frac{Z_0(T_{11}+T_{12}+T_{21}+T_{22})}{T_{11}+T_{12}-T_{21}-T_{22}}$	-	$\frac{Y_{22}}{\lvert Y\rvert}$	$\frac{A}{C}$
Z_{12}	$\frac{2Z_0S_{12}}{(1-S_{11})(1-S_{22})-S_{12}S_{21}}$	$\frac{2Z_0(T_{11}T_{22}-T_{12}T_{21})}{T_{11}+T_{12}-T_{21}-T_{22}}$	-	$-\frac{Y_{12}}{\lvert Y\rvert}$	$\frac{AD-BC}{C}$
Z_{21}	$\frac{2Z_0S_{21}}{(1-S_{11})(1-S_{22})-S_{12}S_{21}}$	$\frac{2Z_0}{T_{11}+T_{12}-T_{21}-T_{22}}$	-	$-\frac{Y_{21}}{\lvert Y\rvert}$	$\frac{1}{C}$
Z_{22}	$\frac{Z_0(1-S_{11})(1+S_{22})+S_{12}S_{21}}{(1-S_{11})(1-S_{22})-S_{12}S_{21}}$	$\frac{Z_0(T_{11}-T_{12}-T_{21}-T_{22})}{T_{11}+T_{12}-T_{21}-T_{22}}$	-	$\frac{Y_{11}}{\lvert Y\rvert}$	$\frac{D}{C}$
Y_{11}	$\frac{Y_0(1-S_{11})(1+S_{22})+S_{12}S_{21}}{(1+S_{11})(1+S_{22})-S_{12}S_{21}}$	$\frac{Y_0(T_{11}-T_{12}-T_{21}+T_{22})}{T_{11}-T_{12}+T_{21}-T_{22}}$	$\frac{Z_{22}}{\lvert Z\rvert}$	-	$\frac{D}{B}$
Y_{12}	$\frac{-2Y_0S_{12}}{(1+S_{11})(1+S_{22})-S_{12}S_{21}}$	$\frac{-2Y_0(T_{11}T_{22}-T_{21}T_{12})}{T_{11}-T_{12}+T_{21}-T_{22}}$	$-\frac{Z_{12}}{\lvert Z\rvert}$	-	$\frac{BC-AD}{B}$
Y_{21}	$\frac{-2Y_0S_{21}}{(1+S_{11})(1+S_{22})-S_{12}S_{21}}$	$\frac{-2Y_0}{T_{11}-T_{12}+T_{21}-T_{22}}$	$-\frac{Z_{21}}{\lvert Z\rvert}$	-	$-\frac{1}{B}$
Y_{22}	$\frac{Y_0(1+S_{11})(1-S_{22})+S_{12}S_{21}}{(1+S_{11})(1+S_{22})-S_{12}S_{21}}$	$\frac{Y_0(T_{11}+T_{12}+T_{21}+T_{22})}{T_{11}-T_{12}+T_{21}-T_{22}}$	$\frac{Z_{11}}{\lvert Z\rvert}$	-	$\frac{A}{B}$
A	$\frac{(1+S_{11})(1-S_{22})+S_{12}S_{21}}{2S_{21}}$	$\frac{(T_{11}+T_{12}+T_{21}+T_{22})}{2}$	$\frac{Z_{11}}{Z_{21}}$	$-\frac{Y_{22}}{Y_{21}}$	-
B	$\frac{Z_0(1+S_{11})(1+S_{22})-S_{12}S_{21}}{2S_{21}}$	$\frac{Z_0(T_{11}-T_{12}+T_{21}-T_{22})}{2}$	$\frac{\lvert Z\rvert}{Z_{21}}$	$-\frac{1}{Y_{21}}$	-
C	$\frac{(1-S_{11})(1-S_{22})-S_{12}S_{21}}{2Z_0S_{21}}$	$\frac{(T_{11}+T_{12}-T_{21}-T_{22})}{2Z_0}$	$\frac{1}{Z_{21}}$	$-\frac{\lvert Y\rvert}{Y_{21}}$	-
D	$\frac{(1-S_{11})(1+S_{22})+S_{12}S_{21}}{2S_{21}}$	$\frac{(T_{11}-T_{12}-T_{21}+T_{22})}{2}$	$\frac{Z_{22}}{Z_{21}}$	$-\frac{Y_{11}}{Y_{21}}$	-

References 5

[1] ENGEN, Glenn F. et HOER, Cletus A. Thru-reflect-line: An improved technique for calibrating the dual six-port automatic network analyzer. IEEE transactions on microwave theory and techniques, 1979, vol. 27, no 12, p. 987-993.
[2] RUMIANTSEV, Andrej et RIDLER, Nick. VNA calibration. IEEE Microwave magazine, 2008, vol. 9, no 3, p. 86-99.
[3] https://ziadhatab.github.io/posts/trl-calibration/
[4] EUL, H.-J. et SCHIEK, B. Thru-match-reflect: One result of a rigorous theory for de-embedding and network analyzer calibration. In : 1988 18th European Microwave Conference. IEEE, 1988. p. 909-914.
[5] DOERNER, Ralf et RUMIANTSEV, Andrej. Verification of the wafer-level LRM+ calibration technique for GaAs applications up to 110 GHz. In : 65th ARFTG Conference Digest, 2005. Spring 2005. IEEE, 2005. p. 5 pp.
[6] SCHOLZ, René F., KORNDORFER, F., SENAPATI, Biswanath, et al. Advanced technique for broadband on-wafer RF device characterization. In : ARFTG 63rd Conference, Spring 2004. IEEE, 2004. p. 83-90.